THERMO-MECHANICAL EFFECTS OF MAGMA CHAMBERS AND CALDERA FAULTS

A thesis submitted for the degree of
Doctor of Philosophy at the
University of London

John Browning

Rock Fractures and Fluid Flow research group
Department of Earth Sciences
Royal Holloway, University of London

December 2015

Declaration

I, John Browning, hereby declare that this thesis and the work presented in it is entirely my own, unless otherwise stated. The main body of thesis, Chapters 3-6, forms a collection of co-authored papers which are either published, in press or in prep for publication. I am responsible for the data collection throughout this thesis, for primary authorship of all four of the included papers. Statements of my contribution are included on the cover page of each paper.

Signed

Dated

Abstract

Shallow magma chambers influence a range of crustal processes at active volcanoes. For example many and perhaps most dyke fed eruptions originate from shallow magma storage regions. Magma chamber failure, resulting in the initiation of caldera faults or magma filled fractures (dyke) is likely governed by a complex interplay between regional and local mechanical stresses and thermal effects. This study utilises a multitude of techniques to decipher salient thermo-mechanical processes occurring as a result of magma stored at shallow (<10 km) depth. A new model to forecast magma chamber rupture and dyke initiation is proposed. The analytical solutions presented are applied to field data from Santorini, Greece, and combine poro-elastic material constraints with geodetic data to estimate both magma volumes stored beneath the caldera and internal excess pressure generated during periods of magmatic recharge. Predicting the path or propagation of magma once it has left a shallow magma chamber is an important but so far unachievable goal in volcanology. Caldera faults offer pathways for magma and often develop ring-dykes. A previously unreported mechanism for the formation of ring-dykes is the capture of inclined sheets at caldera fault boundaries. Geological field observations of an exceptionally well-exposed ring-fault at Hafnarfjall in Western Iceland were used as input to the finite element method numerical modelling software COMSOL multiphysics to infer a mechanism of principal stress rotation within a fault damage zone. The same modelling technique was then used to estimate the far-field crustal displacements resulting from the failure and collapse of a shallow magma chamber roof. This study is framed within the context of the 2014-15 Bardarbunga-Holuhraun (Iceland) dyke injection and eruptive episode, and hypothesises that significant ice subsidence was not solely associated with crustal subsidence but instead related to ice flow within Bardarbunga caldera generated by the dyke emplacement. Thermal stresses resulting from hot magma emplacement and gradual cooling likely combine to weaken volcanic edifices. For example, field evidence suggests many normal faults nucleate from cooling joints. A suite of thermal stressing experiments finds that cooling and contraction produces larger and more abundant micro-cracks when compared with heating expansion. This is an important result when considering that almost all previous studies concerned with thermal stressing focused on the heating cycle.

Acknowledgements

First and foremost, my thanks go to Agust Gudmundsson and Philip Meredith as without their support and guidance this thesis would not have been possible. I thank Agust for introducing me to the world of volcano-tectonics, and allowing me substantial academic freedom such that I was able to develop a project and research framework that matched my interests. I thank Phil for agreeing to be a part of this project, and by doing so providing an unrivalled enthusiasm for experimental studies that has definitely caught on. Thank you both for the time devoted to helping me through this process. Thanks to the examiners Philip Benson and Valerio Acocella who contributed to improving the final thesis and providing interesting insights and ideas during my VIVA. Large components of this project involved fieldwork and for assistance in Iceland I thank Zoe Barnett (RHUL) and Hannah Reynolds (University of Iceland), and for making Greece my second home I thank Sandy Drymoni (RHUL). Much of this work benefitted from collaboration and discussions with numerous academics, of whom there are far too many to mention here but special thanks are owed to Yan Lavallée, Felix Von Aulock (University of Liverpool), Hugh Tuffen (Lancaster University), Tom Mitchell and Rick Wall (UCL). For assistance with designing and building our experimental apparatus I thank Neil Hughes, and I am indebted for almost constant assistance from Steve Boon. Jim Davey deserves a special mention for assistance with thin sections and SEM. I benefited greatly from attending several training courses and events organised by the EU network NEMOH in the early stages of my PhD. I am very happy to be considered an 'honorary NEMOH', and I am eternally grateful to have met many wonderful colleagues and friends from around the world during NEMOH events. Thanks to those who read, and re-read various sections of my thesis, especially Nathaniel Forbes-Inskip, Mohsen Bazargan, Jon Pownall, Ozgur Karaoglu and Hannah Reynolds (again). Thanks to my friends and family for supporting me through the last three years (and more). Thanks to Mike Murphy, all of my office workmates at RHUL and UCL and the residents of 61 St Judes Road. I feel at this point that I must apologise to my band for disappearing for large periods of time, normally when away on fieldwork, not always! In the time of completing this PhD we also finished a new record and for that I am equally proud. Finally, huge thanks to my closest friend Prof. Resheed for offering support, encouragement, ambition and distraction, always.

Contents

List of figures

List of tables

Chapter 1: Introduction

Eruptions from caldera volcanoes represent one of only a few potential processes for major (natural) extinction events. As such it is vital to have as complete an understanding as possible, of the processes governing mechanisms of magma transport and storage in and around caldera settings. This thesis investigates various volcano-tectonic processes with the aim of increasing our understanding of caldera volcanoes. In this first chapter I provide a brief overview and introduction to the relevant fields of study and suggest areas that require further or better understanding.

1.2 Magma chambers

Magma stalls and accumulates in the crust at various depths below the ground surface (Marsh, 1989). Our predominant understanding of magma storage conditions, in terms of storage depths and host rock interactions, come from structural field studies (e.g Gudmundsson, 1986a; Menand, 2011), petrological analyses of fluid inclusions in crystals (e.g Druitt et al., 2012; Walker, 1960), statistical studies of ground deformation (e.g Mogi, 1958) and analyses of magma derived gases (e.g Stevenson and Blake, 1998). Mechanisms controlling the formation of magma chambers are still widely debated (Menand, 2011), but it seems clear that many chambers form from the accumulation of sills (Barnett and Gudmundsson, 2014; Gudmundsson, 2011a). It is apparent from geodetic and field studies that most magma chambers form an approximate sill like geometry (Burchardt and Gudmundsson, 2009; Burchardt et al., 2013; Camitz et al., 1995; Gudmundsson, 2012; Yun et al., 2006), although other geometries such as spheres and ellipsoids are plausible (Gudmundsson, 1986a; Hickey et al., 2013; Lipman, 1997; Menand, 2011; Parks et al., 2012). In fact magma chambers are most commonly approximated as spheres, or as small points of pressure, when modelling volcano deformation (Anderson, 1937; Mogi, 1958; Parks et al., 2012; Sturkell et al., 2006b). Such models are used to provide 1st order estimates of magma chamber pressure and volume changes as well as constrain depth ranges, although the model assumptions are inherently erroneous (Manconi et al., 2007; Masterlark, 2007). These crude approximations are considered valid partly because the crust acts primarily

as a linear elastic material and therefore any significant pressure changes cause the surrounding rocks to become stressed and undergo strain which is then represented instantaneously as ground deformation at the surface (Segall, 2013). As well as inducing stresses in the crust, magma chambers commonly intrude into cooler host rock and therefore the magma and host rock can undergo many cycles of thermal stressing. Some authors challenge the notion that magma chambers exist as significant volume reservoirs, and instead favour a more complex model of packages of melt (Cashman and Giordano, 2014). However, in order to form large sustained eruptions and potentially collapse calderas, magma must be present at shallow depth and in sufficient volume (Gudmundsson, 2012). The precise pressure and stress conditions required to form eruptions are less well known, and these may be significantly influenced by thermal degradation (Annen, 2011; Gregg et al., 2012) and mechanical heterogeneity (Gudmundsson and Philipp, 2006) in crustal host rocks.

1.3 Dykes and inclined sheets

A magma chamber can fail in one of several ways, namely through dyke or inclined sheet injection, gravity driven roof collapse, or a combination of the two producing ring-dykes. Dykes, or 'dikes' (US spelling), are magma driven fractures which propagate in a direction perpendicular to the minimum compressive (maximum tensile) principal stress σ_3 (Figure 1). The shape of an underlying shallow magma chamber and the regional tectonic controls (boundary conditions) dictate the orientation of stresses in shallow volcanic systems. As a consequence magma, as dykes, does not propagate vertically in many cases, instead favouring an inclined trajectory toward the surface (Burchardt et al., 2011; Gautneb and Gudmundsson, 1992), Figure 1.2. Dykes that dip less than around 75° are commonly referred to as inclined sheets. It is possible in some cases to estimate the location of a shallow magma chamber based on the attitude of a collection of inclined sheets (e.g Burchardt et al., 2013; Gautneb and Gudmundsson, 1992), assuming that the direction of magma propagation does not change significantly away from the magma chamber. Whilst statistically this may be a valid treatment, it has been shown that stress fields are complex ahead of dyke tips (Gudmundsson and Phillip, 2006). As a consequence of these complex stress fields, which tend to arrest dykes, most dykes recorded geodetically or in the field are non-feeders (Geshi et al., 2010;

Gudmundsson, 2011a; Hooper et al., 2011; Pollard, 2010), i.e. they stall inside the volcano to form intrusions rather than provided magma for an eruption (Gudmundsson and Philipp, 2006). The complexity of volcanic stratigraphy and tectonic relations probably affects dyke propagation paths to a greater degree than generally recognised. Therefore, new models or findings that provide insights into magma propagation in various settings are useful and important to the volcanological community.

1.4 Calderas and caldera faults

Calderas are typically bounded by circumferential faults, or ring-faults. In piston and trapdoor type calderas, ring-faults, or part ring-faults, represent the calderas structural boundary. It is not possible to directly observe the structural boundary of many calderas; the faults are often obscured or eroded by subsequent water emplacement (caldera lakes) or mass wasting (landslides) (Lipman, 1997). The boundary observed at such calderas is a topographic boundary, which is largely related to the structural boundary although the main subsidence accommodating faults may be situated several tens (Hartley and Thordarson, 2012) to hundreds of meters (Wilson et al., 1994) away from the topographic collar. Therefore, caldera fault geometry must be largely inferred from geophysical (e.g Saunders, 2001), analogue (e.g Acocella, 2007) and numerical (e.g Gray and Monaghan, 2004) studies. In rare circumstances it is possible to observe caldera faults in geologic outcrops at deeply eroded volcanoes. In fact much of our early understanding of caldera processes comes from studies of ancient and eroded systems in the USA (Lipman, 1984), Iceland (Gudmundsson, 1987a), and Scotland (Branney, 1995).

The mechanics governing caldera ring-fault formation are reasonably well studied, although studies considering the effects of pre-existing faults on caldera dynamics are less numerous. A combination of geodetic observations, analogue and numerical models and field work have shown that calderas are formed from a combination of inward (normal) and outward (reverse) dipping faults. For example, the 650 m deep and 2.5 km wide caldera formed during the 1991 silicic eruption of Pinatubo was shown to subside along predominantly outward dipping ring-faults inferred predominantly from seismicity (Mori et al., 1996). Similar outward dipping structures have also been

inferred from seismicity recorded at Rabaul caldera (Mori and McKee, 1987) and Mt St Helens (Scandone and Malone., 1985), although normal faults seem to control subsidence at Bardarbunga caldera in Iceland (Fichtner and Tkalčić, 2010). Most analogue models of caldera formation suggest that collapse occurs predominantly along reverse faults, with a contribution from peripheral normal faults (see the review by Acocella, 2007). Whereas numerical modelling seems to suggest both inward (Gudmundsson and Nilsen, 2006) and outward (Holohan et al., 2015) dipping faults, depending on the modelling technique implemented (Geyer and Marti, 2014). There have been several studies investigating or observing the influence of caldera faults on deformation patterns at active calderas (Bathke et al., 2015; De Natale and Pingue, 1993; Hutnak et al., 2009; Masterlark, 2007), but relatively few that investigate how magma transport is effected by caldera structures (Jónsson, 2009; Saunders, 2004, 2001).

There have been only four, possibly five events involving caldera formation or slip on caldera faults in the past century. Those events occurred in 1968 at Fernandina in the Galapagos (Filson et al., 1973), in 1991 during the ignimbrite forming eruption of Pinatubo (Mori et al., 1996), in 2000 at the Miyakejima volcano in Japan (Geshi et al., 2002), in 2007 at Piton de la Fournaise at La Reunion (Michon et al., 2009; Peltier et al., 2009), and possibly in 2014 at Bardarbunga in Iceland (Sigmundsson et al., 2014). Apart from large volume eruptions in Iceland and the Philippines, most of the calderas formed in association with moderate to small volume eruptions. The two best monitored collapses in terms of geodetic data were Bardarbunga and Piton de la Fournaise, although ideas regarding the mechanism of caldera deformation at both remain controversial. It is still not clear if a caldera actually slipped during the 2014 Bardarbunga event, visual inspection is limited because the volcano lies beneath approximately 800 m of glacial ice. The best evidence for collapse comes from the location and type of earthquakes surrounding the volcano (the inferred ring-fault), and over 60 m of ice surface subsidence (Sigmundsson et al., 2014) directly above the caldera. All of the aforementioned collapse events were monitored by various combinations of seismometers and GPS, but only Bardarbunga offers data on the ground deformation effects of a caldera collapse from a great distance (>10 km) away the centre of collapse, although the situation was made more complex by the intrusion of at least one major dyke. All of the other caldera forming collapses have occurred on

small islands where the coverage of GPS is limited predominantly to the summit region, and while this is not the case at Pinatubo there are no published GPS data in the far-field. As such there remains a substantial gap in our knowledge of expected ground surface deformation signals associated with collapse caldera formation.

1.5 Ring dykes

An important process concerning the timing and dynamics of caldera fault formation is the emplacement of ring-dykes. Anderson's (1937) model is the most widely used to explain the occurrence of ring-dykes (Figure 1.1). In this model, ring-dykes (and ring-faults) form as a consequence of a pressure decrease in a magma reservoir, the fundamental basis for the under-pressure or withdrawal of magmatic support model for the formation of collapse calderas. Gravity driven failure of the magma chamber follows magma withdrawal, with the general principle being that dykes are then squeezed out of the chamber through shear (Mode II-III) ring fractures, which appears to be supported by field evidence in some cases (e.g Kokelaar, 2007). As is well known however, dykes are predominantly mode I fractures which require a pressure in excess of the tensile strength of the host rock to propagate. The simple Anderson (1936) model begs the question: how does a dyke remain open and supply magma out of a chamber which contains magma at a pressure less than lithostatic (i.e Gudmundsson and Nilsen, 2006)? One solution is that ring-dykes form from magma chamber overpressure conditions, such that the caldera collapse is the cause of large eruptions rather than being the consequence (Gudmundsson, 2015, 1998).

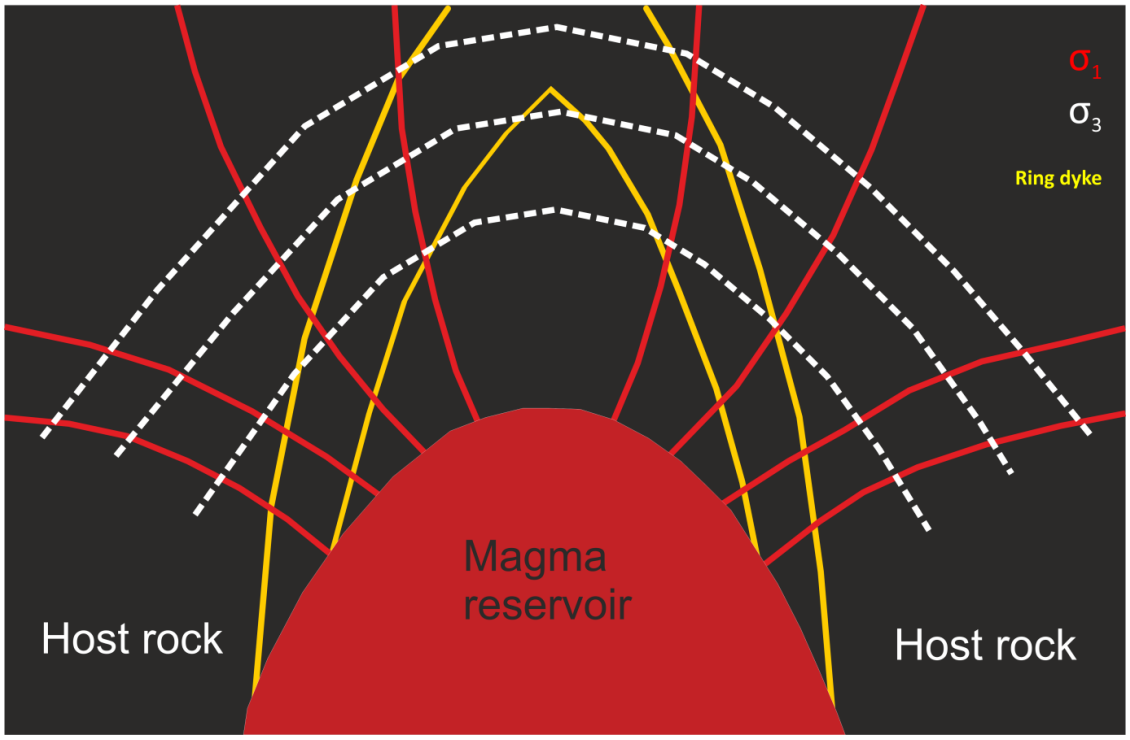

Figure 1.1: Traditional model for the formation of ring-dykes (outward-dipping, yellow lines) based on Anderson's (1937) analytical solution. Trajectories of maximum tensile principal stress, σ_3, as dashed white lines, and maximum compressive principal stress, σ_1, as solid red lines. Those red lines indicate the likely direction of magma propagation in this simple example, modified after Gudmundsson and Nilsen, 2006.

1.6 Field sites

Three main field areas were chosen as sites of either data collection or sites of rock sample collection. The following section describes volcanological and tectonic aspects of each field area in respect to the project aims. All sites were selected based on the suitability of outcrops and exposures of volcano-tectonic features.

1.6.1 Iceland

Many of the fundamental ideas from the field of volcano-tectonics were created by investigating processes at active and extinct volcanoes in Iceland (Gudmundsson,

1986b, 1987a, 1986b; Walker, 1960). Iceland is one of the best monitored volcanic fields in the world and home to many active caldera volcanoes, as well as many more extinct caldera volcanoes. Utilisation of various monitoring techniques at active volcanoes and along the divergent margin has shown that spreading occurs at a rate of around 10 mm/yr, and that Iceland's volcanoes deform in numerous ways (Sigmundsson, 2006). Krafla, Askja and Hengill (shown in Figure 1.2) have for more than 30 years been subsiding (deflating) at relatively steady rates (Miller et al., 1998; Sturkell and Sigmundsson, 2000; Sturkell et al., 2006a, 2006b), whereas Eyjafjallajokull, Grimsvotn and Bardarbunga have all experienced both local inflation and regional doming with intermittent periods of rapid subsidence (Sigmundsson, 2006). The signals represent a complex interplay between magma transfer from depths greater than 10 km to shallow storage regions (Gudmundsson, 1987b), at depths around 2 to 5 km, where this shallow magma also cools and contracts. Cooling shallow magma chambers are inferred to be the main cause of ground surface deflation at many of Iceland's volcanoes (Sturkell and Sigmundsson, 2000), although crustal spreading also likely contributes to the signal (Camitz et al., 1995; De Zeeuw-van Dalfsen et al., 2012). The 2014-15 unrest and rifting episode at Bardarbunga caldera was one example of an incredibly well monitored volcano-tectonic episode (Gudmundsson et al., 2014; Sigmundsson et al., 2014). The event raised a number of questions regarding dyke propagation, stress accumulation at central volcanoes and caldera deformation. For example, the rifting episode appeared to confirm a long held hypothesis that dykes can propagate laterally over a distance of more than 40 km before coming to the surface to produce eruptions (Sigmundsson et al., 2014), an idea which originates from the discovery of Bardarbunga signature lavas near the Torfajokull complex (McGarvie, 1984), and numerous fissure eruptions North and South of the Askja volcanic system (Hjartardóttir et al., 2009; Key et al., 2011). Many of these eruptions were probably fed by deeper reservoirs (Hartley and Thordarson, 2013), and this appears to be the case for the 2014 Holuhraun eruption (Haddadi et al., 2015), rather than lateral flow of magma from a shallow source. Whilst the dynamics of magma propagation have been very well studied in Iceland (Gudmundsson, 2011b; Sigmundsson et al., 2014), there is still no comprehensive model to predict where and when an eruption is likely to take place.

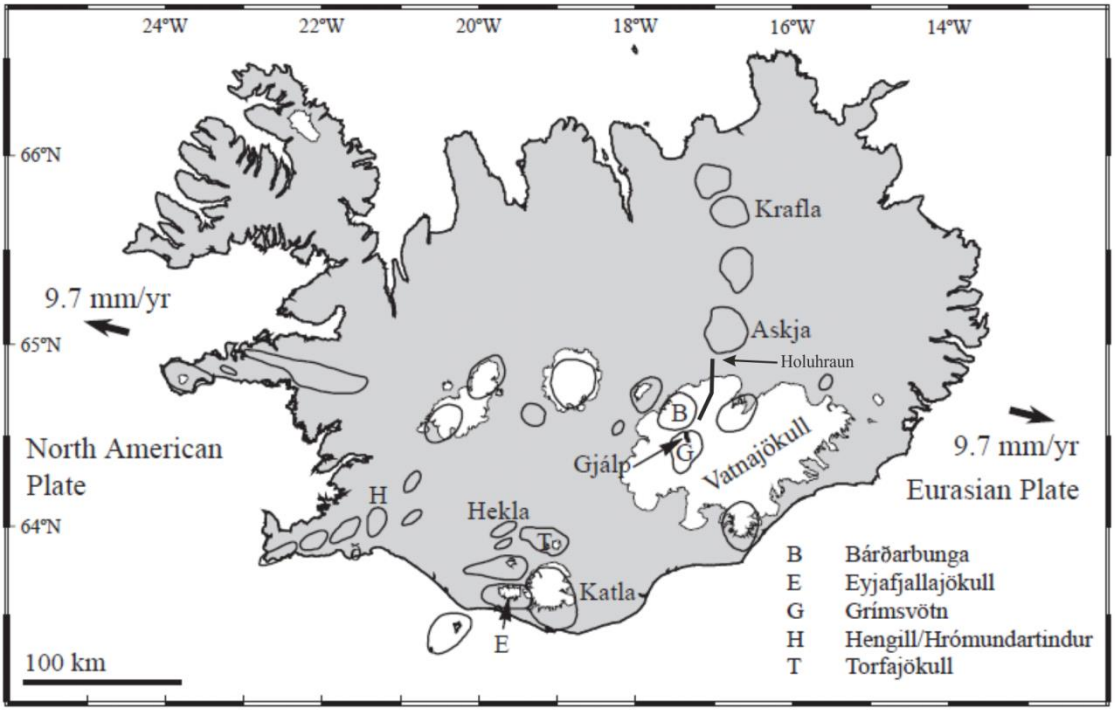

Figure 1.2: Active volcanoes of Iceland, many have calderas and some are associated with very recent dyke intrusions at Holuhraun, Gjalp and Eyjafjallajokull (marked). All of the volcanoes and associated calderas in Iceland are subject to overall regional tensile stress, exhibited as plate divergence at a rate of approximately 9.7 mm/yr, modified after (Sturkell et al., 2006a).

The ancient and eroded, 'Tertiary' volcanics of Eastern and Western Iceland offer insights into the dynamics of magma plumbing systems and processes occurring at currently active volcanoes. Many of the eroded central volcanoes host dyke swarms (Walker, 1974), for example Geitafell in the East (Burchardt and Gudmundsson, 2009) and radial and concentric dykes such as at Hafnarfjall (Gautneb et al., 1989). In some locations the extent of erosion is such that it is possible to observe the tops of plutons and extinct magma chambers (Gudmundsson, 2012), perhaps the best exposed of such sections is the Slaufrudalur pluton and central volcano, which hosts a granophyre body extending roughly 8 km in length and 2 km in diameter (Burchardt et al., 2010). At the top of the granophyre much of the host rock into which it was emplaced still exists. At these localities it is possible to observe the sharp contact between the once felsic magma and mafic host. A number of dykes can also be seen to cut through the roof of the chamber, indicating that it probably acted as a magma supply for eruptions. Outside of

central and shield volcanoes in 'Tertiary volcanics' the attitude and dimensions of dykes change such that they become generally thicker and steeper (Gudmundsson, 1990; Gautneb and Gudmundsson, 1992), these type of dykes are referred to as regional dykes. There exists a clear relationship between the occurrence of dyke swarms (and inclined sheets) and magma chambers and the occurrence of regional dykes generally away from shallow magma centres. This finding suggests that dyke sheets and swarms are controlled by local stress fields generated by shallow magma bodies, whereas regional stress fields associated with divergent plate movements and deeper and larger magma reservoirs control the emplacement of regional dykes (Gudmundsson, 1983; Gudmundsson et al., 2014).

1.6.2 Santorini

Santorini is a very well-studied caldera volcano located in the southern Aegean of Greece. Arc related volcanism in this region began in the early Pliocene (Fytikas et al., 1984), forming the islands of Santorini, Nisyros, Milos, Kos, Aegina, Methana and Poros. All volcanism exhibits a strong tectonic control, related to NE-SW lithospheric normal-fault rupture zones (Papazachos and Panagiotopoulos, 1993) (Figure 1.3). Therefore whilst volcanism is clearly a consequence of subduction related processes, the volcanic arc has formed in an overall extensional stress regime. Magmas in the Aegean arc are commonly andesite to dacite, only Santorini produces abundant basaltic successions (Druitt et al., 1999; Fytikas et al., 1984). Santorini is a stratigraphically and chemically complex stratovolcano, made up of many hundreds to thousands of distinct lava and ignimbrite successions (Druitt et al., 1999). Several of the ignimbrites are associated with catastrophic caldera formation (Druitt and Francaviglia, 1992; Druitt and Sparks, 1982; Roche and Druitt, 2001). There have been four well documented caldera forming events in the geologic record (Druitt et al., 1999). Structurally, this means that the present day volcano contains abundant ring-fracture and fault systems (Giannopoulos et al., 2015; Heiken and Mccoy, 1984). As well as the caldera faults, arguably the two most important volcano-tectonic features are the Coloumbo and Kameni lines which constitute a series of sub-parallel NE-SW trending normal faults which run through the northern and central sectors of the present day caldera (Druitt et

al., 1999; Konstantinou et al., 2013; Papoutsis et al., 2013). Associated with the Coloumbo line in the northern part of the caldera is a 1-2 km thick dyke swarm made up of around 60 individual dykes (Browning et al., in press), only around 5% of which feed eruptions at the Megalo Vouno shield complex (Druitt et al., 1999). Present day volcanism within the caldera is located along the Kameni line in the form of predominantly dacitic domes and a lava bearing shield complex named the Kameni islands (Nomikou et al., 2014). Recent geodetic studies have postulated the existence of a growing shallow magma chamber (Parks et al., 2014) that probably feeds recent eruptions at Nea Kameni (Druitt et al., 2012). Of greatest interest to this study are the are the post Minoan caldera lavas which are described in detail by Barton and Huijsmans (1986). All lava flows at Nea Kameni are dacite in composition and exhibit glassy textures with numerous vesicles. It is estimated that the magma that supplied these lavas is compositionally zoned and contains approximately 3-4 wt % H_2O, of which most (2.5-3.7 %) is lost during eruptive degassing (Barton and Huijsmans, 1986; Druitt et al., 2012). Samples of the lava were collected from the margin of each flow for use in thermo-mechanical testing (see Chapter 5). Whilst the geochemistry of individual Nea Kameni lavas, and in fact many of Santorini's deposits, are well studied, very little attention has been given to the geomechanical properties of these rock units. A combined understanding of geochemical and geomechanical properties is essential to estimating eruption hazards at Santorini volcano. It is especially important here because the caldera forming eruptions, whilst largely overestimated in their destructive potential (Dominey-Howes and Minos-Minopoulos, 2004), can produce significant damage to the islands inhabitants and tourists. Examples of the destructive power can be seen throughout Santorini as ignimbrite covered ruins, associated with the Bronze age demise of the Minoan civilisation (Bond and Sparks, 1976; Druitt, 2014; Pyle, 1997).

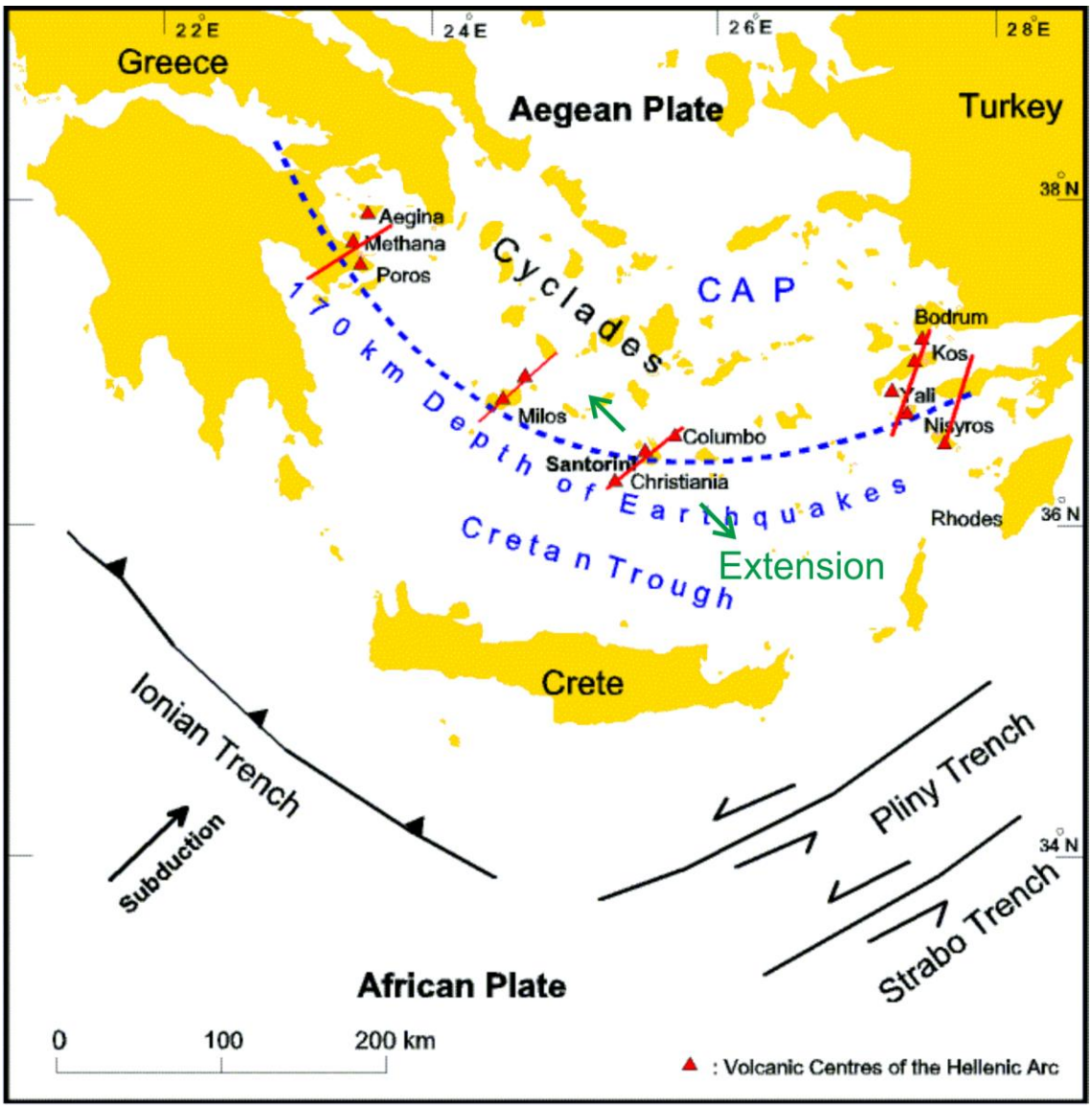

Figure 1.3: Tectonic setting of Santorini in the Aegean arc, after Friedrich (2009)

1.6.3 Tenerife

Whilst the volcanic island of Tenerife was not studied directly in this thesis, rock samples were collected and used in experimental studies in Chapter 5. Therefore a brief description of salient volcano-tectonic features and previous studies is appropriate.

Tenerife is the largest of the Canary Islands covering 2058 km^2, with a roughly triangular or 'mercedes star' shape (Marti et al., 1994). The present day island is characterized by a summit caldera (Las Canades) and central edifice (Teidi), but was originally built by the conglomeration of three volcanic shields; in the North West,

Teno, in the Northeast, Anaga and the South, Roque del Conde. Several distinct steep sided rift-zone or 'arms' periodically become unstable and produce huge volume landslides (Garcia-piera et al., 2000; Hu et al., 1999). Whilst many agree that the summit caldera is a result of the vertical collapse of the Las Canadas magma chamber, possibly over three separate cycles (Coppo et al., 2008; Marti and Gudmundsson, 2000), others believe the caldera is a giant landslide scarp (Carlos et al., 1999; Carracedo, 1999; Watts, 1998). A block was collected from one dyke in a swarm of dykes near the town of Taganana in the Anaga province of Tenerife. These dykes have been well-studied structurally (Marinoni and Gudmundsson, 2000) and chemically (Hernández-Pacheco, 1996). Most of the dykes are altered and mafic to phonolite in composition, they form from a minimum compressive stress field orientated NE-SW and WNW-ESE.

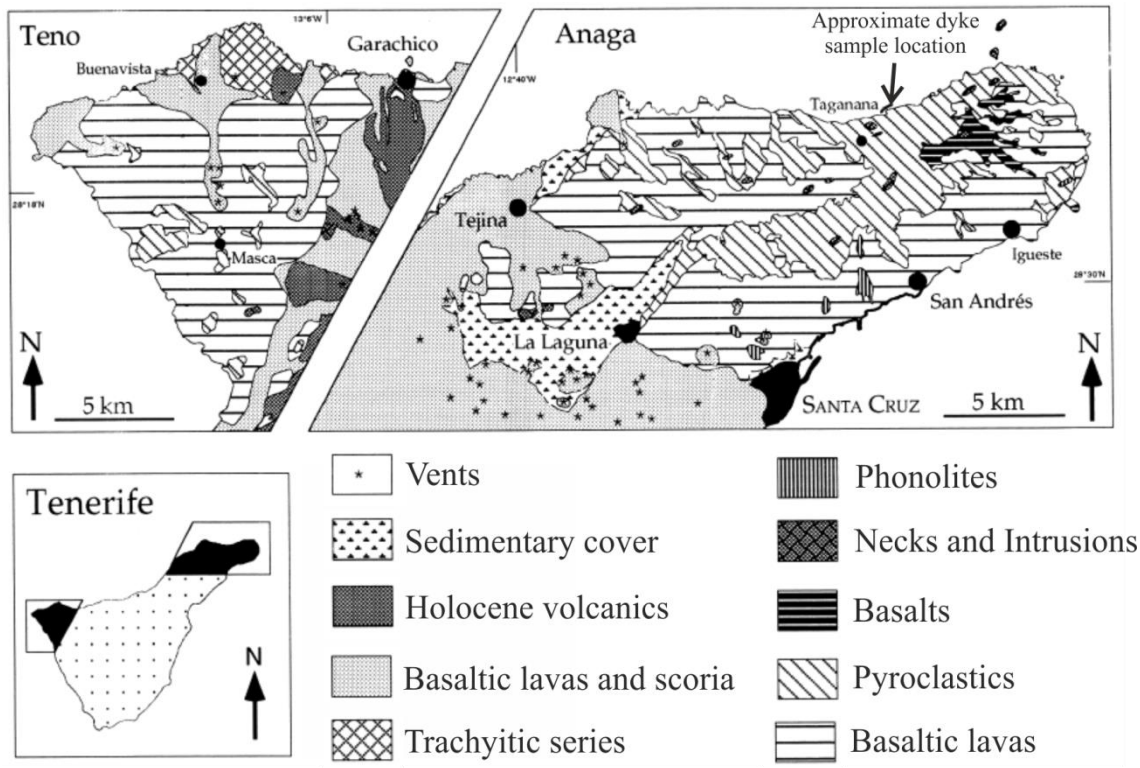

Figure 1.4: Geologic map of the Anaga and Teno massifs of Tenerife, showing the approximate location of a sampled dyke, modified after Marinoni and Gudmundsson (2000).

1.7 Contributions

In this thesis I use a range of techniques to study problems in volcano-tectonics, volcano deformation and fracture mechanics with specific application to areas of Iceland and Greece. The scientific contributions of this work can be distinguished by three categories. First are contributions to volcano research where applied forward models are proposed to aid the temporal forecasting of magma chamber failure and estimate ground surface changes resulting from roof collapse. Second are contributions to ongoing research activities at the locations mentioned previously, these are of interest to those who study the regions or similar areas. And third are contributions to fracture mechanics through the design of new experimental methods and applications, which are of interest to those studying rock mechanics and commercial geothermal activities.

The research reported within this thesis is not focused on solving any one large geophysical problem. Instead a number of smaller problems are tackled, that may sometimes seem only loosely connected to one another. Here is a summary of the main scientific contributions within this thesis.

1. We estimate, using poro-elastic analytical models, continuum mechanics and fracture mechanics that the volume of shallow magma stored at Santorini volcano is approximately 120 km^3. We postulate a range of magma chamber rupture conditions based on magma recharge from a deep seated source. Our findings suggest that the magma chamber came close to rupture during 2011-2012 magmatic unrest.

2. We report on a previously unrecognised mechanism concerning the propagation of dykes and inclined sheets at caldera faults. New field observations and data collected from a well exposed inward-dipping caldera fault suggest that magma is captured within caldera faults due to changes in the mechanical properties of the rocks surrounding and within the fault.

3. We present a new experimental apparatus and method for detecting acoustic emissions in material undergoing cooling and contraction from high temperature.

4. The experimental design and method are used to infer that cooling contraction produces a greater abundance of larger micro-fractures when compared to thermal expansion related fractures. This finding is important as most previous studies of thermal cracking concentrated only on damage accumulation during heating.

5. We find that magma chamber roof collapse is an unlikely mechanism for the generation of ice surface subsidence related to the Bardarbunga-Holuhraun rifting event in 2014-15. Instead we postulate that the ice subsided as a consequence of dyke induced stress changes within the steep caldera walls, which is an entirely novel and unreported mechanism.

1.8 Thesis roadmap

Each chapter of this thesis can be considered as an independent study with some chapters presented as peer-reviewed and published papers and others which are in preparation or review for publication in scientific journals. It is possible, therefore, for the reader to examine chapters of interest without having to lookup background material in previous chapters, aside from Chapter 2 which contains a thorough description and analysis of the methods throughout, and Chapter 7 which critically evaluates and discusses the main findings as well as suggesting possible routes for future research. As three of the four results chapters have been published or accepted for publication, they are presented as stand-alone works with independent page numbers. Chapter 4 is presented using the journals printed format, it is expected that three chapters in total will be formatted by journal specifications when the final thesis is complete.

In Chapter 2 the main methodological frameworks that govern each independent study are presented. This chapter is divided into three main sections, relating to the techniques used throughout, namely numerical and analytical studies, field data collection and laboratory experiments. All of the methods are critically evaluated, with suggestions for improvements or erroneous or incomplete results discussed.

In Chapter 3 we present a simple analytical technique for monitoring the pressure evolution within a shallow magma chamber during periods of magma recharge and resultant unrest, based on fracture mechanics and continuum mechanics principles. Field data of dykes observed and measured within the caldera wall at Santorini are presented and used to inform the analytical model results. We apply the results to the well documented unrest period at Santorini volcano in 2012, and suggest that future work could seek to generate similar forecasts at other well monitored volcanoes.

In Chapter 4 the field campaign switches to Western Iceland where an exceptionally well-exposed caldera ring-fault outcrops at the Hafnarfjall volcano. Field data is used to constrain finite element method numerical models built using COMSOL Multiphysics. Using a combination of those methods we present a novel interpretation for ring-dike formation. In this work we find that inferred mechanical heterogeneities across a caldera fault zone influence magma propagation to the extent that inclined sheets can become deflected and captured within the fault. The model is used as an explanation for the high frequency of volcanic eruptions and edifices around the margins of calderas.

We depart from field studies and numerical modelling in Chapter 5, to examine volcanic rocks in the laboratory. Here we investigate the role of thermal stresses in generating micro-cracks in a range of differentially emplaced igneous rocks. A new apparatus is used for detecting in-situ micro crack development during both heating and cooling by recording acoustic emissions. Contemporaneous data acquisition is complimented by a suite of micro-crack analyses under SEM and P-wave velocity determination. All rock types undergo thermo-mechanical analysis to determine their respective mechanical response to high temperature treatment.

Chapter 6 presents a series of numerical models designed to better understand the surface deformation associated with magma chamber roof failure and subsidence. The results are applied to the Bardarbunga-Holuhraun eruptive episode which exhibited signals of a caldera collapse origin (Sigmundsson et al., 2014). Our findings suggest an offset between roof subsidence as a function of depth below the surface and total ground subsidence. We suggest that roof collapse generating ring-fractures was an unlikely cause of ice subsidence observed at Vatnajokull, which instead may relate to compressive stresses being formed within the caldera as a result of regional dyke emplacement.

Chapter 7 draws all of the key findings together and evaluates in a critical manner the methods and techniques used throughout. How the work can be expanded and insights into future research directions are also discussed.

Chapter 2: Methodologies

2.1 Numerical modelling methodology

2.1.2 Introduction

Numerical models are used to simulate physical problems and solve complex equations when analytical solutions become too complex Detailed guides explaining the computational domain of finite element method modelling already exist (e.g Pryor, 2011) and are therefore not repeated here. In addition the software used (COMSOL Multiphysics versions 4.1 to 5.1) is extremely well tested and benchmarked (e.g Hickey & Gottsmann, 2014) for solving problems in volcanology and structural engineering. Within this section I provide the constitutive equations that are solved numerically and discuss their limitations and assumptions. Stress solution comparisons are discussed with respect to previous studies to show the (in)consistency of results throughout different finite element method software.

2.1.3 Software

All numerical modelling within the papers presented as part of this thesis were conducted using the commercial finite element code within COMSOL Multiphysics versions 4.1 to 5.1 (www.comsol.com). All models use the 'Structural Mechanics' module which solves Navier-Cauchy equations for linear elastic stress and displacement as a result of load application. As the software is extremely well tested, relatively simple to use, and has many published instructional manuals I do not provide a detailed step by step guide to model creation in COMSOL, but only discuss points salient to those models created in the studies within this thesis.

2.1.4 Theory and constitutive equations

All numerical models assume linear elasticity through Hooke's law, i.e

$$\sigma = E\epsilon \tag{2.1}$$

where σ is stress, force over area, E is Young's modulus and ϵ is strain, change in length over original length of an object. A linear, isotropic elastic solid simply means that when an applied force is removed from the material it will return to its original shape. The prinicipal stress and strain axes in this material coincide such that the coordinate system can be conveniently written as (Turcotte and Schubert, 2002):

$$\sigma_1 = (\lambda + 2G)\varepsilon_1 + \lambda\varepsilon_2 + \lambda\varepsilon_3 \tag{2.2}$$

$$\sigma_2 = \lambda\varepsilon_1 + (\lambda + 2G)\varepsilon_2 + \lambda\varepsilon_3 \tag{2.3}$$

$$\sigma_3 = \lambda\varepsilon_1 + \lambda\varepsilon_2(\lambda + 2G)\varepsilon_3 \tag{2.4}$$

where λ, Lame's constant, and the modulus of rigidity G are the Lame's parameters. The state of stress at any point in a solid can be calculated by providing σ_{xx}, σ_{yy}, σ_{zz}, σ_{xy}, σ_{xz} and σ_{yz}, or the value of the principal stress and the orientation of the principal axes, highlighted in Figure 2.1a. The normal stresses on planes perpendicular to the principal axes are the principal stresses, denoted as σ_1, σ_2 and σ_3. By convention the meaning of the maximum and minimum principal stress in physics and engineering is the opposite of standard geological meanings, as COMSOL is primarily an engineering tool, it utilises engineering definitions. It is simple to reverse the notation so that the standard convention is chosen such that $\sigma_1 \geq \sigma_2 \geq \sigma_3$. Therefore, σ_1 is the maximum principal compressive stress, σ_2 is the intermediate principal stress and σ_3 is the minimum principal stress (Turcotte and Schubert, 2002).

The stresses and displacements around circular holes can be solved analytically using the Kirsh solution as shown below (Eq.2.5-2.9) and in Figure 2.1b:

$$\sigma_{rr} = \frac{P}{2}\left[(1+K)\left(1-\frac{a^2}{r^2}\right) - (1-K)\left(1-4\frac{a^2}{r^2}+3\frac{a^4}{r^4}\right)\cos 2\theta\right] \tag{2.5}$$

$$\sigma_{\theta\theta} = \frac{P}{2}\left[(1+K)\left(1+\frac{a^2}{r^2}\right) + (1-K)\left(1+3\frac{a^2}{r^2}\right)\cos 2\theta\right] \tag{2.6}$$

$$\tau_{r\theta} = \frac{P}{2}\left[(1-K)\left(1+2\frac{a^2}{r^2}-3\frac{a^4}{r^4}\right)\sin 2\theta\right] \tag{2.7}$$

$$U_r = \frac{Pa^2}{4Gr}\left[(1+K)-(1-K)\left(4(1-\nu)-\frac{a^2}{r^2}\right)\cos 2\theta\right] \tag{2.8}$$

$$U_\theta = \frac{Pa^2}{4Gr}\left[(1-K)(2(1-2\nu)+\frac{a^2}{r^2}\sin 2\theta\right] \tag{2.9}$$

Refer to Figure 2.1b for explanation of the geometrical terms used, *P* and *K* relate to applied pressure, *a* is radius and *r* distance from the model edge. The elastic behaviour of a material can be characterised by supplying either λ and *G*, or *E* and *v*. All of the models used in this study are created by specifying Young's modulus *E* and the Poisson's ratio *v*. All models were created in a two-dimensional regime; however, Figure 2.1 highlights the potential for extension of results to three-dimensions.

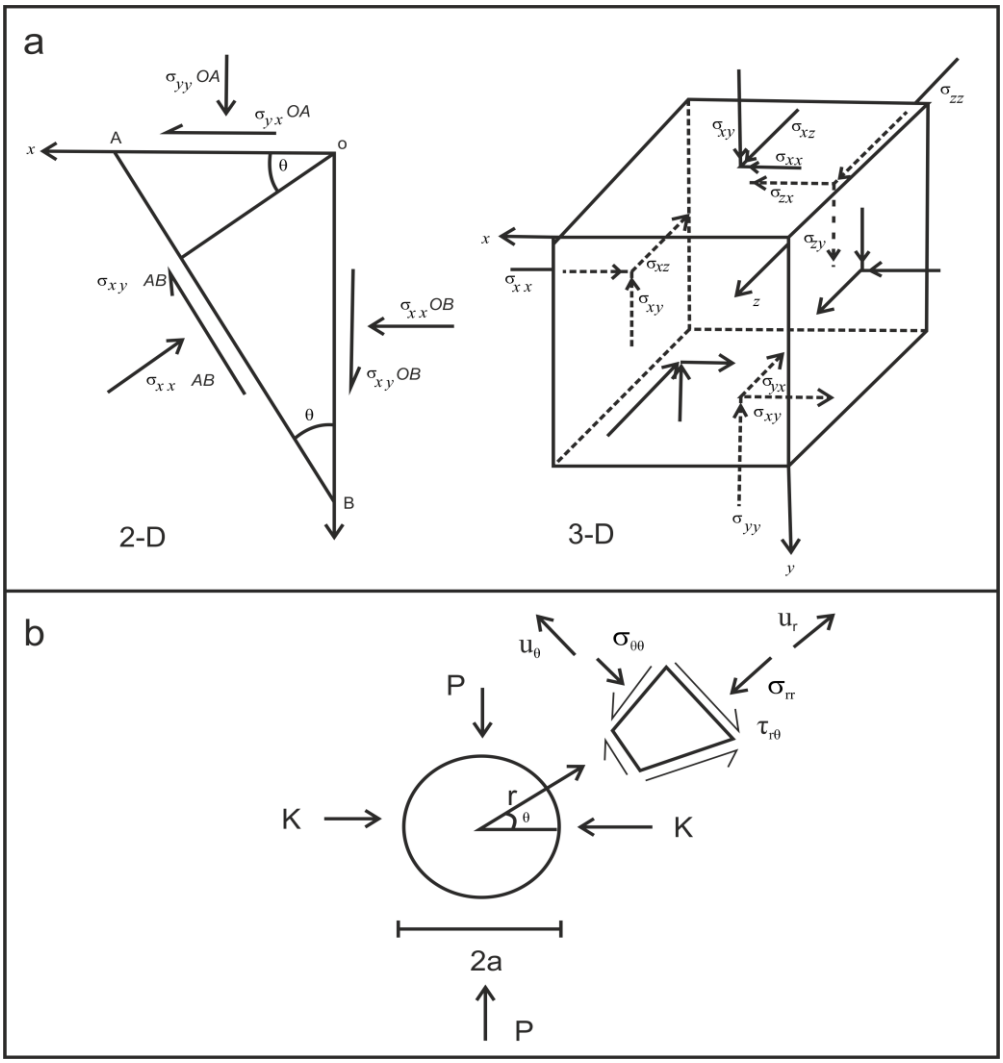

Figure 2.1: Components of stress in two and three dimensions and relation to displacements (b), modified from Turcotte and Schubert (2002).

2.1.5 Model set-up and design

All models presented throughout utilise a two dimensional (2d) domain which can be selected in COMSOL as either an axisymmetric or symmetric plane. Essentially the physics governing either symmetrical or axisymmetrical models are the same, however certain studies such as ground surface deformation have traditionally been displayed using axisymmetry type displays (e.g Mogi 1958), and I therefore attempt to follow those conventions for clarity when dealing with ground deformation (e.g Browning and Gudmundsson, in press). All models are created with sufficient length and width to ensure that edge effects become negligible (Figure 2.2). The full range of model details, including descriptions of input parameters are given in Chapters 4 and 6. Initial pre-processing involves the input of geologically relevant geometries which are defined and imported into the model. Model geometries in Chapter 4 (Browning and Gudmundsson, 2015) are informed by geological field measurements, whereas the geometries in Chapter 6 are inferred predominantly from previously published geodetic data (e.g Fichtner & Tkalčić 2010). Mechanical and physical properties are taken directly from relevant laboratory and field studies.

Boundary conditions are prescribed as either pressure with the units Pa or displacement field with the value given as the amount of total displacement in metres. Boundary conditions are commonly applied to the edges of each model to simulate far-field tectonic stresses, for example in the 2D symmetric model shown in Figure 2.2, the hypothetical tectonic situation is that of regional extension as may occur in a rift zone. Typical values of stress for such areas are around 5 MPa (Gudmundsson, 2011b). The corners or edges of models are fixed in order to avoid solid-body rotation. Roller constraints are occasionally used when a model interface or edge is to be allowed to slide. Finally, infinite element domains are normally placed around the inner boundary of each model in order to reduce computational processing requirements, and therefore reduce the time taken to solve each model. A free surface condition is applied to the upper edge of each model to simulate the ground surface, or more specifically the contact with air or water, i.e. a zone free from shear stresses. None of the studies within

this thesis model the effect of topographic loading, such as a volcanic edifice, there are some consequences related to this admission which are further discussed in Chapter 7.

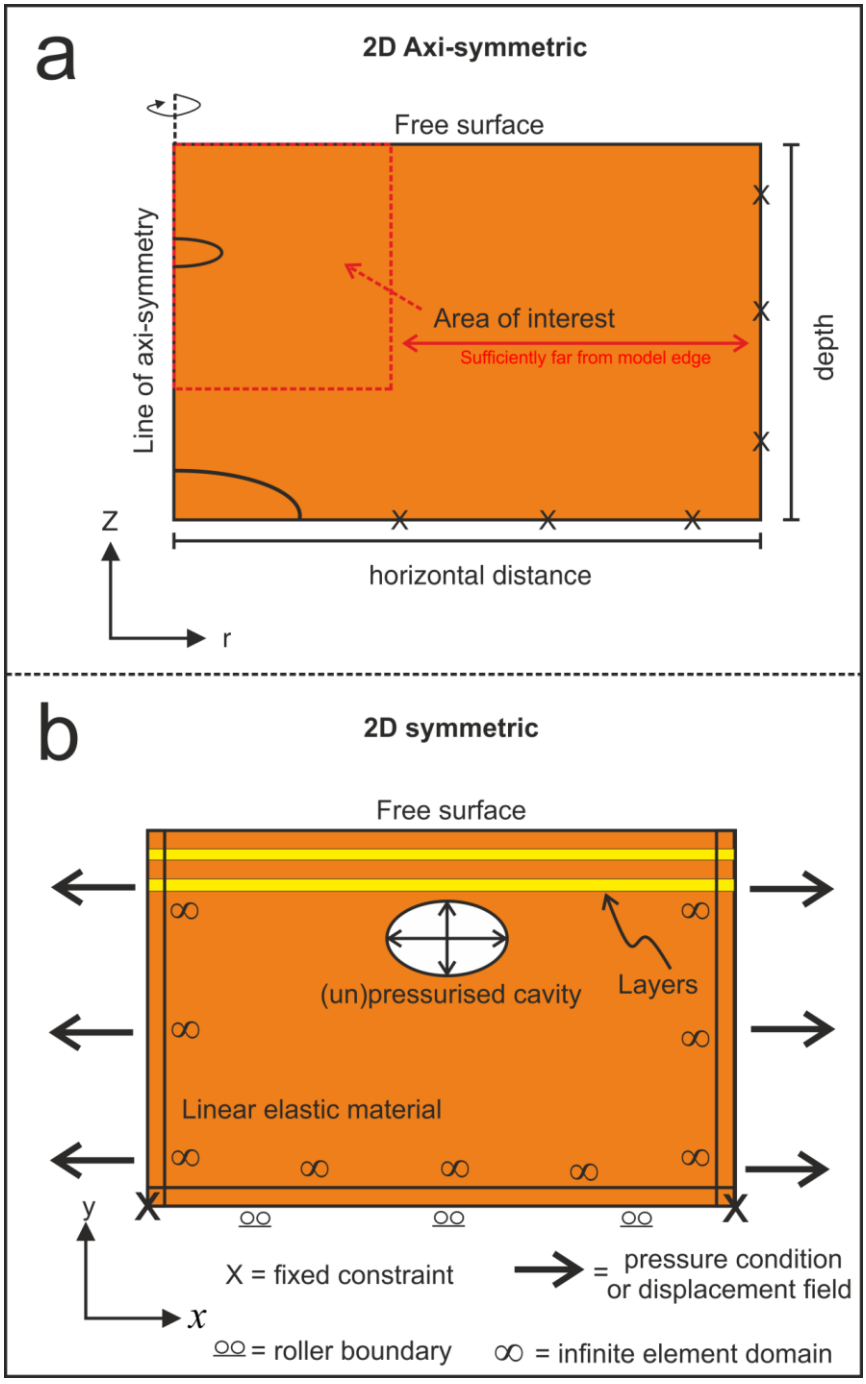

Figure 2.2: Typical COMSOL numerical model set-up, a) in 2d axi-symmetric and b) in 2d symmetric. Features such as elliptical cavities are placed with a rectangular box of horizontal and depth dimensions of sufficient size to ensure minimal boundary effects. In addition boundaries are divided by infinite element domains to reduce computational

requirement and boundary effects. At the outer edges of each model a range of different boundary effects are applied.

2.1.6 Model meshing

The next step in a COMSOL model preparation is mesh definition and construction. It is upon the elements (or lines) which make up a computational mesh that the relevant simultaneous equations are solved in order to produce a suitable solution (of resultant stresses, strains, displacements etc). Mesh elements vary in size throughout models, but typically provide centimetre scale resolution near an area of interest, transitioning into coarser metre scale resolution in distal areas (Figure 2.3). COMSOL offers various geometrical arrangements for mesh elements, the most commonly used are triangular elements, and whilst changing geometry does not significantly alter results a triangular mesh is used throughout the studies that comprise this thesis.

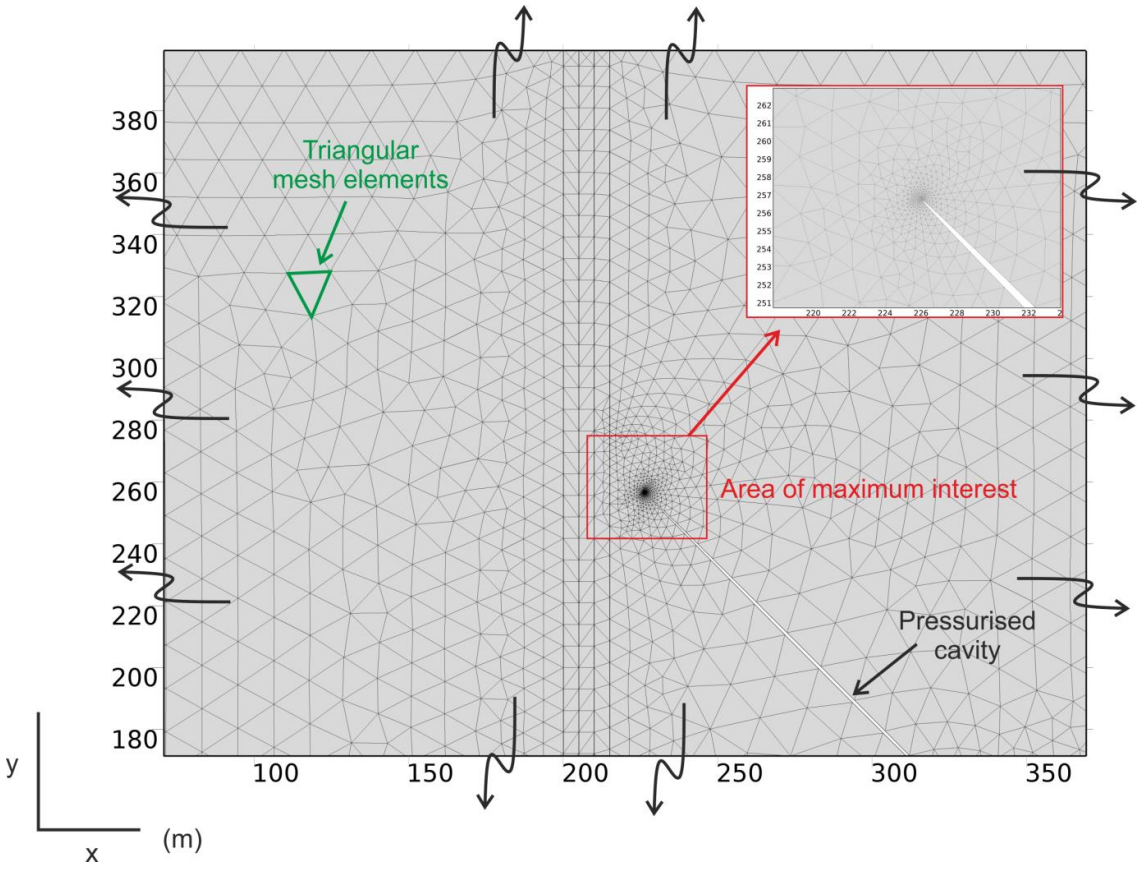

Figure 2.3: Typical triangular mesh setup in an asymmetric model type. In this example the mesh has been created to be finest (highest resolution) around the tip of a

pressurised cavity (red inset box), at this location individual elements may be as short as 0.05 m. The maximum length of any element in this case is 15.5 m (green triangle). The example shown is part of a larger model, and therefore the edges of the image do not represent the edges of the model.

2.1.7 Model outputs and interpretation of results

COMSOL outputs a variety of graphic tools which can be used in order to assess, or estimate the location of rock failure or the distribution of strain and resultant displacement. Here those most relevant to the studies presented in this thesis are discussed, with a brief explanation of how each output is interpreted in a geological sense. Firstly the minimum principal compressive stress or maximum tensile stress (σ_3) is plotted and interpreted alongside the trajectories of maximum principal compressive stress (Figure 2.4a&c). All results plotted as two dimensional stress maps or 1 dimensional 'stress magnitude over lateral distance' using the convention that tensile stress is positive (Figure 2.4d). In addition von Mises shear stress, i.e σ_1-σ_3 is usually presented in the same format (Figure 2.4b). The direction of principal stress axes are plotted as stress trajectories, since we are normally concerned with the propagation of dykes or inclined sheets, the maximum principal stress (σ_1) is plotted as cones or arrows. It is important to note that whilst COMSOL outputs give the impression of stress directionality, the direction is purely aesthetic and has no physical meaning. The orientation rather than the specific direction of stress trajectories is of interest in all models.

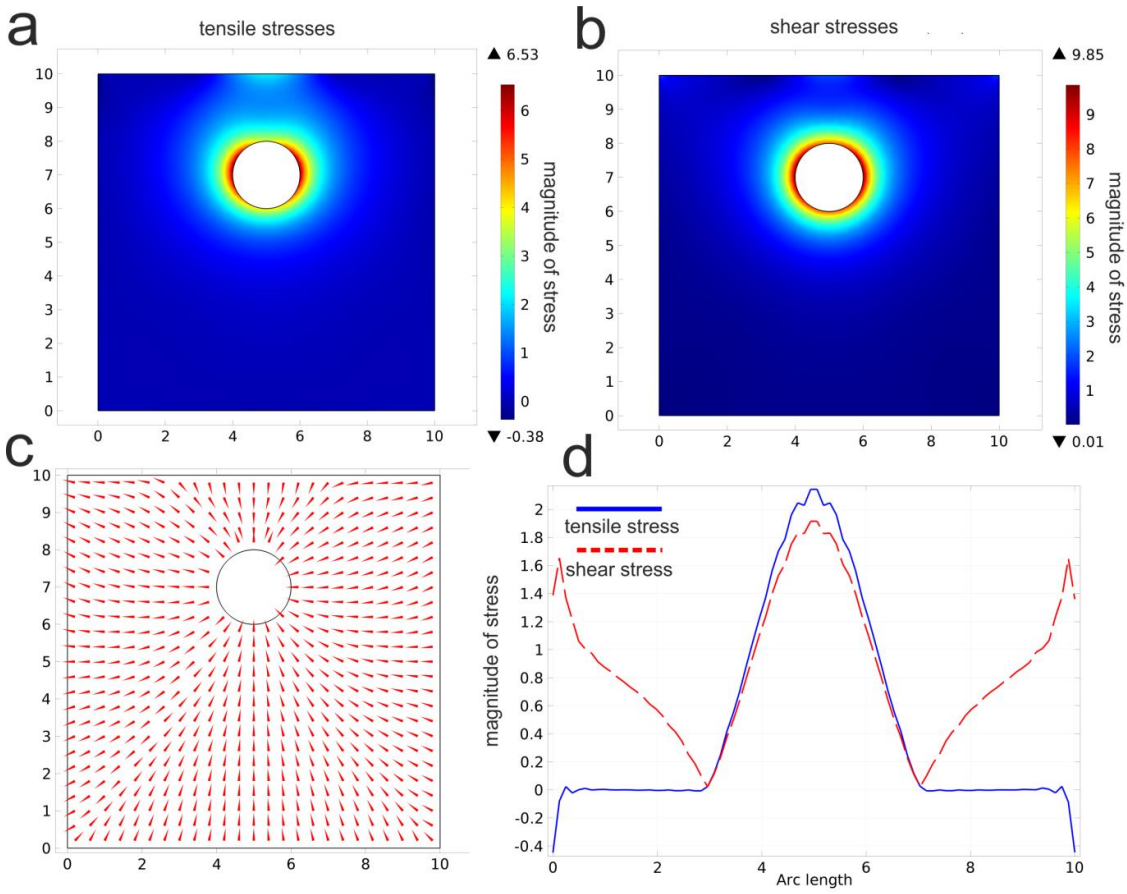

Figure 2.4: Typical COMSOL model result output generated from an symmetric model setup where the dimensions of the x and y co-ordinate are in kilometres. a) a stress map showing the magnitude and distribution of minimum principal compressive stress, termed tensile stress. b) a stress map showing the magnitude and distribution of von Mises shear stress, i.e σ_1-σ_3. c) trajectories or orientations of the maximum principal compressive stress. d) magnitude of stress along a horizontal plane, in this case the plane is that of the free surface (upper edge of the model), both shear and tensile stress values are plotted.

2.1.8 Limitations of the FEM method

A limitation of the majority of numerical modelling methods that calculate stress and resultant strains and displacements is that they are essentially static models which provide a snapshot of conditions as a function of the model geometry and boundary/loading conditions. That does not mean of course that many models cannot

simulate time-dependant processes such as visco-elastic strain, but all FEM models rely on a geometrical setup that does not alter with each time-step. Take the example of a propagating fracture, like the ones (dykes) shown in chapter 4. In order to characterise the propagation pathway it is necessary to interpret the stress signal (or stress map) and then re-build the model based on the previous results.

A comparison of FEM models to standard analytical benchmarks suggests that the maximum percentage error is $\ll 1\%$ (e.g Grosfils 2007). This translates to absolute differences in strain and displacement fields of 10^{-4} to 10^{-5} m (Grosfils, 2007; Hickey and Gottsmann, 2014), and absolute stress differences of 10^{-3} MPa near an area of interest (Grosfils, 2007; Hobbs, 2011). Grosfils (2007) has proposed that FEM models which do not apply additional gravity loading give misleading results, a claim which has been refuted by Gudmundsson (2012). The topic is covered in further detail in Chapter 7.

2.1.9 Alternative software and numerical methods

Discrete element method numerical software is growing in popularity in structural studies. The method differs from boundary element and finite element in that the model mesh is made from many spherical nodes with the surrounding edge containing a cohesion parameter which is used to input values of *E* and other salient parameters. The main advantage of this technique is that the bonds between individual nodes can be broken, and therefore dynamic fracturing processes can be directly observed rather than interpreted from stress snapshots, as shown in Figure 2.5 (Holohan et al., 2015). The problem with this method, and the predominant reason why it was not utilised, is that spherical nodes are not a good representation of crustal materials. The method provides a similar problem as often experienced in analogue models which use sand as the crustal material. When scaled often the individual sand particles become much larger than any possible fractures or spaces at depths below 1 km. It is perhaps convenient that many of the advocates of the discrete element method are those who use analogue type sandbox models, often the results are supportive which comes as little surprise when considering the mesh and material physics.

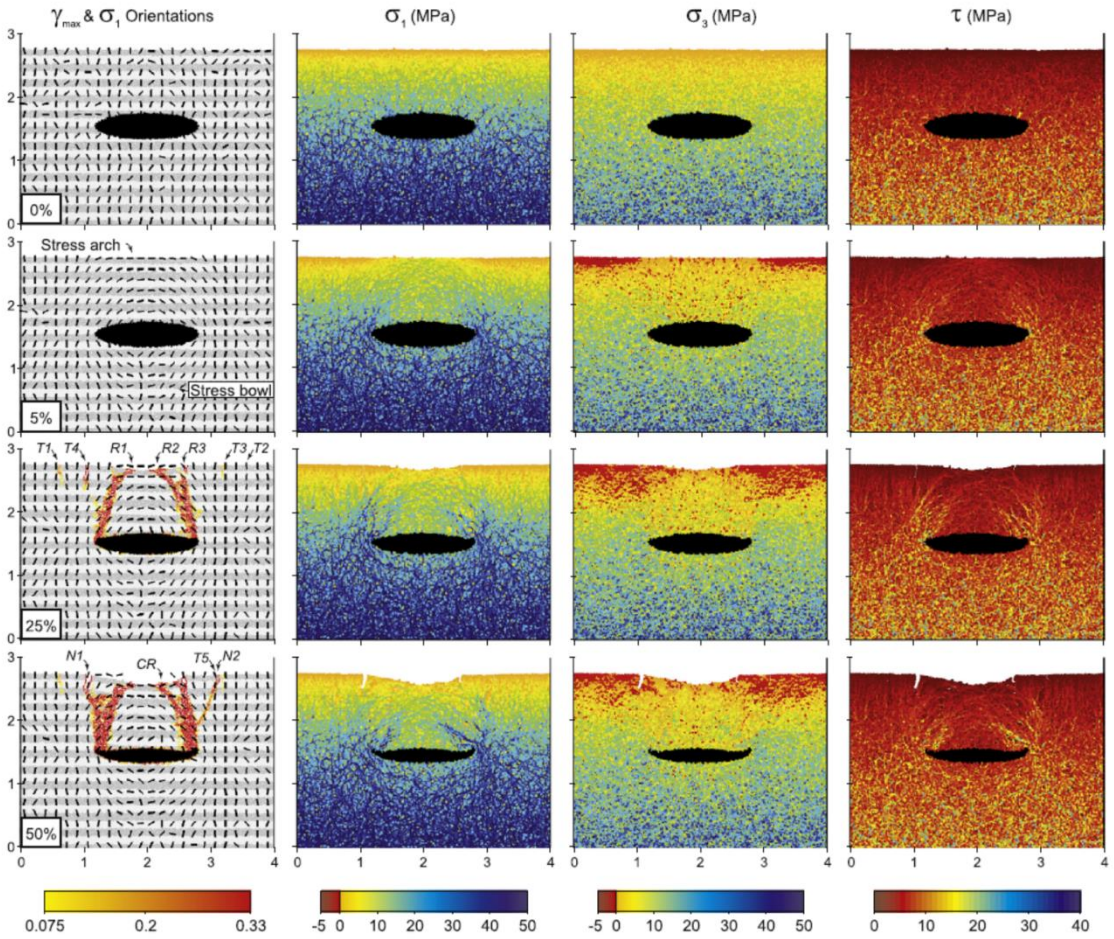

Figure 2.5: Results of a Discrete Element Method (DEM) model showing stress and strain evolution during a 'piston type' magma chamber failure. With increasing magma chamber depletion (from top to bottom) it is possible to track the development of faults from kinematic relations as well as stress concentrations. The method can also be utilised to estimate the propagation path of new fractures from principal stress orientations, after Holohan et al (2015).

Results obtained from COMSOL and other FEM modelling techniques, i.e ANSYS and boundary element techniques, i.e BEASY compare very well (Barnett and Gudmundsson, 2014; Gudmundsson and Philipp, 2006; Gudmundsson, 2012, 2007).

2.1.10 Displacement mode of cracks

Throughout this thesis we consider three displacement modes of cracks, namely, mode I, mode II and mode III. Mode I cracks, also referred to as tensile cracks, occur when the crack walls move directly apart from each other. Mode II and Mode III cracks refer to sliding, or tearing of the crack walls. In simple analytical models of an extension

fraction such as a dyke, the appropriate model is a mode I crack (Gudmundsson, 2011). Similarly a large strike-slip fault can be modelled as a mode III crack, and a dip-fault (a caldera fault) can be modelled as a mode II or mode III crack. Many fractures are best modelled as hybrid, or mixed-mode cracks.

2.2 Experimental methodology

2.2.2 Introduction

Cooling induced micro-cracking is an important but poorly understood process in volcanic systems. The suite of experimental methods detailed in this chapter aim to provide insights into the types of fractures induced by thermal contraction in volcanic rocks. A new experimental setup is introduced, and a new technique for quantifying crack annealing suggested. The vast majority of studies on thermal cracking have concentrated on those fractures produced as a sample expands during heating, and is therefore subjected to overall compressive stress. Our study seeks to understand the fractures generated as a sample contracts during cooling, and is therefore subjected to overall tensile stress.

Experimental studies of cooling induced fractures are complicated because it is difficult to ascertain at which stage fractures were formed during the heating and cooling cycle. To overcome this difficulty we investigated a method of annealing fractures by forming melt at high temperature. We attempted to capture measurements of P-wave velocity (V_p) throughout the thermal stressing tests. The hypothesis was that V_p would decrease during heating as micro-cracks formed from thermal stresses, but would then increase at maximum temperature as the viscous melt produced relaxed into open fractures. As the experimental methodology developed it became clear that measurements of P-wave velocities were not achievable during thermal stressing tests with the current setup.

In order to characterise fractures during thermal stressing tests we measure acoustic emission (AE) output. A common method for providing insights into fractures during rock deformation experiments is the acquisition of acoustic emission (AE). This technique requires AE transducers to be in either direct contact with the sample surface,

or in contact with a sample loaded wave-guide. In high temperature experiments AE transducers would become damaged if they were in direct contact with the sample surface inside a furnace, and therefore a wave-guide of sufficient length was needed to position transducers outside of the furnace. The jig which hosts that wave guide had to be capable of accommodating sample expansion as well as sample contraction. As such, high force springs were attached to either end of the jig to ensure constant loading and parallel contact between wave guide and sample throughout heating and cooling cycles. Measurements of P-wave velocities provide an indication of the relative amount of pore space (fractures) contained within a sample and were measured and compared prior to and post heat treatment. These measurements were complemented by image analysis of micro-fractures using Scanning Electron Microscopy. Attempts to characterise fracture annealing at high temperature eventually proved unfruitful. All sample materials were characterised prior to heat treatment and following heat treatment using a range of methods highlighted within this chapter.

2.2.3 Sample selection and preparation

Three rock types are utilised throughout this study, an intrusive basalt from Seljadur in Iceland (IB), previously described by Vinciguerra et al (2005), an intrusive phonolite dyke from Anaga in Tenerife (AP) and an extrusive dacite lava from Nea Kameni, Santorini (NKD). All calibration and initial experiments were conducted using the Icelandic basalt, this follows for a number of reasons. 1) There was an abundant supply of the material, 2) many of the rock's mechanical properties have been previously investigated and are therefore quite well known, 3) previous attempts have been made to understand thermal cracking processes using this rock (e.g Vinciguerra et al., 2005), 4) the melting point of the rock was understood to be sufficiently high as not to melt in the furnace during high temperature calibrations.

Samples were cored into 25 mm diameter cylinders from their respective blocks using a diamond core drill at University College London (UCL). The ends of each core were then ground using a surface grinder to ensure parallelism and smoothness of the two end surfaces. Sample lengths ranged from 70 mm to 45 mm. It is important that the sample

ends were ground as smooth and even as possible to ensure a flush contact with the wave guide cones.

Length and diameter of each sample were taken using a digital calliper. Three independent measurements were taken at 120^{o} intervals, in order to fully encompass any variation in sample size. Any samples which have a difference in length of +/- 0.1 mm were re-ground so that maximum area contact was achieved when clamped into the experimental jig. Average radial length discontinuity was +/- 0.05 mm.

2.2.4 Sample characterisation

In order to characterise each sample type prior to and following heat treatment we undertook the following analysis:

1) Optical light microscopy and scanning electron microscopy (SEM) to investigate pre-existing crack populations and rock mineralogy.

2) Benchtop P-wave velocity analysis to investigate sample isotropy and initial void space

3) Porosity measurements as a proxy for the amount of pre-existing void space

4) Thermo-mechanical analysis to determine the materials elastic and plastic response to heating and cooling, as well as determine the thermal expansion co-efficient (α) of each sample type.

5) X-ray fluorescence (XRF) in order to understand the chemistry of each sample type

6) Hot-stage microscopy to gain insights into sample softening temperatures

2.2.4.1 Optical light and scanning electron microscopy

Initially cylindrical samples were cut into thin sections along axis and observed using an optical microscope. Whilst this technique was useful for constraining petrological

aspects of the samples, it gave little information on the number and size of fractures. Against the dark groundmass of the sample matrix it is difficult, perhaps impossible in most cases to see any fractures. In fact, the only fractures that can be confidently measured are those which occur within crystal planes. These fractures are likely related to crystal formation however, and represent cleavage planes normally associated with the crystals observed. This method was therefore deemed unsuitable for analysing crack morphologies, and instead was used only to determine the petrology of each rock type based upon standard igneous petrographic techniques (Shelley 1993). Petrologic data are used to complement other analytical methods (TGA-DSC, Dilatometry) to inform about possible phase transitions and estimate likely melting points.

The scanning electron microscope technique provided much greater detail with respect to fractures. In all sample types and sections fractures can be observed in clear detail with a resolution and measurement uncertainty of approximately +/- 5 μm, derived from repeat measurements.

2.2.4.2 Benchtop P-wave velocity measurements

Preliminary ultrasonic wave velocity measurements were made on all sample types at ambient conditions. An Agilent Technologies 1.5 GHz 'Infiniium' digital oscilloscope was connected to a JSR DPR300 35MHz Ultrasonic pulser/receiver which was used to excite one Panametrics V103 P-wave transducer at 1 MHz resonance frequency (Fig. 2.6). Waveforms captured from an identical transducer, both of which have 12.7 mm diameter piezoelectric elements, were pre-amplified and then displayed on the digital oscilloscope (Figure 6). Radial measurements were taken at 20° increments around the circumference of each sample. Pre-heat treated samples were re-measured using the same technique following each thermal cracking test. Wave velocities are calculated as a function of the time taken for the induced wave to travel (t) through a measured length of sample (d). P-wave travel times were measured by picking the signal break from a stacked signal which was relatively noise free and therefore possible to pick the first deviation from zero. All measurements of P-wave travel times take account of travel time through the transducer's tungsten carbide face-plates, calibrated previously as 0.14 μs for the P-wave transducer.

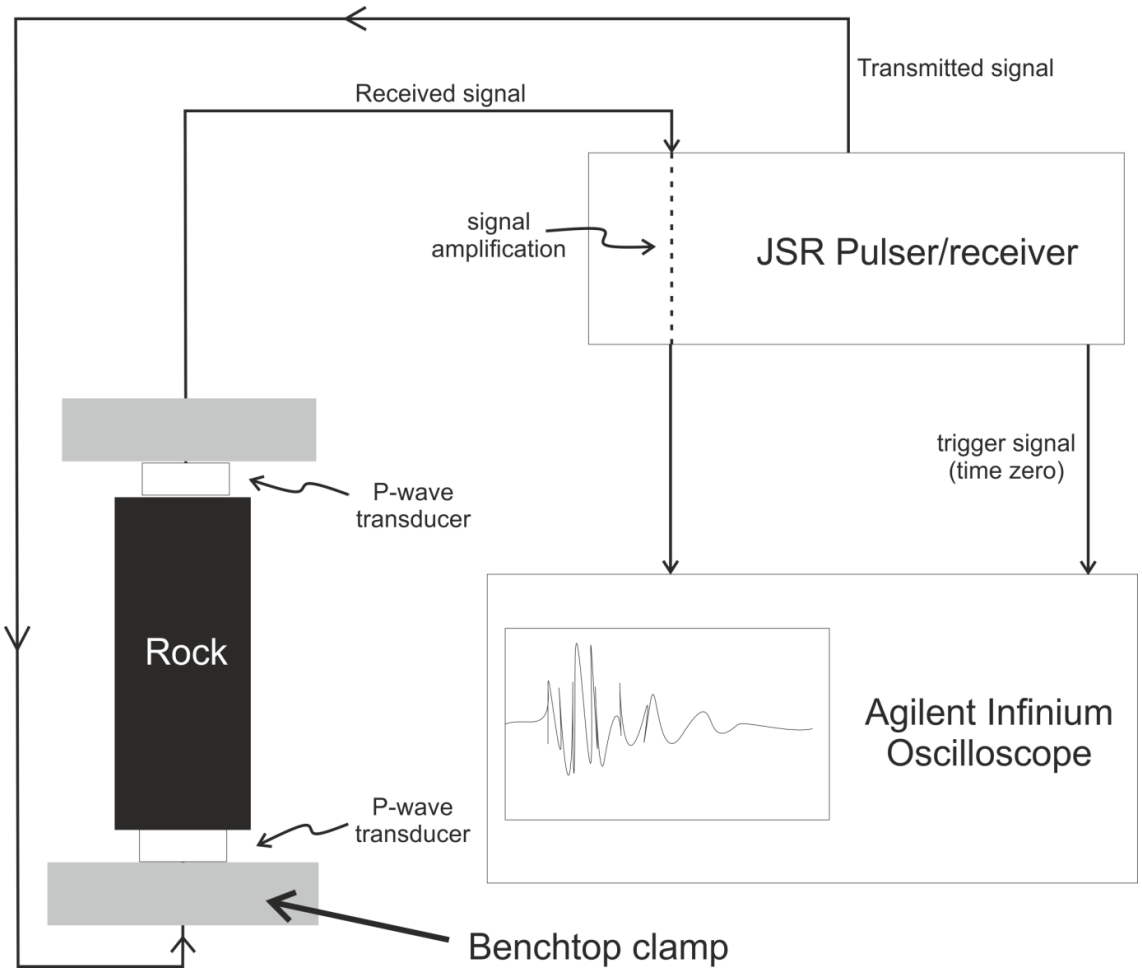

Figure 2.6: Apparatus layout for benchtop seismic velocity measurements. P-wave transducers held in an assembly clamp are connected to the rock surface. A P-wave is transmitted from a pulser which travels through the rock and back to a receiver. The resultant wave can then be analysed on an oscilloscope.

2.2.4.3 Density and Porosity measurements

Bulk density, ρ, of all materials were measured using cylindrical samples. Volume was calculated using caliper measurements of the diameter and length with an error of ± 0.02 mm. All measurements were repeated three times, with the mean diameter and length calculated. The mass of each dry sample was measured using digital scales with an error of ± 0.02 g.

Porosity is the proportion of bulk rock volume V_{bulk} that is not occupied by solid material. If the volume of solid V_s and the volume of pore space is $V_p = V_{bulk} - V_s$, then porosity ϕ can be defined as:

$$\phi = \frac{V_p}{V_{bulk}} = \frac{V_{bulk} - V_s}{V_{bulk}} \tag{2.8}$$

Porosity was measured using an AccuPyc II 1340 Helium pyconometer, which involves the injection of Helium gas into a chamber containing a rock of known volume (Figure 2.7). The Helium penetrates the pore-space of the rock, and the volume of gas which has been injected is calculated using Boyle's law:

$$pV = k \tag{2.9}$$

where p is the systems pressure, V is the volume of gas, and k is a constant. Porosity is then calculated from the volume of gas injected into the sample and expressed as a percentage.

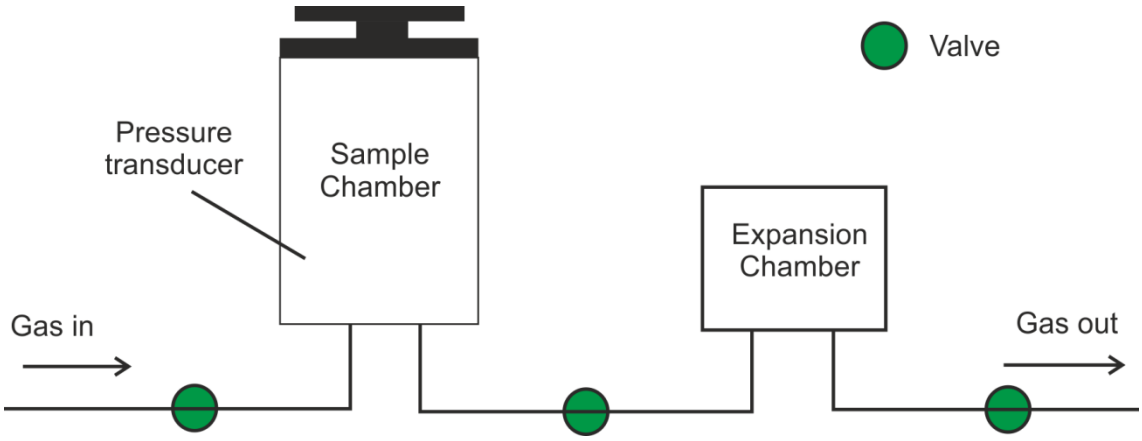

Figure 2.7: Schematic of a helium pycnometer setup where a sample chamber is filled with a volume of gas, this volume is then released through a valve into an expansion chamber and the volume difference calculated.

2.2.5 Thermo-mechanical measurements

The maximum temperature and potential annealing timescale τ set for each thermal stressing test was determined from thermal mechanical analysis. A Netzsch TMA 402 F1/F3 Hyperion thermo-mechanical analyser (TMA) at University of Liverpool (Figure 2.8) was used to determine linear thermal expansion (α) and strain (dL/L_o). A sample load of 3 N was applied to a linear displacement transducer (LVDT) and the measured change in sample length was obtained with a resolution of 0.125 nm (Siratovich et al., 2015). Each materials volumetric thermal expansion coefficient can be defined as (Simmons and Cooper, 1978):

$$\alpha_v = \partial\varepsilon_v / \partial T \, . \qquad (2.10)$$

where α_v is the coefficient of volumetric thermal expansion, $\alpha\epsilon_v$ is the change in strain, and ∂T is the change in temperature. In order to calculate thermal expansion experimentally the change in strain and change in temperature have to be changed from a volumetric to a one-directional (length) solution (Siratovich et al., 2015) by:

$$\alpha_L = \frac{1}{L} \cdot \frac{\partial L}{\partial T} \qquad (2.11)$$

In this solution, α_L is the linear expansion coefficient where L is the reference length of a sample at initial temperature T_o and ∂L is the difference in length of the sample induced by a change in temperature ∂T .

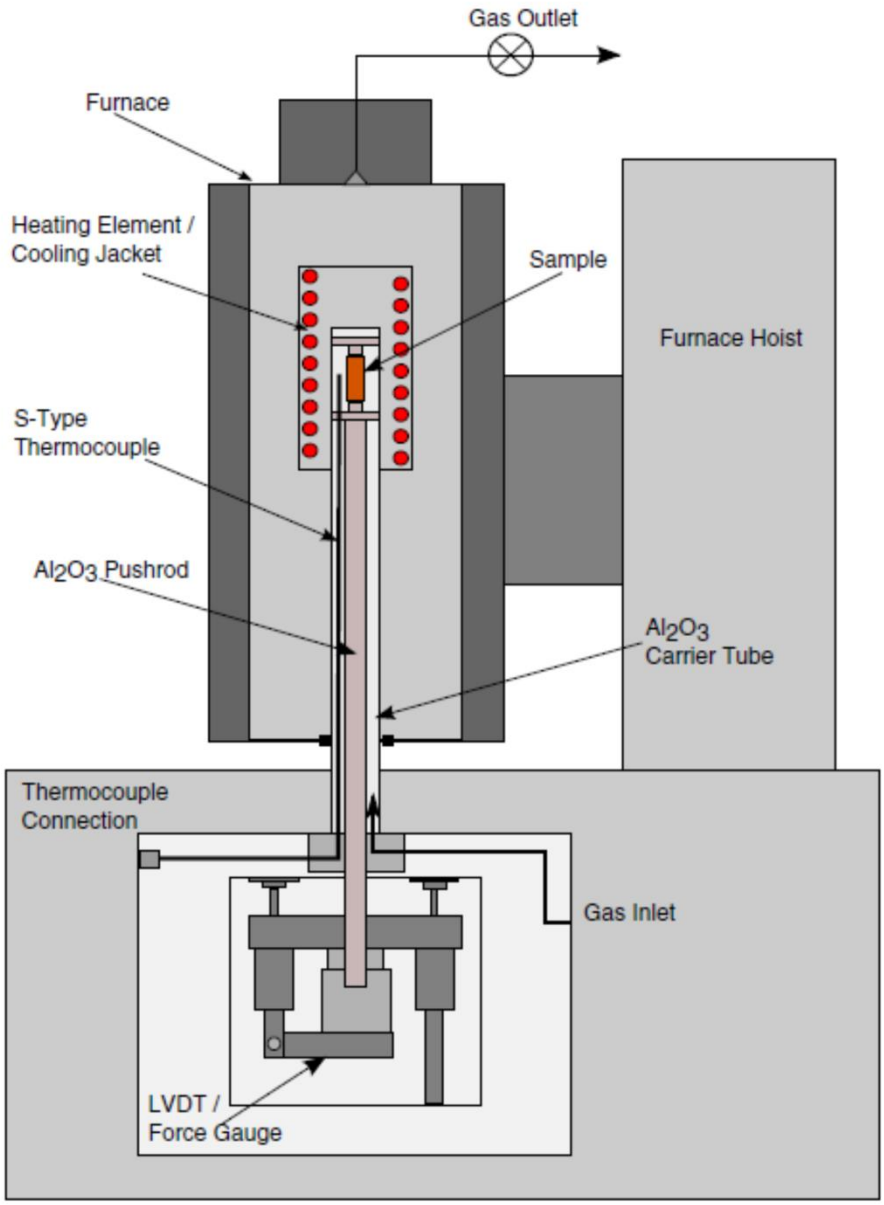

Figure 2.8: Simplified schematic of the Netzsch Hyperion 402 thermo-mechanical analyser used within this study, modified after Siratovich et al (2015).

Thermogravimetric measurements (TG) and differential scanning calorimetry (DSC) were carried out using Netzsch STA 449 simultaneous thermal analysis equipment at University of Liverpool. Small chips of sample around 50 mg were heated in a crucible at a rate of 10˚C/min to a maximum temperature of 800-1100˚C depending on the material used. Measurements were used to inform about 1) the range of temperatures over which the glass transition (Tg) occurs in each material and 2) help characterize bulk melting and re-crystallisation.

2.2.4.4 Whole rock geochemical analysis

Bulk powered samples were analysed for whole rock geochemistry using X-ray fluorescence (XRF) on fused glass discs. All analyses were undertaken on the Philips PW1480 at Royal Holloway using the techniques of Thirlwall et al. (2000).

2.2.4.5 Hot-stage microscopy

Hot-stage microscopy was used as an initial test to investigate the temperature range over which each sample would become plastic or partially molten. A Linkam TS1500 hot-stage connected to a Zeiss Axioscope at Lancaster University was used as the apparatus for these heating experiments (Fig. 2.9), for further details see the description of Applegarth et al. (2013). Thin wafers (<100 μm) of Icelandic basalt and Anaga Phonolite were double polished and heated to 1150˚C. Images captured at a rate of 1/s were compared at the highest temperature to check for fracture annealing or signs of plasticity. Results proved largely inconclusive as individual fractures could not be discerned using this method. However partial melt relaxation was inferred at the highest temperature run in the Icelandic Basalt, the same test showed no obvious relaxation in Anaga Phonolite.

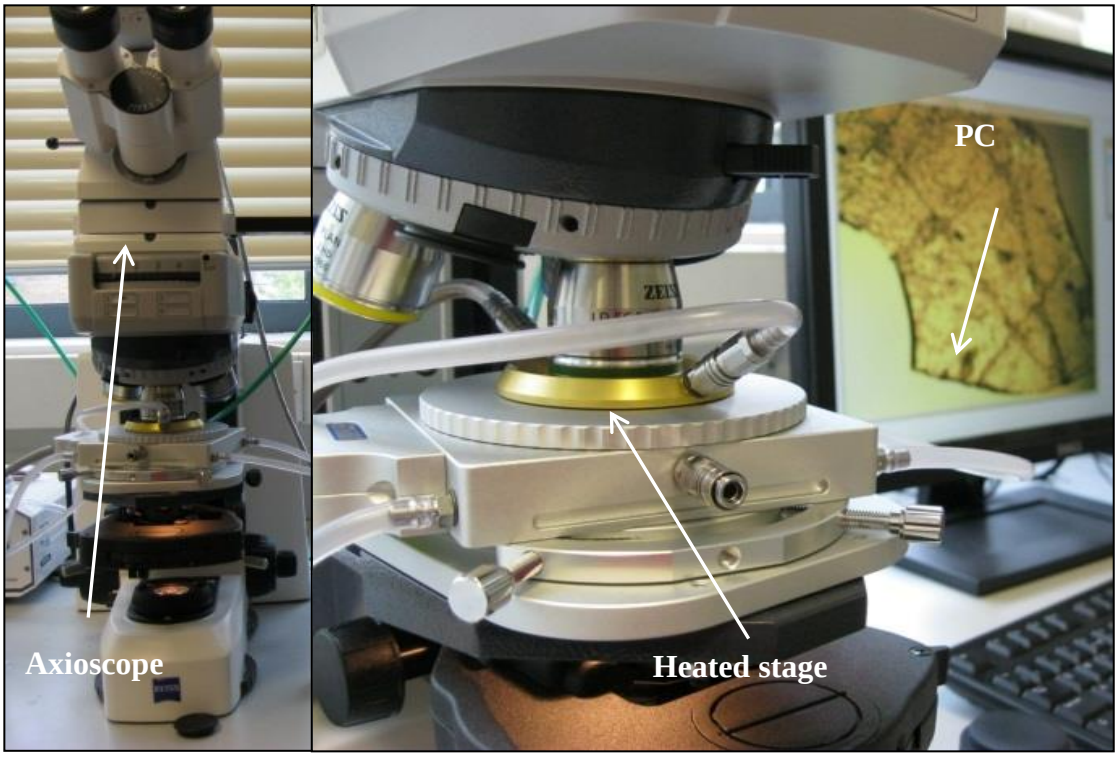

Figure 2.9: Hot-stage microscope setup at the Lancaster University thermal laboratory. A thin (100 μm) sample wafer is placed inside a ceramic furnace, temperature is set by a Linkam TS1500 heated stage mounted on a Zeiss Axioscope. In-situ observations are made using a connected PC.

2.2.6 Experimental apparatus

Samples were placed inside a Carbolite tube furnace using a specially designed jig that is capable of withstanding high temperatures and allows the transmission of ultrasonic waves through a central wave guide (Figure 2.10). The sample is loaded by high force springs which were located, outside the furnace at either end of the jig. Transducers, connected to a PC were used to measure ultrasonic waves and placed on cones at the far end of the waveguide. Temperature was measured using a K-type thermocouple placed on the sample surface during all experiments. Initial temperature calibration tests were conducted using two K-type thermocouples, one placed on the sample surface, and one placed in the sample centre, as well as a thermocouple in-built to the furnace. During

these calibration tests, temperature was measured digitally using a thermocouple conditioner connected to a PC and also manually by noting the temperature display on each conditioner and the furnace temperature display.

A new stainless steel jig capable of resisting oxidation up to a maximum temperature of 1100˚C was designed and built at the UCL rock physics laboratory (Figure 2.11). The steel, an alloy 310 (UNS S31000) is an austenitic stainless steel developed specifically for use in high temperature environments. It was important that the jig remained relatively free from oxidation to ensure the free movement of key parts and to ensure contact surfaces (cones) on the wave guide remained clean and with a smooth surface. Previous similar steel jigs have undergone significant oxidation and resultant corrosion during high temperature tests. A rock sample (30 mm to 75 mm in length) was held in between two cones, connected by 1.1m long wave guide using a yoke system which could move longitudinally independent from the rest of the jig. The yoke system comprised a set of two high force springs which were located near the ends of the jig. The springs ensured constant sample loading throughout the full heating (sample expansion) and cooling (sample contraction) cycle. When assembled the entire jig was slid into a Carbolite tube furnace so that the sample was in the centre of the furnace. Acoustic emissions were recorded by transducers placed on cones at the end of the central waveguide.

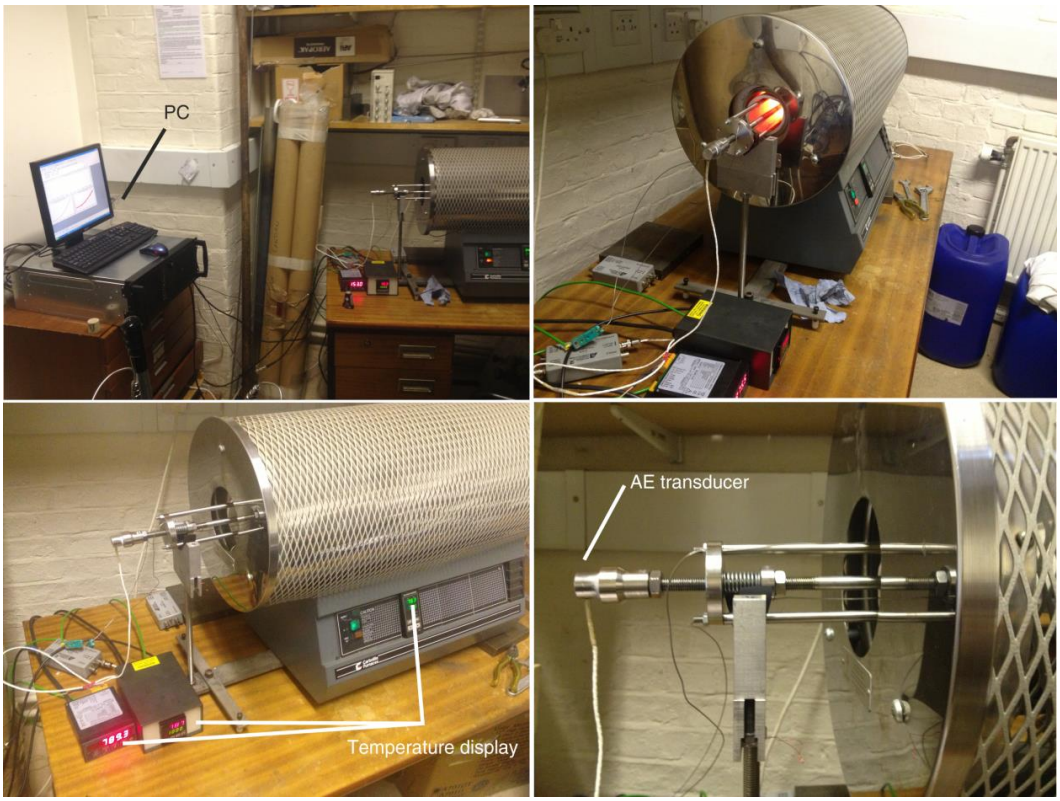

Figure 2.10: Thermal stressing test experimental setup. Rock samples are held within a tube furnace using a specially designed steel jig, which acts as a waveguide. During calibration tests, as the setup is shown here, two K-type thermocouples were placed at the rock interface inside the furnace. AE transducer signal and temperature is recorded on a connected PC.

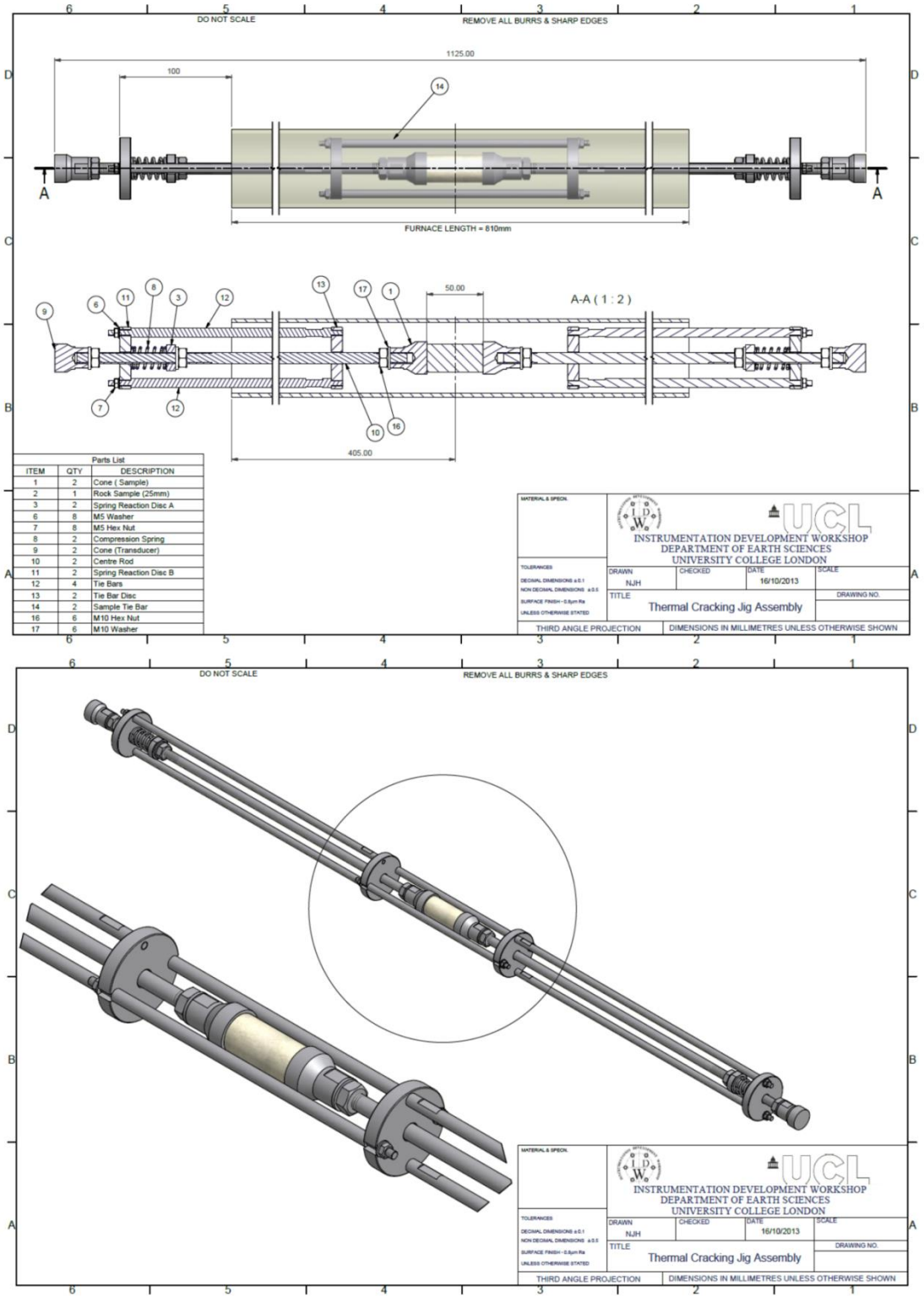

Figure 2.11: Thermal stressing test jig design and assembly, original drawing by N.Hughes, personal communication (2015).

2.2.7 Temperature calibration setup

The Carbolite CTF12/75/700 tube furnace contains an in-built thermocouple and Eurotherm 808 temperature control unit. The control unit allows temperature to be set with the option of two programmable heating and cooling profiles. A set of temperature calibration experiments were carried out with two main aims, 1) to ensure that the temperature reading on the furnace controller could be matched to a known temperature at the sample interface, and 2) to calculate the temperature gradient within a typical sample during differential heating and cooling rates. Each temperature calibration utilised a maximum hold temperature of 1100 ˚C, this temperature is well below the calculated softening point of typical basalt and therefore crack annealing was not expected or tested for.

A basalt core was specifically manufactured to allow a thermocouple to be placed within the sample centre during heat treatment (Figure 2.12). This method made it possible to calculate a temperature gradient, as an additional thermocouple was placed on the outside of the sample. In total three thermocouples and therefore three sets of temperature measurements were taken, one built-in to the furnace and connected to the Eurotherm 808 controller unit, a second placed on the outside of the sample within the furnace and connected to a thermocouple controller, and a third placed within the sample core and connected to a second thermocouple controller (Figure 2.13). Both of the thermocouples placed on or in the sample were also connected, through the controller unit; to a PC which allowed the simultaneous recording of temperature, time and acoustic emissions data. Unfortunately there was no provision for connecting the furnace thermocouple to the PC to allow continuous recording of temperature, so temperature was recorded manually at 5 to 10 minute intervals.

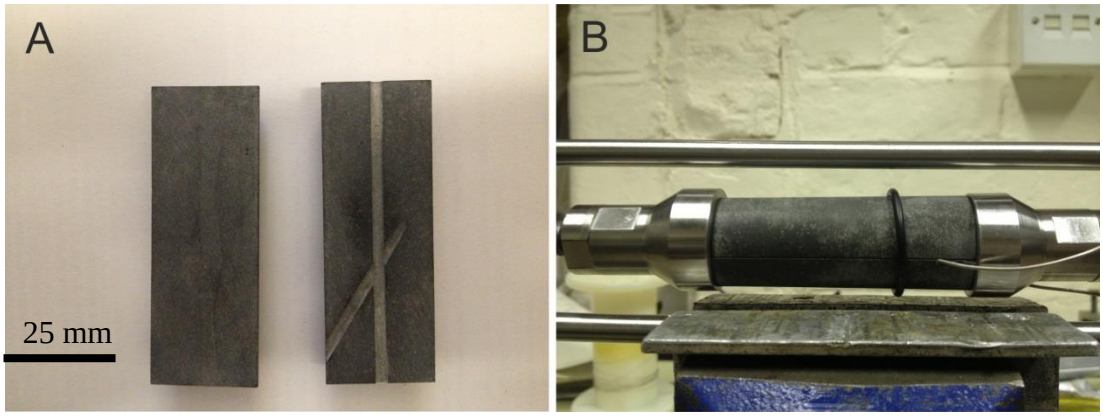

Figure 2.12: Basalt sample modified to allow temperature to be measured in the centre of the sample during heat treatment. A) The basalt sample core was cut in half with a 1.5 mm grove cut into the centre and another thin grove cut at a ~45° angle perpendicular to the centre grove to allow for a thermocouple to be placed inside, as shown in (B).

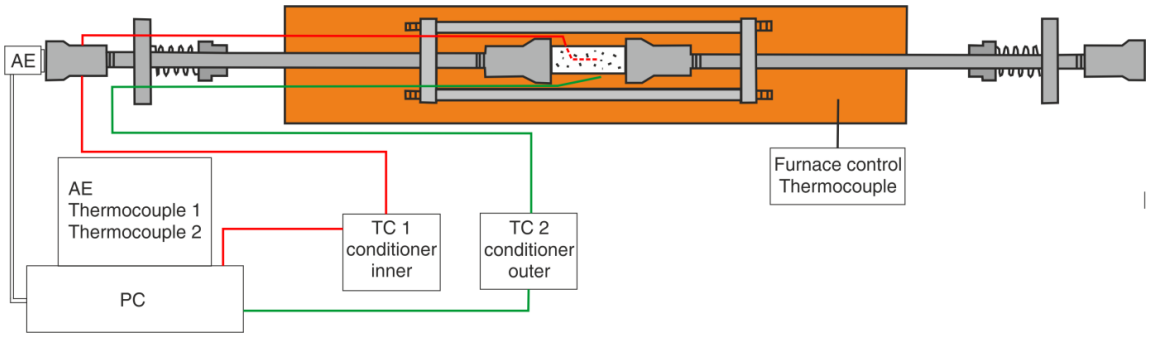

Figure 2.13: Thermal jig setup for acoustic emissions capture during initial temperature calibration experiments.

The slowest heating and cooling rate used was 1˚C/min, and the fastest heating rate was 10˚C/min, in Figure 2.14 the temperature recorded at the sample surface and furnace is shown as well as the programmed furnace temperature. Sample and furnace temperature profiles are consistent aside from an initial heating phase up to ~400˚C (Figure 2.15). This is in contrast to the cooling phase where the fastest possible cooling rate was ~4˚C/min, and therefore the furnace program and measured temperature deviate significantly during tests with a set cooling rate >1˚C. Cooling rate was limited by atmospheric cooling conditions, and therefore it was not possible to cool faster than

~4˚C/min, a rate which is reached for only a small fraction of the total cooling cycle. The slowest cooling rate of 1˚C/min was used as this limited the total length of individual experiments whilst capturing the range of temperatures over which salient annealing and fracturing processes were likely occur (350 to 1150˚C). As such we define a cut-off limit for all cooling that occurs below the 1°C/min rate, indicated as a green line in Figure 14 and corresponding to a temperature of 350°. The natural rate of sample cooling is approximated using a 2nd order polynomial (Figure 2.16), and is consistent among all cooling calibration tests.

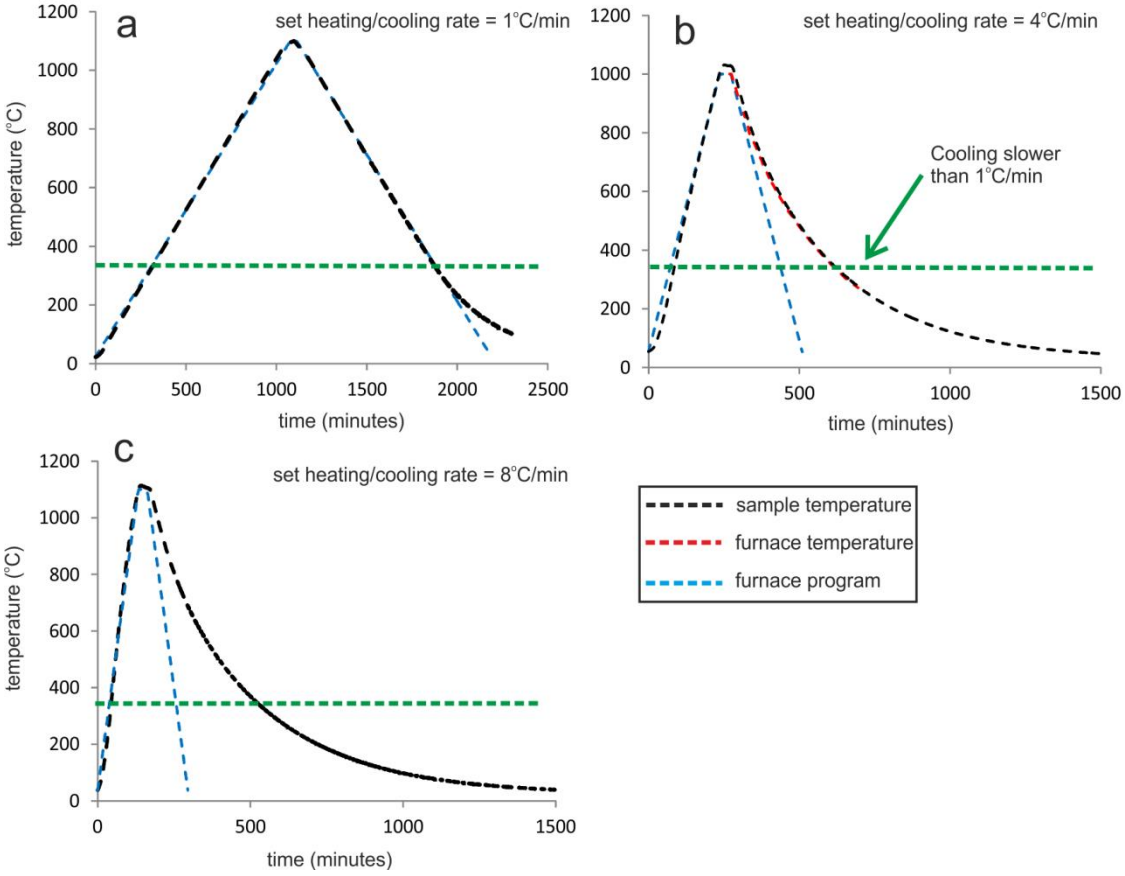

Figure 2.14: Programmed and actual heating and cooling profiles for a range of temperature ramp rates, A) 1˚C/min, B) 4°C/min and C) 8˚C/min. Temperatures were measured at the sample surface. A green line indicates the temperature at which cooling rates decrease below 1˚C/min, the slowest programmed rate of cooling.

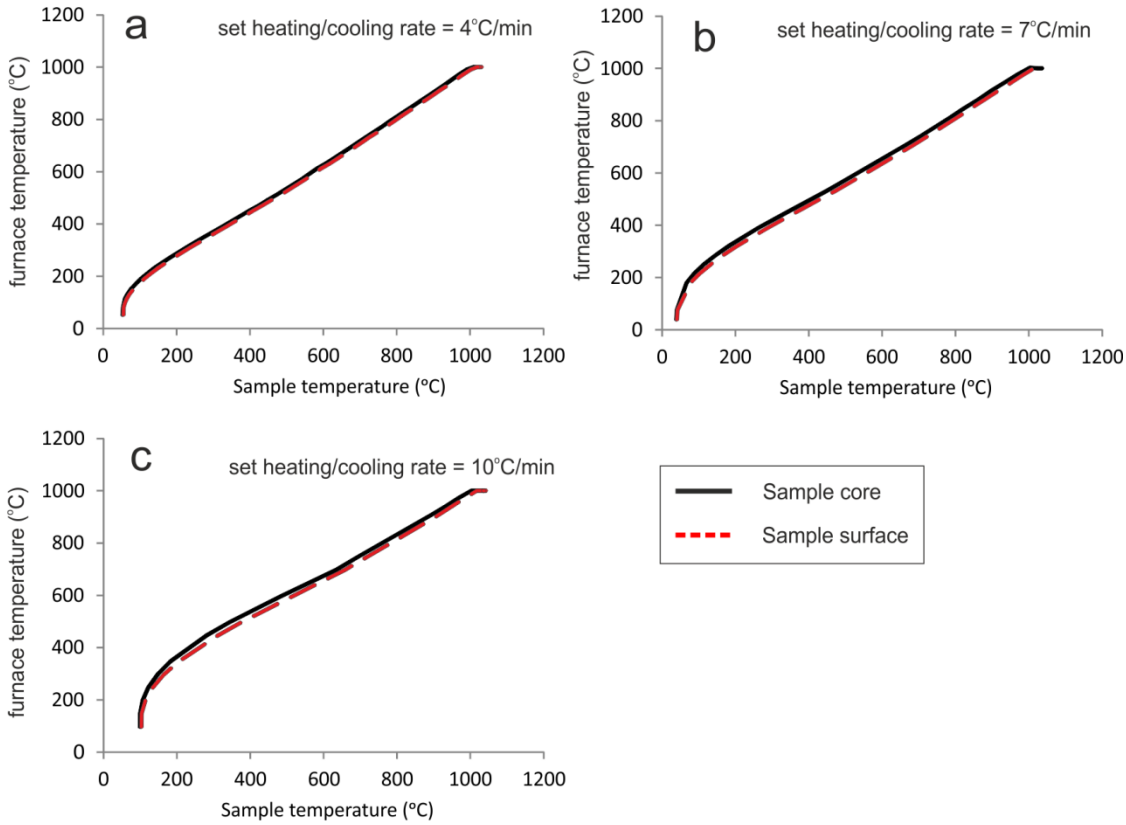

Figure 2.15: Outer sample temperature against temperature recorded inside the sample and at the furnace thermocouple for three differential heating rates.

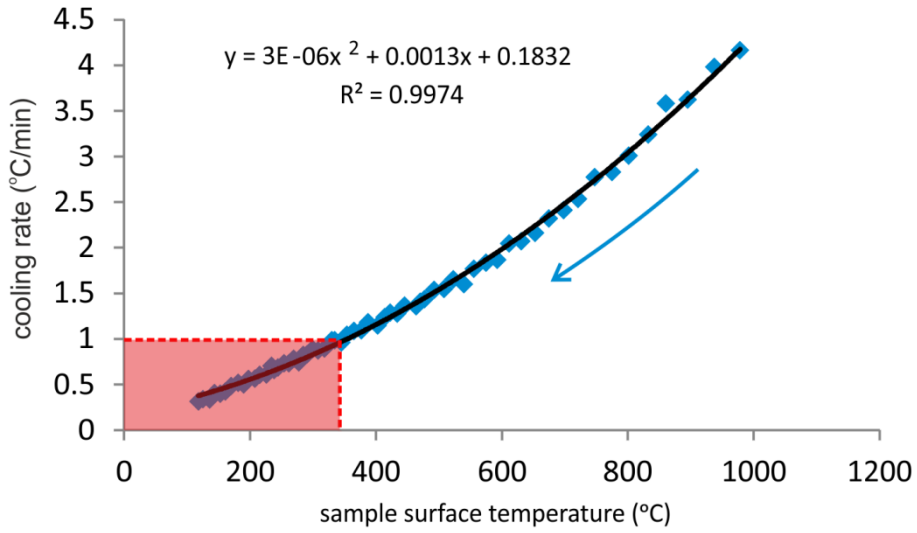

Figure 2.16: Natural sample cooling rate, where maximum cooling occurs at a rate of approximately 4°C/min. All samples cool slower than 1°C/min below 350° independent of programmed cooling rate. A 2nd order polynomial model is fitted with a R^2 correlation of 0.99.

2.2.8 Thermal gradients and timescales of thermal equilibration

It is important to know how long a typical sample takes to thermally equilibrate as a function of heating and cooling rate. In the calibration tests described in this section, the furnace is set to complete a 'ramp and hold' program in which a heating and cooling rate is set with temperatures held for 30 minutes, Figure 2.17. Sample temperature, both surface and core is consistently higher than the recorded furnace temperature, except during the initial furnace ramp where a delay in sample heating is observed. During cooling, sample and furnace temperature are more closely matched.

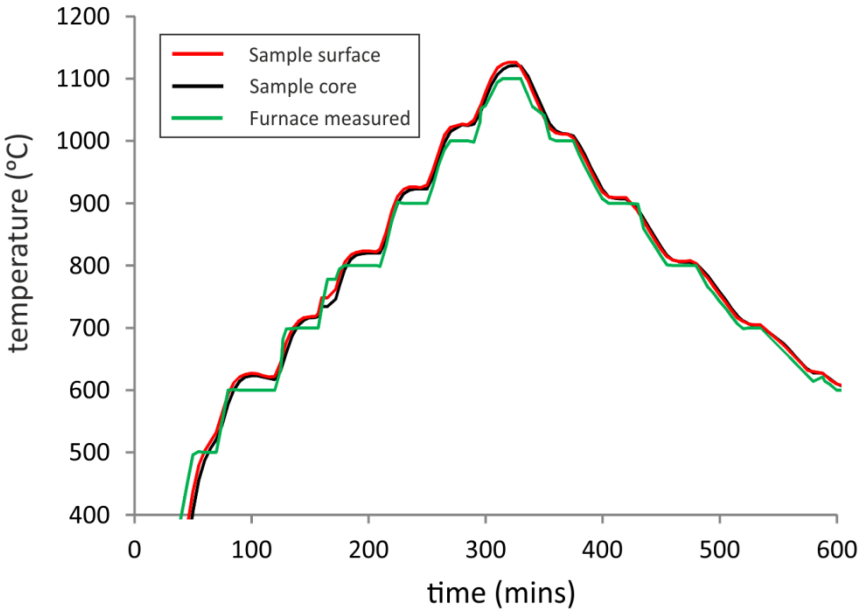

Figure 2.17: Temperatures at the sample and furnace recorded during a 10˚C/min ramp and hold cycle.

The experiment was used to test the timescale of thermal equilibration within a test sample, thermal equilibration is said to be complete when the thermocouple on the inside of the sample (core) gives a reading within error of the thermocouple on the sample surface. The offset or error is temperature dependant (Figure 2.18c) but on average is around 5˚C. When the prior condition is met it is assumed that temperature within the sample is uniform, i.e there exists no radial or longitudinal thermal gradient. Sample surface temperature is consistently higher than sample core temperature during heating and perhaps more surprisingly, also during cooling. At each hold cycle it is possible to observe the timescale with which thermal energy ceases to be input or output from the sample, as recorded by a zero heating/cooling rate (Figure 2.18). This scale is recorded during heating as the time between maximum heating rate and zero heating rate. This timescale is commonly between 20 and 30 minutes (Figure 2.18b). The same timescales are observed during a cooling cycle. The same method can be conducted when considering the internal sample thermal gradient. The temperature difference between the inner and outer sample is observed and the timescale of thermal equilibrium calculated when the difference reaches zero. However there exists an offset

between the two thermocouples and temperature controllers used, so there is always a difference of ~5˚C which increases slightly with increasing temperature (Figure 2.18c).

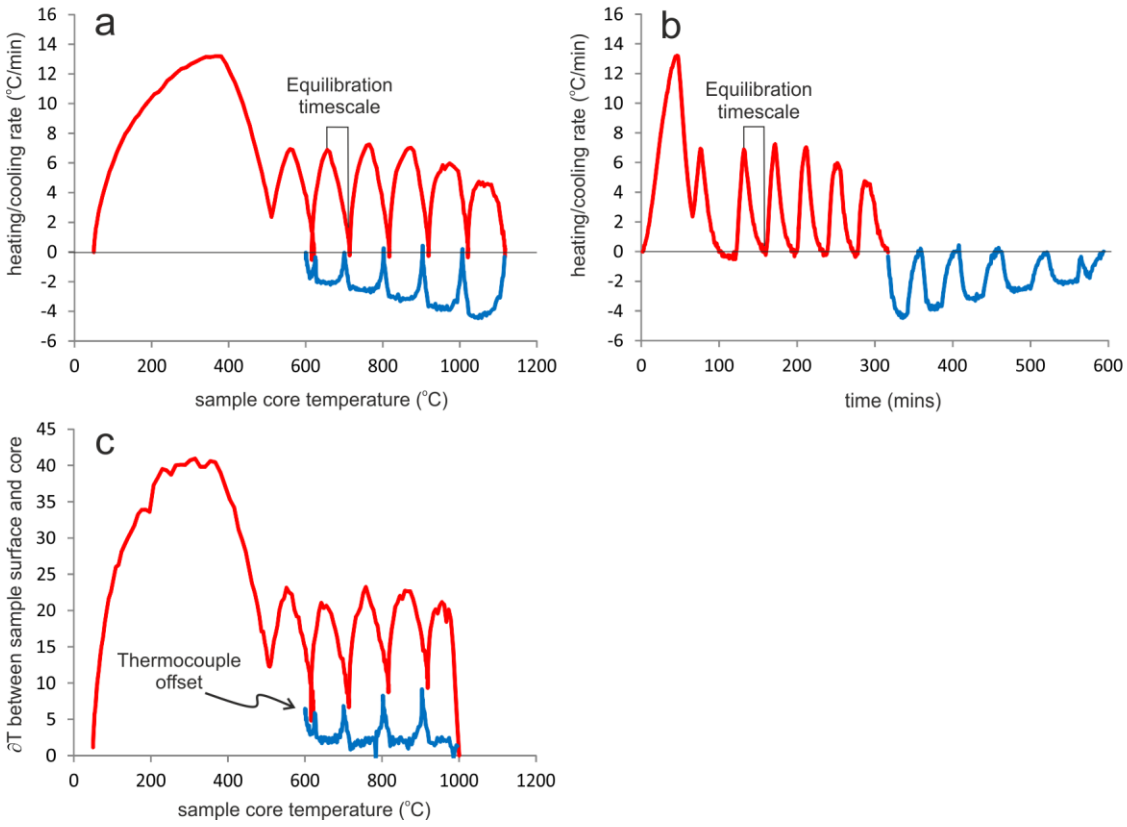

Figure 2.18: Heating and cooling rate of a basalt sample centre during a ramp and hold calibration test. a) heating and cooling rate as a function of temperature , b) heating and cooling rate as a function of time in minutes and c) temperature difference between sample surface and sample core. Red line indicates temperature recorded during heating and the blue line is temperature recorded during cooling Thermal equilibration is defined by the point at which heating or cooling rate decreases to zero, or the difference between recorded sample surface and sample core temperature is zero. In this case there is a temperature offset between the two thermocouples used to measure surface and core temperatures, which increases slightly with increasing temperature.

2.2.9 Acoustic emission (AE)

Acoustic emissions are elastic strain waves generated as a result of energy release during crack interactions and propagation in materials (Lockner et al., 1992). The energy release is a manifestation of transient waves which propagate from the area of failure. Each discrete AE event over time is termed throughout as an AE hit. Within any one AE hit it is possible to distinguish the relative size of a corresponding fracture based on the signal amplitude (dB) and duration (μs) (Nelson and Glasar, 1992). The stored waveform from any discrete AE hit can be used to calculate relative energy, which in the experiments described always has arbitrary units (au). All energy is calculated using the same method and therefore is directly comparable. The energy of any AE event is calculated digitally by summing the envelope of the AE waveform (Fig. 2.19), (see Cox & Meredith 1993 for a detailed description of the AE recording methodology). Acoustic emissions can be measured simply as a rate of emission over time, which provides a proxy for relative damage in a rock body. The emissions can also be characterized by the frequency response (Figure 2.19) and energy released from each event. Here a full seismic response study is not attempted or performed, this is because we are not interested in the precise location or waveform of each discrete event but merely wish to carry out a comparison of the relative 'size' and number of events.

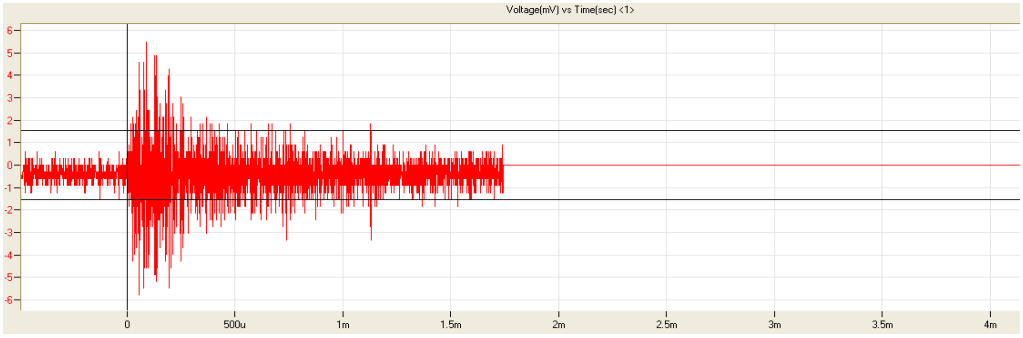

Figure 2.19: Individual AE hits produces a seismic coda such as that shown. An event such as this is likely generated due to micro-crack development within the rock. Time (seconds) is along the x-axis and signal size, in mV on the y-axis

AE hit and corresponding energy rate were averaged per ten AE events in order to reduce the size of the often very large (>10,000 events) AE database, making data interpretation more manageable. AE event rates ($\dot{AE}$) were calculated as:

$$\dot{AE} = \frac{AE_f - AE_i}{t_f - t_i} \tag{2.12}$$

Where subscripts *i* and *f* indicate the initial and final AE events over time (*t*) within the 10 hit interval specified, and the dot refers to derivative with respect to time.

Acoustic emissions were recorded on two separate hardware devices, 1) the Vallen AMSY-5 and 2) the AEWin Pac kit. All experiments utilised one Panametrics V103 piezoelectric P-wave transducer located at one end of the wave-guide. As previously described, AE transducers were located outside of the furnace to ensure that the Curie point, whereby piezoelectric properties are limited or lost due to temperature exposure, was not reached. All AE was filtered at a minimum cut-off of 35 dB to avoid the presence of excessive noise.

2.2.10 Jig generated AE

In Figure 2.20 the acoustic response of the steel jig undergoing a typical thermal stressing cycle is shown, no rock sample is loaded in these tests. A dummy sample made of the same 310 alloy steel used for the waveguide construction was loaded in place of a rock specimen. Acoustic emissions were recorded during a heating and cooling cycle using a maximum temperature differential. It is shown that the apparatus does produce AE but the vast majority occurs below approximately 300˚C and predominantly during the cooling cycle. The test results are repeated through three identical stressing experiments. It is likely that AE is generated by slip and movement on the steel apparatus and springs during contraction, why the jig should be so ‘noisy’ at low temperatures is not clear.

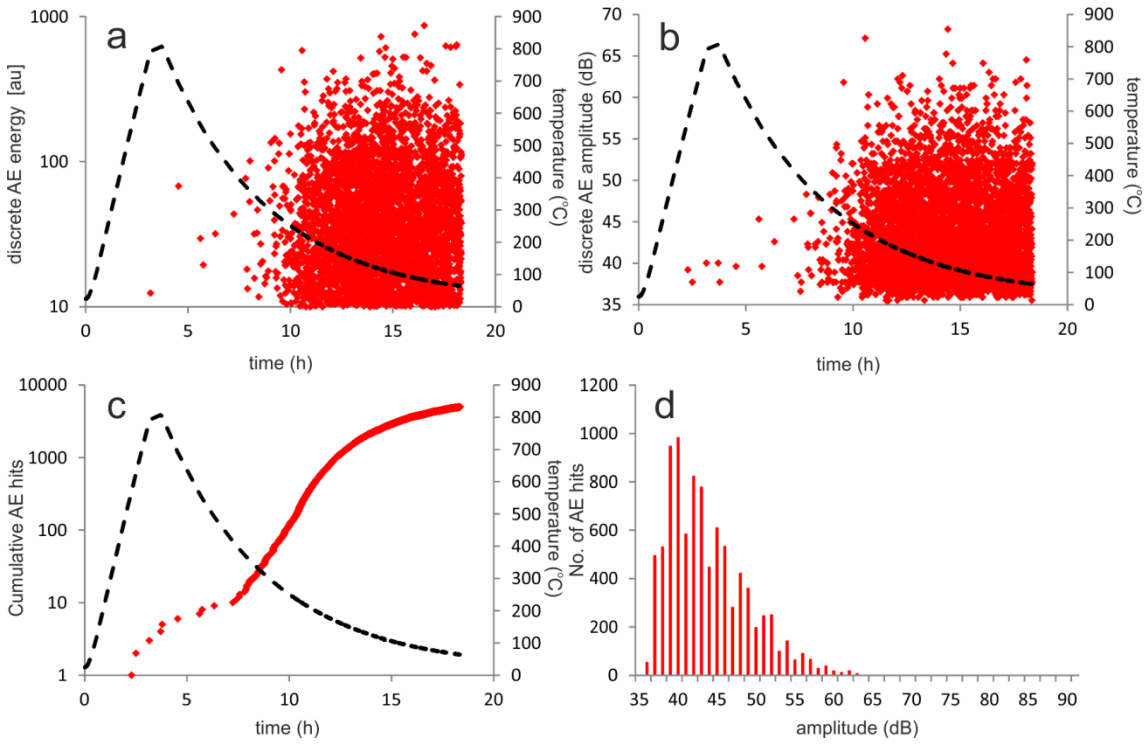

Figure 2.20: Acoustic emissions generated from the steel jig heated and cooled to and from 800 ˚C at a rate of 8˚C/min. Most AE's occur below 300˚C during the cooling cycle. Those tend to have small to moderate amplitudes, and low energy.

In comparison to a typical thermal stressing experiment with a rock sample loaded, as in Figure 2.21, it can be seen that significant moderate to high amplitude and energy AE is produced throughout heating and cooling at all temperatures. This indicates that over the temperature range of interest, >300˚C, we can be confident that those AE recorded are associated with sample cracking as oppose to an artefact or noise associated with movement on the jig and waveguide.

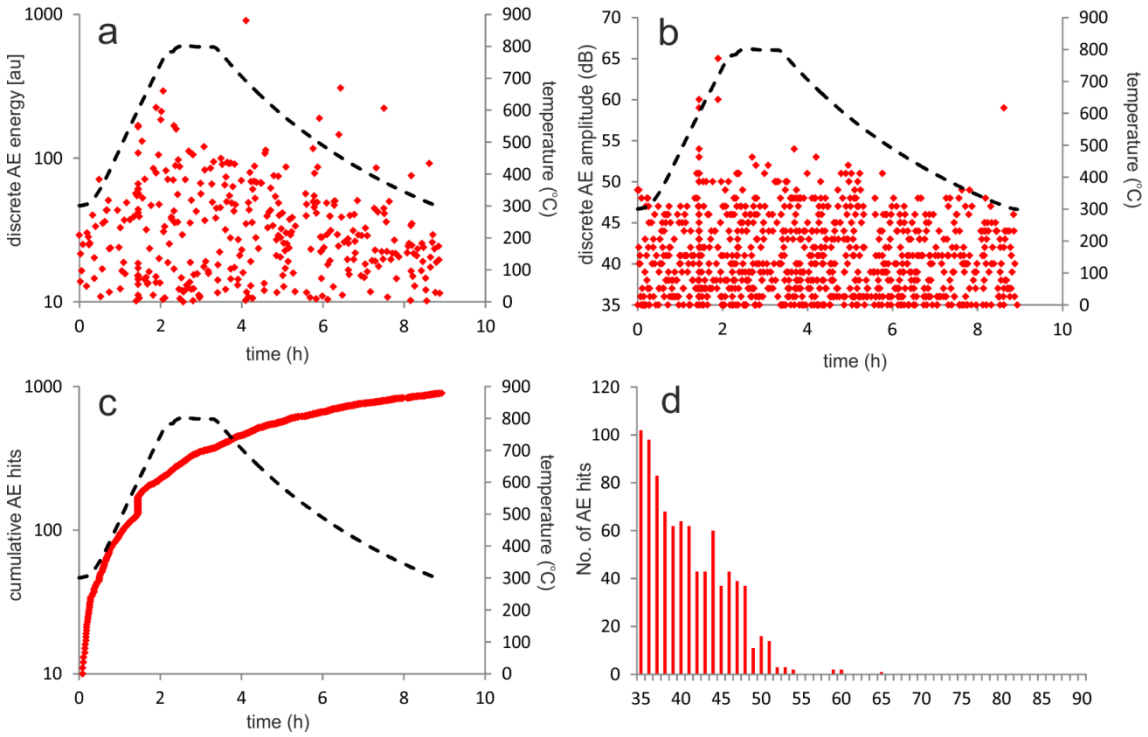

Figure 2.21: Acoustic emissions generated from a basalt sample heated and cooled to and from 800˚C at a rate of 4˚C/min.

2.2.11 Wave-guide and sensor modifications

As the wave guide needed to be sufficiently long to ensure that transducers and springs were positioned outside of the furnace, elastic wave attenuation became a significant issue. As the experimental methodology developed, the steel wave-guide underwent a number of modifications in order to attempt to improve acoustic wave transmission. This was especially important for the acquisition of P-wave velocities, as the generated pulse needed to pass through the entire length of the wave guide and the rock sample, but less so for the acquisition of AE where the elastic waves only passed through half of the wave guide. Despite many attempts and much improvement to the efficiency of wave transmission through the various interfaces of the wave-guide, through for example smoothing contact surfaces, it was not possible to detect a pulsed P-wave through the entire wave-guide length. Whilst a determination of P-wave arrival times and calculated velocities would therefore have been very useful in determining the

presence of crack annealing, it was not possible to do so using the current experimental setup, shown in Figure 2.22.

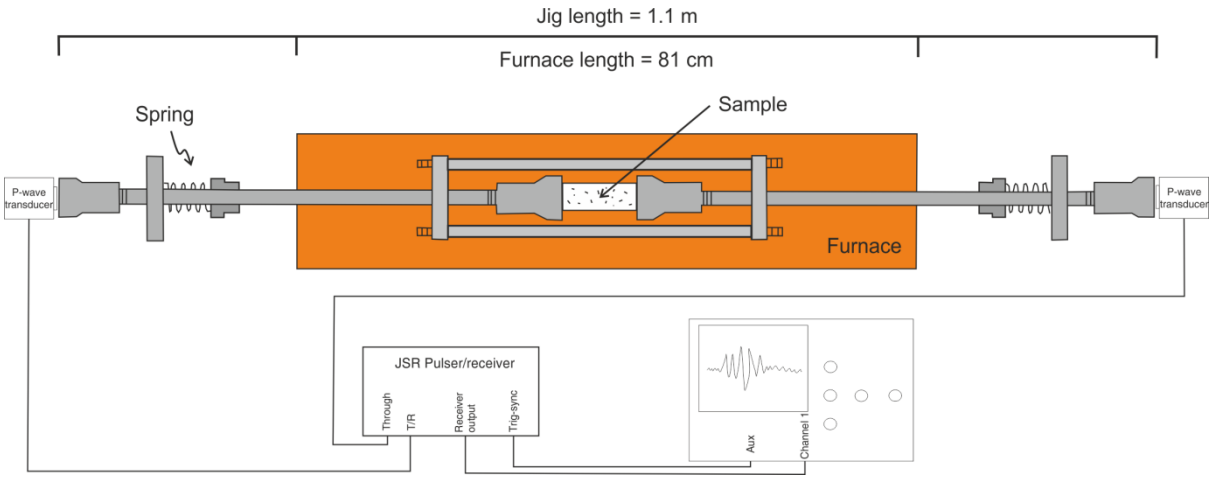

Figure 2.22: Thermal stressing test setup for in-situ P-wave velocity measurements

In the first high temperature experiment (>1100˚C) we attempted to track dynamic wave velocities using two P-wave transducers glued to the ends of the wave-guide. At the end of the experiments, which did not successfully record the transmission of P-waves, the transducers were terminally damaged when being removed from the wave-guide. Transducers at this stage were applied to the wave-guide with adhesive, and removed simply by applying a sharp object in between the contact of the transducer plate and the steel. The transducer holding mechanism was redesigned in order to ensure that the new transducers would not be damaged upon removal. The new design used a plate which was screwed to the outer most ring of the jig in order to apply a force to the transducer, no additional adhesive was needed or used (Figure 2.23).

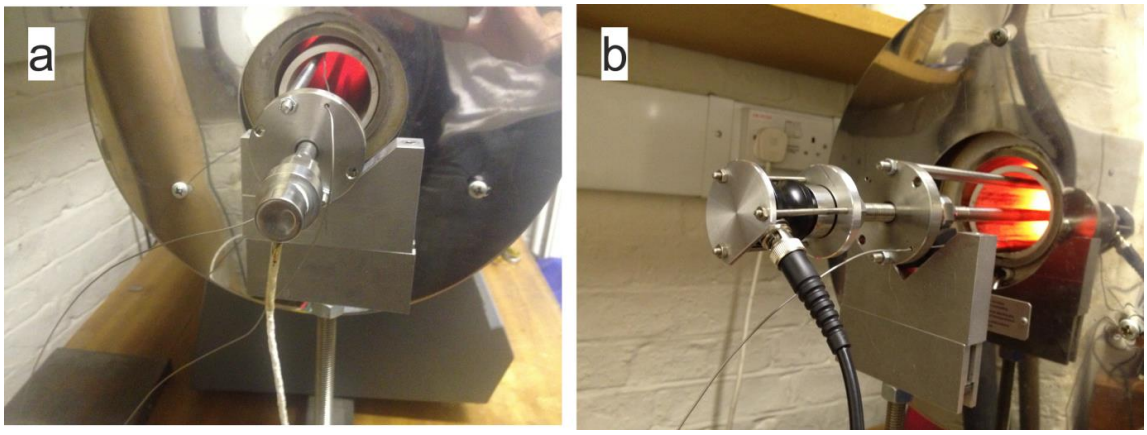

Figure 2.23: (a) Original method of attaching the P-wave transducer at the end of a

cone on the steel wave guide using adhesive, and (b) new method utilising a back-plate and studding to avoid the use of adhesive

2.3 Field methods

All field measurements were taken using standard geologic techniques and conventions as described in many structural geology textbooks (e.g Fossen, 2010). All field measurements utilised a compass clinometer to record dip and strike of faults, fractures and dykes. Strike is here defined as the trend of the plane or body being measured. Dip is the angle between the plane of the structure and a horizontal plane. Together strike and dip define the attitude of a structure, written using the convention strike, dip and dip direction (i.e 005/60E). Where possible and in order to reduce human measurement error, multiple measurements of the same structures where taken with the repeat measurements averaged. Measurements of attitude commonly possessed an error of ± 5 degrees. A standard tape measure was used to record fracture openings (dilation), and when filled with magma or minerals; this is can be referred to as paleoaperture and measured as thickness. Observations of dykes and inclined sheets represent minimum values as strictly they are partly molten features that have cooled and contracted over time. This shrinkage is normally considered to represent approximately 10% of the total dyke thickness known from considerations of the density differences between magma and host rock (Gudmundsson, 2011b). Measurements of dyke thickness taken remotely, from distance have a larger uncertainty which was crudely estimated by taking repeat measurements. Where possible, photos taken in the field contain a scale, otherwise a scale-bar is drawn near the subject of interest.

Chapter 3

Nature Scientific Reports

Forecasting magma-chamber rupture at Santorini volcano, Greece

Browning, J, Drymoni, K., and Gudmundsson, A

Scientific reports, 2015, **5**, DOI 10.1038/srep15785

Statement of contribution:

All authors contributed to original idea

Analytical solutions were developed by JB from earlier work of AG. Specifically, novel modifications were made to allow the estimation of pressure increase and failure.

Fieldwork conducted by all authors

Data interpreted by JB

1st draft of all figures by JB, with later input from all authors

1st manuscript draft by JB

SCIENTIFIC REPORTS

OPEN

Forecasting magma-chamber rupture at Santorini volcano, Greece

Received: 18 June 2015
Accepted: 01 October 2015
Published: 28 October 2015

John Browning[1], Kyriaki Drymoni[1,2] & Agust Gudmundsson[1]

How much magma needs to be added to a shallow magma chamber to cause rupture, dyke injection, and a potential eruption? Models that yield reliable answers to this question are needed in order to facilitate eruption forecasting. Development of a long-lived shallow magma chamber requires periodic influx of magmas from a parental body at depth. This redistribution process does not necessarily cause an eruption but produces a net volume change that can be measured geodetically by inversion techniques. Using continuum-mechanics and fracture-mechanics principles, we calculate the amount of magma contained at shallow depth beneath Santorini volcano, Greece. We demonstrate through structural analysis of dykes exposed within the Santorini caldera, previously published data on the volume of recent eruptions, and geodetic measurements of the 2011–2012 unrest period, that the measured 0.02% increase in volume of Santorini's shallow magma chamber was associated with magmatic excess pressure increase of around 1.1 MPa. This excess pressure was high enough to bring the chamber roof close to rupture and dyke injection. For volcanoes with known typical extrusion and intrusion (dyke) volumes, the new methodology presented here makes it possible to forecast the conditions for magma-chamber failure and dyke injection at any geodetically well-monitored volcano.

Santorini is a volcanic island built predominantly by lava effusion and dome-forming eruptions[1], periodically interrupted by catastrophic ignimbrite-forming eruptions[2]. The most recent caldera-forming event occurred approximately 3650 years ago (at 3.6 ka) and is commonly referred to as the Minoan eruption. Since that eruption Santorini has experienced primarily effusive activity, located centrally in the caldera complex, which over time has formed the Kameni islands[1]. Nea Kameni (Fig. 1) produced at least three well documented eruptive episodes during the 20th century[1]. The volume of magma extruded during each individual event is estimated from the subaerial shapes and sizes of the lava flows and domes[1]. Volumes of older submarine eruptions have also be estimated using bathymetric data[1,3]. The Kameni islands lie along the Kameni line[4], a tectonic lineament which may influence magma emplacement and caldera faulting[5]. The average volume of magma issued during each individual effusive eruption is around 0.06 km^3. This is much smaller than the estimated volume of magma involved in Santorini's caldera forming events at 3.6 ka and ~26 ka with the dense-rock equivalent (DRE) volumes of 20–30 km^3 [2]. Whilst spectacular and impressive, the 20th century eruptions posed little risk to the majority of Santorini's inhabitants. However, the islands are now a major tourist destination with a summer population in excess of 50,000[6]. Even a small future eruptive event coupled with caldera-wall instabilities could therefore have negative consequences.

In January 2011 Santorini volcano entered a period of unrest, meaning that the ground surface began inflating[3,7–9] and the magnitude and frequency of earthquakes increased[3–5,7,8] . This period lasted until April 2012 when signs of unrest ceased. The unrest was triggered by magma being transported as a dyke

[1]Department of Earth Sciences, Royal Holloway University of London, Egham, TW20 0EX, United Kingdom. [2]Department of Mineralogy and Petrology, National and Kapodistrian University of Athens, Greece. Correspondence and requests for materials should be addressed to J.B. (email: john.browning.2012@live.rhul.ac.uk or A.G. (email: rock.fractures@googlemail.com)

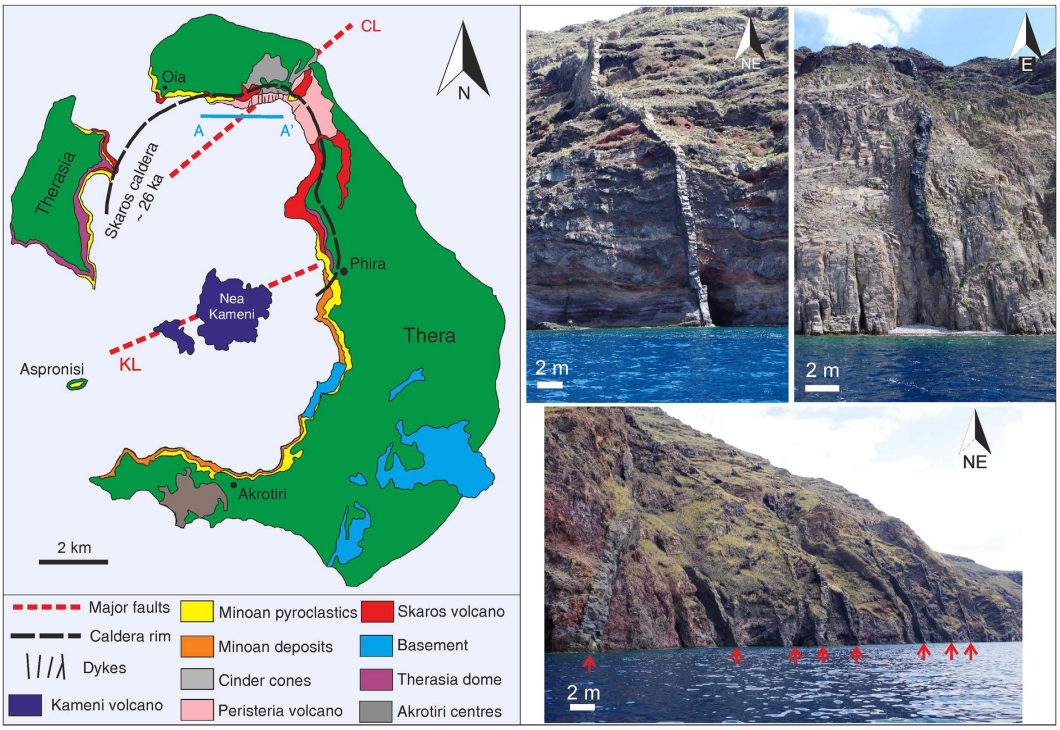

Figure 1. Simplified geological map of Santorini. Showing two main tectonic elements: the Kameni and Coloumbo lines, the inferred Skaros caldera rim, and the approximate location of dykes within the northern caldera wall. All the exposed dykes are located along the northernmost extent of the Skaros caldera wall and the island of Therasia; some are marked in the photographs with red arrows. Most dyke measurements were taken from a boat along the profile A–A′. The stratigraphy of the caldera is complex, being made up of many different types and ages of deposits. Many dykes within the wall are arrested, i.e. are non-feeders. Santorini geological map is modified from[29]. Photos: John Browning.

(a fluid-driven fracture) from great depths (>10 km) below the surface to a much shallower (~4 km deep) magma chamber[3,7–9]. Using geodetic techniques, it is estimated that a combined volume of approximately 0.021 km^3 (21 million cubic metres) of magma entered the shallow magma chamber, presumably in two main phases, in just over one year[3]. None of the geodetic or seismic signals indicate that magma rose from the shallow chamber as a dyke towards the surface, suggesting that increased pressure in the shallow chamber due to the volume of new magma was insufficient to rupture the chamber roof. But how close to rupture was the chamber? To answer that question for Santorini and other well-monitored volcanoes, we provide a model to calculate the excess pressure in the chamber following the receipt of new parental magma.

Results

In the simplest terms, a magma chamber roof will rupture when[10–12]

$$p_l + p_e = \sigma_3 + T_0 \quad (1)$$

where p_l is the lithostatic or overburden pressure (due to the weight of the overlying rocks), p_e is the magmatic excess pressure within the chamber, σ_3 is the local minimum compressive principal stress and T_0 is the local tensile strength of the host rock. Since σ_3 is the local stress, at the margin of the chamber, stress-concentration effects due to magma-chamber shape and loading are automatically taken into account in Eq. (1)[11,12]. Typical values of solid-rock tensile strengths range from 0.5 to 6 MPa, the most common values being 3–4 MPa[11,13]. It follows from Eq. (1) that for a part of the chamber to fail in tension the local value of p_e must during an unrest period reach T_o. At any other time the chamber is considered to be in lithostatic equilibrium with the surrounding host rock, in which case the excess pressure p_e is zero (this assumption is discussed in the section Methods). Evidence for the mechanism of chamber rupture comes from fracture mechanics principles and field observations of extinct and now fossil magma chambers, in Iceland and elsewhere, some of which have the well-exposed roofs dissected by dykes[12].

Common intrusive (dyke) volumes at Santorini volcano. Geological exposures at Santorini also offer insights into the dynamics of magma movement within the volcano over time. At least 63 dykes

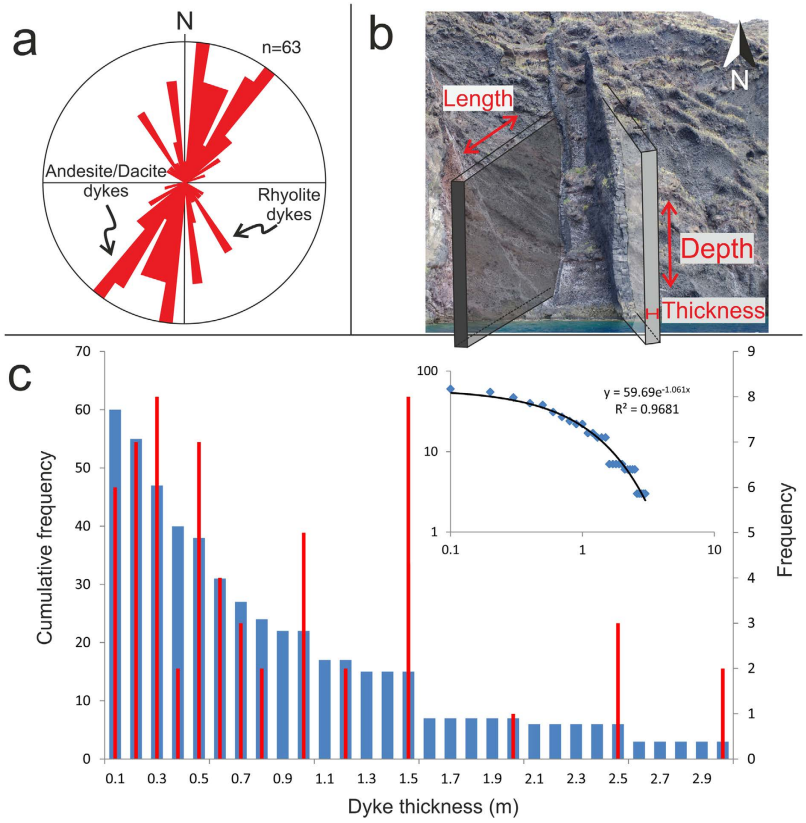

Figure 2. (**a**) Orientation and (**c**) thickness of 63 dykes in (**b**) the northern caldera wall of Santorini. Most dykes are less than 1.5 m thick and strike dominantly NE-SW; those dykes which strike NW-SE generally tend to be thicker and composed of felsic magmas. The average thickness of dykes measured is 1 m, the minimum being 0.1 m and the maximum 5 m. For visualisation purposes the thickest dyke shown is 3 m. (**c**) Dykes thicknesses plotted as cumulative frequency distributions follow an exponential trend (blue bars). Individual dyke measurements plotted as a histogram with bin size 0.1 m are shown as red bars[28]. Photo: John Browning.

(frozen or solidified magma-filled fractures) can be observed cutting the scalloped caldera wall in the northernmost part of the island of Thera (Fig. 1). The dykes range from andesite to trachydacite in composition[14] and are primarily exposed over a narrow section of the caldera wall at around 3.5 km east of the town of Oia and south of Finikia. The caldera wall is accessible by boat, and abseiling in some parts, making it possible to measure the thickness (roughly the palaeo-aperture or dyke-fracture opening) and the strike and dip (attitude) of the dykes. Dykes strike dominantly NE-SW (Fig. 2), matching the inferred strike of the Coloumbo line, a tectonic lineament which connects the Santorini volcanic complex to the nearby Coloumbo volcano[15,16]. Fifteen dykes strike NW-SE. These dykes tend to be thicker and lighter in colour, indicating a more evolved (felsic) composition. The thickest of the NE-striking dykes is 2 m, the average thickness being 0.7 m. By contrast, the thickest of the NW-striking dykes is about 5 m, the average thickness being 1.7 m. Dyke thicknesses fit an exponential scaling law when plotted as a cumulative frequency distribution (Fig. 2). Alternatively, the finding may reflect the relatively small dataset or indicate two power-law sets with different scaling exponents—larger data sets normally suggest dyke thicknesses following power-laws[11]. The dykes are predominantly sub-vertical, dipping on average around 80°. The dip of individual dykes, however, varies considerably, indicating local stress variations in the host rock[17].

In order to estimate the volume of magma contained within any one individual dyke generated from a shallow magma chamber at Santorini caldera we assume a dyke-length (along strike or strike dimension) to thickness ratio of 1500[10,11]. This ratio, a common value based on measurements of dykes worldwide, is used because it is not possible to measure the lateral extent of any dykes within the caldera at Santorini. The assumed ratio also takes into account that dykes tend to become longer at greater depths because of general increase in Young's modulus (E) with crustal depth[11]. Many dyke tips are seen, suggesting that most of the dykes within the caldera wall are non-feeders, i.e. did not supply magma to an eruption but rather became arrested at contacts between dissimilar layers within the volcano. Arrested dykes, non-feeders, are commonly observed in well-exposed outcrops such as caldera walls and cliffs[18,19], as in Santorini, indicating that magma-chamber rupture and dyke injection is no guarantee for an eruption.

In particular, Santorini has a complex geologic stratigraphy made up of many rock units and layers with contrasting mechanical properties[1,17] (Fig. 1) whose contacts tend to arrest dykes[11,17].

There is little difference between the thicknesses of the feeder-dykes and non-feeders (arrested dykes)[18]. Since dyke thickness is linearly related to the dyke strike and dip dimensions[11], we use an average dyke dimension when calculating the volume of magma transported out of the chamber during common eruptions. Using an average dyke thickness of 1 m, then, based on the length/thickness ratio above, the average length or strike-dimension is 1500 m. Similarly, based on the geodetically determined depth to the present magma chamber (about 4000 m), the average dyke depth or dip-dimension is 4000 m. Using these dimensions and a thickness of 1 m, the average dyke volume is 0.006 km^3. This average dyke volume can then be combined with the known average volume of material erupted during the Santorini's 20th century eruptions to estimate the volume of the shallow source chamber and the necessary added volume needed to rupture the chamber and inject a new dyke.

Estimating the volume of Santorini's magma chamber. The total volume V_m of a shallow chamber located within host rock of average compressibility β_r and tensile strength T_0 is related to the total volume V_e of magma leaving (being squeezed out of) the chamber to produce the eruptive materials and/or the injected dyke through the equation[10,12,20]

$$V_m = \frac{V_e}{T_0(\beta_m + \beta_r)} \tag{2}$$

where β_m is the magma compressibility. Using a typical shallow-crustal compressibility of 3×10^{-11} Pa^{-1} [12], an average *in-situ* tensile strength of 3.5 MPa[6], and magma compressibility of 1.25×10^{-10} Pa^{-1} [10], then Eq. (2) reduces to

$$V_m = 1850\, V_e \tag{3}$$

Here we use an average value taken from experimentally derived ranges for compressibility of various magmas and compressibility and tensile strength of host rocks[6,10,12], assuming a totally molten magma chamber. Many magma chambers may be partly compartmentalised with zones of differential volatile concentrations and crystal mushes, in which case they should be modelled as poro-elastic. These and related topics are discussed further in the section Methods.

Using the estimated average volume of a typical individual dyke within the Santorini caldera, 0.006 km^3, and the average measured volume of magma erupted for a typical individual eruptive phase on the Kameni islands, 0.06 km^3, then V_e in Eq. (3) becomes 0.066 km^3. It follows then from Eq. (3) that the total volume V_m of the shallow chamber active during these eruptions is about 122 km^3. For a penny-shaped or sill-like chamber, as are common[12], and based on the dimensions of the three caldera structures which make up Santorini, the chamber radius would be about 4 km and the thickness about 2 km. The geometry may, of course, be different. We do not aim to constrain the precise chamber geometry, since it is not needed for the present purpose. The main points are to assess the trade of between radius and thickness and to show that, for the estimated volume, the chamber must be so large as to encompass a significant area of the present-day caldera.

Magma-chamber rupture during recharge. Since the excess pressure at the time of magma-chamber rupture is normally equal to the local tensile strength at the rupture site (Eq. 1), we can substitute p_e for T_0 in Eq. (2). Also, assuming that the volume added to the chamber before rupture ΔV_m is roughly equal to the magma volume leaving the chamber following the rupture V_e, we can rewrite Eq. (2) as

$$p_e = \frac{\Delta V_m}{V_m(\beta_m + \beta_r)} \tag{4}$$

Here it is assumed that before the new magma of volume ΔV_m entered the chamber (from a deeper source or reservoir), the chamber was in lithostatic equilibrium with the host rock and its excess pressure p_e thus zero. This is a normal assumption for periods of quiescence and follows partly because unrest (e.g., inflation and earthquakes) would be expected in case of rising p_e ($p_e > 0$) whereas quiescence periods are characterised by the absence of unrest signals[10,12].

During the 2011–12 unrest period in Santorini, the volume of new magma that entered the shallow chamber ΔV_m is estimated at around 0.021 km^3 [Ref. 7]. Substituting this in Eq. (4) and using the above values for the size of the chamber and the compressibilities, the corresponding excess pressure p_e in the chamber increased from zero to 1.1 MPa during the unrest period. Our results indicate that whilst the total amount of new magma which entered the shallow chamber during the 2011–2012 unrest period at Santorini represents a very small fraction (~0.02%) of the estimated total magma stored, the excess pressure increase within that shallow chamber came close to the surrounding host rock's tensile strength[10], and therefore close to rupturing the chamber boundary and injecting a dyke (Fig. 3). For completeness we also consider the slow inflation episode of 1994–1999 where the volume of new magma that entered a chamber to the north of the caldera was estimated at around 0.78×10^{-5} km^3 [Ref. 21]. For the five

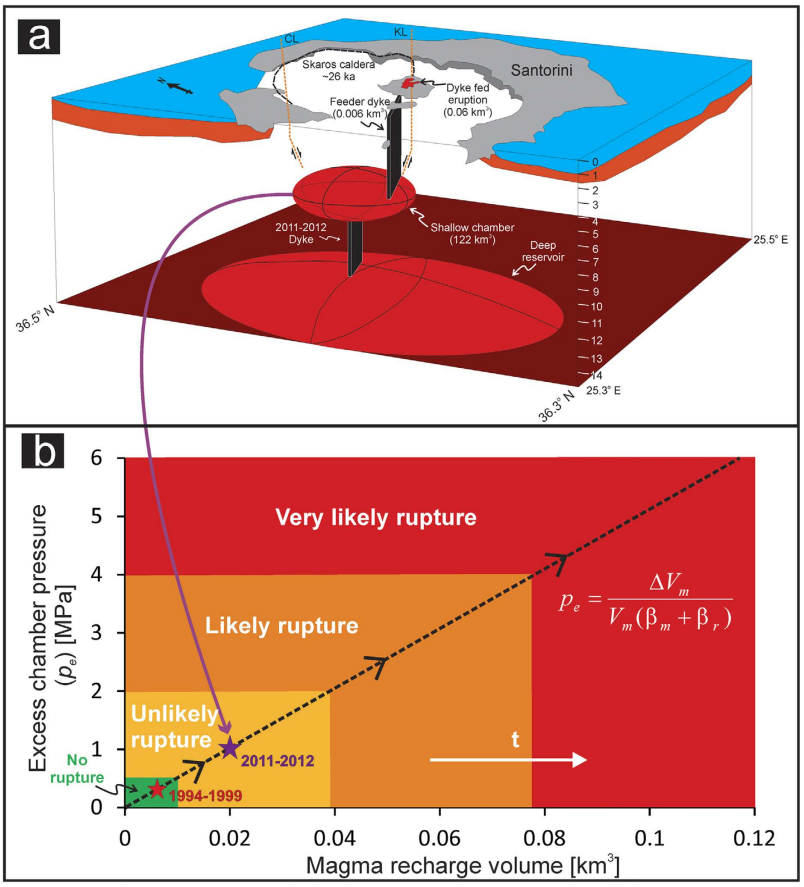

Figure 3. (**a**) Simplified 3D model of Santorini volcanic system based on geodetic[3,4,7–9] and geological data. A deep reservoir feeds magma into a shallow system at around 4 km depth; this shallow chamber has a current total volume of approximately 122 km^3. The volume is estimated using the average volume of dykes (0.006 km^3) and the average volume of 20th century eruptions (0.06 km^3) together with fracture-mechanics and continuum-mechanics principles. The exact nature of the Kameni and Colombo tectonic lineaments is unclear, but here both are drawn as normal faults. The box is drawn between 25.3–25.5° E and 36.3–36.5° N to a depth of 15 km below the surface. (**b**) Excess pressure (p_e) within the shallow magma chamber at Santorini as a function of the volume of new magma (ΔV_m) entering the chamber from a deeper source over time. Here the results are applied to the shallow chamber of Santorini based on the estimated size of the chamber. The method, however, can be applied to any active central volcano for which (1) there exist extrusion (lava and pyroclastic flows) and intrusion (primarily dyke) volume estimates and (2) geodetic data as to inflation volumes. Rupture probability statements based on increasing excess pressure within the shallow chamber allow forecasts of dyke formation to be made in real time during magma recharge events. The model has been applied to the inflation episodes of 1994–1999 (red star) and 2011–2012 (purple star).

year period we estimate the excess pressure increase within the shallow chamber as about 0.3 MPa. In all the unrest episodes, even if the chamber boundary ruptures and injects a dyke, the local stresses within the edifice ultimately govern whether the dyke becomes arrested or, alternatively, reaches the surface to supply magma to an eruption[17] at Nea Kameni or elsewhere in Santorini.

Most models used to explain periods of unrest at Santorini simulate one shallow magma chamber pressure centre north of the Kameni islands[3,7–9]. Other models, however, relate the unrest to two shallow magma sources[4,21,22], some citing the anomalous distribution of seismicity along the Kameni line and a separate pressure source at a depth of 1 km, or possibly 5.5 km further north in association with the 1994–1999 inflation. Our calculated volume constraints easily incorporate the area of the proposed two magma sources[4,21]. Two chambers are thus not needed in our model—a single, moderately large and partly compartmentalised[12] chamber is sufficient—but our results certainly do not rule out that possibility. Focussed seismicity on the Kameni line during periods of unrest may be related to its mechanical properties being different from those of the surrounding crust, resulting in stress concentration along the line, or deep-seated reservoirs. Further considerations of that topic, however, are outside the scope of the present paper.

Eruptions at Santorini volcano are mostly with volumes $\ll 0.1\,km^3$. However, much larger eruptions, with volumes $>30\,km^3$, occur occasionally and presumably from the same magma chamber. For a chamber with a volume of some $122\,km^3$, a large fraction (about one-fourth) of its magma must be squeezed out to generate such a large eruption. Ordinary elastic and poro-elastic models of the type described here cannot explain such large magma removal from the chamber. The forced chamber volume reduction during piston-like caldera collapse, however, is apparently able to squeeze out a high proportion of the magma in the chamber, thereby explaining occasional large eruptions from moderately sized chambers. Then the large-volume eruptions are not the cause but rather the consequence of the caldera collapse[23]. Combining the ordinary poro-elastic mechanism with the collapse-driven mechanism, the estimated moderately large shallow chamber at Santorini volcano can supply magma to both small and large eruptions.

Conclusion

The methodology presented here and applied to Santorini volcano can be used alongside real-time geodetic observations to help forecast magma chamber rupture at any geodetically well-monitored volcano. This new method, therefore, represents a valuable first-order tool for volcano observatories during periods of volcanic unrest. Further steps must be taken in order to better constrain the local stresses within the shallow parts of volcanic edifices, as these provide primary control on dyke propagation paths. As yet no comprehensive model exists to ascertain whether a dyke injected from a ruptured magma chamber will reach the surface and supply magma to an eruption. Even so, estimating the volume of magma stored at shallow depths and the conditions required to mobilise that magma are important steps in the development of reliable volcano-tectonic models for forecasting volcanic eruptions.

Methods

Dyke measurements at Santorini were conducted during a five day field campaign in April 2014. Dykes dissecting the northern caldera wall were measured directly on land as well as from a boat. Outcrops of dykes are mostly limited to the northern caldera wall and parts of Therasia. Dyke attitudes (strike and dip) were measured using a compass clinometer and thicknesses and morphological data of some dykes were measured directly in the field, but mostly spotted from the boat at a distance of around 10–15 m.

Lava flow volumes are taken directly from previous studies[1,7]. Here we average all of the known lava flow volumes to obtain the individual eruption average of $0.06\,km^3$. Maximum and minimum lava volumes are given in the Supplementary Data.

Excess pressure (p_e) is derived from the difference between total fluid pressure (p_t) within the chamber and the lithostatic stress (p_l) where

$$p_e = p_t - p_l \tag{5}$$

For lithostatic equilibrium, an assumed condition when the chamber is not undergoing unrest, all the principal stresses at the chamber boundary are equal ($\sigma_1 = \sigma_2 = \sigma_3$) and equal to the lithostatic stress (p_l). It then follows from Eq. (1) that $p_e = T_0$, which is used to derive Eq. (4). The assumption of lithostatic equilibrium is valid because any pressure deviation from lithostatic results in stress concentration in the host rock of the chamber, and thus in volcanic unrest as would be reflected in e.g., geodetic changes and seismicity. Even relatively small-scale unrests are detected on well-monitored volcanoes, such as the creep-like inflation during 1994–1999 at Santorini[22]. When the chamber ruptures and injects a dyke the overpressure or driving pressure p_o in that dyke is given by[11]

$$p_o = p_e + (\rho_r - \rho_m)gh + \sigma_d \tag{6}$$

where p_e is the excess magma pressure in the magma chamber, ρ_r is the average host rock density, ρ_m is the average dyke-magma density, g is acceleration due to gravity ($9.81\,ms^{-2}$), h is the height of the dyke above its contact with the chamber (or the dip dimension of the dyke), and σ_d is differential stress, i.e. the difference between vertical stress and the minimum principal horizontal stress in the rock layer where the dyke overpressure is calculated. Note that this formulation includes the effects of gravity. The opening displacement of dykes and the depth to magma chamber intersection can also be calculated analytically[24] but is not within the scope of the current work.

To calculate the ratio of erupted material to volume of the shallow magma chamber we assumed the chamber to be totally molten. This is the standard assumption used in the inversion of geodetic data to infer the depths to magma chambers associated with inflation and deflation (unrest) periods[25]. However, many chambers contain volatiles and crystals and therefore may be closer to a poro-elastic material, in which case Eq. (4) becomes modified to[10,12,26]

$$p_e = \frac{\Delta V_m}{V_m\left(\beta_m + \beta_p\right)} \tag{7}$$

where β_p is the pore compressibility of the chamber, i.e. the fractional change in pore volume (magma fraction) of the chamber for unit change in the excess pressure. In this case, when new magma is received

by the chamber (from the deeper source), the new magma is partly accommodated through compression of the old magma and partly by expanding chamber pore space. Compression of old magma leads to an increase in magmatic pressure ($+p_e$), whereas pore expansion leads to a decrease in magmatic pressure ($-p_e$). The excess pressure increase as new magma is added to the chamber then depends on the values of the pore and magma compressibilities. The magma compressibility, however, is generally much higher than either the host-rock compressibility (Eq. 4) or the pore compressibility (Eq. 7). It follows that the calculated excess pressure for a given addition of new magma to the chamber depends primarily on the magma compressibility, and the results are similar when using Eqs (7 and 4) for shallow magma chambers. Our model assumes that magma compressibility remains constant throughout an unrest period and is homogeneously distributed. More data is needed on magma compressibilities and their variations, and until such data become available the present assumption has to be made, as is the case in most deformation studies[3,7]. Also, we focus on the magma chamber compressibility as a whole. Therefore, whilst variations in compressibility almost certainly exist in compartmentalised chambers[12], and will influence aspects of associated localised volume changes, when the chamber is treated as a single homogeneous system our assumptions are justified.

More specifically, there are no doubt significant uncertainties or errors in the estimated compressibilities of the rocks and the magmas used in eqs (2–4 and 7). The calculated compressibilities are based on earlier data provided by Murase and McBirney[20]. However, no uncertainties are provided for these original data, so that the standard propagation of uncertainties or errors estimates, whereby the uncertainties or errors add in quadrature[27], cannot be made. In contrast to the compressibilites, which may vary considerably, the *in-situ* tensile strengths may be regarded as close to constant. The most common values are 3–4 MPa[11], so that the average value of 3.5 MPa, used here, has an uncertainty or error of about 0.5 MPa, or less than 15%. A rough estimate of the total error in the excess pressure estimates, based on the assumptions used, would suggest an uncertainty of perhaps 50%.

Dyke thicknesses are plotted on a histogram (Fig. 2) with bin widths of 0.1 m together with cumulative frequency distributions where the probability $P(x)$ that x has a value greater than or equal to x, is given by[28],

$$P(x) = \int_x^\infty p(x')\,dx' \tag{8}$$

References

1. Nomikou, P. *et al.* The emergence and growth of a submarine volcano: The Kameni islands, Santorini (Greece). *GeoResJ* **1–2,** 8–18 (2014).
2. Druitt, T. H. & Francaviglia, V. Caldera formation on Santorini and the physiography of the islands in the late Bronze Age. *Bull. Volcanol.* **54,** 484–493 (1992).
3. Parks, M. M. *et al.* From quiescence to unrest: 20 years of satellite geodetic measurements at Santorini volcano, Greece. *J. Geophys. Res.* **120,** 1309–1328 (2014).
4. Saltogianni, V., Stiros, S. C., Newman, A. V., Flanagan, K. & Moschas, F. Time-space modeling of the dynamics of Santorini volcano (Greece) during the 2011–2012 unrest. *J. Geophys. Res.* **119,** 8517–8537 (2014).
5. Konstantinou, K. I., Evangelidis, C. P., Liang, W. T., Melis, N. S. & Kalogeras, I. Seismicity, Vp/Vs and shear wave anisotropy variations during the 2011 unrest at Santorini caldera, southern Aegean. *J. Volcanol. Geotherm. Res.* **267,** 57–67 (2013).
6. Dominey-Howes, D. & Minos-Minopoulos, D. Perceptions of hazard and risk on Santorini. *J. Volcanol. Geotherm. Res.* **137,** 285–310 (2004).
7. Parks, M. M. *et al.* Evolution of Santorini Volcano dominated by episodic and rapid fluxes of melt from depth. *Nat. Geosci.* **5,** 749–754 (2012).
8. Newman, A. V. *et al.* Recent geodetic unrest at Santorini Caldera, Greece. *Geophys. Res. Lett.* **39,** 1–5 (2012).
9. Papoutsis, I. *et al.* Mapping inflation at Santorini volcano, Greece, using GPS and InSAR. *Geophys. Res. Lett.* **40,** 267–272 (2013).
10. Gudmundsson, A. Formation and mechanics of magma reservoirs in Iceland. *Geophys. J. R. Astr. Soc.* **91,** 27–41 (1987).
11. Gudmundsson, A. *Rock fractures in geological processes.* (Cambridge University Press, Cambridge, 2011).
12. Gudmundsson, A. Magma chambers: Formation, local stresses, excess pressures, and compartments. *J. Volcanol. Geotherm. Res.* **237–238,** 19–41 (2012).
13. Amadei, B. & Stephansson, O. *Rock stress and its measurement.* (Chapman Hall, New York, 1997).
14. Puchelt, H., Hubberton, H. W., Stellrecht, R. The geochemistry of the radial dykes of the Santorini Caldera and its implications, Thera and the Aegean World III *Pro. 3rd Int. Cong., Santorini, Greece, 1989* (D. A. Hardy *et al.*, eds) 229–236 (Thera Found, London 1990).
15. Nomikou, P. *et al.* Submarine volcanoes of the Kolumbo volcanic zone NE of Santorini Caldera, Greece. *Glob. Planet. Change* **90–91,** 135–151 (2012).
16. Konstantinou, K. I. & Yeh, T. Y. Stress field around the Coloumbo magma chamber, southern Aegean: Its significance for assessing volcanic and seismic hazard in Santorini. *J. Geodyn.* **54,** 13–20 (2012).
17. Gudmundsson, A. & Philipp, S. L. How local stress fields prevent volcanic eruptions. *J. Volcanol. Geotherm. Res.* **158,** 257–268 (2006).
18. Geshi, N., Kusumoto, S., Gudmundsson, A. Effects of mechanical layering of host rocks on dyke growth and arrest. *J. Volcanol. Geotherm. Res.* **223–224,** 74–82 (2012).
19. Geshi, N., Kusumoto, S., Gudmundsson, A. The geometric difference between non-feeders and feeder dykes. *Geology* **38,** 195–198 (2010).
20. Murase, T. & McBirney, A. R., Properties of some common igneous rocks and their melts at high temperatures. *Geol. Soc. Am. Bull.* **84,** 3563–3592 (1973).
21. Saltogianni, V. & Stiros, S. C. Modeling the Mogi magma source centre of the Santorini (Thera) volcano, Aegean Sea, Greece, 1994-1999, based on a numerical-topological approach. *Stud. Geophys. Geod.* **56,** 1037–1062 (2012).
22. Stiros, S. C., Psimoulis, P., Vougioukalakis, G. & Fyticas, M. Geodetic evidence and modeling of a slow, small-scale inflation episode in the Thera (Santorini) volcano caldera, Aegean Sea. *Tectonophysics* **494,** 180–190 (2010).

23. Gudmundsson, A. Collapse-driven large eruptions. *J. Volcanol. Geotherm. Res.* **304,** 1–26 (2015).
24. Becerril, L., Galindo, I., Gudmundsson, A. & Morales, J. M. Depth of origin of magma in eruptions. *Sci. Rep.* **3,** 6 (2013).
25. Dzurisin, D., *Volcano `deformation: new geodetic monitoring techniques.* (Springer, 2007).
26. Bear, J. *Dynamics of fluids in porous media*. (Elsevier, New York, 1972).
27. Taylor, J. R. *An introduction to error analysis*. (University Science Books, 1997).
28. Mohajeri, N. & Gudmundsson, A. The evolution and complexity of urban street networks. *Geogr. Anal.* **46,** 345–367 (2014).
29. Druitt, T. H., Edwards, L. & Mellors, R. Santorini volcano. *Geol. Soc. Lond. Mem.* **19,** pp. 1–165. (1999).

Acknowledgements

J.B. is grateful for a Kirsty Brown memorial fund grant which enabled fieldwork. We thank Valerio Acocella and two anonymous reviewers for comments that improved the manuscript. Thanks also to Nathaniel Forbes-Inskip for discussions throughout.

Author Contributions

J.B., A.G. and K.D. contributed equally to the development of ideas and collection of data. Analytical calculations were completed by J.B. and A.G. and the manuscript was compiled and written by J.B. with input from A.G.

Additional Information

Supplementary information accompanies this paper at http://www.nature.com/srep

Competing financial interests: The authors declare no competing financial interests.

How to cite this article: Browning, J. *et al.* Forecasting magma-chamber rupture at Santorini volcano, Greece. *Sci. Rep.* **5**, 15785; doi: 10.1038/srep15785 (2015).

Chapter 4

Bulletin of Volcanology

Caldera faults capture and deflect inclined sheets: an alternative mechanism of ring dike formation

Browning, J and Gudmundsson, A

Bulletin of Volcanology 2015,77, **4**. DOI 10.1007/s00445-014-0889-4

Statement of contribution

Collection of primary field data by JB with support from co-author and field assistants

All field photographs by JB

JB Conceived and built all numerical models and resulting figures

Complete 1st draft of manuscript and figures by JB

Revisions and subsequent drafts made with co-author input

Interpretation of field and numerical data along with final model conducted by JB with support from co-author

Bull Volcanol (2015) 77:4
DOI 10.1007/s00445-014-0889-4

RESEARCH ARTICLE

Caldera faults capture and deflect inclined sheets: an alternative mechanism of ring dike formation

John Browning · Agust Gudmundsson

Received: 27 July 2014 / Accepted: 3 December 2014

Abstract The subsurface structures of caldera ring faults are often inferred from numerical and analog models as well as from geophysical studies. All of these inferred structures need to be compared with actual ring faults so as to test the model implications. Here, we present field evidence of magma channeling into a caldera ring fault as exhibited at Hafnarfjall, a deeply eroded and well-exposed 5-Ma extinct volcano in western Iceland. At the time of collapse caldera formation, over 200 m of vertical displacement was accommodated along a ring fault, which is exceptionally well exposed at a depth of approximately 1.2 km below the original surface of the volcano. There are abrupt changes in the ring fault attitude with depth, but its overall dip is steeply inward. Several inclined sheets within the caldera became arrested at the ring fault; other sheets became deflected up along the fault to form a multiple ring dike. We present numerical models showing stress fields that encourage sheet deflection into the subvertical ring fault. Our findings provide an alternative mechanical explanation for magma channeling along caldera ring faults, which is a process likely to be fundamental in controlling the location of post-caldera volcanism.

Keywords Calderas · Inclined sheets · Numerical modeling · Ring-dikes · Ring-faults

Editorial responsibility: G. Giordano

Electronic supplementary material The online version of this article (doi:10.1007/s00445-014-0889-4) contains supplementary material, which is available to authorized users.

J. Browning (✉) · A. Gudmundsson
Department of Earth Sciences, Royal Holloway, University of London, Egham TW20 0EX, UK
e-mail: john.browning.2012@live.rhul.ac.uk

Published online: 22 January 2015

Introduction

Many ring faults around the world are intruded by dikes (e.g., Smith and Bailey, 1968; Johnson et al., 2002). These dikes are believed to have been emplaced either during the injection of magma during collapse caldera formation (Anderson, 1936; Sparks, 1988; Walter, 2008) or incrementally through many injections along the ring fault (Saunders, 2001). The common assumption, based on Anderson's (1936) model, is that ring dikes are injected directly into the ring fault at its contact with the magma chamber.

Dikes and sheets commonly intrude pre-existing weaknesses such as joints (Delaney et al., 1986) and faults (Gudmundsson, 2011; Magee et al., 2013; Bedard et al., 2012). While there are numerous examples of well-studied ring faults, for example Glencoe caldera (Clough et al., 1909; Kokelaar, 2007) and Hannegan caldera (Tucker et al., 2007) as well as many others (see Lipman 1984), observations of well-exposed ring faults and ring dikes in the same vertical cross section at depth are extremely rare. As such, the mechanics of magmatic interaction with caldera faults is still poorly understood.

Many calderas experience post-collapse resurgence which may culminate in eruptive activity. Commonly, post-caldera volcanism concentrates spatially above the vertical extent of a caldera ring fault (Geyer and Martí 2008; Saunders, 2004). Therefore, understanding the subsurface structure of caldera ring faults is important for identifying the location and timing of renewed volcanic activity within active calderas. Caldera ring faults have traditionally been studied using analog (e.g., Acocella et al., 2000; Acocella, 2007; Geyer et al., 2006; Holohan et al., 2005; Kennedy et al., 2004), numerical (e.g., Gudmundsson, 1998; Hardy, 2008), and analytical methods (e.g., Gudmundsson, 1998), with the subsurface structure often inferred from such models, as well as from seismicity (e.g., Ekstrom, 1994), geodetic studies (e.g., Jonsson, 2009),

and near-surface observations (e.g., Geshi et al., 2002; Troll et al. 2002). Caldera ring faults are primarily subvertical dip-slip shear fractures, although in some cases, the faults accommodate an oblique slip (Holohan et al., 2013). Whether a caldera ring fault dips inward or outward from the center of subsidence is a long-debated and contentious issue (Gudmundsson and Nilsen, 2006; Burchardt and Walter, 2010; Geyer and Marti, 2014). For example, Branney (1995) suggests that most ring faults dip outward, whereas observations from the collapse of Miyakejima, Japan, in 2000 (Geshi et al., 2002; Burchardt and Walter, 2010) and Piton de la Fournaise, La Reunion, in 2007 (Michon et al., 2009) indicate both inward- and outward-dipping ring faults. The use of near-surface observations of ring faults (e.g., Michon et al., 2009) may be misleading as caldera walls are subject to mass wasting and erosion (Lipman, 1997). Furthermore, it may be difficult to infer correctly the subsurface structure from surface observations because the fault-generating local stresses are likely to vary with depth in the volcanic edifice, thereby affecting the overall geometry of the fault structure (Gudmundsson, 2011).

Here, we present field data and numerical models which show that dikes and sheets can become deflected at and along a ring fault, the deflection being primarily due to the difference in material properties between (and within) the fault zone and the host rock. These observations and associated modeling provide an alternative mechanism for the formation of ring dikes.

A well-exposed caldera ring fault in western Iceland

Hafnarfjall is an inactive and deeply eroded 5-Ma-old central volcano (stratovolcano with a caldera) in western Iceland. The volcano is composed of a predominantly basaltic lava pile overlain by brecciated andesite and andesitic lava, as described in detail by Franzson (1978) (Fig. 1). The volcano originally formed in the southwest volcanic zone of Iceland but subsequently drifted, through crustal spreading, 40–50 km (Gautneb et al., 1989) to the west-northwest of the rift zone. Hafnarfjall therefore offers the opportunity to study a caldera formed in a divergent plate boundary setting. We estimate that glacial erosion has removed the uppermost parts of the volcano based on the assumptions of Walker (1960) and Johannesson (1975) who used zonation of amygdale minerals to estimate the level of erosion in a nearby area. Hafnarfjall volcano contains numerous inclined sheets, predominantly basaltic, which dip on average at around 65°, trend NE, and have thicknesses that are commonly about 1 m or less (Gautneb et al., 1989). The thickest sheets, however, reach about 10 m and tend to be composed of rhyolite. Many of these intrusions in Hafnarfjall are highly altered, and it is often difficult to discern characteristic intrusive features such as chilled selvages and cooling jointing. In Fig. 2, we show several dikes and inclined sheets ranging in thickness from

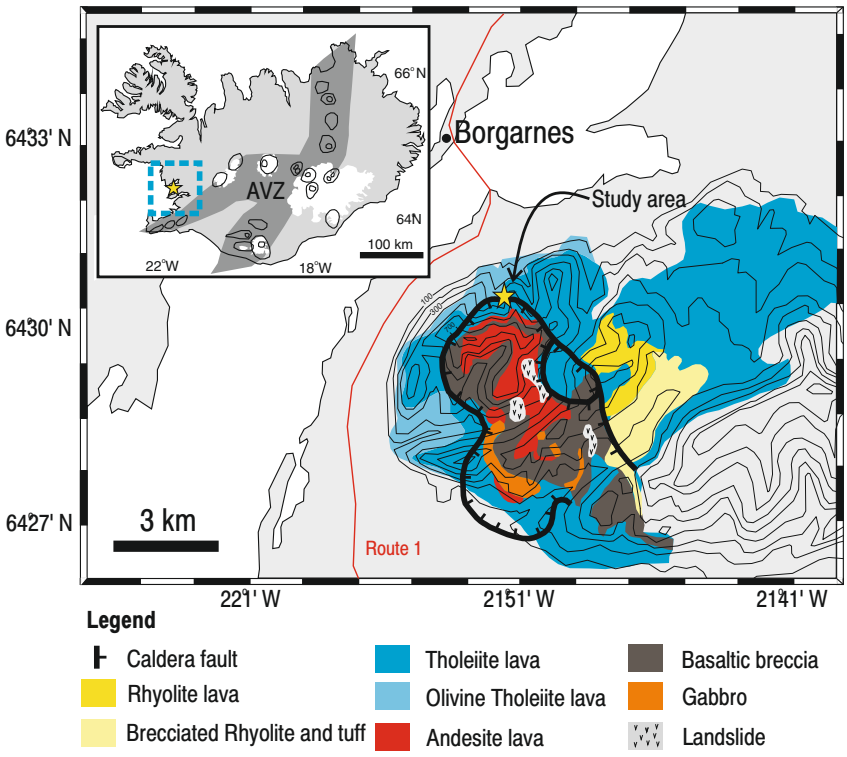

Fig. 1 Geological map of Hafnarfjall central volcano, located in western Iceland, approximately 50 km northwest of the active volcanic zone (*AVZ*). The ring fault of the 7.5×5-km NW-SE elongated caldera is shown. Study area is marked with a *yellow star*. Modified after Franzson (1978)

2.5 m (Fig. 2a) to 3 cm (Fig. 2c). They are all clearly intrusions which are discordant to bedding; however, very few display characteristic chilled selvages or discernible horizontal fracture patterns.

At around 4.6 Ma, Hafnarfjall experienced a major collapse event, forming part of a NW-SE elongated caldera approximately 7.5×5 km in diameter (Franzson, 1978). The most striking evidence of this collapse is the exposed ring fault in a gulley, oriented roughly NW-SE, at the northernmost margin of the caldera, as shown in Fig. 3. At this locality, an E-W trending segment of the ring fault can be observed in a vertical cross section for 200 m along dip and around 700 m along strike (Fig. 3a). Here, the ring fault cuts a 300-m-thick lava pile composed of 2–5-m-thick flows of basaltic tholeiite. Around the outer caldera margin, lavas dip 15° S, whereas the dip of lavas which constitute the caldera block increases to ~35° S. This implies that the caldera block has tilted during faulting. Dips of intra-caldera lavas also increase with depth toward the center of the caldera, i.e., individual lava layers at the outcrop base exhibit a steeper dip than those near the present-day surface. The caldera fault can be traced in several localities as mapped by Franzson (1978) and shown in Fig. 1 as a single fault plane with displacement in excess of 100 m. The exposure described in detail here indicates a throw in excess of 200 m, although the normal fault offset is considered a minimum and is based on the inability to trace individual lava flow layers horizontally, across the entire vertical section. As mentioned, the vertical section is 300 m, although individual lava layers can only be obviously discerned for approximately 200 m of this section.

The studied vertical section of the ring fault does not display a constant attitude. This finding is in contrast to those of many models on ring fault formation that often predict a simple inward- or outward-dipping trend (Acocella, 2007). Instead, the fault alternates in dip between 85 N–90° and 85 S–90°, suggesting that a number of stress perturbations occurred during fracture propagation. Such subtle changes in fault attitude are unlikely to be detected in models unless a heterogeneous, in particular, a layered, edifice is considered. On average, the fault has a normal trend and dips steeply inward, at ~85° S.

Steep-sided slopes surrounding the fault exposure limit observations to the base of two gullies and, from a distance, to a parallel topographic high (Fig. 3a, b). At the base of the caldera fault (Fig. 4) are five thin (<0.7 m) basaltic, but highly altered, dikes. Thin (0.5–1 cm) mineral veins separate some of the individual intrusions, as shown in Fig. 4c. Surprisingly, no breccia or fault gouge is found along the main fault plane. We interpret the dikes within the fault plane as ring dikes and now refer to them as such throughout. In Fig. 4b, two ring dikes can be clearly observed within the fault plane; the northernmost dike strikes N086° E, and it becomes offset around 25 m vertically in the pile. The strike of the second dike is variable between approximately 095 and 115 and appears to follow the fault plane. In the intra-caldera lava pile, thin (<1 m) inclined sheets dip between 45 and 75° S, and upon contact with the fault, the sheets either become arrested or change attitude and deflect vertically into the fault. No sheets can be traced from inside of the caldera margin, across the fault, and to the outside of the caldera.

On the intra-caldera margin, synclinal drag folding indicates a normal sense of dip-slip shear and displacement (see Fig. 3a). The zone of folding extends for approximately 10–15 m horizontally toward the caldera center. In this region, it is difficult to distinguish between individual lava flows, as their

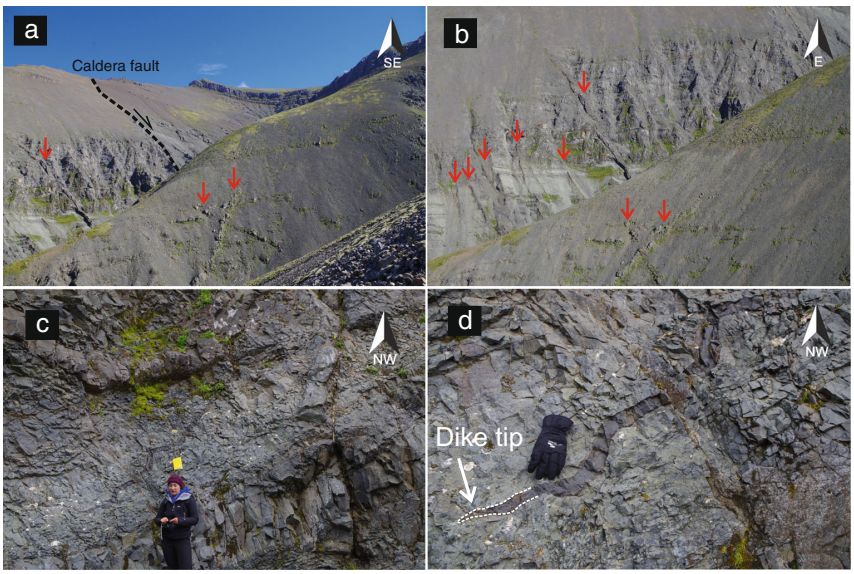

Fig. 2 Examples of sheets and dikes found in the Hafnarfjall lava pile. **a** View southeast toward the caldera ring fault, indicated as a *dashed line*. **b** Dikes and sheets are discernible as discordant linear features within the lava pile, in this example a pair of cross-cutting dikes, the largest and youngest of which is approximately 2.5 m in thickness and dips 65–75° S. Other dikes and sheets are indicated by *red arrows*. **c**, **d** A 3-cm-thick arrested dike exhibiting a narrow and pointed dike tip. Due to weathering and alteration, it is difficult to observe any chilled selvage or horizontal fracture pattern within the dike; this is common in many of the intrusions in Hafnarfjall

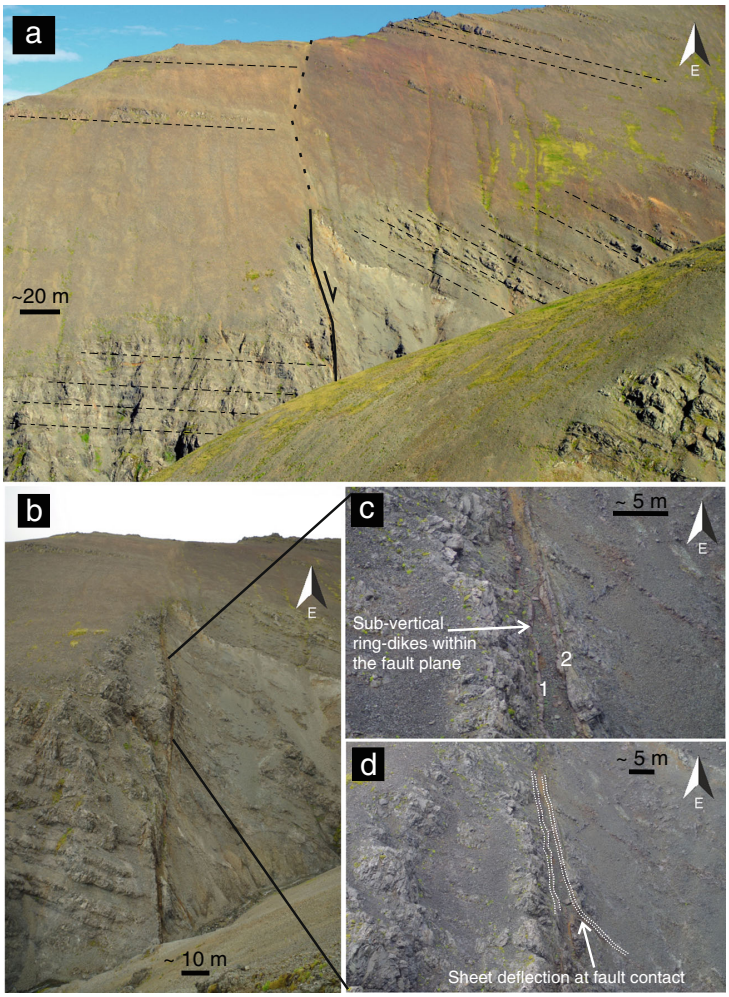

Fig. 3 **a** Caldera ring fault exhibits a general inward-dipping normal trend, although subtle variations in attitude occur throughout. The height from the base to the top of the fault is ~300 m. Lavas on the inner caldera margin dip more steeply than those outside, and generally dip increases with depth. Several markers are used to infer synclinal drag folding, perhaps the most prominent is a light white tuff which clearly bends into the fault. Displacement is greater than the vertical section, so no horizontal markers can be traced across the fault plane. **b** Many individual lava layers with thicknesses between 1 and 2 m can be traced to the fault contact on the outer margin; however, most lavas on the inner margin are sufficiently deformed and not discernible. **c**, **d** Section of the upper observable part of the fault. Individual dikes shown and numbered are around 1 m thick. (Location 64° 30′ 01″ N 21° 52′ 39″ W)

characteristic scoria margins have been sufficiently deformed. There is no indication of reverse-sense displacement or motion on the fault, which is a commonly interpreted mechanism during caldera unrest due to magma intrusion (Acocella et al., 2000; Walter and Troll 2011; Jonsson, 2009). This is important to note, as our later numerical models simulate an overpressured condition, which is of course a requirement for propagating the original sheets described throughout.

Factors influencing the propagation of dikes and sheets

Stress barriers

In order for a sheet to successfully propagate, tensile stress magnitudes should exceed the in situ host rock tensile strength, which is generally between 0.5 and 6 MPa (Amadei and Stephansson, 1997; Gudmundsson, 2011). The direction of propagation is based on Anderson's (1936) theory of sheet and ring dike propagation and on numerous field observations of dikes and sheets which suggest that magmatic fractures will propagate in a direction parallel to the trajectories σ_1 and perpendicular (or normal) to σ_3 (cf. Gudmundsson, 2011). A stress barrier is a layer or unit where the local stress field is unfavorable for the propagation of a particular type of fracture. For example, for a vertically propagating extension fracture, a stress barrier would be a layer where the maximum compressive stress flips to horizontal, a situation which favors dike arrest (Gudmundsson and Phillip, 2006). Both stiff (high Young' modulus) and soft (low Young's modulus, compliant) layers can act as stress barriers (Gudmundsson and Phillip, 2006).

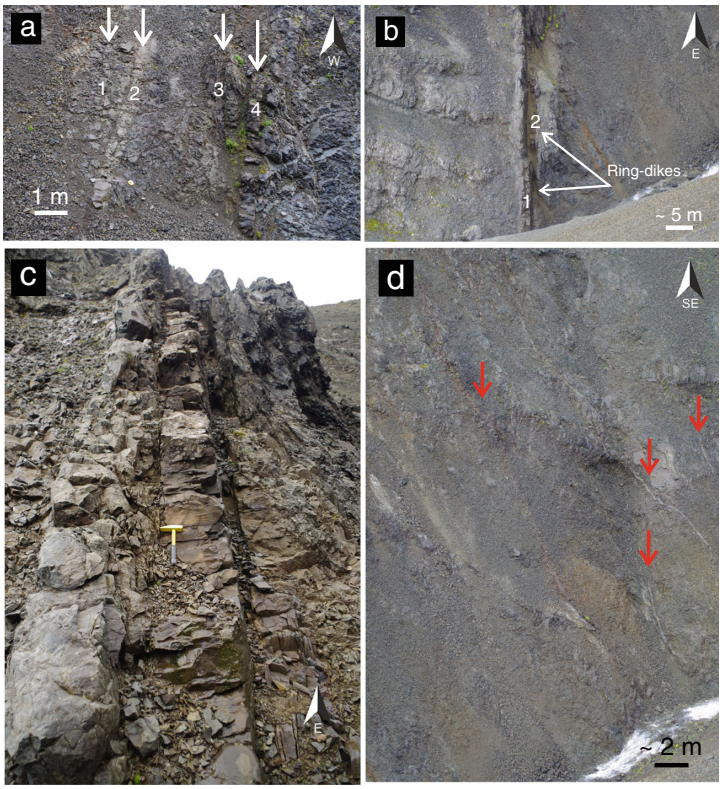

Fig. 4 Base of the outcrop of the ring fault, where four thin ring dikes (<0.7 m) of basaltic composition occupy the subvertical segment (**a**). Two of these dikes are observable in the vertical section (**b**, **c**): one can be traced inside the caldera margin (**d**), several inclined sheets strike E-W to NE-SW and dip between 65 and 80° S; at least two of the sheets meet the fault contact higher in the pile

Elastic mismatch

The second mechanism responsible for dike deflection is related to the difference in material properties of the layers hosting, and directly in front of, a propagating fracture and the associated contacts. Dikes and sheets are extension fractures or mode I cracks. However, when such fractures meet and become deflected into a contact or discontinuity, they temporarily become mixed-mode (He and Hutchinson, 1989; Xu et al., 2003). Consider the total strain energy release rate G_{total} in mixed-mode fracture propagation:

$$G_{\text{total}} = G_{\text{I}} + G_{\text{II}} + G_{\text{III}} = \frac{(1-\nu^2)K_{\text{I}}^2}{E} + \frac{(1-\nu 2)K_{\text{II}}^2}{E} + \frac{(1+\nu)K_{\text{III}}^2}{E} \quad (1)$$

$G_{\text{I–III}}$ are the energy release rates (Jm^{-2}) of ideal mode I–III cracks (Anderson, 2005; Gudmundsson, 2011), E is the Young's modulus, ν is the Poisson's ratio, and $K_{\text{I–III}}$ are the stress intensity factors. When the rock layer which hosts the dike or sheet has the same or similar mechanical properties to a rock layer above, then the strain energy release rate for a mode I crack, G_{p}, reaches a value suitable for fracture extension, which is equal to the material toughness of the layer, Γ_{L}. Therefore, from Eq. (1), the condition becomes

$$G_{\text{p}} = \frac{(1-\nu^2)K_{\text{I}}^2}{E} = \Gamma_{\text{L}} \quad (2)$$

However, the dike or sheet will deflect into the discontinuity if the strain energy release rate becomes the same as the material toughness of the discontinuity, Γ_{D}. Deflection at the discontinuity then occurs when

$$G_{\text{d}} = \frac{(1-\nu^2)}{E}\left(K_{\text{I}}^2 + K_{\text{II}}^2\right) = \Gamma_{\text{D}} \quad (3)$$

It follows that a dike or sheet will continue on the same trajectory, through a discontinuity if (He and Hutchinson, 1989)

$$\frac{G_d}{G_p} < \frac{\Gamma_D(\Psi)}{\Gamma_L} \quad (4)$$

or become deflected at the discontinuity if

$$\frac{G_d}{G_p} \geq \frac{\Gamma_D(\Psi)}{\Gamma_L} \quad (5)$$

where Ψ denotes the measure of the relative proportion of mode II to mode I:

$$\Psi = \tan^{-1}\left(K_{II}/K_I\right) \quad (6)$$

In Fig. 5, the ratio of G_d/G_p is plotted as a function of α, which represents the Dundurs elastic mismatch parameter and can be presented in the following form (He and Hutchinson, 1989):

$$\alpha = \frac{E_1 - E_2}{E_1 + E_2} \quad (7)$$

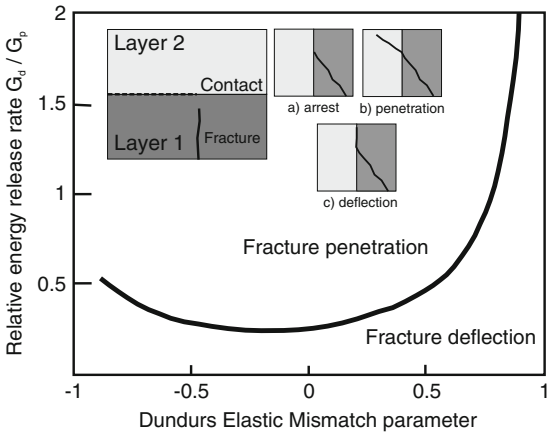

Fig. 5 Conditions for fracture propagation: upon meeting a contact between two layers with contrasting material properties, a fracture will either (*a*) arrest, (*b*) penetrate the contact, or (*c*) deflect at the contact. The ratio of strain energy release rate for fracture deflection (G_d) against fracture penetration (G_p) is plotted as a function of the Dundurs elastic mismatch parameter (α; see text for details). Modified after He et al. (1994)

Here, E denotes the plane strain Young's modulus, and the subscripts 1 and 2 relate to the moduli of the rock above and hosting the dike, respectively. The ratio below the curve in Fig. 5 indicates areas where the deflection of a dike or sheet is favored, whereas those areas above the curve indicate continued propagation with no deflection.

Cook-Gordon mechanism

Experiments on crack propagation have shown that Cook-Gordon debonding is a common mechanism in the delamination of composite materials (Xu et al., 2003; Wang and Xu 2006). It has been shown that the tensile strength ahead of a propagating dike can open up a contact ahead of the dike tip (Gudmundsson, 2011). Such a mechanism is important in where there is an abrupt change in the mechanical properties or rocks across an interface or a contact, particularly when the contact is clearly defined and mechanically weak (with a low tensile strength). However, in a fault zone such as that described previously, the contact between the fault and host rock is not clearly defined. As such, we do not consider this mechanism as important for capturing sheets within the fault, at least initially.

Numerical model setup

To test the proposal that sheets can become arrested at or deflected into a caldera fault, we made several numerical models. In all the models, we calculate the stress field around a 1-m-thick dike subject to an internal magmatic excess pressure of 5 or 10 MPa as the initial loading. The weight of overlying host rock or the overburden pressure is included in the lithostatic stress (Jaeger and Cook, 1979) and is therefore taken into account when considering loading as excess pressure in the sheet (Gudmundsson, 2011).

In the numerical models presented here (Figs. 7, 8, 9, 10, and 11), the focus is on the mechanical properties of the caldera fault zone, namely the stiffness or Young's modulus (E) of the layers that constitute the damage zone and the core of the fault, and the more gently dipping layers through which the sheet propagates. Density and Poisson's ratio are kept constant in all model runs, with values of 2500 kg m^{-3} and 0.25, respectively. We estimate that the damage zone surrounding the ring fault is approximately 15 m thick and occurs predominantly on the southern, down-throw ("hanging wall") side of the fault. The damage zone is qualitatively estimated based on the ability to discern individual lava flows, which on the northern wall can be traced to the fault contact but on the southern wall are highly altered and deformed. This deformation zone is observed laterally south for around 15 m from the fault core, which contains the ring dikes, to a point where

individual lava flow characteristics are discernible. Fault core and damage zones have been recognized and measured on different scales in many areas of Iceland (Gudmundsson et al. 2011). The fault zone is modeled simply as three individual layers of similar thickness but with differing mechanical properties. The models presented are designed to test how the local stress field changes as an inclined sheet (a) approaches a ring fault and (b) becomes captured by the fault.

The sheet is situated perpendicular to the fault zone (see the model setup in Fig. 6). A section of the ring fault is modeled in two dimensions as a series of subvertical layers decreasing in stiffness toward a fault core, replicating the variation in stiffness of the fault damage zone (e.g., Gudmundsson, 2011). In this setup, the softest layer is the fault core which is characterized by the lowest value of Young's modulus or stiffness (0.1 GPa); this is surrounded by a fault damage zone which stiffens gradually approaching that of the host rock (40 GPa). For simplicity, here, the damage zone stiffness is assumed constant at any particular time. Fault zone stiffness, however, was varied over time in separate model runs to incorporate the dynamic nature of fault development both syn- and post-collapse. Temporal changes reflect initial fault growth, and subsequent healing and intrusion by dikes. All models simulate snapshots of the magnitudes and directions of principal stress around the pressurized sheet; the likely propagation path is then inferred based on the trajectories of the maximum principal compressive stress (σ_1). Boundary conditions were used to test the model's response to a simulated vertical normal-fault dip-slip displacement (Fig. 11), modeled as a compressive stress, of 5 MPa applied to the collapsing block, and normal-fault dilation (Fig. 11), modeled as a tensile stress, of 5 MPa applied perpendicular to the fault. Trajectories of the maximum principal compressive stress (σ_1) and the magnitude of the minimum principal compressive stress (σ_3) are shown in all model runs.

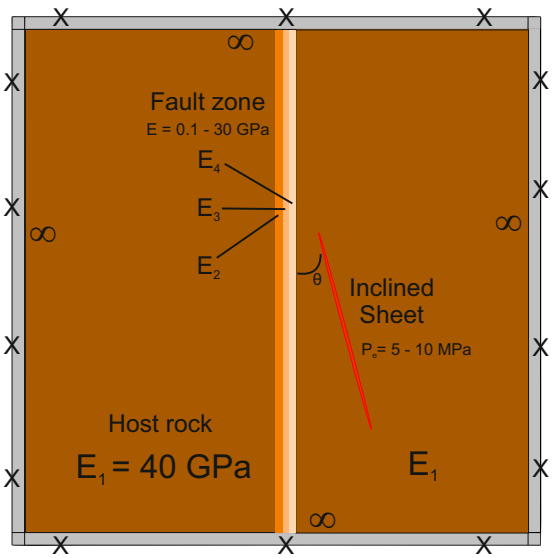

Fig. 6 General COMSOL model setup used throughout. In all runs, the models are fastened at the outer boundary using a fixed constraint; this is coupled with an infinite element domain on the inner model margin to ensure the fixed boundary effects do not influence results. The host rock and fault zone are modeled using different values for Young's modulus (E) as specified in the "Model results" section. An inclined sheet is modeled as a cavity with an excess pressure (P_e); sheet angle is varied throughout model runs

Model results

Several numerical models were run with different fault zone setups, generated by varying the mechanical properties (Young's modulus) across the fault. A homogeneous setting, whereby the fault zone shared the same mechanical properties as the host rock, was initially modeled and provided a reference to compare other model results. In this setup, the fault has little or no effect on sheet propagation. Additional model runs are displayed throughout (Figs. 7, 8, 9, 10, and 11).

Several geometrical setups were run by varying the sheet dip angle (θ), to confirm the relative effects of fault zone mechanical heterogeneity against intrusion angle. We observe that shallow-dipping sheets, those with dips less than 45°, do not alter the local fault stress significantly enough to promote deflection or arrest, unless additional boundary conditions are applied (see Fig. 11). In all models, the maximum tensile stress (σ_3) occurs at the sheet tip, and the maximum compressive stress (σ_1), shown as white cones, are used to interpret the likely fracture pathway. All models show stress contours in the range of 0.5–6 MPa, the upper end of this range being the most likely to induce fracturing (Amadei and Stephansson, 1997).

When a mechanical contrast between the fault and host rock is modeled, a rotation of principal stress occurs near the sheet tip and a temporary change in principal stress orientation at the contact between the fault and host rock. In order for the sheet to become deflected into a subvertical dike along the ring fault, as observed in Hafnarfjall, the values of Young's modulus must be sufficiently different between the individual modeled fault zone layers, in order to induce an elastic mismatch. Figure 7 highlights a situation whereby the layers which constitute the fault damage zone are not significantly different from those of the host rock and thus promote neither elastic mismatch nor principal stress rotation. This condition, namely similar elastic properties of the fault zone and the host rock, favors transverse sheet propagation through the fault. In contrast, models shown in Figs. 8 and 9 simulate a more mechanically heterogeneous fault zone, with Young's modulus differing by orders of magnitude. In these situations, sheet deflection is favored due to the mechanical mismatch between the individual layers. The fracture propagation path at the

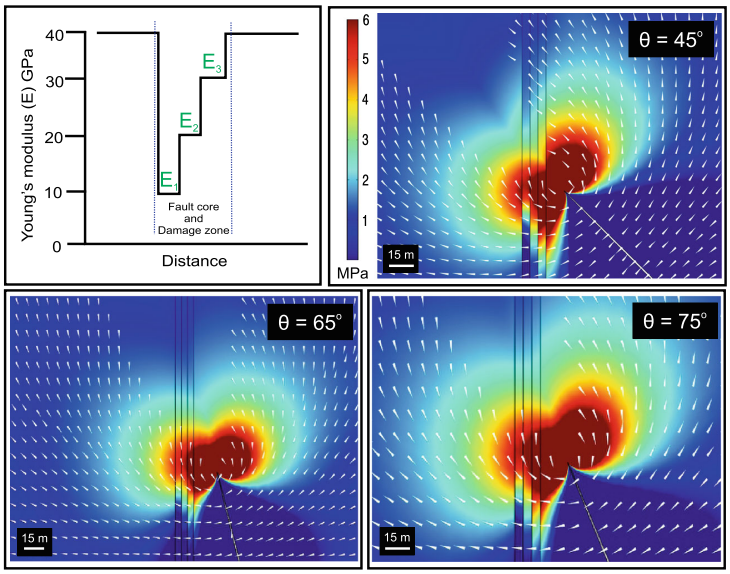

Fig. 7 Young's modulus in the fault zone ranges between 10 and 30 GPa. Sheet dips shown are 45°, 65°, and 75°, and sheet overpressure is 10 MPa. In all models, tensile stress concentrates through the fault plane, indicating that any fracture would likely propagate through the fault. Rotation of the maximum principal compressive stress (*white cones*) occurs in line with the fault dip for those sheets that dip 65° and greater, suggesting that a fracture may align preferentially with the fault. Large stress shadows are created ahead of fracture tip, as indicated by the absence of stress trajectories

sheet tip is inferred from the trajectories of σ_1 (which the sheet follows), surrounding the sheet and fault zone. It is only when these trajectories rotate to subvertical that the sheet will deflect into a dike within the fault. Such a situation is much more likely in models which simulate a sheet with an initially steep dip (i.e., >65°).

To model the effect of a previously intruded dike in the ring fault, a stiff layer is added to the center of the fault zone (Fig. 10). Such a situation is likely if a lower part of the fault was intruded by a ring dike in the conventional manner described by Anderson (1936) and Walter (2008) or if inclined sheets were previously captured and deflected (see Appendix 1). The stiff layer creates a clear stress barrier and zone of elastic mismatch, indicating that transverse sheet propagation in this scenario is unlikely. Instead, any sheet would likely become deflected or arrested at the contact between the weak damage zone and the stiff dike (Fig. 10).

Boundary conditions were applied to the model edge to simulate (1) extension across the fault and (2) block subsidence. A compressional stress of 5 MPa was applied to the intra-caldera block (Fig. 11). In this model run, the modeled principal stress axis rotates to subvertical with little

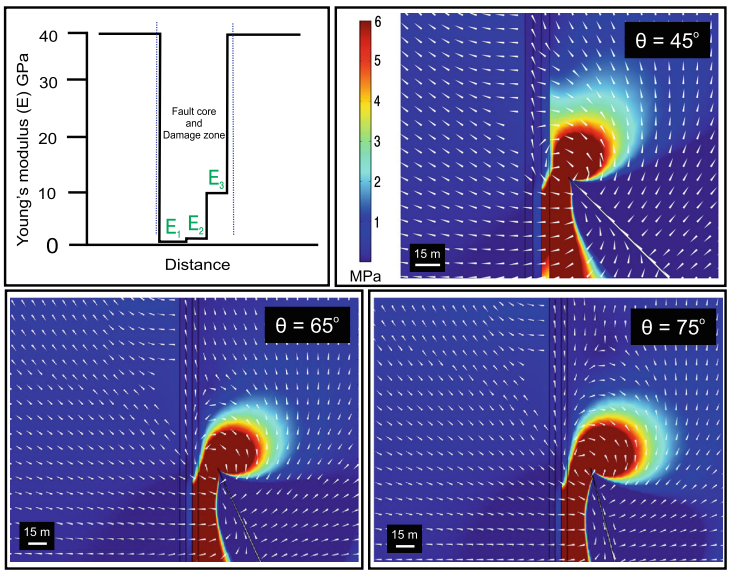

Fig. 8 Young's modulus in the fault zone ranges between 0.1 and 10 GPa, and sheet overpressure is 10 MPa in all models. In all model runs, tensile stress concentrates within the 10-GPa layer closest the sheet. Softer layers suppress most of the tensile stress, and principal stress rotation within the fault core favors vertical sheet deflection. This rotation effect is much less pronounced for those sheets which dip below 60–70°; for example, the 65° model shown displays inclined σ_1 trajectories throughout the vertical fault cross section

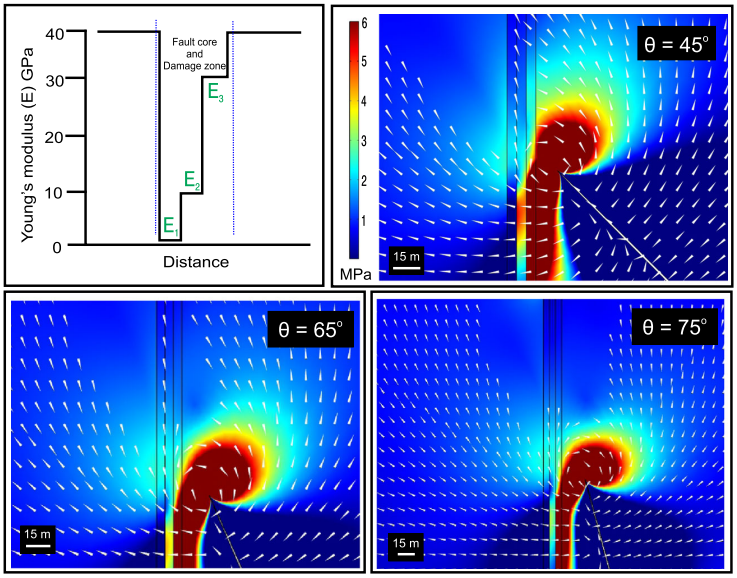

Fig. 9 Fault zone Young's modulus ranges from 1 to 30 GPa, and sheet overpressure is 10 MPa in all models. In models with sheets that dip greater than ~45°, a significant rotation of the maximum compressive stress is observed. **c**, **d** The trajectories of σ_1 rotate to vertical within the fault, whereas in **b**, trajectories are initially vertical but become inclined higher up the fault

dependence on the angle of the sheet; this situation would favor sheet propagation into and along the plane of the ring fault, thereby allowing magma to propagate in a manner consistent with that interpreted from field observations, although principal stress rotation further up dip of the fault may induce fracture arrest later on. The second boundary condition simulates an extensional force acting perpendicular to the fault, which would likely encourage fault dilation. In these situations, it is much easier for a low-angle sheet to deflect into the fault; in Fig. 11, we show a 35° dipping sheet.

Finally, a model is included to assess the background boundary effects of a magma chamber subject to pressure in excess of lithostatic, a necessary requirement for the propagation of a sheet. In this model (Fig. 12), an 8-km-wide and 1-km-thick sill-like magma chamber is situated in a homogeneous crustal segment at 5-km depth. The magnitude and orientation of stresses highlight the potential for inclined sheet propagation, particularly at the chamber outer margins. Several softer layers were added to the model; these were placed vertically to simulate the caldera fault zones previously

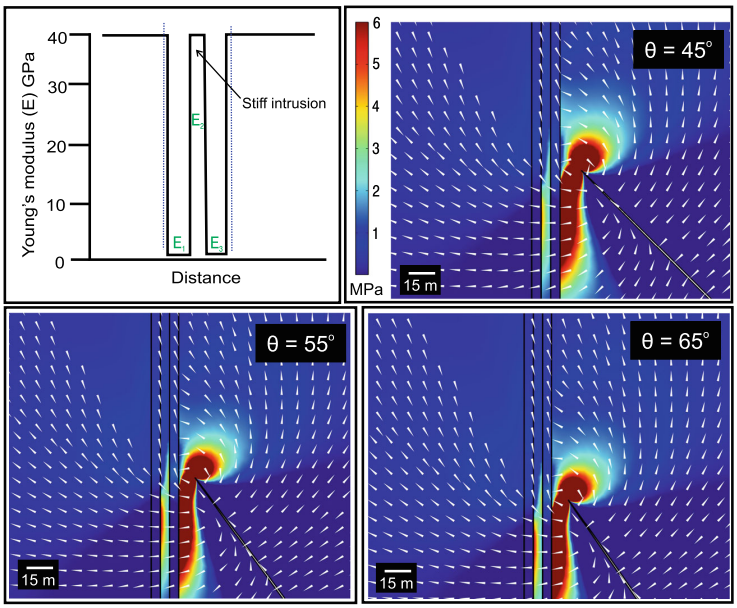

Fig. 10 A stiff layer (40 GPa) is added to the center of the fault zone to simulate a previous dike intrusion. Principal stress rotation at the sheet tip and stress concentration within the stiff layer favor fault capture, most likely along the nearside edge of the previous intrusion. Sheet approach angle has little effect on the stresses within the fault zone above 35°

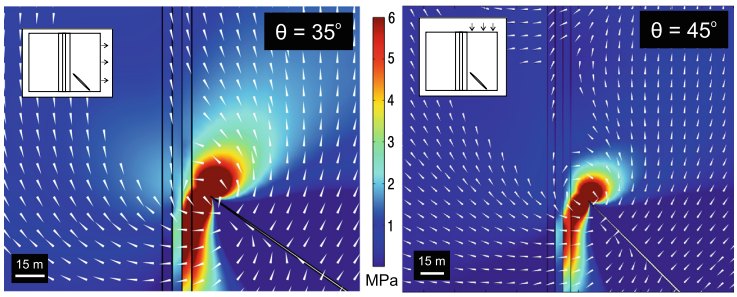

Fig. 11 Models showing the effect of various boundary conditions. Here, a tensile stress (5 MPa) is applied to the far right of the model (**a**) and a compressive stress (5 MPa) to the upper part of the intra-caldera block in the model (**b**)

discussed and horizontally to simulate, in a simple way, mechanical layering in a volcanic edifice. Stresses clearly concentrate within the fault margins in the caldera block, indicating that faults act as stress barriers. There is little principal stress rotation observed at the fault contact, indicating that if the tensile stress was high enough (0.5–6 MPa) to generate a fracture, then the likely propagation path would be through the fault. However, the required stress concentration is rarely met as the inner (core) part of fault tends to suppress stresses.

Once a fault captures an inclined sheet and deflects it into the first subvertical dike, it is generally much easier for subsequent sheets to deflect at the contact between the lava pile and the first dike (Fig. 3). This follows because the stiffness of a vertical intrusion is much greater than that of the area surrounding the fault damage zone, and therefore, principal stress rotation and elastic mismatch parameters favor dike propagation over continuation of an inclined sheet.

Discussion and conclusions

It is well known that normal faults can alter the propagation pathway of subvertical dikes (Valentine and Krogh, 2006; Gaffney et al., 2007; Ziv and Rubin, 2000) and sills (Magee et al., 2013). Several assumptions and inferences have been made regarding the role of caldera ring faults in channeling magma (Anderson, 1936; Saunders 2001; Jonsson, 2009); the most common mechanical explanation offered to decipher this process relies on magma chamber underpressure (Anderson, 1936). This model suggests that many ring dikes form during

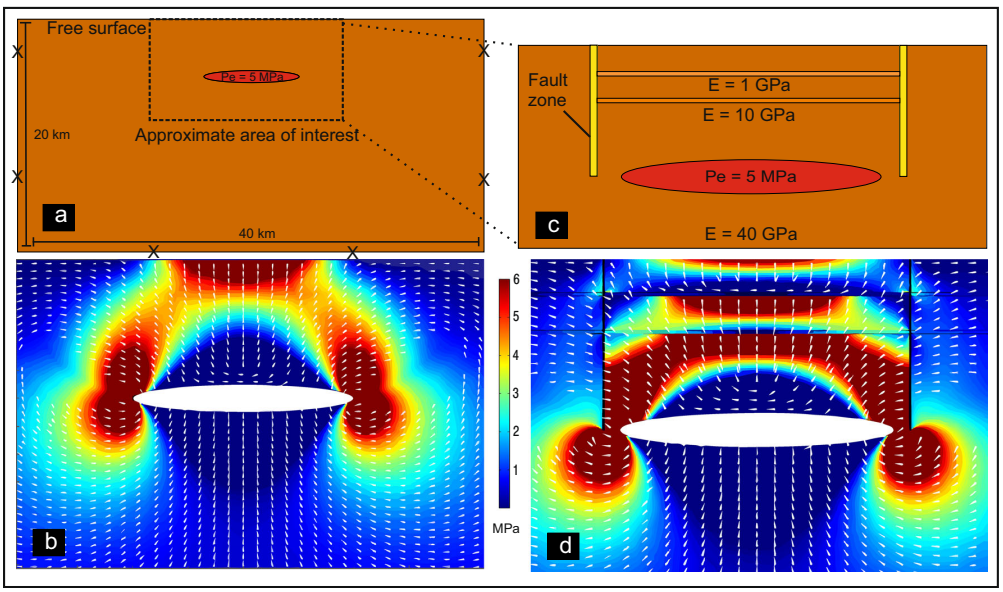

Fig. 12 Background stresses associated with a modeled **a** 8-km-wide and 1-km-thick sill-like magma chamber at 5-km depth with an overpressure of 5 MPa. **b** Principal stresses become oriented in a manner which favors inclined sheet propagation from the chamber margins. **c** Model setup includes a peripheral fault zone, with a lower Young's modulus than the surrounding host rock, as well as two soft horizontal layers at 1- and 2-km depth. **d** Results indicate that the fault acts as a significant stress barrier. Furthermore, the soft horizontal layers act in a similar manner, also exhibiting significant principal stress rotation at the boundary of the uppermost and softest layer

large explosive eruptions, leading to chamber roof collapse and the flow of evolved magmas up into the ring faults. Alternative mechanical models are hampered by the poor availability of data on the structure of ring faults at depth and the lack of detailed observations of the interactions between ring faults and magma.

Here, we present an alternative mechanism of ring dike formation which suggests that some ring dikes do not channel magma directly from the margins of a magma chamber but rather form through inclined sheets being captured and deflected along the ring fault (Fig. 13). This mechanism is in agreement with observations of restless calderas (e.g., Saunders, 2001) and the location of numerous dike-fed eruptive centers, located on ring fault margins (Walker, 1984; Geyer and Martí 2008). However, several caldera volcanoes experience eruptive activity located outside of their ring fault margins, for example the fissure eruptions of Fernandina in 1995 (Chadwick et al., 2011). Our model supports the interpretation that the sheet which fed these fissures had a shallow dip (12–14°) at a depth of ~1 km, near the chamber margin (Chadwick et al., 2011). This follows because sheet deflection is unlikely at dip angles lower than ~45° (see Figs. 7, 8, 9, and 10). Note, also, that many mafic calderas have complex ring fault structures controlled by post-collapse subsidence, for example Colli Albani (Giordano et al., 2006).

Dikes can become arrested and deflected at contacts between layers with mechanical mismatch (contrasting mechanical properties) such as stiff lava flows and compliant (or soft) tuff layers (Gudmundsson, 2011; see Fig. 12). It has been suggested that elastic mismatch and associated local stresses partly control the frequency with which dikes reach the surface to feed eruptions (Gudmundsson and Phillip, 2006). In this view, it is only when the state of stress in a volcanic edifice becomes roughly homogeneous that a dike can propagate to the surface, a condition more likely to be reached in edifices composed of mechanically similar layers. Similarly, if a caldera fault develops a fault core, it may act as a single vertical and roughly homogeneous layer, thereby promoting stress field homogenization and providing a pathway for magma channeling toward the surface.

A large proportion of the world's volcanism occurs within or around active calderas (Newhall and Dzurisin, 1988), and therefore, understanding the control of caldera structures on magma movement is vital for predicting the location and timing of eruptive activity. The caldera fault at Hafnarfjall is one of the best exposures of its kind in the world. It represents a segment of the ring fault, visible as a 200-m vertical exposure. The fault has variable attitude, but overall, it is a steeply inward-dipping normal fault.

Many faults offer potential pathways for magma. However, very steeply dipping faults, such as the ring fault in Hafnarfjall, are perhaps particularly favored paths because the normal stress on steep faults in rifting environments tends to be comparatively small (Gudmundsson, 2011). In this particular case, the ring fault has deflected and acted as a channel for inclined sheet propagation; some of the sheets may have reached the surface to supply magma for eruptions. In addition, the ring fault has captured and deflected inclined sheets to form a ring dike, a mechanism of ring dike formation that has not been reported earlier. These results further underline the importance of understanding magma-fault interaction in relation to volcanic hazards. It is likely that the process of sheet deflection and ring dike formation, described here, provides a major control on the location of resurgent caldera volcanism.

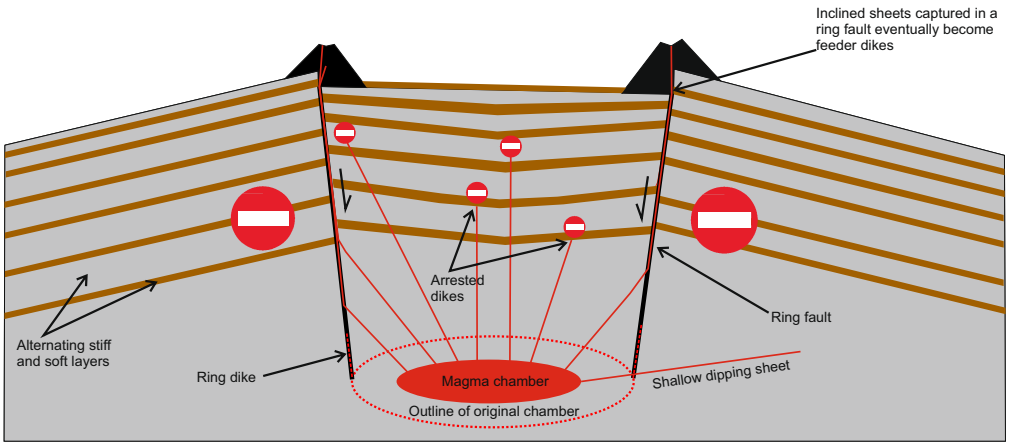

Fig. 13 Conceptual resurgent caldera model. In the model, an edifice is made of layers of contrasting mechanical properties, e.g., stiff lavas and soft tuffs and sediments. A number of dikes fail to reach the surface and become arrested at layer contacts. Inclined sheets propagating from the shallow magma chamber become captured by the ring fault. The ring fault deflects many sheets into subvertical dikes, some of which may have propagated to the surface. Shallow-dipping sheets may penetrate the fault to force eruptions outside of the ring fault margin

Acknowledgments Fieldwork of JB was partly funded by the geologists' association Baker-Arber Fund. We would like to thank Adelina Geyer and an anonymous reviewer for their very helpful comments. We also thank the editor Guido Giordano for his helpful suggestions. We are grateful to Hjalti Franzson for providing his geological map of the area and advice on field exposures, Hannah Reynolds and Zoe Barnett for field assistance, and Jonathan Pownall for fruitful discussion.

References

Acocella V, Cifelli F, Funiciello R (2000) Analogue models of collapse calderas and resurgent domes. J Volcanol Geotherm Res 104:81–96

Acocella V (2007) Understanding caldera structure and development: an overview of analogue models compared to natural calderas. Earth Sci Rev 85:125–160

Amadei B, Stephansson O (1997) Rock stress and its measurement. Chapman and Hall, New York

Anderson EM (1936) The dynamics and formation of cone-sheets, ring-dikes, and cauldron-subsidence. R Soc Edinb Proc 128–157

Anderson TL (2005) Fracture mechanics: fundamentals and applications, 3rd edn. Taylor & Francis, London, p 621

Bedard JH, Naslund HR, Nabelek P, Winpenny A, Hryciuk M, Macdonald W, Hayes B, Steigerwaldt K, Hadlari T, Rainbird R, Dewing K, Girard E (2012) Fault-mediated melt ascent in a Neoproterozoic continental flood basalt province, the Franklin sills, Victoria Island, Canada. Geol Soc Am Bull 124:723–736

Branney MJ (1995) Downsag and extension at calderas: new perspectives on collapse geometries from ice-melt, mining, and volcanic subsidence. Bull Volcanol 57:303–318

Burchardt S, Walter TR (2010) Propagation, linkage, and interaction of caldera ring-faults: comparison between analogue experiments and caldera collapse at Miyakejima, Japan, in 2000. Bull Volcanol 72: 297–308

Chadwick WW, Jonsson S, Geist D, Poland M, Johnson DJ, Batt S, Harpp KS, Ruiz A (2011) The May 2005 eruption of Fernandina volcano, Galapagos: the first circumferential dike intrusion observed by GPS and InSAR. Bull Volcanol 73:679–697

Clough CTH, Maufe HB, Bailey EB (1909) The cauldron subsidence of Glen Coe and the associated igneous phenomena. Q J Geol Soc Lond 65:611–678

Delaney PT, Pollard DD, ZIony JI, McKee EH (1986) Field relations between dikes and joints: emplacement processes and paleostress analysis. J Geophys Res 91:4920–4938

Ekstrom G (1994) Anomalous earthquakes on volcano ring-fault structures. Earth Planet Sci Lett 128:707–712

Franzson H (1978) Structure and petrochemistry of the Hafnarfjall_Skardsheidi central volcano and the surrounding basalt succession, W-Iceland [Ph.D. thesis]: Edinburgh, Scotland, university of Edinburgh 264 pp

Gaffney ES, Damjanac B, Valentine GA (2007) Localization of volcanic activity: 2. Effects of pre-existing structure. Earth Planet Sci Lett 263:323–338

Gautneb H, Gudmundsson A, Oskarsson N (1989) Structure, petrochemistry and evolution of a sheet swarm in an Icelandic central volcano. Geol Mag 126:659–673

Geyer A, Folch A, Martí J (2006) Relationship between caldera collapse and magma chamber withdrawal: an experimental approach. J Volcanol Geotherm Res 157:375–386

Geyer A, Marti J (2014) A short review of our current understanding of the development of ring faults during collapse caldera formation. Front Earth Sci 2:22. doi:10.3389/feart.2014.00022

Geyer A, Martí J (2008) The new worldwide collapse caldera database (CCDB): a tool for studying and understanding caldera processes. J Volcanol Geotherm Res 175:334–354

Geshi N, Shimano T, Chiba T, Nakada S (2002) Caldera collapse during the 2000 eruption of Miyakejima volcano, Japan. Bull Volcanol 64:55–68

Giordano G, De Benedetti AA, Diana A, Diano G, Gaudioso F, Marasco F, Miceli M, Mollo S, Cas RAF, Funiciello R (2006) The Colli Albani mafic caldera (Roma, Italy): stratigraphy, structure and petrology. J Volcanol Geotherm Res 156:49–80

Gudmundsson A (1998) Formation and development of normal-fault calderas and the initiation of large explosive eruptions. Bull Volcanol 60:160–170

Gudmundsson A, Nilsen K (2006) Ring-faults in composite volcanoes: structures, models and stress fields associated with their formation. Geol Soc Lond, Spec Publ 269:83–108

Gudmundsson A, Berg SS, Lyslo KB, Skurtveit E (2011) Fracture networks and fluid transport in active fault zones. J Struct Geol 23:343–353

Gudmundsson A (2011) Rock fractures in geological processes. Cambridge University Press, Cambridge. doi:10.1017/CBO9780511975684

Gudmundsson A, Phillip SL (2006) How local stress fields prevent volcanic eruptions. J Volcanol Geotherm Res 158:257–268

Hardy S (2008) Structural evolution of calderas: insights from two-dimensional discrete element simulations. Geology 36:927

He MY, Hutchinson JW (1989) Crack deflection at an interface between dissimilar elastic materials. Int J Solids Struct 31:3443–3455

He MY, Evans AG, Hutchinson JW (1994) Crack deflection at an interface between dissimilar elastic materials. Int J Solids Struct 25:1053–1067

Holohan EP, Troll VR, Walter TR, Münn S, McDonnell S, Shipton ZK (2005) Elliptical calderas in active tectonic settings: an experimental approach. J Volcanol Geotherm Res 144:119–136

Holohan, EP., Walter, TR., Schöpfer, MPJ., Walsh, JJ., van Wyk de Vries, B. and Troll, VR. (2013). Origins of oblique-slip faulting during caldera subsidence. J Geophys Res Solid Earth, No. 2, p. n/a–n/a

Jaeger JC, Cook NGW (1979) Fundamentals of rock mechanics. Chapman and Hall, London

Johannesson H (1975) Structure and petrochemistry of the Reykjadalur central volcano and surrounding areas, midwest Iceland. PhD Thesis, University of Durham, Durham, 273 pp

Johnson SE, Schmidt KL, Tate MC (2002) Ring complexes in the Peninsula Ranges Batholith, Mexico and the USA: magma plumbing systems in the middle and upper crust. Lithos 61: 187–208

Jonsson S (2009) Stress interaction between magma accumulation and trapdoor faulting on Sierra Negra volcano, Galapagos. Tectonophysics 471:36–44

Kennedy B, Stix J, Vallance JW, Lavallée Y, Longpré MA (2004) Controls on caldera structure: results from analogue sandbox modeling. Geol Soc Am Bull 116:515

Kokelaar P (2007) Friction melting, catastrophic dilation and breccia formation along caldera superfaults. J Geol Soc 164:751–754

Lipman, PW (1984) The roots of ash flow calderas in Western North America: Windows into the tops of Granitic batholiths. J Geophys Res 89:8801–8841

Lipman PW (1997) Subsidence of ash-flow calderas: relation to caldera size and magma chamber geometry. Bull Volcanol 59:198–218

Magee C, Jackson CAL, Schofield N (2013) The influence of normal fault geometry on igneous sill emplacement and morphology. Geology 41:407–410

Michon L, Villeneuve N, Catry T, Merle O (2009) How summit calderas collapse on basaltic volcanoes: new insights from the April 2007 caldera collapse of Piton de la Fournaise volcano. J Volcanol Geotherm Res 184:138–151

Newhall CG, Dzurisin D (1988) Historical unrest at large calderas of the world. US Geol Sur Bull 72:85–100

Saunders ST (2001) The shallow plumbing system of Rabaul caldera: a partially intruded ring fault? Bull Volcanol 63:406–420

Saunders ST (2004) The possible contribution of circumferential fault intrusion to caldera resurgence. Bull Volcanol 67:57–71

Smith RL, Bailey RA (1968) Resurgent cauldrons. Geol Soc Am Mem 116:613–662

Sparks RSJ (1988) Petrology and geochemistry of the Loch Ba ring-dike, Mull (NW Scotland): an example of the extreme differentiation of theolitic magmas. Contrib Mineral Petrol 100:446–461

Troll V, Walter TR, Schmincke HU (2002) Cyclic caldera collapse: piston or piecemeal subsidence? Field and experimental evidence. Geology 30:135–138. doi:10.1130/0091-7613(2002)030<0135

Tucker D, Hildreth W, Ullrich T, Friedman R (2007) Geology and complex collapse mechanisms of the 3.72 Ma Hannegan caldera, North Cascades, Washington, USA. Geol Soc Am Bull 119:329–342. doi:10.1130/825904.1

Valentine GA, Krogh KEC (2006) Emplacement of shallow dikes and sills beneath a small basaltic volcanic center—the role of pre-existing structure (Paiute Ridge, southern Nevada, USA). Earth Planet Sci Lett 246:217–230

Walker GPL (1960) Zeolite zones and dike distribution in relation to the structure of the basalts of eastern Iceland. J Geol Soc 68:515–527

Walker GPL (1984) Downsag calderas, ring faults, caldera sizes, and incremental growth. J Geophys Res 89:8407–8416

Walter TR (2008)Facilitating dike intrusions into ring-faults. In: Gottsmann J, Joan Martí (eds) Caldera volcanism: analysis, modelling and response, vol 10. Elsevier, Heidelberg, pp 351–374

Walter TR, Troll VR (2011) Formation of caldera periphery faults: an experimental study. Bull Volcanol 63:191–203

Wang P, Xu LR (2006) Dynamic interfacial debonding initiation induced by an incident crack. Int J Solids Struct 43(21):6535–6550

Xu LR, Huang YY, Rosakis AJ (2003) Dynamic crack deflection and penetration at interfaces in homogeneous materials: experimental studies and model predictions. J Mech Phys Solids 51:461–486

Ziv A, Rubin AM (2000) Stability of dike intrusion along pre-existing fractures. J Geophys Res 105

Chapter 5

Manuscript in preparation for journal submission

Cooling dominated cracking in thermally stressed volcanic rocks

Browning, J, Meredith, P.G., and Gudmundsson, A

Statement of contribution

Initial idea for experiments from all authors
Experimental apparatus designed by all authors with input from technicians at UCL
JB conducted all experiments with initial assistance from PGM
JB completed 1st draft of manuscript
JB made all figures and images
Data interpretation with input from co-authors
JB collected and interpreted all sample characterisation data

Cooling dominated cracking in thermally stressed volcanic rocks

John Browning[1&2]*, Philip Meredith[1], Agust Gudmundsson[2]

[1]Department of Earth Sciences, University College London, London

[2]Department of Earth Sciences, Royal Holloway University of London, Egham, TW20 0EX, United Kingdom

*e-mail: john.browning.2012@live.rhul.ac.uk

Abstract

Several hypotheses have been proposed regarding the role of thermo-mechanical contraction in producing cracks and joints during cooling of volcanic rocks. Nevertheless, most studies of thermally-induced cracking to date have focused on the generation of cracks formed during heating and thermal expansion. In this latter case, the cracks are formed under an overall compressional regime. By contrast, cooling cracks are formed under an overall tensile regime. Therefore, both the nature and mechanism of crack formation during cooling are hypothesised to be different from those for crack formation during heating. Furthermore, it remains unclear whether cooling simply reactivates pre-existing cracks, induces the growth of new cracks, or both.

We present results from experiments based on a new method for testing ideas on cooling-induced cracking. Cored samples of volcanic rock (basaltic to dacitic in composition) were heated at varying rates to different maximum temperatures inside a tube furnace. In the highest temperature experiments samples of both rocks were raised to the softening temperature appropriate to their composition, determined using thermal mechanical analysis, forcing melt interaction and crack annealing. We present in-situ acoustic emission data, which were recorded throughout each heating and cooling cycle. It is found consistently that the rate of acoustic emission is much

higher during cooling than during heating. In addition, acoustic emission events produced during cooling tend to be significantly higher in energy than those produced during heating. We therefore suggest that cracks formed during cooling are significantly larger than those formed during heating. Seismic velocity comparisons and crack morphology analysis of our cyclically heated samples provide further evidence of contrasting fracture morphologies. These new data are important for assessing the contribution of cooling-induced damage within volcanic structures and layers such as sills and lava flows. Our observations may also help to constrain evolving ideas regarding the formation of columnar joints.

1. Introduction

Crustal segments hosting magma chambers experience complex stress regimes, generated by the often combined effects from regional tectonics and local magmatic intrusions. Magma residing within a chamber at depth exerts stress within an edifice due to changes in pressure as a consequence of bulk volume change due to magma supply from a deeper source (Gudmundsson, 1998) or due to volatile exsolution (Turner et al., 1983). An additional but perhaps less well understood inputs are the effect of thermal expansion and contraction of rocks hosting magmatic intrusions. Any thermal stressing produces damage in rocks (David et al., 1999), but in volcanic systems these stresses, like mechanical stresses are likely to be generated cyclically (Heap et al., 2013b) by repeat intrusion and extrusion of magma. The cyclic process may combine to produce an additive stress thereby contributing to instability, as well as influencing the location and pathway of magmatic flow (Chouet, 1996) but there may be annealing and healing of fractures at high temperature in between events. Normal faults for example, are thought to commonly nucleate from cooling joints (Acocella et al., 2000). When magma is intruded into a cooler host rock, its time of solidification is proportional to the thickness of the intrusion in the 2^{nd} power (Gudmundsson, 2011), with the cooling surface generally located perpendicular to the direction of propagation. Dykes and inclined sheets will tend to intrude pre-existing weaknesses such-as cooling joints (Figure. 1); and therefore understanding the mechanics of cooling induced fracturing and joint formation is important in forecasting magma pathways. Targeted injection of cool fluids is a technique

employed by the geothermal industry to force rapid contraction of the host rock around a borehole and force pre-existing cracks to dilate and re-open or to induce the formation of new tensile cracks (Axelsson et al., 2006; Brudy and Zoback, 1999; Kitao et al., 1990; Tarasovs and Ghassemi, 2012). The aim is to increase permeability and fracture surface area and thereby enhance the efficiency of the geothermal system (Axelsson et al., 2006). Non-double couple earthquakes have been related to cooling and tensile fractures induced by cooling fluid injection at geothermal sites (Julian et al., 2010), and by cooling contraction of magma chambers (Miller et al., 1998). Field relations can indicate the mechanisms of cooling-induced fracturing but it is often difficult to characterise the dynamic processes involved. For example many aspects concerning the formation of columnar joints still remain unclear (Hetényi et al., 2012). In addition to deep sub-surface processes, it is likely that cooling related fractures play a key role in the degassing of magma in shallow conduits (Tuffen and Dingwell, 2005; Tuffen et al, 2003) as well as at the surface in viscous domes and lava flows (Cabrera et al, 2011). In all these cases it is clear that understanding volcanic systems requires knowledge of the physical properties of volcanic rocks as a function of stress, pressure and temperature.

When subjected to a change in temperature a rock mass will experience fracture when the thermal stresses caused by expansion or contraction of individual grains in contact with other grains become high enough to exceed the localised tensile or shear strength (Figure 2). These thermal stresses are generated by two main mechanisms, 1) the mismatching thermal expansion co-efficient of mineral grains, and 2) differential mineral grain orientation and anisotropy. Consider a mono-mineralic rock in which the individual grains are randomly oriented, here stress builds up between the grains as they expand, through heating, in direction directions. In a poly-mineralic rock the situation above still likely applies but now each of the grains expands through thermal expansion at different rates and therefore contributes further strain and resultant stress. A less important mechanism with respect to this study is that of thermal shock whereby rocks are subjected to a very high rate of heating or cooling. All the experiments reported here heat and cool the rocks significantly slowly as to not induce thermal shock.

A salient previous study with respect to this work presented is that conducted by Vinciguerra et al (2005), in which the seismic properties of an intrusive basalt from Iceland were compared with a basalt from a lava flow on Mt Etna. The study found that P-wave velocities decreased in both rock types as a consequence of thermal stressing; in this case velocity decrease was associated with the growth of micro-cracks. Velocity decrease was noticeably higher for the Icelandic basalt (around 2.0 km s^{-1}) in comparison to the Etnean basalt (negligible), indicating that faster cooled extrusive Etna basalt contained significantly more crack damage than the slow cooled intrusive basalt prior to thermal stressing (Vinciguerra et al, 2005). The results are used to explain the low seismic velocities (approximately 3-4 km s^{-1}) often found in basaltic volcanic edifices. Cracking was monitored contemporaneously by acoustic emission output during the heating phase.

A difficulty with studying cooling induced cracking in the laboratory is that any rock must first be heated, and therefore any end member produced will show a composite pattern of cracks generated during both the heating and cooling cycle. We therefore provide contemporaneous measurements of acoustic emissions (AE) which act as a proxy for the number and relative size of micro-cracks. This dataset is complemented by static measurements of ultrasonic wave velocities and micro-crack image analysis of rocks both pre and post heat-treatment.

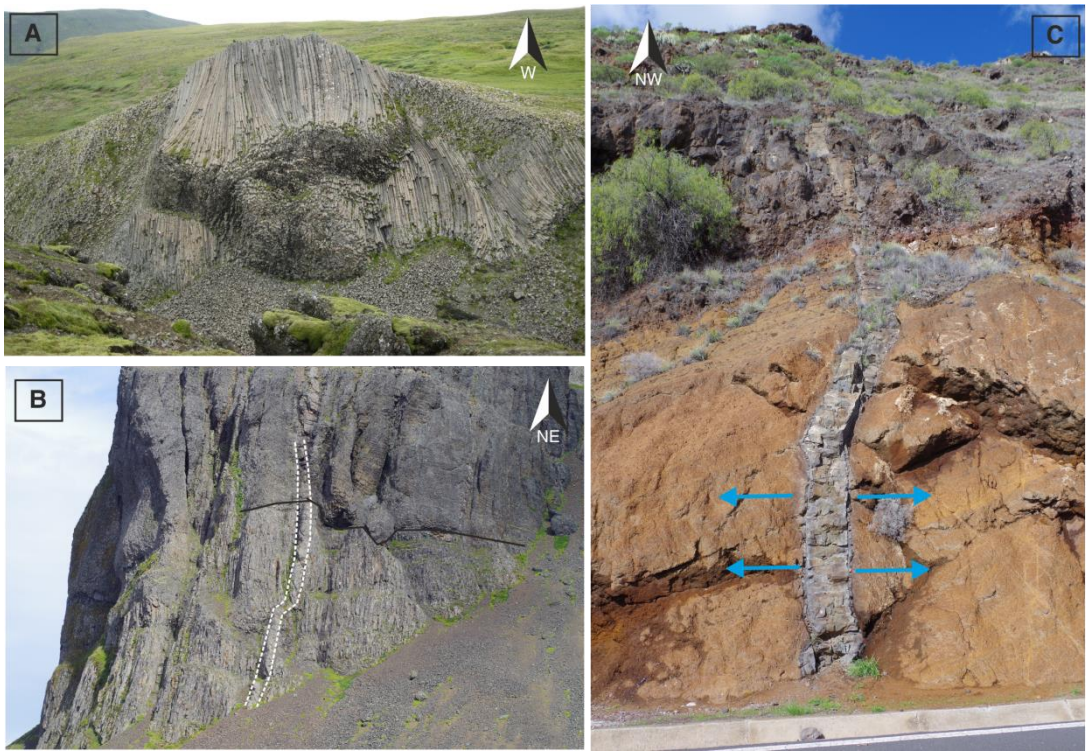

Figure 1. A) Large cooling joints formed during cooling contraction of a sill in Stiflisdalsvatn, South-West Iceland. B) A sub-vertical dyke intrudes a layer of sub-vertically oriented cooling joints at Brekkufjall, West Iceland. C) A Sub-vertical dyke intrudes a Hyalaclastite unit in Anaga, Tenerife, principle cooling direction is shown as blue arrows, perpendicular to the direction of emplacement.

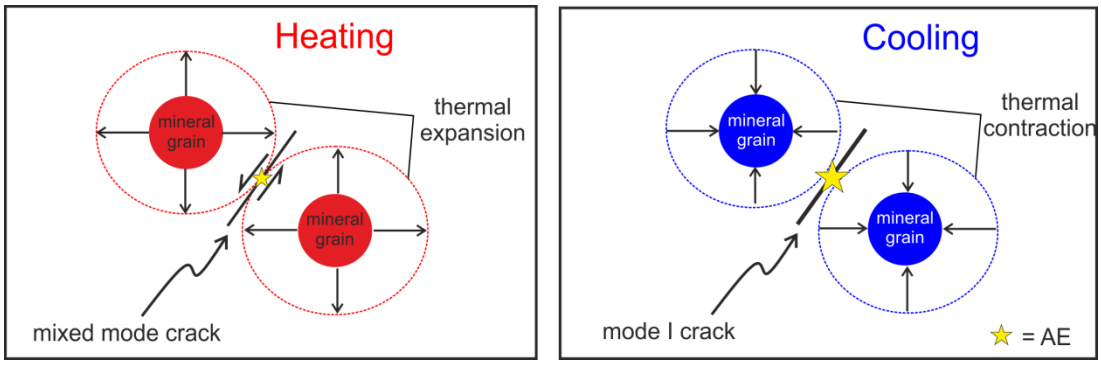

Figure 2. Individual grains expand during heating, when the grains come into contact the resultant stress induces fracture and the propagation of mixed mode cracks. During cooling, the individual grains contract which is likely to induce mode I tensile cracks although the process is not fully understood.

Here we present a series of experiments using a new apparatus designed to acquire acoustic emissions during expansion and contraction of thermally treated cores of volcanic material. These experiments are designed to test ideas on the magnitude and frequency of cracking as a consequence of thermal stresses, with a direct comparison between expansive and contractive stresses. Acoustic emissions, ultrasonic wave velocities and micro-crack analyses are used as proxies to understand likely fracture modes.

2.1 Sample characterisation and preparation

The type of material used in any high temperature experiment that induces melting must be carefully chosen. The three rocks selected for this study are all fine grained igneous rocks. Icelandic basalt (IB) has been widely used in rock physics studies (e.g Vinciguerra et al. 2005) and so the chemical and mechanical properties of this rock type are well known. IB is an intrusive tholeitic basalt dominated by an intergranular matrix of plagioclase, granular pyroxene and iron oxides. Partially oriented plagioclase is found along with a rare abundance of augite, olivine and an interstitial glass phase. IB has a density of 2900 kg/m^3 ± 10 kg/m^3 and an initial porosity of around 4 %. A section of a phonolitic dyke from the Anaga province of Tenerife (AP) was additionally selected as an ideal material for comparison with the mafic Icelandic basalt. AP has a trachytic and porphyritic texture dominated by amphibole, feldspar and sanidine with minimal abundance of glass phase. AP has a density of 2300 kg/m^3 and an initial porosity of around 7 %. The final rock type is a silica rich (Table 1) Dacite lava from the 1939-40 Reck flow on Nea Kameni (NKD), Santorini (Pyle and Elliott, 2006). The dacite lavas are petrophysically well studied (e.g Barton and Huijsmans, 1986), however remarkably little work has been conducted on the mechanical properties of Santorini's recent lavas. NKD is a glass bearing dacite with a density of 2200 kg/m^3 ± 10 kg/m^3 and an initial porosity of around 10%. By nature the lavas are extrusive and have therefore undergone a significantly contrasting cooling history to those previously described rocks. NKD has a porphyritic texture dominated by plagioclase, pyroxene, iron oxides and rare sanidine.

Samples were cut into ~65 mm in length and 25 mm in diameter cores with the surfaces ground using a surface grinder to ensure parallelism and smoothness of the two end surfaces.

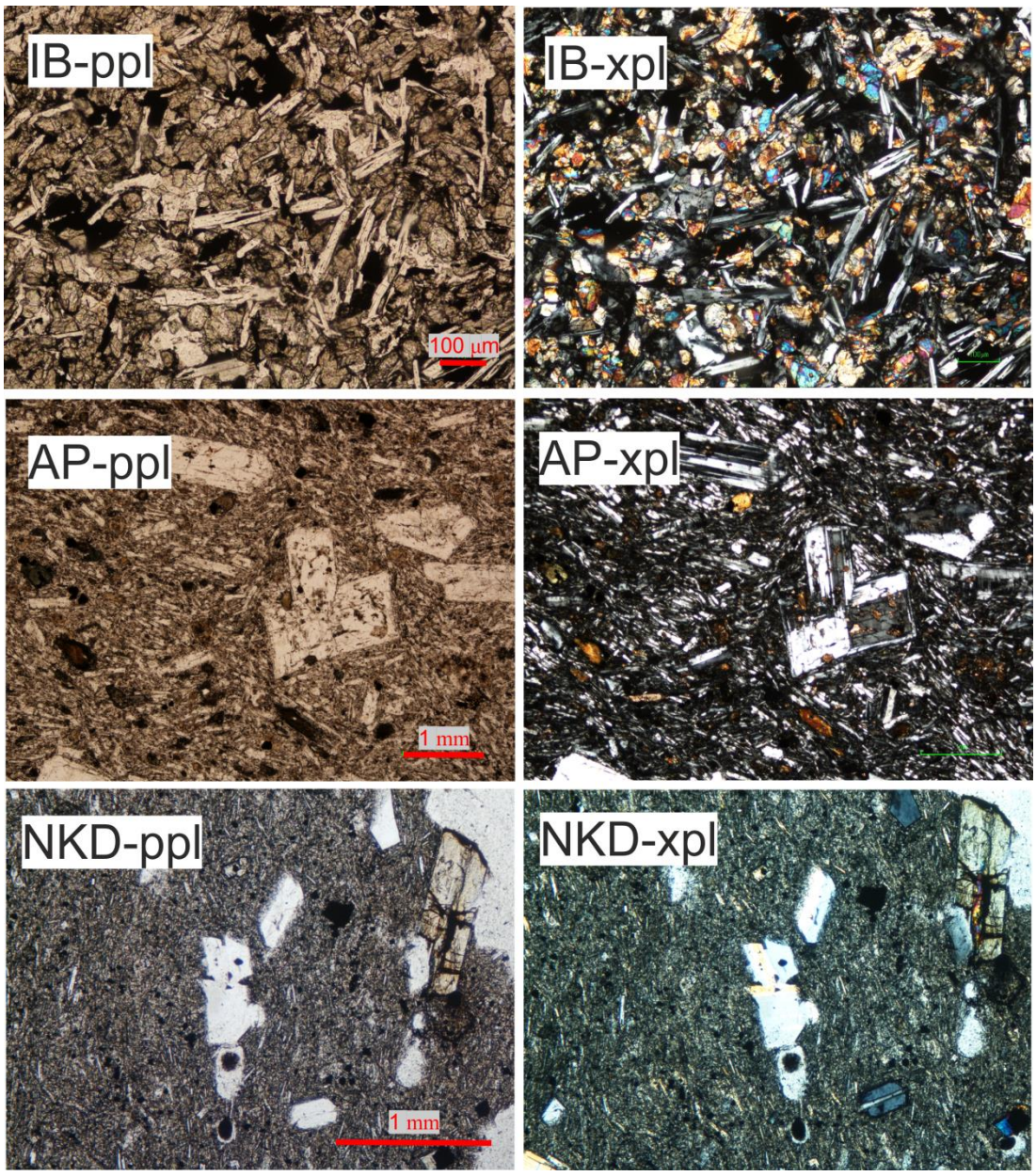

Figure 3. Optical light microscope images in ppl (left) and xpl (right). Samples are IB, AP and NKD from top to bottom.

Table 1. Whole rock x-ray fluorescence results for materials used within this study.

Material	SIO2 (%)	AL2O3 (%)	FE2O3 (%)	MGO (%)	CAO (%)	NA2O (%)	K2O (%)	TIO2 (%)	MNO (%)	Total (%)
Basalt (IB)	47.13	13.87	14.99	7.16	11.43	2.28	0.16	2.15	0.23	99.66
Phonolite (AP)	56.75	20.32	4.65	1.08	3.71	5.51	4.77	1.01	0.17	99.27
Dacite (NKD)	65.45	15.68	5.73	1.4	3.97	4.99	1.92	0.80	0.15	100.32

2.2 Thermal characterisation

As we are heating each rock to high temperature with the aim of partly annealing fractures then it is important to have an understanding of each materials baseline thermal properties. We determined thermal expansion co-efficients (α) and material softening by thermo-mechanical analysis (TMA) using a Netzsch TMA 402 thermo-mechanical analyser. In Fig. 4b we show the total thermal expansion plotted as change in length of each sample type and thermal expansion co-efficient (α) values as a function of temperature (Fig. 4a) and time (Fig. 4c). Generally there is very little variation in α between heating and cooling, provided that the temperature throughout each sample is homogeneous. α is similar in all three rocks and ranges commonly from around 15 x 10^{-6}/˚C to 25 x 10^{-6}/˚C apart from a deviation and increase at around 800˚C in NKD and 1100˚C in IB and AP (Figure 4). TMA was used to characterise each materials softening point (Fig. 5), which is in turn defined as a point at time and temperature where the material begins to show negative expansivity as a result of a small force (3 N) applied to each end. We take this point to indicate when the material is beginning to form melt phases and behave plastically or as viscoelastically. A sharp softening point is easily observable in NKD at 800˚C, which corresponds well with the measured temperature of Tg (glass transition) from separate differential scanning calorimetry measurements (Appendix A). The precise softening points of IB and AP are less well defined, in fact AP appears to exhibit two softening points, and IB may well too, however in order to avoid bulk melting and potential damage to the equipment tests were concluded at 1130˚C. The apparent stiffening of AP may be related to expansion due to volatile exsolution and resultant pressure increase. For all standard thermal stressing tests (section 3.1) we take the softening point of each rock type to be the maximum hold temperature used, that is 1100˚C for IB and AP, and 800˚C for NKD.

Once each material's softening point was calculated we then estimate the time taken for any melt within the samples to relax into pre-existing cracks or those cracks formed during heating. The timescale of viscous relaxation (τ) of melt into cracks and pores was calculated from (Dingwell and Webb, 1989):

$$\tau = \frac{\eta}{G_\infty} \qquad (2)$$

where η is melt viscosity and G_∞ is infinite frequency elastic shear modulus, normally given as $10^{10\pm0.5}$ GPa for silicate melt (Dingwell and Webb, 1989; Hess et al., 2008). Melt viscosity is calculated using ViscosityCalc (Giordano et al., 2008) with a standard value of 0.5 wt% H_2O (Barton and Huijsmans, 1986) and whole rock chemical composition obtained from XRF analysis (Table 1). We obtain a viscosity of $10^{7.53}$ Pa s for dacite at 800˚C containing 0.5 wt% H_2O, which gives a relaxation time of ~0.003 s. To allow significant relaxation and therefore the best chance for annealing, we use the common convention that a sample should be left at temperature for $\geq 10^3\tau$, which in this case gives ~30 minutes. The model of Giordano et al (2008) falls down when using comparatively low silica content rocks such as basalt and to a lesser extent phonolite, where we obtain unrealistic melt viscosities of $10^{1.64}$ Pa s and $10^{3.77}$ respectively at the softening point for each material, previously measured as 1130˚C.

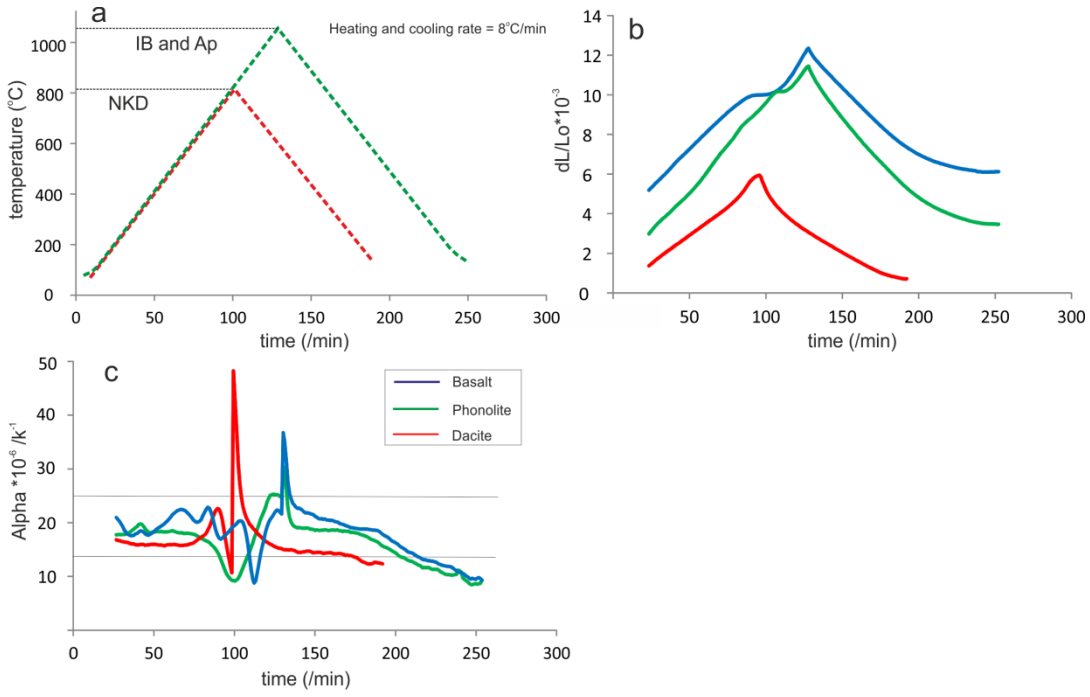

Figure 4. Thermo-mechanical analysis results. (a) Temperature profiles for each material tested, (b) thermal strain during heating and cooling at 8˚C/min, (c) thermal expansion co-efficient (α) as a function of time and resultant temperature.

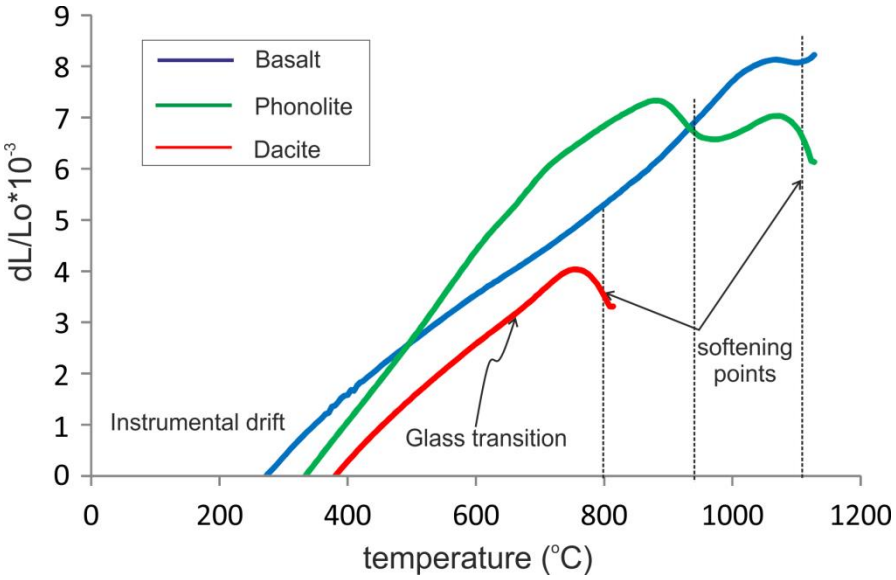

Figure 5. Thermal strain and resultant material softening, indicated at ~800˚C for NKD, and 1100˚C for AP and IB, although AP appears to exhibit an earlier lower temperature softening.

2.3 Experimental apparatus

Temperature profiles were controlled using a two-stage programmable Eurotherm 808 controller attached to a tube furnace. Samples were heat treated inside the Carbolite CTF12/75/700 tube furnace, which is capable of reaching temperatures up to 1200 ^{o}C. Sample cores were held within a purpose built jig manufactured from a 310 steel alloy capable of sustaining temperatures up to 1100 ^{o}C without significant corrosion. The jig is 1.1 m in length and comprises a series of rods and springs to hold the sample under constant end-load within the central, uniform temperature section of the furnace, as illustrated in Figure 7. The central rods act as waveguide which had to be of sufficient length so that the transducers and springs were held outside of the furnace to remain cool. Those springs allow the central rods to move in response to sample expansion and contraction during heating and cooling and therefore maintain a flush contact throughout the experiments. All experimental runs are conducted at 1 atm, as the setup was not in its current state, capable of adding a confining pressure.

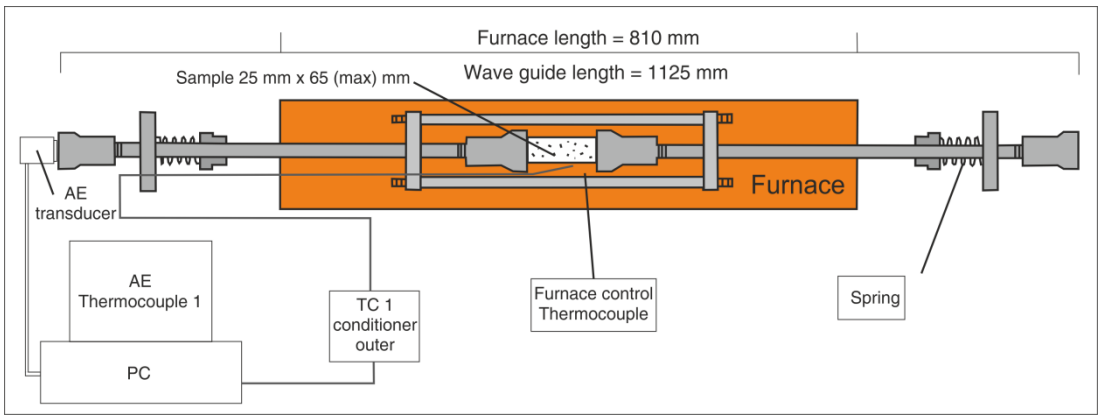

Figure 6. Schematic diagram of the experimental arrangement used for our thermal stressing experiments.

2.4 Methodology

In all thermal stressing tests samples were heated at set constant control rates of 1, 4 and 8˚C/min in order to investigate the effect of differential heating rate. The samples were then held at a maximum temperature determined from TMA for length τ, in most standard tests this is around 30 minutes, although for targeted tests the hold time varies. Samples were then cooled to room temperature at a maximum of 4˚C/min, but cooling rates varied. This is because the sample assembly did not make it possible to cool faster than a natural cooling rate (Figure 7). Two rates of cooling were performed, one constant control rate of 1˚C/min and one variable natural cooling rate.

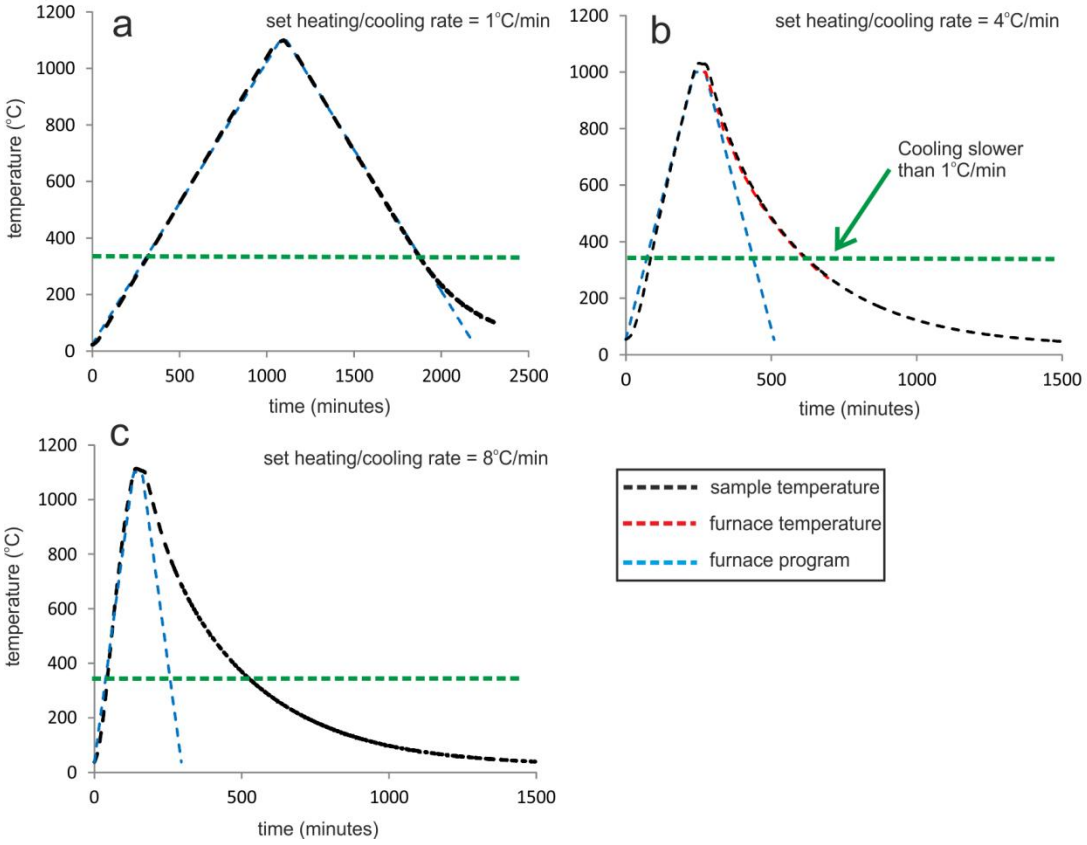

Figure 7. Programmed and actual heating and cooling profiles for a range of temperature ramp rates, A) 1˚C/min, B) 4°C/min and C) 8˚C/min. Temperatures were measured at the sample surface. A green line indicates the temperature at which cooling rates decrease below 1˚C/min, the slowest programmed rate of cooling.

In order to capture dynamic crack growth and nucleation events during our thermal stressing tests we record contemporaneous acoustic emissions (AE). One Panametrics V103 piezoelectric P-wave transducer was attached at the end of the steel wave guide; the signal was passed through a preamplifier and recorded using a Vallen AMSY-5 connected to a PC. Each discrete AE event is termed an AE hit. Within any one AE hit the recovered waveform can be used to measure the amplitude (dB) and duration (μm) to calculate discrete AE energy by summing the envelope of the AE waveform (see Cox and Meredith 1999 for a detailed description of the AE recording method) which acts as a proxy for the relative size of fracture events.

3. 0 Results

We report on two main types of experiments that record contemporaneous AE during thermal stressing tests, and then show results from static image analysis and ultrasonic wave velocity tests conducted on pre- and post- heat treated end member samples. The first set of AE tests are systematic or standard tests which heat each rock type to a maximum temperature defined from earlier TMA measurements, held for 30 minutes and then cooled at a set rate. The second set of tests are targeted to report on the effect of hold times and maximum temperature predominantly in NKD. Targeted tests are also reported in the discussion where we consider the Kaiser 'thermal memory' effect. In Figure 8 we show the temperature profile and AE generated during a standard test on IB which has been heated at a rate of 8˚C/min held at 1100˚C for 30 minutes and then cooled at a natural cooling rate. We show the AE hit rate (Fig. 8a) which is averaged per 10 AE hits and given as discrete AE hits/h, although not shown here, the same method can be applied to calculate AE energy rate. Instead we show discrete AE amplitude (Fig. 8c) and discrete AE energy (Fig. 8e), amplitude has also been separated to show the number of AE hits that occur as a function of amplitude (Fig. 8d). Finally AE hits and energy are given as cumulative plots (Fig. 8b and f). In this initial test we find that the maximum amplitude, energy and rate of AE hits occurs during the cooling cycle. A sharp inflection on both cumulative plots indicates an increase in the total number (Fig. 9b) and relative size (Fig. 8f) of AE hits at around 800˚C during the cooling cycle. Throughout we choose to use AE energy as the best proxy for cracking. Whilst previous studies have shown AE hit events and amplitudes (e,g Vinciguerra et al., 2005), in many of our studies AE is characterised by an increased rate of AE hits and higher amplitude hits, in which case the energy output during this period is significantly higher, so therefore AE energy gives the best indications.

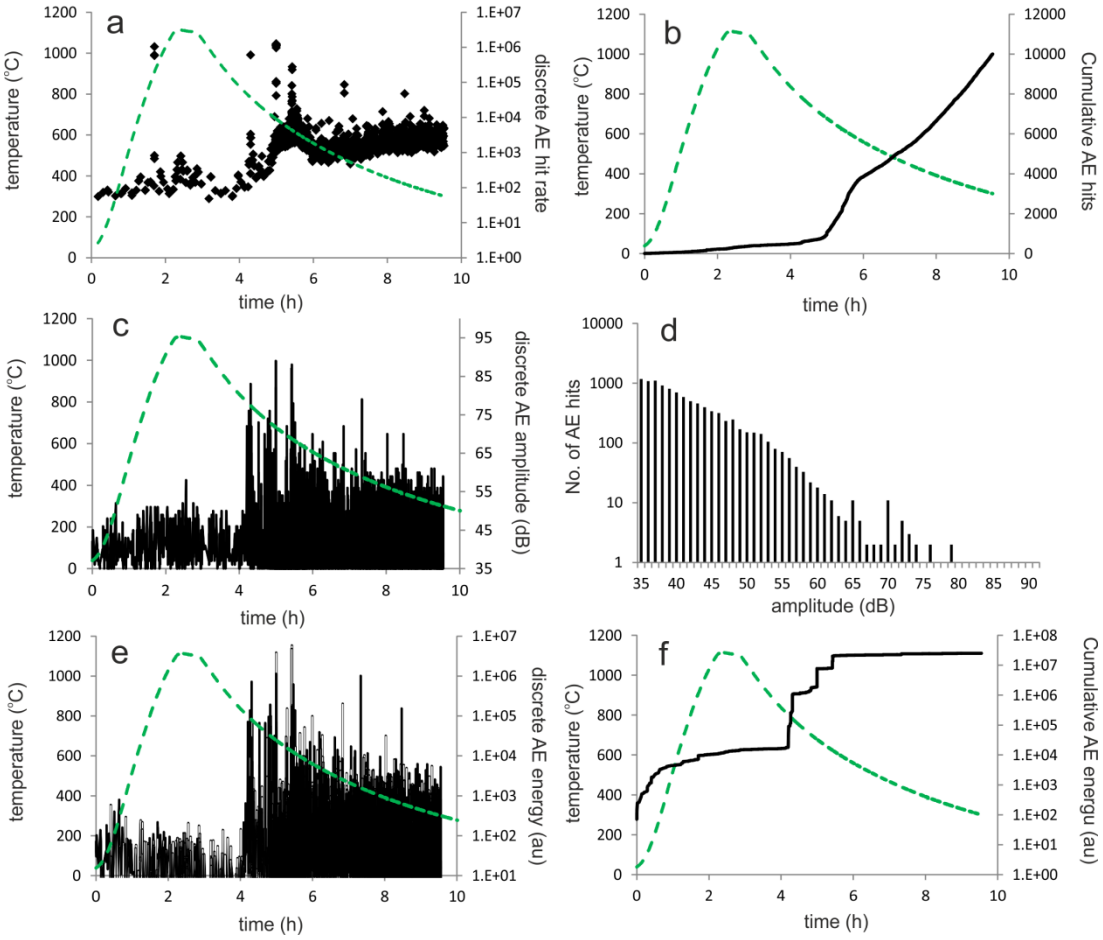

Figure 8. Standard acoustic emissions dataset for a basalt sample heated at 4˚C/min and cooled at a natural rate. a) discrete acoustic emissions hit rate, b) cumulative number of acoustic emissions hits, c) discrete acoustic emission amplitude (dB), d) number of acoustic emission hits binned as a function of amplitude (dB), e) discrete acoustic emission energy (arbitrary units), f) cumulative acoustic emissions energy.

3.1 Standard tests

In Fig. 9 we plot AE energy as function of time and temperature for all materials and at two heating and cooling rates, 1°C/min and 8°C/min, for clarity 4˚C/min is given in Appendix A. In all tests, the relative size and rate of AE hits are notably higher during the cooling cycle of thermal treatment than the heating cycle. The onset of sustained high AE hit energy is very similar during cooling in all experimental runs and occurs at around 800°C, apart from in the slowest cooled basaltic sample where the onset occurs around 650°C (Figure. 9). AE hit onset, rate and energies are not

significantly different between the two cooling rates tested in all rock types. Although IB and AP produce a larger magnitude and frequency of AE events as a consequence of faster heating, the effect is less apparent in NKD. The lowest AE hit rate consistently occurs during the maximum temperature hold period, which suggests thermal equilibration and therefore minimal thermal stress occurs at this point.

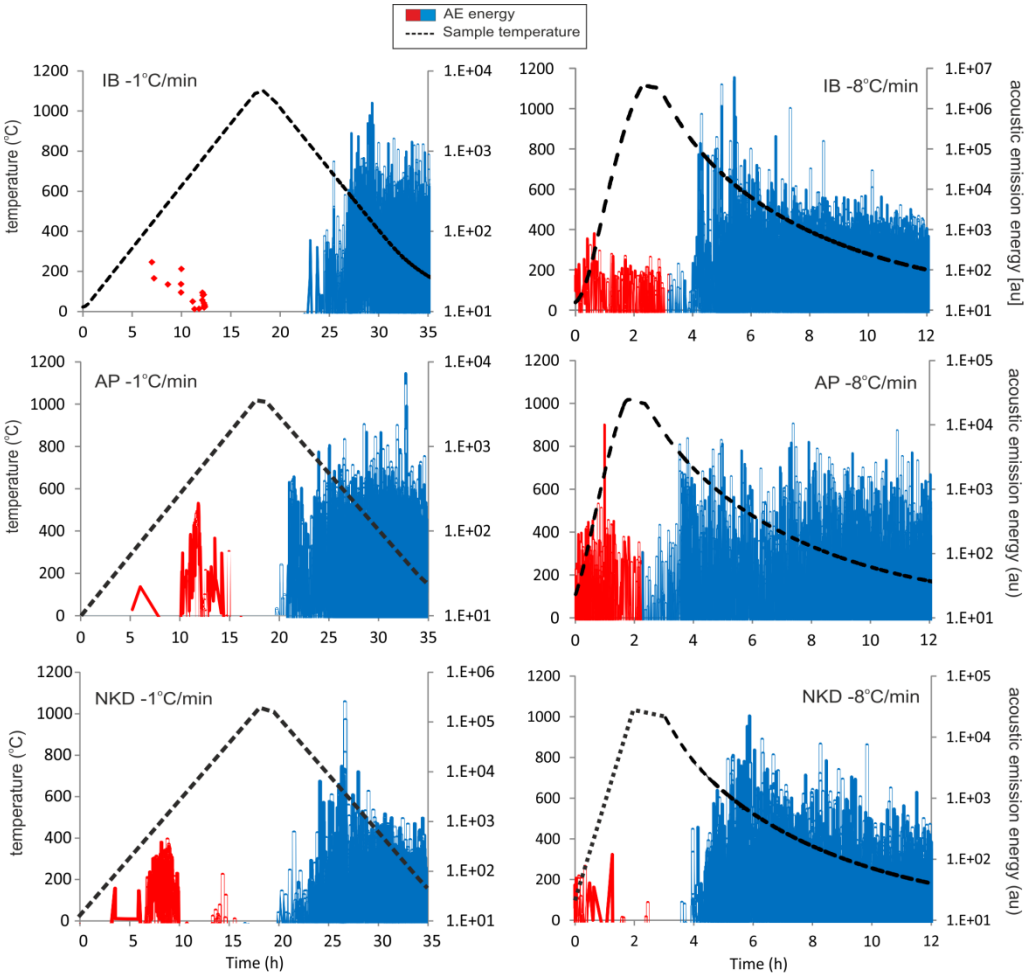

Figure 9. Acoustic emission hit energy as a function of temperature for three rock types (Basalt, IB, Phonolite, AP, Dacite, NKD) and two different heating (1°C/min – and 8°C/min) and cooling rates (black dashed line). Onset of high energy bursts occur at the onset of cooling (blue lines) with most energy generated around 800˚C upon cooling. Time in hours is scaled differently for each heating and cooling rate test to encompass the full range of results. Similarly AE hit energy is shown on different scales for the same reason.

In table 2 we compare the total number of acoustic emission hits and resultant energy for each rock type during a 1˚C/min heating and cooling cycle. As both the heating and cooling cycle in these tests have the same duration, it is useful to compare direct totals. A direct comparison of the number of AE hits is not possible in those tests where a natural cooling rate is induced as the duration of cooling is much greater than during heating, in this case we prefer to look at the AE hit rate or AE energy rate. In table 2 AE hit and energy rate are values averaged over the full heating and cooling duration. In all rock types it is clear to see that there are a significantly greater number of AE generated during cooling.

Table 2. AE hit and energy totals and rates for a 1°C/min thermal stressing experiment.

Heating/cooling rate = 1°C/min	No. Hits	Hit rate (/min)	Total Energy (au)	Energy rate (/min)
IB Heating	42	0.04	8.03×10^{2}	3.91×10^{-1}
IB Cooling	6166	6.45	3.78×10^{5}	3.96×10^{2}
AP Heating	131	0.19	4.91×10^{3}	3.75×10^{1}
AP Cooling	5051	6.15	2.30×10^{5}	2.80×10^{2}
NKD Heating	1310	1.60	2.54×10^{4}	3.09×10^{1}
NKD Cooling	8573	9.02	1.01×10^{6}	1.06×10^{3}

3.2 Targeted tests

To test the effect of high temperature residence timescales and degree of potential fracture annealing we perform three tests of samples of NKD. This sample type was chosen as it is characterised by the lowest temperature softening point. In the first test a sample of NKD was heated to 800˚C, the experimentally determined softening point, and held for ~1 minute (Figure 10). The AE from this test where then compared with results from the AE hits occurring when a different sample of NKD was held for ~ 2 hours at the softening point (Figure 11). AE hit energy are similar in both tests, thereby indicating that either the relaxation timescale in both tests was sufficient to anneal a similar amount of fractures, or that the melt was still too viscous at this temperature range and therefore the annealing timescale was too small

in both cases. As the time taken to accumulate events in each cycle is dependent on the temperature differential we also consider the number of hits and amount of AE energy as a function of time, i.e a rate of AE hits (Fig 10b and Fig 11b). A noticeable decrease in AE output is observed at high temperatures (>800˚C), corresponding to either a) the material starting to behave plastically or more likely b) the reduction of thermal stress due to sufficient thermal equilibration as previously noted in the standard tests. When the cumulative number of AE events or AE energy is plotted against time (Fig. 10c and Fig. 11c) we notice a consistent plateau during the temperature hold phase, consistent with thermal stress reduction.

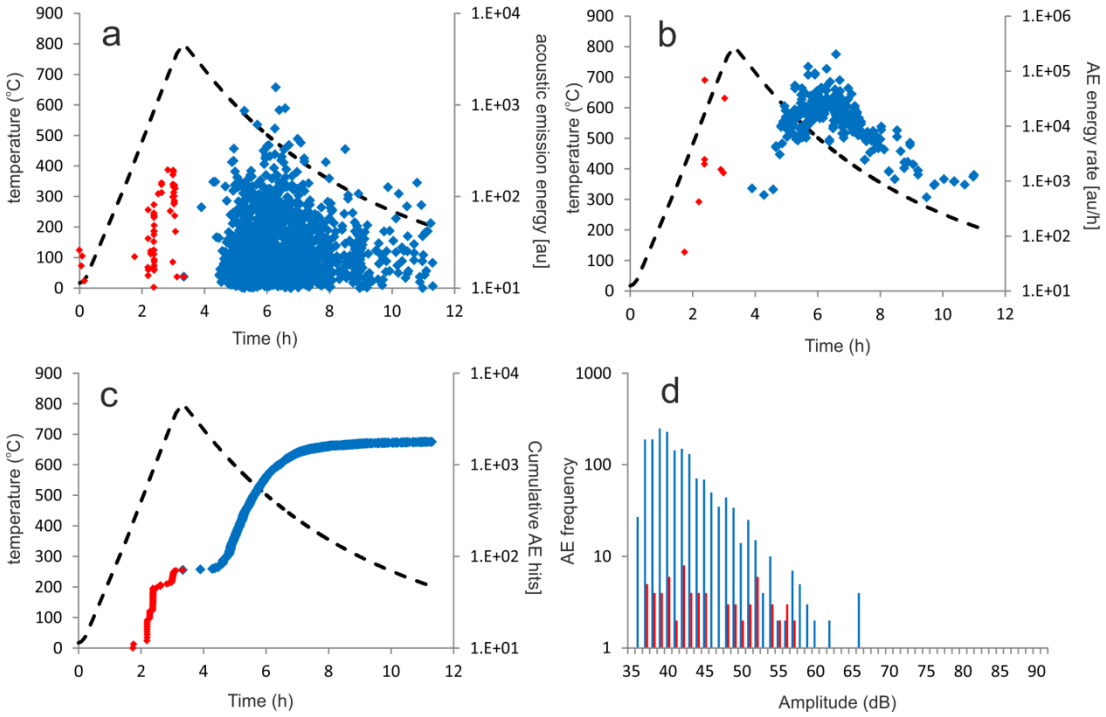

Figure 10. Acoustic emission energy and events during a heating and cooling cycle in NKD, held at 800˚C for ~1 min. a) discrete AE hit energy as a function of time and temperature. b) AE hit energy rate. c) cumulative number of AE hits and d) frequency of AE hits as a function of amplitude.

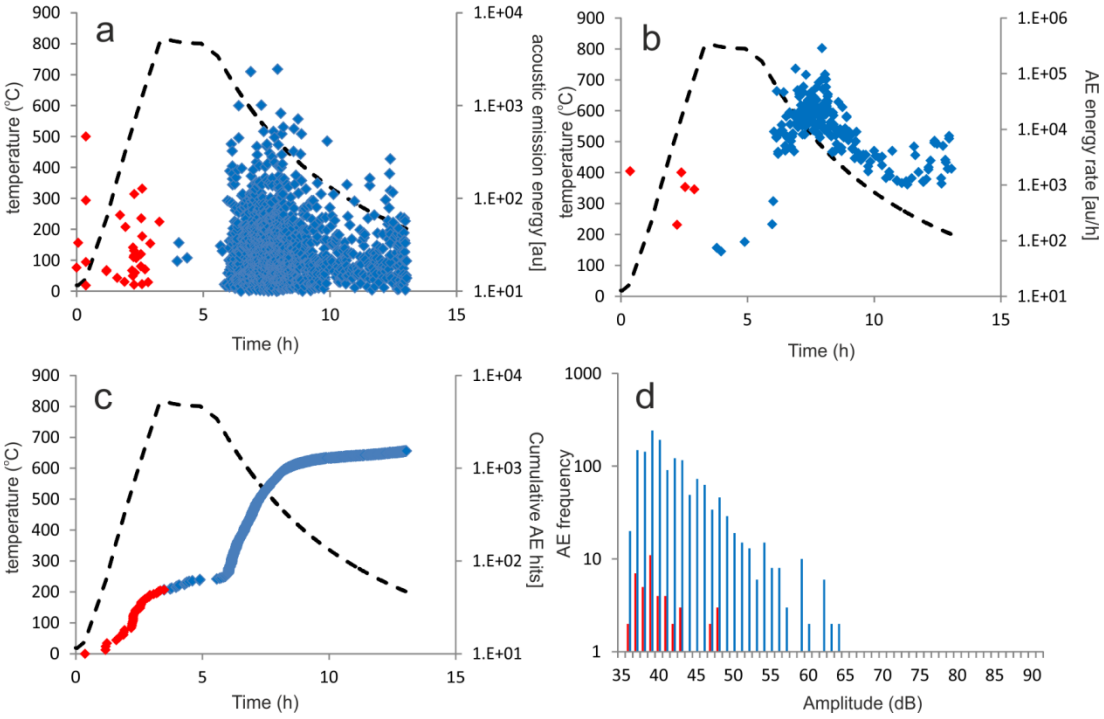

Figure 11. Acoustic emission energy and events during a heating and cooling cycle in NKD, held at 800˚C for ~2 hours. a) discrete AE hit energy as a function of time and temperature. b) AE hit energy rate. c) cumulative number of AE hits and d) frequency of AE hits as a function of amplitude.

In Fig. 12 we show the results of a final annealing test whereby NKD was heated to 200˚C above the determined softening point, producing a melt viscosity which ranges from ~10^8 Pa s to ~10^5 Pa s over a period of approximately 2 hours (Fig. 12c inset). Upon cooling we note very high energy bursts of AE occurring around 600˚C, whilst the general pattern of AE hit amplitude, energy and rate is similar to previous tests we do note a number of slightly higher amplitude events and an increased frequency of AE hits. At viscosities of the order of ~ 10^5 Pa s we would expect the melt to be on the cusp of flowing and therefore infer that some fracture annealing is highly likely. We therefore conclude that because the AE hit response in this final test is similar to that of the previous two targeted tests, then sufficient fracture annealing took place even with the smallest length of high temperature hold.

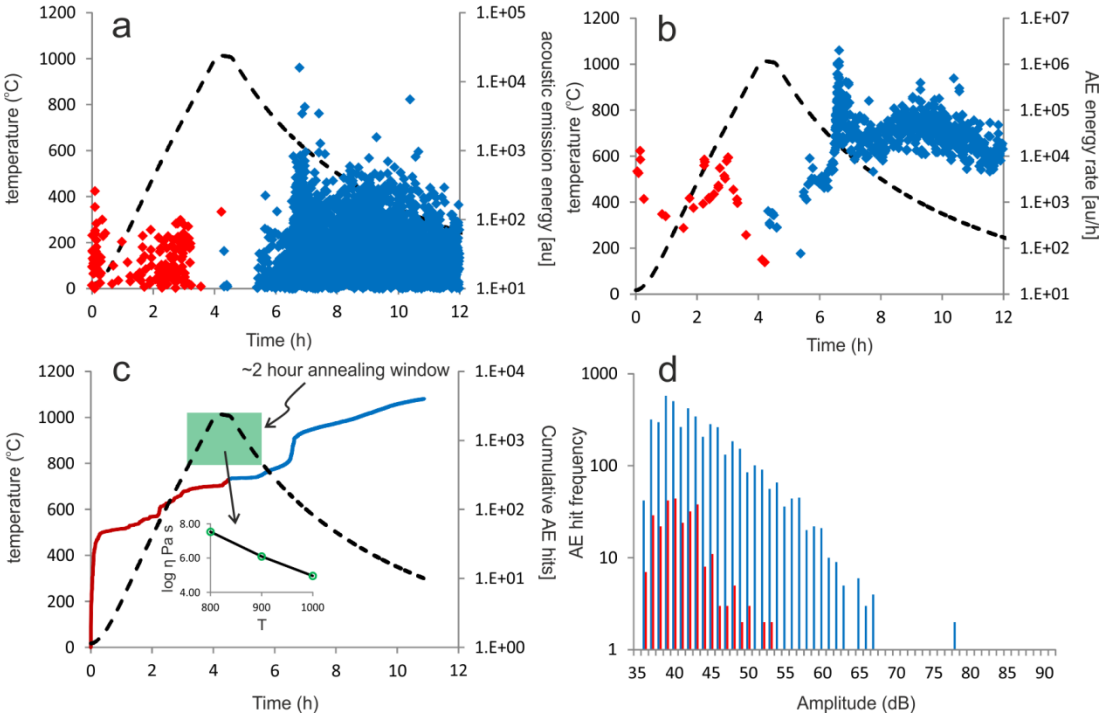

Figure 12. Acoustic emission energy and events generated during a heating and cooling cycle, held at 1000˚C for 30 minutes. NKD lies within an annealing window (c) for approximately 2 hours in which time melt viscosity continually decreases (inset) thereby increasing the likelihood of viscous annealing. a) discrete AE hit energy as a function of time and temperature. b) AE hit energy rate. c) cumulative number of AE hits and d) frequency of AE hits as a function of amplitude.

3.3 Acoustic wave velocities

Radial P-wave velocities as a function of azimuth are reported in Figure 13. Values for non-heat treated (NHT) Icelandic basalt (IB) range from 5.42 to 5.55 km/s, Anaga Phonolite (AP) between 4.38 to 4.58 km/s and Nea Kameni Dacite (NKD) from 5.27 to 5.31 km/s. Within individual samples, anisotropy value (A) ranges from 0.01 to 0.09 indicating that grain and crack populations are relatively isotropic. Samples were heat treated to the maximum temperature determined from TMA, i.e 1100˚C for IB and AP, and 800˚C for NKD. The degree of internal sample isotropy remained following heat treatment, but P-wave velocities decreased in all samples. Velocity decreases are most significant in the intrusive IB and AP rocks where V_p drops by around 45%, whereas the change whilst still significant, is less so in NKD

where V_p drops by 21%. With an initial P-wave velocity of 5.29 km/s in NKD, an extrusively cooled lava, this is unusually faster than the intrusively cooled AP. Although the drop in P-wave velocity is much less in NKD than the other rock types, we would expect the initial value to be substantially less too, owing to an abundance of pre-existing micro-cracks and pores.

Table 2. P-wave velocities in Icelandic basalt (IB), Anaga phonolite (AP) and Nea Kameni dacite (NKD) tested with no heat treatment (NHT) and following heat treatment (HT).

	max	min	mean	anisotropy value (A)	Vp % change
Vp (km/s)					
IB NHT	5.57	5.40	5.52	0.03	42.55
IB HT	3.20	2.92	3.03	0.09	
AP NHT	4.58	4.38	4.46	0.04	45.85
AP HT	2.48	2.45	2.48	0.01	
NKD NHT	5.33	5.25	5.29	0.02	21.58
NKD HT	4.18	4.05	4.15	0.03	

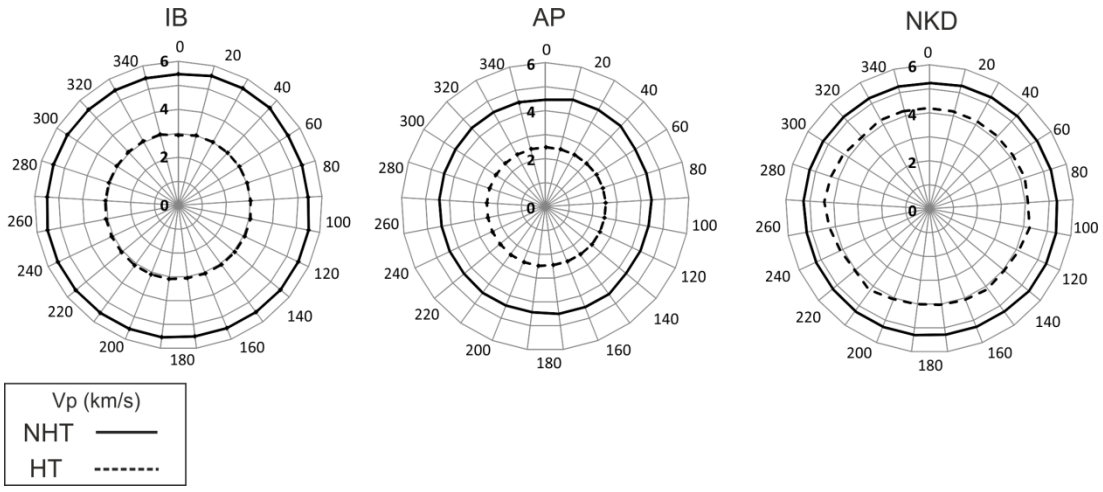

Figure 13. Radial P-wave velocities for all materials no heat treatment (NHT) (solid line) and heat treated (HT) (dashed line). In all cases P-wave velocity decreases following heat treatment, but the effect is less apparent in NKD. All samples are relatively isotropic.

3.4 Crack sizes and morphologies

Crack morphologies observed under scanning electron microscope were analysed and mapped using a MATLAB measuring code (see Mitchell & Faulkner 2008 for

further details). Individual fractures identified from SEM images were imported into Adobe illustrator. Fracture lengths and orientations are manually recorded and then counted using the MATLAB code. The method does not provide a fracture density but it allows a quantitative description of the relative total number and size of fractures across comparable sample types. In order to reduce bias in user measurements, all images for fracture analysis and counting were chosen randomly. When quoting numbers of micro-cracks we are referring to the number found within the randomly chosen square. The size of the square changes between each sample type, but remains the same between samples of the same composition and can therefore be used for direct comparison. Although it is important to note that the analysis of heat treated and non-heat treated rocks is made on separate samples, and therefore whilst we draw comparisons and parallels between the two, the method is subjective and prone to issues regarding sample heterogeneity. The technique can therefore be considered at best, complimentary to the previously described results and techniques.

SEM images of end member pre- and post- heat treatment samples were analysed in terms of the numbers of micro-cracks. Non-heat treated IB and AP samples exhibit an abundance of micro-cracks evenly distributed throughout the samples. The cracks range in size from approximately 25 μm to 150 μm in length. Following heat treatment it is found that the length of fractures in these sample types does not increase significantly but the total number of fractures observed increases markedly. In Fig. 14 we show a crack map indicating the location of all micro-cracks counted in a sample of heat treated IB. Cracks are isotropically oriented and distributed throughout. The total number of cracks recorded in this sample was 420, which was compared to a randomly picked section of a non-heat treated basalt sample where 282 cracks were measured. This represents a 42 % increase in the number of micro-cracks observed. It should be noted that crack length increases only within the measurement error, rising from 78 μm in NHT IB to 82 μm in HT IB. We estimate the error in individual measurements to be approximately 5 μm found through repeat measurements. A comparable level of micro-crack frequency increase is found in AP were the total number of fractures rises 70% following heat treatment, but less so in NKD where the increase is around 20%. Micro-cracks in NHT AP tend to be slightly longer than those in HT AP (Figure 15). NKD initially contains very few micro-

cracks (<61), but a much greater abundance of pores prior to heat treatment, those fractures which are present tend to be quite large (> 200 μm) and orientated preferentially along an azimuth at approximately 90˚. It is important to also consider that in SEM we are studying a two-dimensional plane, we consider that the same effects can be extrapolated into the third-dimension and therefore the micro-cracks recorded represent a minimum.

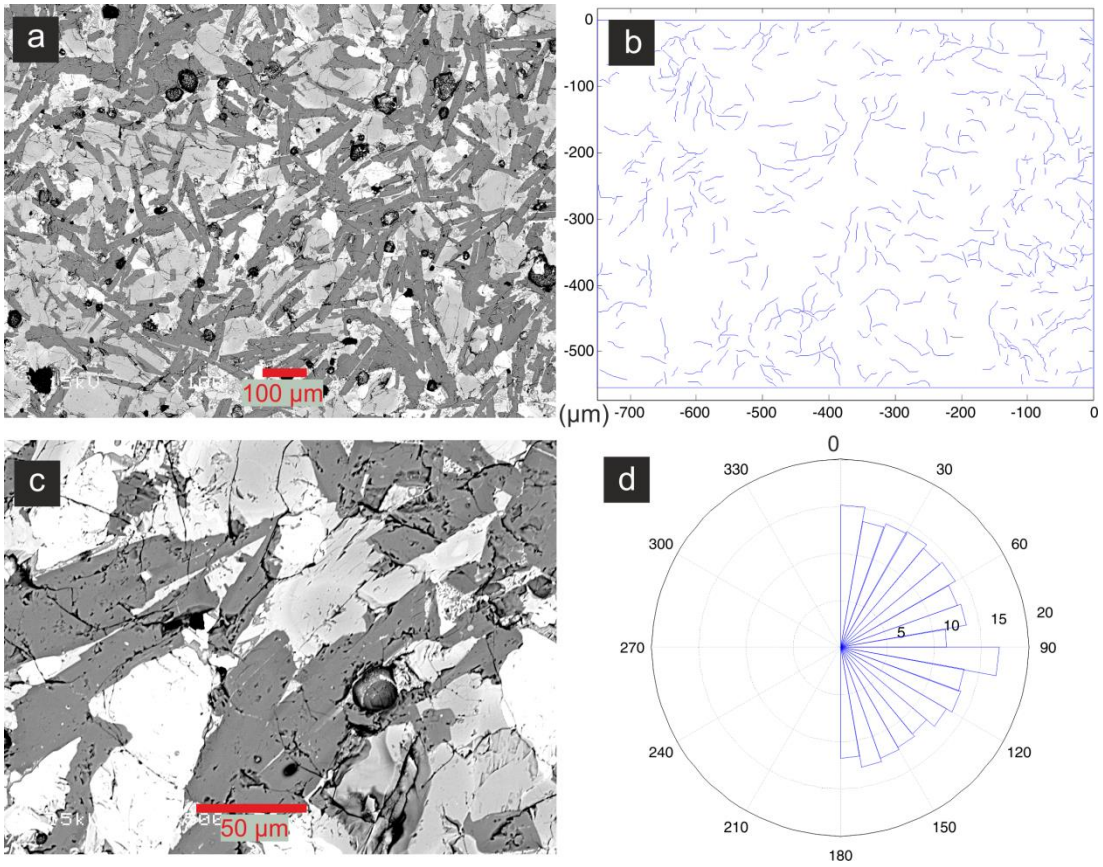

Figure 14. SEM images and crack analysis of a heat treated basalt sample. Total number of cracks measured is 418 with an average length of 82 μm ± 5 μm. a) original SEM image with scale shown, b) manually recorded crack map produced from MATLAB, c) a close-up section of the image of the above image, d) fracture numbers with respect to orientation (azimuth).

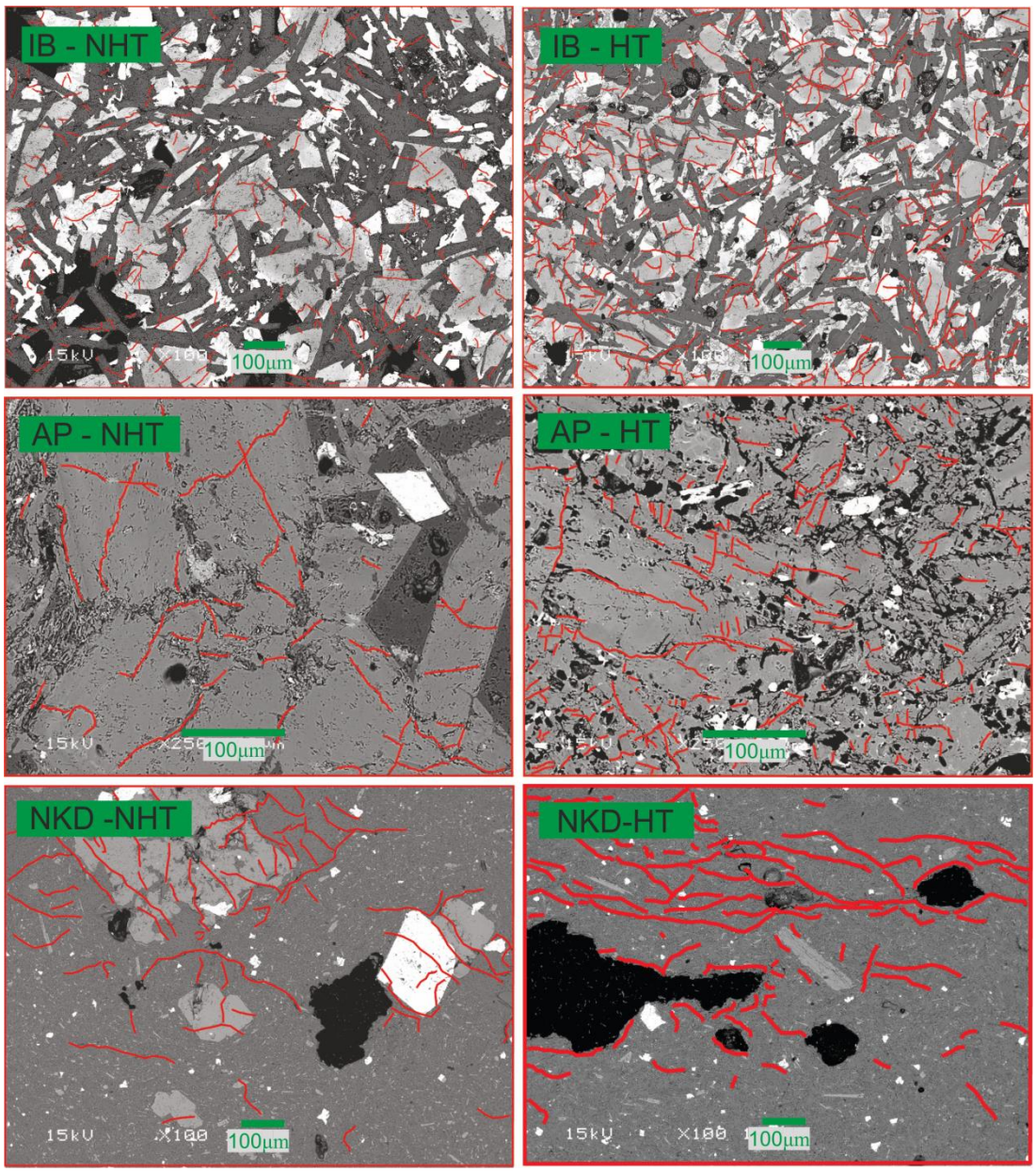

Figure 15. Comparison of crack sizes in non-heat treated (left) and heat-treated (right) samples. From top to bottom materials are basalt, phonolite and dacite.

Whilst highly subjective, it is possible to draw comparisons between orientation of cracks and the increase in number of cracks observed pre- and post- heat treatment and the reduction in P-wave velocities, and P-wave isotropy. The two methods therefore largely confirm the contemporaneous AE data which shows significantly more cracking occurring during cooling.

4.0 Discussion

The vast majority of studies dealing with thermal cracking have concentrated primarily on the heating cycle (Meredith et al., 2001; Richter and Simmons, 1974; Simmons and Cooper, 1978; Vinciguerra et al., 2005). Although some previous studies of thermal cracking in poly-crystalline materials have presented anecdotal evidence of increased cracking during cooling (Heap et al., 2013; Mollo et al., 2013). Our results suggest that low energy AE on heating within an all-round compressive stress regime are likely associated with small increments of pre-existing micro-crack extension; possibly with some new mixed-mode cracks forming. By contrast high energy AE on cooling within an all-round tensile stress regime are associated with larger increments of crack growth; and formation of new mode I cracks. Our contemporaneous AE results are supported by complimentary static measurements on pre- and post- heat treated rocks indicating substantially reduced seismic velocities related to thermal cracking and increased number of cracks in SEM analysed images. We suggest that those studies which have focused on thermal cracking only within the heating and compressive regime (e.g Vinciguerra et al., 2005) substantially underestimate the role of thermal stressing.

4.1 Seismic *b* value

In Figure 16 we show the same data as per Figure 9, but now include seismic *b* values. *b* values were obtained for all experimental runs using a MATLAB script (P. Benson, personal communication, 2015) that calculates the maximum likelihood method (Aki, 1965), these values were then plotted alongside acoustic emission energy for each rock type at the fastest and slowest rates of heating and cooling. The *b* value provides an indication of the frequency and relative size of cracks, in the case where *b* value decreases this generally indicates the presence of a greater number of larger cracks. Interestingly we note much higher and varied values of *b* obtained for NKD, ranging between 0.5 to 3, than IB and AP which range from around 0.4 to 1. Generally, *b* values drop sharply at around 800°C in the cooling cycle corresponding with increased AE as previously described. In those cases where it is possible to obtain *b* values during the heating cycle, we find that the values tend to be higher than during the cooler cycle.

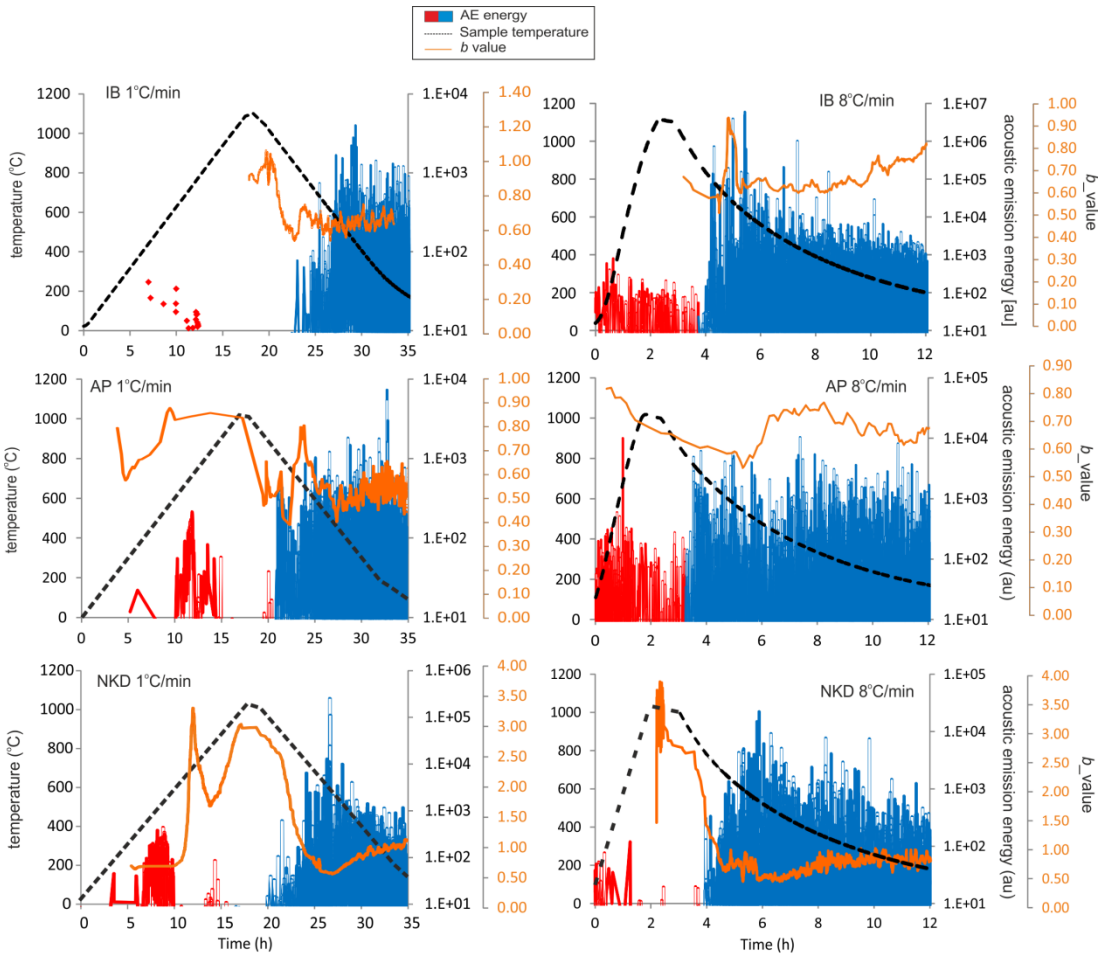

Figure 16. Acoustic emission energy and seismic *b* values as a function of temperature for IB, AP and NKD heated and cooled at two different rates (1˚C/min and 8˚C/min). *b* value was calculated using Aki's maximum likelihood method for 200 hits at 100 hit intervals.

4.2 Fracture annealing

Fracture annealing is a relatively poorly studied topic, but the mechanics of the process in silicic material relies on the ability for melt to fill the fracture voids and then overcome fracture surface tension (Vassuer et al., 2013). This is obviously only possible where melt can be produced in a rock type. The three chosen rock types have vastly differing characteristics in terms of melt production at high temperature. Generally, glass is the first phase to melt, at the glass transition temperature (*Tg*). Neither IB nor AP contain an abundant glass phase and therefore any melting will be associated with crystal phase or iron oxide melting. *Tg* was best constrained in NKD at around 800˚C. This material therefore offered the best chance for characterising

fracture annealing and resultant fracture generation upon cooling. Two-main issues that make the problem of fracture annealing more complicated, one concerns the practicality of traditional annealing timescales in complex partially solid silicate systems, and the other concerns the development of melt driven overpressure within partially solidified rocks.

Thermal mechanical analysis shows that all test materials experience large volume expansion at the highest temperatures, a process which may counter the ability to anneal fractures. Each material will have undergone various phases changes, partial melting during heating and re-crystallisation during cooling. Therefore the bulk material may be quite different from the starting material upon cooling from the maximum hold temperature. It has not been possible to ascertain those precise petro-physical alterations, and it is beyond the scope of this study to do so. However, it is possible to note that thermal expansivity (α) upon heating and contraction upon cooling are within a similar α range. Therefore increased rates and size of acoustic emission hits during cooling are created as a result of the overall tensile stresses created by thermal contraction.

As well as a greater number and size of cracks distributed throughout the sample volume, some samples of IB indicate evidence of melt textures post heat-treatment (Figure. 17). Samples of IB held above 1130˚C exhibit macro fractures, up to 3 mm in width and > 1cm in length on the sample surface (Figure. 17) aligned predominantly along axis. Highly vesicular melt nodules emanate from many of the sample surface fractures, indicating that melt was generated and either filled previously formed fractures or played a role in generating new fractures. Melt over this temperature range is most likely formed due to phase changes in Fe oxides or a hydrous mineral such as amphibole. Melt-like textures can be observed in thin section and SEM analysis surrounding the much larger tension cracks (Figure 17). In this case the melt textures are shown as high contrast areas of spherical to elongated material randomly dispersed between a plagioclase and pyroxene matrix. Individual melt nodules which emanate from the basaltic samples at high temperature are highly vesicular, indicating significant viscous relaxation and degassing. It is possible to consider that the macro-fractures on the sample surface are a type of hydraulic fracture, formed primarily due to magma overpressure rupturing the clearly

solidified and brittle outer crust of the sample. If this is the case then those melt nodules essentially represent basaltic dykes. How and why they form in this instance remains poorly known, particularly why for instance parts on the inner sample can form melt whereas the sample surface remains with a solid brittle crust. The features may be related to excess pressure generated from melt volume expansion at high temperature. In all rocks types we find sharp increases in expansivity at highest temperatures, as shown in Fig. 4. However, melt nodules are not formed in either AP or NKD at the maximum hold temperatures. Instead of producing melt rupture features at the highest hold temperatures, samples of NKD behave plastically shortening in length and expanding in width substantially. Samples of AP exhibit macro evidence of melting along planes of pre-existing veins but no whole scale melting such as observed in the form of melt nodules in IB. More work is needed to understand the role of melt volume expansion in generating excess pressure. It is likely that more information is needed on the volatile content of each rock type, which is beyond the scope of this study.

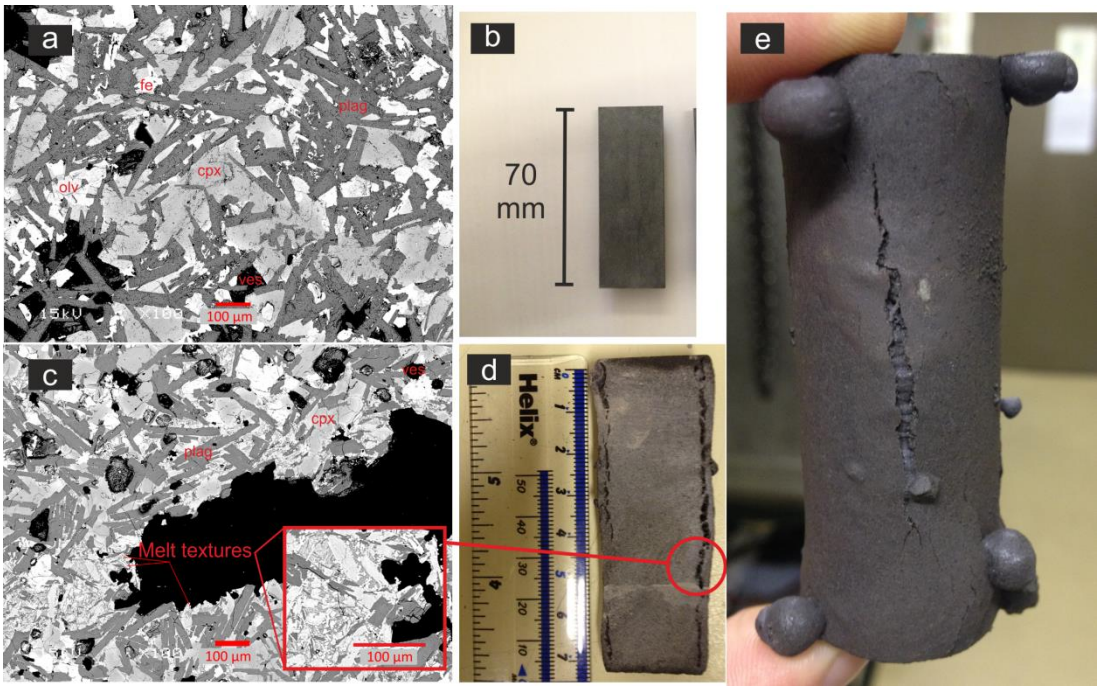

Figure 17. Macro-fracture development in a heat treated sample of IB. a) SEM image of non-heat treated IB and b) photograph of starting material. c) SEM image of a sample of IB heat treated to 1100˚C, d) corresponding photograph of end-member material. The axial tension fracture indicated by the red circle is shown in the SEM image on the left, micro-scale (<10 µm) melt textures observed under SEM

can be observed around the edge of those tension fractures. In many cases melt nodules are observed emanating from tension fractures on the surface of the sample cores, as shown in e).

Thermo-elastic stress can be simplified and calculated from the following relation (Timoshenko and Goodier, 1970):

$$\sigma_t = \frac{\alpha E \Delta T}{(1-\nu)} \qquad (1)$$

where σ_t is tensile thermal stress (MPa), E is Young's modulus (MPa), ΔT is the temperature difference (˚C) and ν is the Poisson's Ratio. Upon heating, stress is generated by thermal expansion, whereas upon cooling by negative thermal expansion or thermal contraction. The thermal expansion coefficient (α) of any material, which has previously been shown to be similar during heating or cooling (Fig. 4), is an important factor in controlling thermally generated cracks (Siratovich et al., 2015). In Figure 16 we show the thermal tensile stress σ_t generated in the bulk rock, an olivine and clinopyroxene mineral as a function of temperature difference. The models assume that each material has a Young's modulus of 10 GPa, and a Poisson's ratio of 0.25, the former is certainly a minimum value. This assumption may be erroneous and therefore provide misleading magnitudes of tensile stress but the model helps to show the relative contribution of each mineral phase in generating thermal stress. Upper and lower values of α were obtained from previous TMA measurements for each bulk rock and range from 15×10^{-6}/˚C to 25×10^{-6}/˚C. Upper and lower values of α for each mineral phase were taken from Clark (1966) and range from 30×10^{-6}/˚C to 35×10^{-6}/˚C for olivine and 25×10^{-6}/˚C to 30×10^{-6}/˚C for pyroxene. Other minerals tend to fall within the ranges previously given and so are not shown. We show that the first minerals that begin to produce stresses sufficient to generate tensile (mode I) fractures, assuming a tensile strength T_o of 0.5-6 MPa (Amadei and Stephansson, 1997), are olivine and pyroxene with a temperature difference of approximately 20˚C. As we previously state, the precise value of tensile stress should be treated with caution. All values of α for bulk rock are lower because the rocks contain pre-existing interval void space, i.e cracks and

pores. During heating, cooling or mechanical loading these voids can close or open internally so the effects measured are reduced. Single mineral crystals do not have any void space and therefore give higher values of α. This reason also indicates that the value of Young's modulus used is too low, although as previously stated we do not provide the precise range of failure, but indications as to which mineral phase contributes.

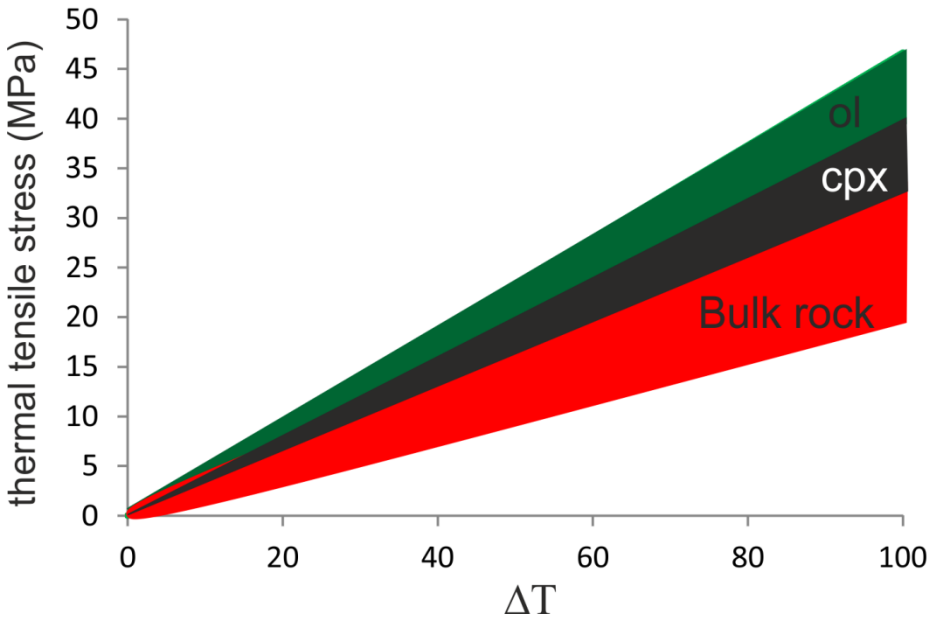

Figure 18. Tensile thermal stress σ_t as a function of temperature difference ΔT. Increasing thermal expansion co-efficient α and ΔT have the effect of increasing σ_t. As the mineral phases have larger values of α they generate the highest values of σ_t within the lowest temperature change.

Each rock type has a similar range of thermal expansion and contraction co-efficient values during both heating and cooling and therefore likely generates similar magnitudes of stress during both temperature cycles. We have found that more cracks are formed during cooling, which can be presumably explained as $T_o \approx 0.1\sigma_c$, where T_o is tensile strength and σ_c is compressive stress. Therefore, as is well known, it is easier for rocks to fail in tension (Gudmundsson, 2011).

4.3 Kaiser 'temperature-memory' effect test

The mechanical Kaiser 'stress memory' effect is a relatively well understood process (Heap et al., 2009; Lockner, 1993), where new cracking growth only once the

previous state of maximum stress has been exceeded. It is not clear of the effects or even existence of a Kaiser 'temperature-memory' effect, although some studies have shown such an effect to exist (Choi et al., 2005; Heap et al. 2013). In order to test ideas surrounding Kaiser 'temperature-memory' effects, we conducted a series of ramp and hold experiments. A sample of IB was heated at between 4°C/min and 8°C/min to maximum cyclic hold temperatures at 100°C intervals, which are then exceeded on the following cycle. Samples are cooled at a natural cooling rate (<4°C/min) to 300°C, and then re-heated once thermally equilibrated. Our tests proved inconclusive to the existence of a Kaiser 'temperature memory' effect in basalt, for the most part indicating that such an effect does not exist. In Figure 19 we show the various heating and cooling cycles performed, the resultant AE energy and corresponding *b* values. Acoustic emissions only commence during cycle 3, at a temperature exceedance of 600˚C, in the following cycle acoustic emissions commence around 650˚C and then again at around 800˚C, very few emissions are recorded above this temperature even though each cycle signifies the exceedance of the previous temperature. AE output is relatively low in all heating parts of each cycle. Interestingly, the maximum AE during cooling is produced only when highest hold temperature (900˚C) is reached, indicating that before this temperature cooling contraction does not form new cracks in basalt but simply reactivates pre-existing ones in a manner similar as during heating. This implies that some fracture annealing was completed before or around 900˚C in Icelandic Basalt. Whilst our data, namely the lack of cyclic AE, can be used to suggest the absence of a Kaiser 'temperature memory' effect, it is difficult to conclude the process does not occur by the absence of signals. However, consider that the Kaiser 'stress memory' effect is based upon the notion of stress loading and unloading, in the case of thermal stressing most of the unloading as we have shown occurs during cooling. Therefore any stress loading that is created upon heating and expansion is effectively reset during cooling contraction.

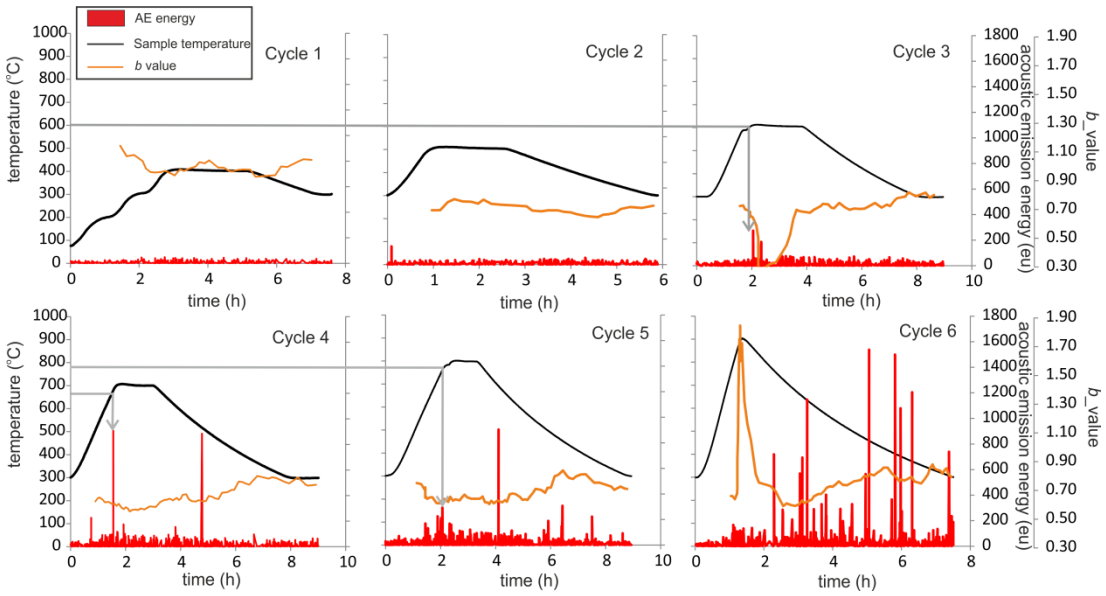

Figure 19. Kaiser 'temperature memory' effect test results. IB was heated at a rate of 4°C/min and held at various temperatures and then cooled at a natural rate to 300°C in five separate cycles, in the final cycle a ramp rate of 8˚C/min was used. Very low energy bursts of AE are indicated by grey lines during the heating cycles 3,4 and 5 but generally there is only substantial AE produced during cooling in cycles 4, 5 and 6, indicating very little evidence for a Kaiser 'temperature memory' effect.

5.0 Conclusions

Our findings suggest that heating and resultant thermal expansion in volcanic rocks acts to propagate, through small increments, previously existing micro-cracks or encourage new mixed mode micro-crack formation. Whereas cooling contraction encourages larger crack growth increments, and the formation of longer predominantly mode I micro-cracks.

- All the evidence suggests that there is far more cracking during cooling than during heating. This is reflected by contemporaneous acoustic emissions that show substantial increase in hit rate, hit amplitude and hit energy during cooling from high temperature. These increases in AE occur immediately on cooling but commonly peak around 800˚C in all rock types studied. Microstructural analysis of heat treated samples supports this view also.

- Evidence from ultrasonic wave velocities and microstructural observation suggests that thermal cracking is isotropically distributed. This is expected because thermal stresses are by nature isotropic.

- Although it has not been possible to directly observe or measure crack annealing at high temperature, all samples were held at a high enough temperature and for a long enough time to infer some cracks healed.

- We suggest that a previously reported Kaiser 'temperature-memory' effect does not exist. This seems a reasonable assumption as the mechanical Kaiser effect, of which the principles of the temperature memory effect are based upon, relies on unloading of mechanical stress. Whereas in temperature tests most cracking occurs during cooling, or the unloading cycle, therefore increased cracking during cooling overrides any stresses that are generated by each new heating cycle.

- Our findings our important for the study of cooling volcanic rocks in different settings. It is already well known that extrusive lava flows such as those on Mt Etna contain substantially more crack damage than intrusive rocks, as noted from lower P-wave velocities. It is clear now that most crack damage in volcanic rocks is generated during the cooling contraction cycle of emplacement.

6.0 References

Acocella, V., Gudmundsson, A., and Funiciello, R. 2000. Interaction and linkage of extension fractures and normal faults: examples from the rift zone of Iceland. *Journal of Structural Geology*, **22**, 1233-1246.

Aki, K., 1965. Maximum Likelihood Estimate of b in the Formula logN=a-bM and its Confidence Limits, **43**, 237–239.

Axelsson, G., Thorhallsson, S., Bjornsson, G., 2006. Stimulation of geothermal wells in basaltic rock in Iceland. *Enhanced geothermal innovation network for Europe Workshop*, Zurich Switzerland, **3**,

Amadei, B., and Stephenson, O., 1997. *Rock stress and its measurement*. Chapman and Hall, London.

Barton, M., and Huijsmans, J. P. (1986). Post-caldera dacites from the Santorini volcanic complex, Aegean Sea, Greece: an example of the eruption of lavas of near-constant composition over a 2,200 year period. *Contributions to Mineralogy and Petrology*, **94**, 472-495.

Brudy, M. and Zoback, M.., 1999. Drilling-induced tensile wall-fractures: implications for determination of in-situ stress orientation and magnitude. *International Journal of Rock Mechanics and Mining Sciences*, **36**, 191–215.

Cabrera, A., R. F. Weinberg, H. M. N. Wright, S. Zlotnik, and R. A. F.Cas 2011, Melt fracturing and healing: A mechanism for degassing and origin of silicic obsidian, *Geology*, **39**, 67–70.

Choi, N.K., Kim, T.W., Rhee, K.Y. 2005 Kaiser effects in acoustic emission from composites during thermal cyclic-loading. *NDT&E International.* **38**, 268-274

Chouet, B.A. 1996 Long-period volcano seismicity: its source and use in eruption forecasting. *Nature*, **380**, 309-316

Clark, Sydney Procter, ed. 1966 *Handbook of physical constants*. 97. Geological Society of America.

Cooper, H.W and Simmons, G. 1977. The effect of cracks on the thermal expansion of rocks. *Earth and Planetary science letters.* **36**, 404-412

Cox, S.J.D., and Meredith, P.G., 1993. Microcrack formation and material softening in rock measured by monitoring acoustic emissions. *Int. J. Rock Mech. Min. Sci. Geomech. Abstr*. **30**, 11–24.

David, C., Menendez, B., and Darot, M. 1999. Influence of stress-induced and thermal cracking on physical properties and microstructure of La Peyratte granite. *International Journal of Rock Mechanics and Mining Sciences*, **36**, 433-448.

Dingwell, D.B. and Webb, S.L., 1989. Structural relaxation in silicate melts and non-Newtonian melt rheology in geologic processes. *Physics and Chemistry of Minerals*, **16**, 508–516.

Fredrich, J. T., and Wong, T. 1986. Micromechanics of thermally induced cracking in three crustal rocks. *Journal of Geophysical research*, **91**.

Giordano, D., Russell, J.K., Dingwell, D.B., 2008. Viscosity of magmatic liquids: A model. *Earth Planet. Sci. Lett*. **271**, 123–134.

Gudmundsson, A. 1998, Formation and development of normal-fault calderas and the initiation of large explosive eruptions, *Bulletin of Volcanology*, **60**, 160–170.

Gudmundsson, A. 2011. *Rock fractures in geologic processes*. Cambridge university press, Cambridge.

Heap, M.J., Vinciguerra, S. & Meredith, P.G., 2009. The evolution of elastic moduli with increasing crack damage during cyclic stressing of a basalt from Mt. Etna volcano. *Tectonophysics*, **471**, 153–160

Heap, M. J., Faulkner, D. R., Meredith, P. G., & Vinciguerra, S. 2010. Elastic moduli evolution and accompanying stress changes with increasing crack damage: implications for stress changes around fault zones and volcanoes during deformation. *Geophysical Journal International*, **183**, 225–236.

Heap, M.J., Lavallée, Y., Laumann, A., Hess, K.U., Meredith, P.G., Dingwell, D.B., Huismann, S., Weise, F., 2013. The influence of thermal-stressing (up to 1000 °c) on the physical, mechanical, and chemical properties of siliceous-aggregate, high-strength concrete. *Constr. Build. Mater*. **42**, 248–265.

Heap, M. J., Silvio Mollo, Sergio Vinciguerra, Yan Lavallée, K-U. Hess, Donald B. Dingwell, Patrick Baud, and Gianluca Iezzi. 2013b Thermal weakening of the carbonate basement under Mt. Etna volcano (Italy): implications for volcano instability. *Journal of volcanology and geothermal research* **250**, 42-60.

Hetényi, G., Taisne, B., Garel, F., Médard, É., Bosshard, S., Mattsson, H.B., 2012. Scales of columnar jointing in igneous rocks: Field measurements and controlling factors. *Bull. Volcanol*. **74**, 457–482.

Julian, B.R., Foulger, G.R., Monastero, F.C., Bjornstad, S., 2010. Imaging hydraulic fractures in a geothermal reservoir. *Geophys. Res. Lett*. **37**, 1–5.

Kitao, K., Aiki, K., Watanabe, H., Wakita, K., 1990. Cold-water well stimulation experiments in the Sumikawa Geotheral field, Japan. *Geotherm. Resourc. Counc. Trans* **14**, 1219–1224.

Kranz, R. L. 1983. Microcracks in rocks: A review. *Tectonophysics*, **100**, 449–480.

Lockner, D. 1993. The role of acoustic emission in the study of rock fracture. *International journal of rock mechanics.* **30**, 833-899

Meredith, P. G., Knight, K. S., Boon, S. A., & Wood, I. G. 2001. The microscopic origin of thermal cracking in rocks: An investigation by simultaneous time-of-flight neutron diffraction and acoustic emission monitoring. *Geophysical research letters*, **28**, 2105-2108.

Miller, A D., Julian, B.R. & Foulger, G.R., 1998. Three-dimensional seismic structure and moment tensors of non-double-couple earthquakes at the Hengill-Grensdalur volcanic complex, Iceland. *Geophysical Journal International*, **133**, 309–325.

Mitchell, T.M. and Faulkner, D.R., 2008. Experimental measurements of permeability evolution during triaxial compression of initially intact crystalline rocks and implications for fluid flow in fault zones. *Journal of Geophysical Research: Solid Earth*, **113**, pp.1–16.

Mollo, S., Heap, M.J., Dingwell, D.B., Hess, K.U., Iezzi, G., Masotta, M., Scarlato, P., Vinciguerra, S., 2013. Decarbonation and thermal microcracking under magmatic P-T-fco2 conditions: The role of skarn substrata in promoting volcanic instability. *Geophys. J. Int.* **195**, 369–380.

Pyle, D.M. and Elliott, J.R., 2006. Quantitative morphology, recent evolution, and future activity of the Kameni Islands volcano, Santorini, Greece. *Geosphere*, **2**, 253–268.

Richter, D and Simmons, G. 1974. Thermal expansion behaviour of Igneous Rocks. *International journal of rock mechanics and mineral science,* **15**. 145-148

Simmons, G., and Cooper, H. W. 1978. Three Igneous Rocks. *International Journal of Rock Mechanics, Mineral Science and Geomechanics*, **15**, 145–148.

Siratovich, P. A., von Aulock, F.W., Lavallée, Y., Cole, J.W., Kennedy, B.M., Villeneuve, M.C., 2015. Thermoelastic properties of the Rotokawa Andesite: A geothermal reservoir constraint. *J. Volcanol. Geotherm. Res*. **301**, 1–13.

Tarasovs, S. and Ghassemi, A., 2012. On the Role of Thermal Stress in Reservoir Stimulation. *Thirty-Seventh Workshop on Geothermal Reservoir Engineering*.

Timoshenko, S.P and Goodier, A, 1970. *Theory of Elasticity*. 3rd ed. McGraw-Hill, New York, NY.

Turner, J.S., Huppert, H.E., Sparks, S.J., 1983. An experimental investigation of volatile exsolution in evolving magma chambers. *J. Volcanol. Geotherm. Res.* **16**, 263-277

Tuffen, H., and D. B. Dingwell. 2005, Fault textures in volcanic conduits: Evidence for seismic trigger mechanisms during silicic eruptions, *Bull. Volcanol.*, **67**, 370–387

Tuffen, H., D. B. Dingwell, and H. Pinkerton. 2003, Repeated fracture and healing of silicic magma generate flow banding and earthquakes?, *Geology*, **31**, 1089–1092.

Vasseur, J., F. B. Wadsworth, Y.,Lavallee, K.-U. Hess, and D. B. Dingwell. 2013, Volcanic sintering: Timescales of viscous densification and strength recovery, *Geophys. Res. Lett.*, **40**, 5658–5664

Vinciguerra, S., Trovato, C., Meredith, P.G. and Benson, P.M. 2005, Relating seismic velocities , thermal cracking and permeability in Mt . Etna and Iceland

basalts, *International Journal of Rock Mechanics and Mineralogical Science* **42**,900–910.

Chapter 6

Journal of Volcanology and Geothermal research

Surface displacements resulting from magma-chamber roof subsidence, with application to the 2014 Bardarbunga-Holuhraun episode

Browning, J and Gudmundsson, A

Journal of Volcanology and Geothermal Research, 2015, **308**, 82-98

DOI 10.1016/j.jvolgeores.2015.10.015

Statement of contribution

Original idea conceived by both authors was inspired by events at Bardarbunga in 2014 following modelling work of JB

All numerical models and figures created by JB

Model interpretation and comparisons by JB

1st draft of manuscript by JB

Revisions and subsequent drafts with input from co-author

Significant input from co-author discussion and interpretation to Bardarbunga episode

Journal of Volcanology and Geothermal Research 308 (2015) 82–98

Contents lists available at ScienceDirect

Journal of Volcanology and Geothermal Research

journal homepage: www.elsevier.com/locate/jvolgeores

Surface displacements resulting from magma-chamber roof subsidence, with application to the 2014–2015 Bardarbunga–Holuhraun volcanotectonic episode in Iceland

John Browning *, Agust Gudmundsson

Royal Holloway University of London, Department of Earth Sciences, Egham TW20 0EX, United Kingdom

ARTICLE INFO

Article history:
Received 22 March 2015
Accepted 7 October 2015
Available online 19 October 2015

Keywords:
Surface deformation
Surface stresses
Magma chambers
Caldera collapse
Bardarbunga–Holuhraun

ABSTRACT

The conditions which lead to caldera collapse are still poorly constrained. As there have only been four, possibly five, well-documented caldera forming events in the past century, the geodetic signals produced during chamber roof subsidence, or chamber volume reduction (shrinkage) in general, are not well documented or understood. In particular, when two or more geodetic sources are operating and providing signals at the same time, it is important to be able to estimate the likely contribution of each. Simultaneous activities of different geodetic sources are common and include pressure changes in magma chambers/reservoirs occurring at the same time as dyke emplacement. Here we present results from numerical models designed to simulate the subsidence of a magma-chamber roof, either directly (chamber shrinkage) or through ring-fault displacement, and the induced surface deformation and crustal stresses. We consider chamber depths at 3 km, 5 km, and 7 km below the crustal surface, using both non-layered (isotropic) and layered (anisotropic) crustal models. We also model the effects of a caldera lake and of a thick ice cover (ice sheet) on top of the caldera. The results suggest that magma-chamber roof subsidences between 20 m and 100 m generate large (tens of centimetres) vertical and, in particular, horizontal displacements at the surfaces of the ice and the crust out to distances of up to tens of kilometres from the caldera/chamber centre. Crustal layering tends to reduce, but increasing chamber depth to enlarge, the horizontal and vertical surface displacements. Applying the results to the ice subsidence in the Bardarbunga Caldera during the 2014–2015 Bardarbunga–Holuhraun volcanotectonic episode indicates that the modelled ice displacements are less than those geodetically measured. Also, the geodetically measured crustal displacements are less than expected for a 60 m chamber-roof subsidence. The modelling results thus suggest that only part of the ice subsidence is due to chamber-roof subsidence, the other part being related to flow in and down-bending of the ice. We show that such a flow is likely within the caldera as a result of the stress induced by the 45-km-long regional dyke emplaced (primarily in vertical magma flow) during the episode. This conclusion is further supported by the model results suggesting that the ring-fault (piston-like) displacements must have been much less than the total 60 m ice subsidence, or else faults with tens-of-metres displacements would have cut through the ice (these are not observed). We suggest that the ring-fault subsidence was triggered by small doming of the volcanic field and system hosting the Bardarbunga Caldera and that this doming occurred as a result of magma inflow and pressure increase in a deep-seated reservoir. The doming is confirmed by GPS measurements and supported by the seismicity results. The magmatic pressure increase in the reservoir was, in terms of the present model, responsible for the regional dyke emplacement, the Holuhraun eruption, and part of the stress concentration around, and displacement of, the Bardarbunga Caldera.

1. Introduction

Caldera collapses are a common occurrence in the evolution of major volcanic systems (Fig. 1). While many of these events are catastrophic and associated with the expulsion of large volumes of magma and ignimbrite formation (Druitt and Sparks, 1984), perhaps the more prevalent situation involves relatively small or no magma expulsion (MacDonald, 1965). Well-documented caldera collapses occurred in 2000 and 2007 at the summits of Miyakejima (Geshi et al., 2002) and Piton de la Fournaise (Peltier et al., 2008). These events have been referred to as periodic (Geshi et al., 2002; Michon et al., 2011) or slow collapses. These terms relate to the total caldera growth occurring over periods of perhaps as much as one month (Geshi et al., 2002). Much of the longer-period caldera growth was due to mass wasting, a process which likely also shaped lake Öskjuvatn (Iceland) following the 1875 caldera forming eruption (Hartley and Thordarsson, 2012). A mechanism of 'slow caldera collapse' has also been suggested as an

* Corresponding author.
E-mail address: john.browning.2012@live.rhul.ac.uk (J. Browning).

http://dx.doi.org/10.1016/j.jvolgeores.2015.10.015
0377-0273/

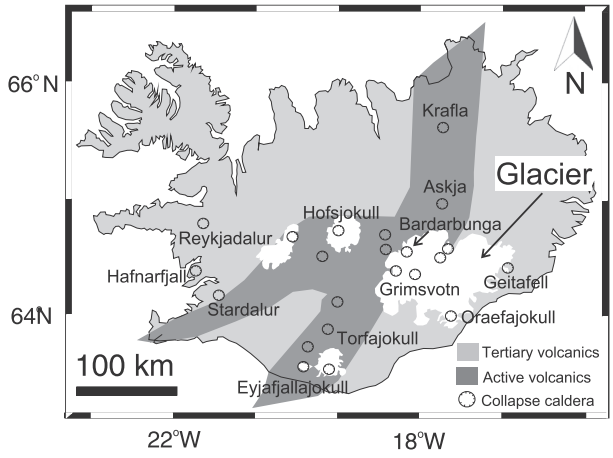

Fig. 1. Simplified geological map of Iceland, showing the main active and inactive volcanoes that contain collapse calderas. Many of these calderas are fully or in part sub-glacial, that is located underneath a body of ice. Glacier outlines are highlighted in this map as white areas.

explanation for the measured ice subsidence during the 2014–2015 Bardarbunga episode (Riel et al., 2015; Sigmundsson et al., 2015).

The timescale of deformation at calderas ranges from events of hours to days (Stix and Kobayashi, 2008) to longer events taking months or years (Hartley and Thordarsson, 2012) as well as cyclic inflation and deflation over tens, hundreds and probably thousands of years (Phillipson et al., 2013). Collapse may occur along pre-existing structures, such as regional faults or earlier-formed ring-faults (Fig. 2), but the shape and size of collapse are significantly influenced by the depth, size, and shape of an underlying magma chamber (Cole et al., 2005; Acocella, 2007).

The movement of large crustal segments, as occurs during the formation or reactivation of collapse calderas, must produce significant crustal deformation. However, the magnitude and type of the deformation are poorly constrained. This is partly due to the lack of geophysical measurements syn-collapse, the exceptions being Piton de la Fournaise (Peltier et al., 2008) and Miyakejima (Geshi et al., 2002), although measurements at these locations were predominantly limited to the central edifice and vent area. Therefore, understanding the far-field effects of crustal subsidence due to caldera formation or chamber shrinkage is useful for constraining geophysical observations at volcanoes where the summit region cannot be observed, either due to cloud cover, inaccessibility, or ice cover. The last point is salient because many, if not most, of the central volcanoes in Iceland are ice covered (Figs. 1 and 3). In addition, understanding the timing and development of collapse is important for hazard and risk estimation, partly because many calderas are associated with the formation of ring-dikes (Fig. 2) (Browning and Gudmundsson, 2015) and give rise to large eruptions (Gudmundsson, 2015).

When magma leaves or flows out of a chamber/reservoir during an eruption and/or dyke injection, the volume of the chamber/reservoir decreases. The same may happen during caldera collapse (Gudmundsson, 2014, 2015). The volume decrease or shrinkage affects the crustal segment hosting the chamber, primarily through changes in stress and associated displacement and strain. The effects of chamber shrinkage are most easily detected through surface deformation. The aim of this work is to understand better (1) how the surface deformation associated with chamber shrinkage, in particular during roof subsidence, is reflected in horizontal and vertical displacements (and stresses) at the surface of the hosting crustal segment (as well as at the surface of the ice cover), (2) how the surface deformation changes with distance from the chamber, and (3) how much surface deformation can feasibly be accommodated in an elastic crust before ring-faults will form or reactivate, resulting in a normal caldera collapse. The results, while completely general, are here applied to the 2014–15 Bardarbunga–Holuhraun volcano-tectonic episode.

2. Stress fields controlling caldera formation

Many analogue models of caldera collapse indicate initial ground surface slumping (Lavallée et al., 2004) followed by the formation of peripheral faults that ultimately control the majority of vertical subsidence (Acocella et al., 2000; Kennedy et al., 2004; Holohan et al., 2005; Geyer et al., 2006; Acocella, 2007). As many of these models use dry sand or other similar granular materials to simulate the crust, it is often impossible to determine surface displacements far from the deformation centre. This follows partly because a dry sand pack lacks cohesion (which corresponds to rock tensile strength) and normally does not transmit tensile stresses as solid linear elastic material. By contrast, the crust behaves approximately as linear elastic solid material with a non-zero tensile strength. More specifically, the range of in-situ tensile strength of solid rocks is 0.5–9 MPa, the most common values being 2–4 MPa (Gudmundsson, 2011). Numerical models which simulate an elastic crustal segment hosting a magma chamber therefore provide a reasonable approximation of surface ground deformation (De Natale and Pingue, 1993; Hickey and Gottsmann, 2014).

In order for a caldera to form, or for slip to occur on a pre-existing ring-fault, there must be suitable state of stress within the crust. The initiation of sub-vertical, normal ring-faults depends on three stress field conditions which must be satisfied simultaneously (Gudmundsson, 1998; Folch and Marti, 2004).

(1) The minimum value of σ_3, the maximum tensile (minimum compressive) principal stress, must be at the surface.
(2) The maximum value of $(\sigma_1-\sigma_3)/2$, the shear stress, must occur above the outer margins or lateral edges of the magma chamber, that is, in a zone extending from the lateral edge of the chamber to the surface and within which the ring-fault forms (or slips).
(3) The maximum tensile stress at the surface must peak at a radial distance approximately equal to the lateral dimension, the diameter, of the magma chamber.

These stress conditions are most likely to be induced by a double magma chamber, where the shallow chamber is sill-like and (1) the crustal segment hosting the double chamber is subject to horizontal extension, or (2) the deeper chamber, a large reservoir, is subject to slight increase in magma pressure so as to dome the crustal segment hosting the shallower chamber (Gudmundsson, 1998, 2007) (Fig. 3). Other predominant collapse trigger mechanisms (Marti et al., 2009) include (a) internal magma chamber overpressures initiating roof and surface fractures (e.g., Gudmundsson, 1998, 2007; Gray and Monaghan, 2004; Gregg et al., 2012) and (b) internal magma chamber underpressure following chamber rupture (e.g., Roche et al., 2000; Folch and Martí, 2004; Geyer et al., 2006; Kusumoto and Gudmundsson, 2009; Holohan et al., 2011). Here we consider in detail a situation more compatible with the second of these two mechanisms, namely an inferred underpressure in the shallow chamber, particularly in view of the suggestions that the ice subsidence during the Bardarbunga–Holuhraun episode being related to pressure decrease in the chamber (e.g., Riel et al., 2015; Sigmundsson et al., 2015).

As indicated above, shallow chambers within crustal segments undergoing slight doming, regional extension, or both are the ones most likely to generate stress concentrations favourable for ring-fault formation (Gudmundsson, 2007). Prime examples of this type of regional settings are the volcanoes of the Eastern Volcanic Zone (EVZ) in Iceland (Gudmundsson, 2007), the Kenyan Rift valley (Acocella, 2007) and the Taupo Volcanic Zone (TVZ) in New Zealand (Cole, 1990). Fig. 4 shows the stresses around a sill-like magma chamber with negative internal pressure, an underpressure, of 5 MPa (e.g., Folch and

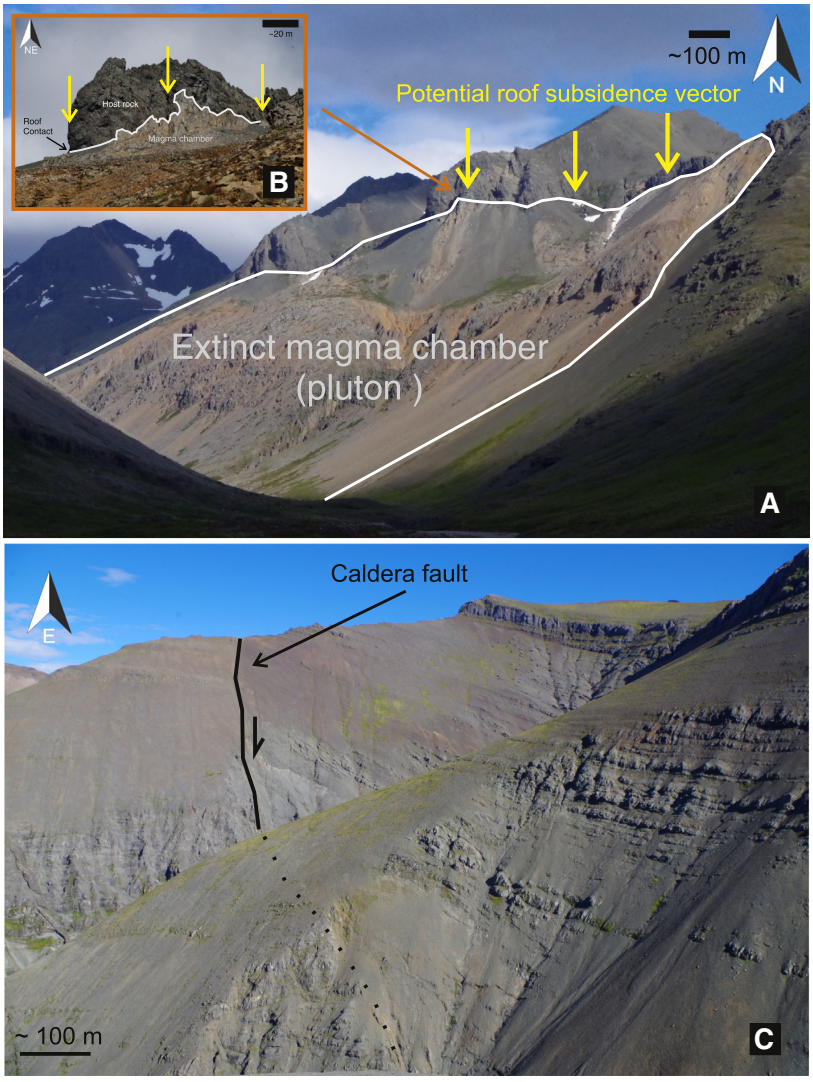

Fig. 2. Exposed sections of extinct central volcanoes in the Tertiary volcanic regions of East (A, B) and West (C) Iceland. (A, B) An extinct – and now well exposed – granophyre magma chamber at Slaufrudalur in East Iceland. The exposure shows the contact (inset) between the granophyre plutonic rocks at the base of the picture and the basaltic lava pile at the top of the picture, into which the chamber was originally emplaced. Shallow chambers such as this one commonly give rise to a vertical collapse, culminating in the formation of a surface caldera. Although no evidence exists for a collapse at Slaufrudalur, many eroded central volcanoes in Iceland show clear ring-faults, perhaps the best example being (C) Hafnarfjall in West Iceland.

Marti, 2004), located at 5 km depth in a 40-km wide and 20-km thick crustal segment but simultaneously subject to excess (doming) pressure of 10 MPa from a deep-seated reservoir. In this example, the doming pressure largely controls the stress/displacement fields and the maximum tensile stress concentrates at the free surface in a zone above the lateral margins or edge of the shallow sill-like chamber. In addition, the maximum shear stress concentrates at the lateral margins of the magma chamber at depth. These conditions are ideal for the formation of, initially, tension fractures at the surface that propagate down towards the chamber and change at a critical depth – normally less than 0.5 km (Gudmundsson, 2011) – to normal faults (Gudmundsson, 1998; Gray and Monaghan, 2004). If the tensile stresses are higher at the magma chamber margin than at the free surface above the margin, then a ring-dyke would be more likely to form (Gudmundsson, 2007).

When a caldera forms, it is common for the depression to be filled with water, generating in a caldera lake. Well-known examples include Crater Lake, USA (Williams, 1941) and Askja, Iceland (Hartley and Thordarson, 2012) amongst many others (Fig. 3). The occurrence of sub-glacial lakes within calderas has also been noted, such as in the Grimsvötn volcanic system in Iceland (Gudmundsson et al., 1997). A caldera lake is important because the solid contact with water gives rise to a free surface, that is, a surface of zero shear stress. Therefore, a caldera lake will reduce the mechanical coupling between bedrock and glacier which in-turn will influence stresses and displacements within the ice.

3. Model setup

The finite element program Comsol was used to investigate the crustal and ice-sheet response to the vertical displacement of the magma-chamber roof (www.comsol.com; cf. Zienkiewicz, 1979; Deb, 2006). In these models the magma chamber is modelled as a cavity (Gudmundsson, 2011; Grosfils et al., 2015). In the first model the

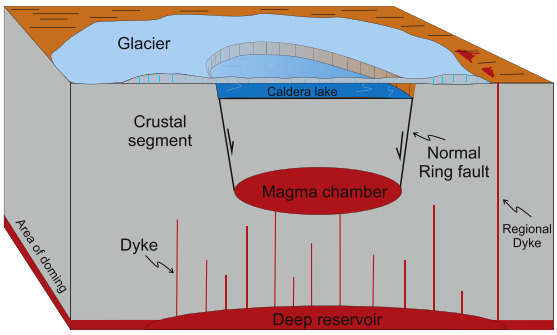

Fig. 3. Sub-glacial caldera occupied by a caldera lake. Here the ring-fault is a normal fault, as is inferred for nearly all collapse calderas in Iceland (Bjarnason, 2014), including the Bardarbunga Caldera (Riel et al., 2015). The shallow chamber is fed by a much larger deep-seated reservoir that undergoes periods of doming and inflation when receiving new input of melt or magma. In this example the area of doming is much larger than the caldera. Modified after Gudmundsson (2007).

chamber is residing within a homogeneous, isotropic elastic half-space with a Young's modulus (E) of 40 GPa and Poisson's ratio (ν) of 0.25 (Fig. 4). In this model, the focus is on the typical conditions for ring-fault formation or reactivation in rift-zone environment. Thus, the loading condition is a combination of doming excess pressure of 10 MPa in the deep-seated reservoir and a horizontal tension of 5 MPa. The results are in agreement with earlier results suggesting that doming, horizontal tension, or both are loading conditions that favour the concentration of shear stress in a zone above the lateral ends or edges of the shallow chamber (Fig. 4C). Furthermore, the induced tensile stress peaks where these zones meet the free surface (Fig. 4D). The zones of high shear stress are thus likely to develop ring-faults, for the given loading conditions.

Horizontal tension, however, will not be much discussed here. In the later part of the paper, we discuss the effects of doming by the deep-seated reservoir. The main focus here is on the effects of shallow-chamber roof subsidence on the associated surface deformation and stresses. The roof (upper boundary) of the chamber is supposed to subside, so that, the loading is prescribed negative vertical (z-axis) displacement. The vertical roof displacements tested in the models range from 20 m to 100 m. To make the models realistic, the crustal segment hosting the chamber is also modelled as anisotropic, that is, layered (Fig. 5). In the anisotropic models, directly above the chamber there are six layers, each with thickness t and of varying stiffness (Young's modulus, E) but constant density ($\rho = 2500$ kg/m^3) and constant Poisson's ratio ($\nu = 0.25$), simulating an anisotropic crust. The number of layers used in the models is arbitrary as most volcanic systems are presumably made of hundreds of layers, while many of these may group into larger units of internally similar mechanical properties. Here we choose to include six layers or units simply to investigate the effects of crustal anisotropy on the local stresses and displacements. The uppermost layer of thickness ($2\,t$) represents an elastic body of ice;

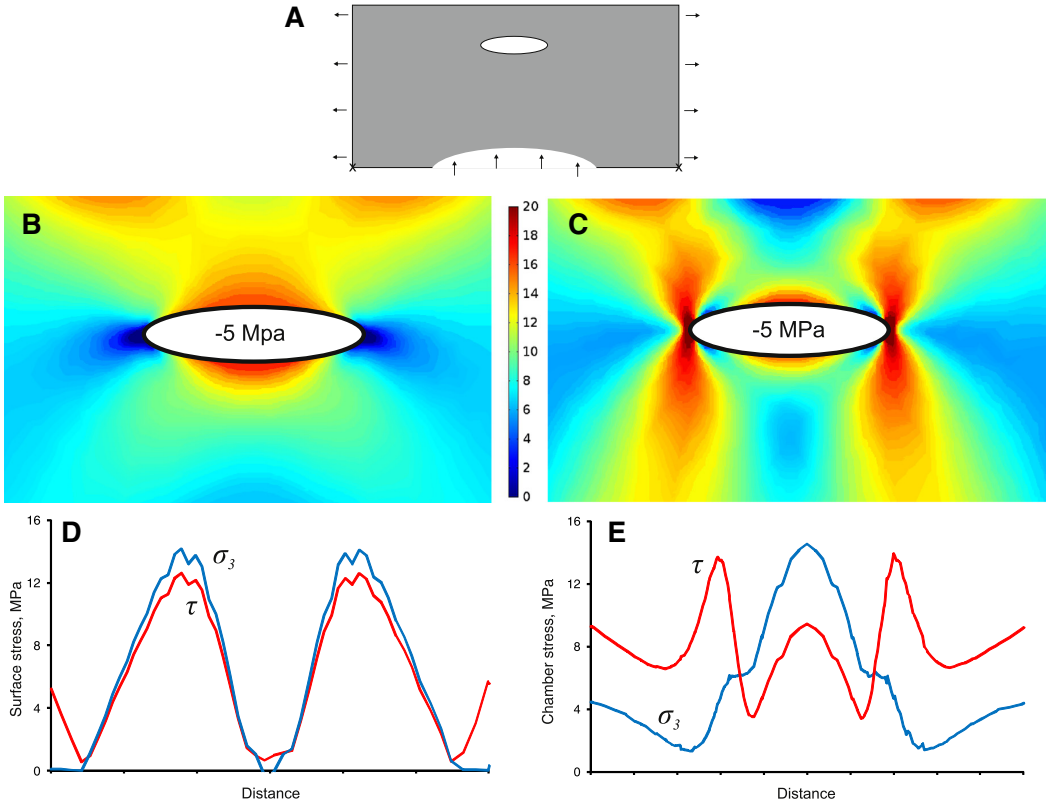

Fig. 4. Stress fields favouring the formation of caldera ring-faults. The stresses shown are generated around a sill-like magma chamber, 8 km wide and 2 km thick, located at 5 km depth in a 20-km-thick and 40-km-wide crustal segment subject to horizontal tensile stress of 5 MPa and doming stress (pressure) from a deep-seated reservoir (at the base of the model) of 10 MPa. Chamber excess pressure is negative (underpressure) 5 MPa and it is hosted within a homogeneous, isotropic crustal segment of stiffness (Young's modulus) 40 GPa and Poisson's ratio of 0.25 (see Table 1). A, model configuration; B, magnitudes of the maximum principal tensile stress σ_3; C, magnitudes of the von Mises shear stress τ; D, maximum principal tensile stress σ_3, and von Mises shear τ stress at Earth's free surface; E, maximum principal tensile stress σ_3, and von Mises shear τ stress around the magma-chamber boundary. Figure C shows clearly that the shear stress concentrates in subvertical zones above the lateral ends of the chamber, thereby encouraging the formation of a subvertical ring-fault.

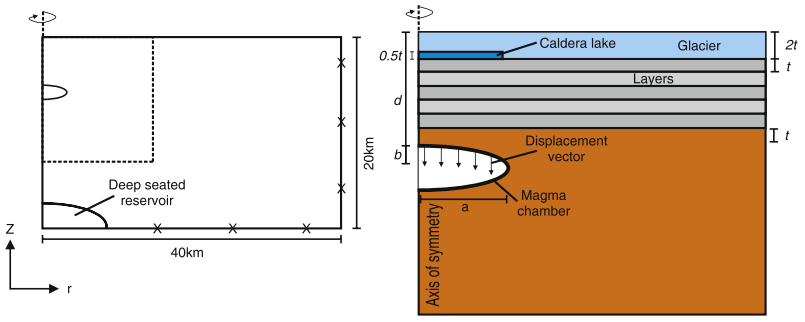

Fig. 5. Sketch of the model setup showing the geometric relationship between a shallow magma chamber within a crustal segment composed of six layers (including the glacier). In some subsequent models (referred to as layered models), the 5 layers have different stiffnesses (Young's moduli), whereas in other models (referred to as non-layered models) all the 6 layers have the same Young's modulus and thus function as a single, thick layer. At the surface of the crust, there is a caldera lake, providing a free surface (surface free of shear stress). In addition, a glacier is on top of the lake and the surrounding crust, the top of the glacial layer is another free surface. All models shown are symmetric with rotation around the z-axis (axi-symmetric), the base and vertical margins are fixed (i.e. experience zero displacement). The magma chamber roof is subject to a prescribed vertical displacement between 20 and 100 m. In addition to the shallow magma chamber, several models include a deep-seated reservoir. (Modified after Folch and Marfi, 2004, and Kinvig et al., 2009).

namely a glacier, with a Young's modulus of 4 GPa. We use ice as the top-most layer primarily because many volcanoes are located beneath ice sheets, particularly in Iceland, including recently erupting volcanoes in Iceland such as Bardarbunga (Gudmundsson et al., 2014; Riel et al., 2015; Sigmundsson et al., 2015), Grimsvotn (Gudmundsson et al., 1997), and Eyjafjallajökull (Gudmundsson et al., 2012).

For the purpose of this study we model the ice as a brittle layer which behaves elastically through its entire thickness (Geyer and Bindeman, 2011). Other studies assume that only certain parts of an ice layer behave elastically, with the remaining parts behaving as ductile – using, for example Glen's flow law (e.g. Paterson, 1994; Gudmundsson et al., 2004; Schulson and Duval, 2009). Ice behaves elastically at high strain rates and comparatively low stresses or pressures (Schulson and Duval, 2009). The brittle deformation of ice is exemplified in the formation or fractures, crevasses, as are common during subsidence associated with volcanism (Gudmundsson et al., 1997, 2004). The assumption of linear elastic behaviour of the ice is thus reasonable and does not significantly affect the calculated displacements and stresses in the crust (the surface rock) itself outside the ice sheet. The crustal layering or anisotropy is of much greater significance than the assumed elastic behaviour of the ice as regards surface deformation (e.g. Manconi et al., 2007; Geyer and Gottsmann, 2010). The mechanical properties of ice are variable (Schulson and Duval, 2009). For example, typical laboratory values of stiffness or Young's modulus (E) can range from as high as 15 GPa (Gammon et al., 1983; Schulson and Duval, 2009) to more commonly 8–9 GPa, depending on temperature, and grain size and orientation (Parameswaran, 1987). The stiffness values are only moderately anisotropic (Schulson and Duval, 2009). These are dynamic values, however. Static values are more difficult to measure because of time-dependent deformation in ice. Estimated typical static or field values for Young's modulus of ice are around 1 GPa (Schulson and Duval, 2009). Poisson's ratios for ice are commonly between 0.2 and 0.4 (Schulson and Duval, 2009). In the modelling we use a Young's modulus somewhere between typical field and (dynamic) laboratory values, or 4 GPa. Also, we use a Poisson's ratio of 0.3 and a density of 920 kg m^{-3}. The general crustal and ice parameters used in the numerical models are given in Table 1.

In all models we assume a strong coupling between glacier and bedrock or crustal surface (except at the location of the caldera lake) using the same assumptions as Geyer and Bindeman (2011). More specifically, if the coupling between the ice and the bedrock is of sufficient strength, stresses within the crust are transmitted to the ice. Then the ice can be considered to act mechanically as part of the layered crust. The other mechanical situation is where the ice and crust are weakly bonded, in which case slip may occur along the weak boundary and stresses would not be transferred from the bedrock surface to the ice. We consider one such scenario where the ice and crust are not directly coupled, designed to represent a caldera lake. The lake depth is $0.5\ t$ (half the thickness of a typical crustal layer) and its width is a (the radius of the magma chamber/caldera). The lake is modelled as a free surface at all edges. This follows because the contact between water and the bedrock below as well as the contact with the ice above are surfaces of zero shear stress. As previously stated, many if not most calderas develop a caldera lake at some point, particularly those calderas formed under ice (Fritz et al., 1990).

If the stresses within a volcano are suitable for the formation of a caldera then displacement would be likely to occur along a bounding ring-fault (circumferential fault). In order to incorporate the mechanical response to ring-faulting we include in one of the models a soft (low-Young's modulus) vertical zone directly above the magma-chamber edge. This zone is supposed to represent a typical caldera fault, a ring-fault (without a ring-dyke) consisting of a highly fractured and mechanically soft damage zone with respect to the host rock (Browning and Gudmundsson, 2015). The magnitudes of the vertical and horizontal displacements depend on the magma chamber size – in this case the chamber radius a is 4 km (its horizontal diameter thus 8 km). All models assume uniform vertical displacement of the roof, that is, a piston-like subsidence irrespective of the absence (as in most models) or the presence (as in one model) of the ring-fault itself.

4. Comparison of numerical and analytical solutions

Periods of unrest are often characterised by surface inflation or deflation of the volcano. This deformation signal is commonly explained in terms of a magmatic excess pressure change (p_e) in the associated magma chamber of radius a and depth d below the surface, modelled as a nucleus of strain. In volcanology, such a nucleus is normally referred to as the "Mogi model" (Mogi, 1958; Fig. 6), although the nucleus-of-strain solution with application to volcanoes was initially derived by Anderson (1936). Mogi's analytical solution can be replicated using the finite element method (e.g., Masterlark, 2007; Hickey and Gottsmann, 2014). If a Poisson's ratio of 0.25 is assumed for the elastic

Table 1
Model parameters.

Material	Young's modulus (E) (GPa)	Density (ρ) (kg/m^3)	Poisson's ratio (ν)
Crust	40	2500	0.25
Glacial ice	4	920	0.3
Hyaloclastite	1	2500	0.25
Ring fault	0.1	2500	0.25

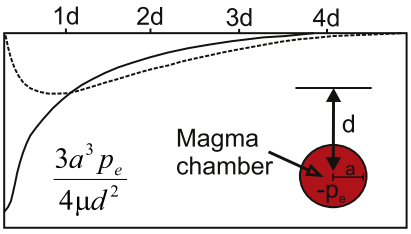

Fig. 6. Point-pressure source, a nucleus of strain, referred to as the Mogi model in volcanology. Such a model is commonly used for explaining surface deformation above an assumed spherical magma chamber. The solid curve gives the vertical surface displacement, which is maximum above the chamber centre. The dashed curve gives the horizontal surface displacements. The magma chamber, with radius (a) is subject to negative excess pressure, that is, underpressure ($-p_e$) and located at a depth (d) below the surface. (cf. Eqs. 1–3).

half-space – generally a reasonable assumption – then the basic equations of the Mogi (1958) can be presented as follows:

$$u_z = \frac{3p_e a^3 d}{4\mu\left(r^2 + d^2\right)^{3/2}} \tag{1}$$

$$u_r = \frac{3p_e a^3 r}{4\mu\left(r^2 + d^2\right)^{3/2}} \tag{2}$$

where u_z and u_r are the vertical and horizontal (radial) displacements at the surface above the magma chamber, respectively. Also, p_e is the magmatic excess pressure in the chamber, a is the radius of the chamber, μ is shear modulus, d is the depth to the centre of the chamber below the surface of the earth (Fig. 6), and r is the radial coordinate at the surface. At the point right about the centre of the magma chamber, we have $r = 0$, and the maximum vertical displacement u_z becomes (Fig. 6):

$$u_z = \frac{3p_e a^3}{4\mu d^2}. \tag{3}$$

Magmatic underpressure, that is, pressure less than lithostatic, is often regarded as the condition for ring-fault and ring-dyke formation. In fact, an underpressure or contracting nucleus-of-strain was Anderson (1936) original model for the formation of ring-dykes and the connection with the Mogi model is straightforward (cf. Kusumoto and Gudmundsson, 2009).

In Fig. 7 we show the numerical results of a two-dimensional (circular) chamber subject to an underpressure of 10 MPa, a common underpressure value when considering ring-fault formation (Geyer et al., 2006; Gudmundsson, 2007; Kusumoto and Gudmundsson, 2009). We model the horizontal and vertical displacement at the surface of the ice and at the surface of the bedrock (the crust under and outside the ice sheet) for two magma-chamber depths: 3 km and 5 km. The modelled chamber radius is 1 km and is thus small in relation to the chamber depth below the surface, as it should be for a "Mogi model". There are two basic model configurations. The first one (Fig. 7A) has no caldera lake, but the second one (Fig. 7B) has a caldera lake between

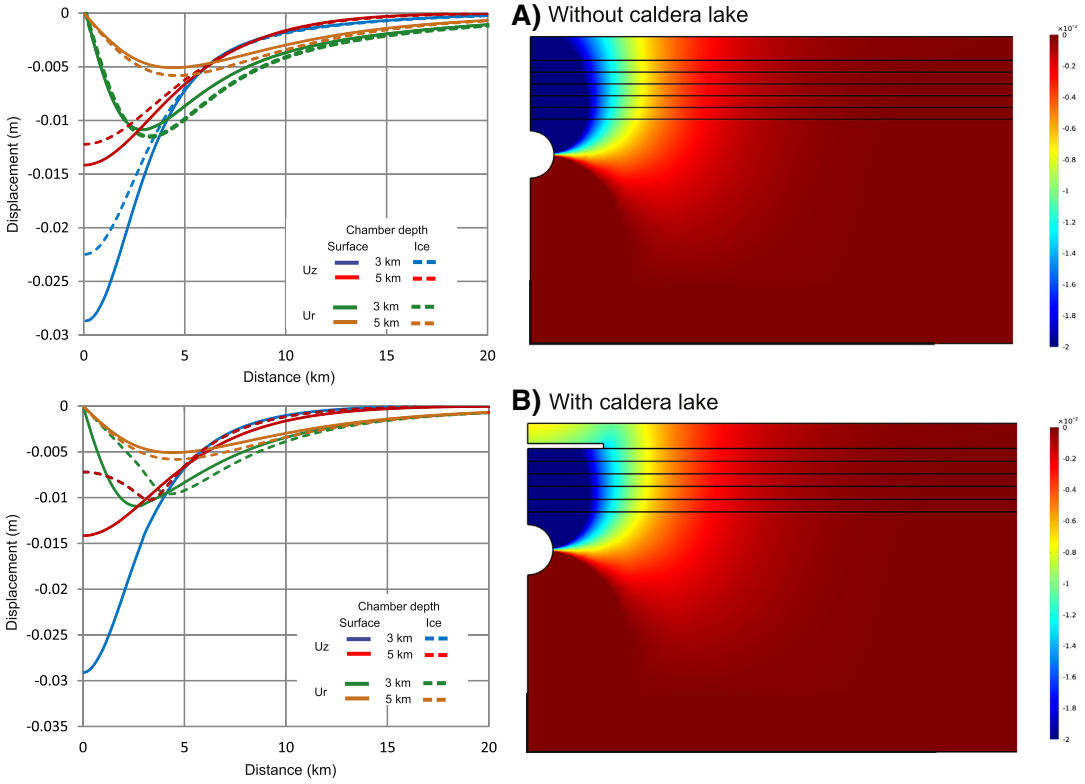

Fig. 7. Crustal surface and ice-surface displacements resulting from negative excess pressure, or depressurisation, of −10 MPa in a circular chamber with a roof at 3 km and 5 km depth below the crustal surface. The upper model (A) shows a homogeneous isotropic crust with an upper ice layer. The lower model (B) also shows a homogeneous isotropic crust but this time incorporates a rectangular free surface, designed to replicate a caldera lake. Total displacement contours are given on the right in metres. The magnitude of displacements in the two models are generally similar, but the displacement patterns differ somewhat, especially in the ice layer.

the bottom of the ice and the bedrock surface. The lake is included in several of the models in this paper because, as indicated above. Such lakes are common in the many calderas located beneath ice in Iceland (Gudmundsson et al., 1997, 2004, 2012).

The surface displacements, vertical and horizontal, are very small (less than 3 cm) for this type of loading (Fig. 7), suggesting that a 'Mogi model' is, as a rule, not very suitable for generating large (tens-of-metre scale) subsidences. The geometries of the displacement curves (Fig. 7), however, are in excellent agreement with those obtained from the Mogi model (Fig. 6). The displacement results (Fig. 7) are shown both for the surface of the rock (the crust under and outside the ice) as solid lines as well as for the surface of the ice itself, as broken lines. As is also seen in subsequent models, the caldera lake has great effects on the displacement curves for the surface of the ice. The other main results as regards the surface-displacement curves will be discussed in context of the later and more realistic models, to which we turn now.

5. Roof subsidence of a sill-like magma chamber

Here we present the results of the stresses and surface displacement induced by a given subsidence of the roof of a sill-like magma chamber. The chamber, modelled as a cavity within a crustal segment, is given a zero excess pressure condition at its lower boundary and prescribed a vertical displacement at the upper boundary in all models apart from those simulating slip on the ring-fault. Thus, in the models the chamber is in lithostatic equilibrium with its surroundings prior to the prescribed vertical displacement, that is, the roof subsidence. While these models are partly "inspired" by the events in Bardarbunga 2014–15, they are completely general and apply to all central volcanoes – collapse calderas in particular – under ice. We explore two main types of models, namely where the magma chamber is located (1) in a homogeneous, isotropic crustal segment, and (2) in a layered, anisotropic, crustal segment. Based on information from Bardarbunga, where the maximum subsidence of the ice surface is estimated at around 60 m (Hensch et al., 2015), we explore vertical roof displacements or subsidences from 20 m to 100 m. To cover the likely shallow chamber depths, we consider chambers with roofs at depths of 3 km, 5 km, and as an extreme shallow-chamber depth, 7 km below the crustal or rock surface.

5.1. Homogeneous crustal segment

These models are somewhat similar in set-up as the elastic half-space or the Mogi model (Mogi, 1958; Kusumoto and Gudmundsson, 2009; Fig. 7). There are, however, three main differences between the present models (Fig. 8) and the numerical models in Fig. 7. First, the shallow magma chamber (cavity) has here (Fig. 8) a sill-like geometry in contrast to the spherical or point-like Mogi source (circular in Fig. 7). Also, here the radius of the chamber a is 4 km (Fig. 8), and thus 4-times the radius of the previous circular chamber (Fig. 7), and with a maximum thickness $2b$ of 2 km. Second, the displacements at the surface of the bedrock (the crust) and the ice result here from prescribed chamber-roof vertical displacement or subsidence rather than the underpressure in the models in Fig. 7. Third, the subsequent sill-like chamber models analyse chambers in a layered (anisotropic) crustal segment rather than in an elastic half-space as is done in the Mogi model (Fig. 7), and some of the sill-like models also include a lake beneath the ice, thereby forming a free surface.

Fig. 8 shows the vertical (u_z) and horizontal or radial (u_r) surface displacements of the ice and the bedrock (or crust) resulting from a vertical chamber-roof displacement or subsidence of 100 m. Here there is no ring-fault. The chamber roof is prior to the displacement at different depths below the bedrock or crustal surface d, namely at

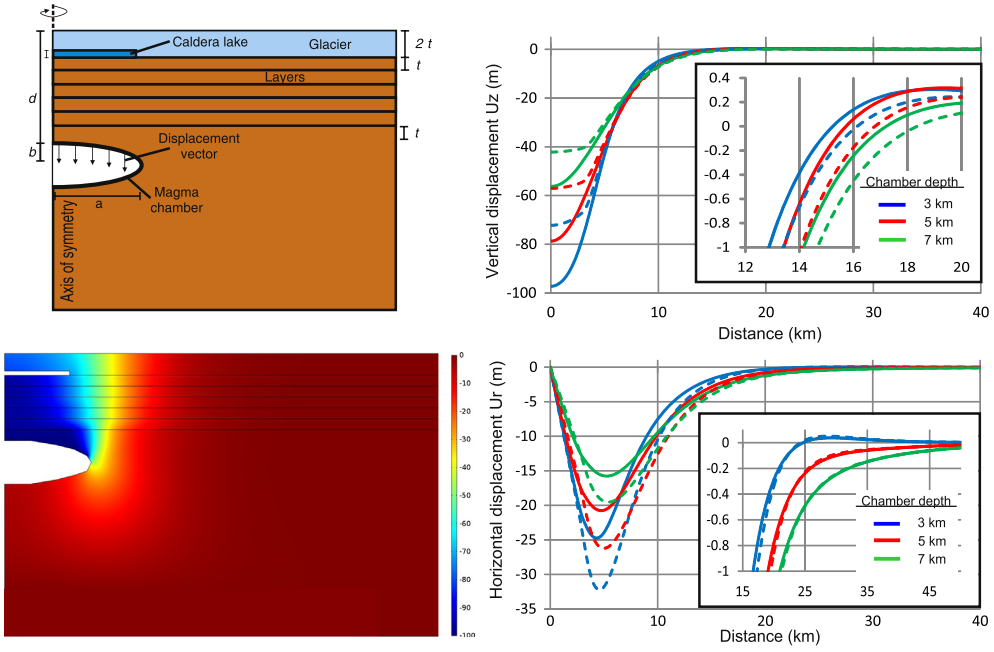

Fig. 8. Vertical and horizontal ground-surface (solid curves) and ice-surface (dashed curves) displacements in metres resulting from a maximum prescribed chamber-roof displacement of 100 m. Here the crust is non-layered. In all model runs the maximum vertical surface displacements of the ice and the crust occur over the chamber centre (in the caldera centre) whereas the maximum horizontal displacements of ice and crust occur around 5 km away from the caldera centre. Vertical crustal surface displacements are larger than the ice displacements, but the opposite is true for the horizontal displacements. Insets display the distances from the chamber where <1 m of vertical and horizontal displacements would be observed. Note that significant (10–20 cm) vertical displacement occurs out to 15 to 16 km from the caldera centre. Similarly, horizontal displacements of 10–20 cm occur out to 30 to 45 km (depending on chamber depth) from the caldera centre. Chamber radius (a) is 4 km and half-thickness (b) is 1 km, depth (d) varies between each model run, as indicated by the separate line colours.

Table 2
Model results assuming a 100 m displacement of a chamber roof residing at 3 km.

Setup	Uz Max (−m)		Ur Max (−m)		x distance (km) when Uz = 0.5 m		x distance (km) when Ur = 0.5 m	
	Crust	Ice	Crust	Ice	Crust	Ice	Crust	Ice
Homogeneous	97.21	71.75	24.75	32.22	13.8	14.4	18.6	19.1
Heterogeneous A	79.12	64.14	2.3	10.26	12.2	12.3	11.8	14.7
Heterogeneous B	84.14	64.68	5.78	6.92	11.6	11.6	16.9	16.3
Ring-fault	98.5	70.18	23.09	30.31	13.5	14.1	18.4	18.9

depths of 3, 5 and 7 km. Salient model results are shown in Table 2, but here we summarise some of the basic results (Fig. 8) as follows:

(1) The maximum vertical displacement (shown as negative displacement or surface subsidence), both of the ice and the crust, is above the centre of the magma chamber. The subsidence reaches about 97 m in the bedrock/crust and about 78 m in the ice (Table 2). The subsidence changes to uplift or doming at distances of 15–18 km (depending on the chamber depth) from the surface point right above the chamber or caldera centre (Fig. 8). Unless otherwise stated, chamber/caldera centre in the discussion that follows refers to this surface point.
(2) The horizontal displacement towards the centre (above the centre of the chamber), shown as negative, reaches its maximum at 4–5 km from chamber/caldera centre. The horizontal displacement reaches a maximum of about 25 m in the crust and about 32 m in the ice (Table 2). For the chamber at 3 km depth, however, the horizontal displacement becomes positive (movement away from the centre) at about 25 km distance from the centre.
(3) The vertical surface displacement, both in the ice and in the bedrock/crust, is less than that of the chamber roof. There is thus not a one-to-one correspondence between the displacement at the surface either of the ice or the crust and the chamber roof subsidence.
(4) The vertical and horizontal displacements extend to distances far from the chamber/caldera centre. Thus, in both the bedrock/crust and the ice the vertical displacement is in excess of 0.5 m out to distances of about 14 km, whereas the horizontal displacements are in excess of 0.5 m out to distances of about 19 km (Table 2).

Generally, significant surface displacements associated with the chamber-roof subsidence of 100 m occur at lateral distances of up to 40–50 km (in the ice as well as in the bedrock/crust) from the chamber/caldera centre. For example, a chamber located at 3 km depth produces horizontal surface displacements of 20 cm at approximately 21 km from the chamber/caldera centre, while a chamber at 7 km depth produces the same displacement at approximately 33 km from the centre. Thus, for the imposed vertical displacement of the chamber roof, large horizontal displacements are expected out to tens of kilometres from the chamber, and these should be easily detected in the ice or at the bedrock/crustal surface by geodetic measurements.

In the second set of homogeneous crustal models, we consider the effects of a pressurised deep-seated reservoir, such as are common as magma sources for shallow chambers in Iceland (Gudmundsson, 2012) (Fig. 9). Doming is modelled as being the effect of 10 MPa excess magmatic pressure acting on the roof (a boundary load) of the reservoir. The general effect of doming is to reduce the magnitude of vertical and horizontal surface displacements but increase the surface area where those displacements are significant. In other words, the subsidence becomes much less concentrated at the surface immediately above the shallow chamber.

In the third set of homogeneous crustal models, we added vertical faults (Fig. 10). These are supposed to represent a two-dimensional version of a caldera ring-fault. The fault is modelled as a soft elastic inclusion, that is, as a zone with a low Young's modulus. This is because active or recently active faults have generally lower Young's moduli than most of the host rock because the fault is composed of a fractured damage zone and breccia fault core (Gudmundsson, 2011; Browning and Gudmundsson, 2015). The precise relationship between damage and Young's modulus evolution in caldera settings is, as yet, poorly constrained. The results (Fig. 10) are similar to those of the previous models without a fault (Fig. 8) but differ in that surface subsidence is concentrated within a narrower region around the chamber margin. In addition the crust experiences significant (~30 cm) positive (doming) displacement, measured as an inflation signal between approximately 15 km and 20 km from the centre.

5.2. Layered (anisotropic) crustal segment

Two layered crustal-segment models were run (Fig. 11). One model (A) has two soft layers in-between stiffer crustal units, while the other model (B) has three soft layers, including the top layer. All the soft layers have a stiffness of 1 GPa, which corresponds to the stiffnesses of soft hyaloclastites (basaltic breccias) and of glacial sediments, such as are common in most active volcanoes in Iceland. The layers are modelled as soft to explore the maximum effects that sediments and soft breccias could have on the displacement fields. Introducing mechanical heterogeneities and anisotropies through soft layers with low Young's moduli into the model setup has the following effects:

(1) There is a general reduction in magnitudes of the far-field displacements. That is, the horizontal and vertical displacements far from the chamber/caldera centre are smaller in the layered models than in the non-layered models (Table 2).
(2) The maximum vertical displacements are also smaller in the layered models than in the non-layered models. More specifically, the maximum surface vertical displacements in the bedrock/crust are 79–84 m in the layered models but 97–98 m in the non-layered models (Table 2). Similarly, the maximum surface displacement in the ice in the layered models is 64–65 m, but 70–72 m in the non-layered models.
(3) The maximum horizontal surface displacements are much smaller in the layered models than in the non-layered models. In the layered models the maximum surface horizontal displacement is 2–6 m but ~25 m in the non-layered models.

The general effect of layering is to reduce the displacements measured at the surface of the bedrock/crust and the ice. The reasons for the reductions are partly that the stresses become “dissipated” at the contacts with the soft layers. Similar results have been obtained in general studies of surface deformation associated with various pressure sources, such as dykes (Gudmundsson, 2003). Crustal segments with alternating stiff and very soft layers generally transport less stress and deformation to the surface than non-layered segments, or segments where all the layers have similar mechanical properties. Well-known examples of the reducing effects of mechanically contrasting layers on

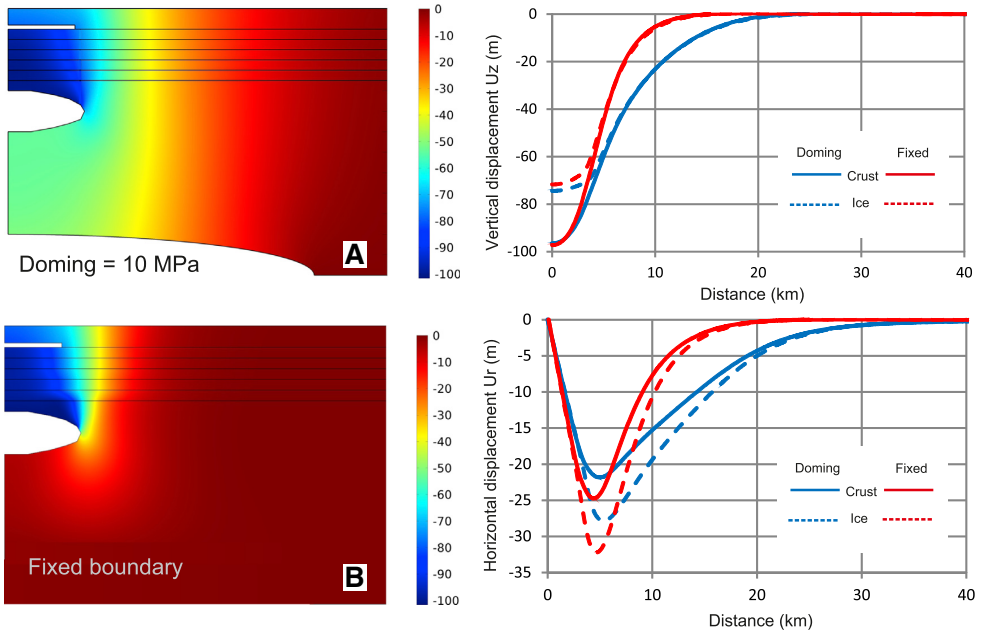

Fig. 9. Vertical and horizontal ground-surface and ice-surface displacements in metres resulting from a maximum prescribed chamber-roof displacement of 100 m, and either A) doming overpressure of 10 MPa in a deep-seated reservoir (blue lines) or B) fixed lower boundary (red lines). Here the crust is non-layered. Doming has the general effect of reducing the maximum horizontal displacement but increasing the radial distance or area over which significant horizontal displacement occurs. Magnitudes of vertical displacement are not greatly affected by doming, but the area of vertical subsidence increases in the absence of a fixed boundary. Shallow chamber radius (A) is 4 km and half-thickness (B) is 1 km, depth (d) is 3 km. Deep reservoir radius is 16 km with a half-thickness of 2 km at a depth of 10 km.

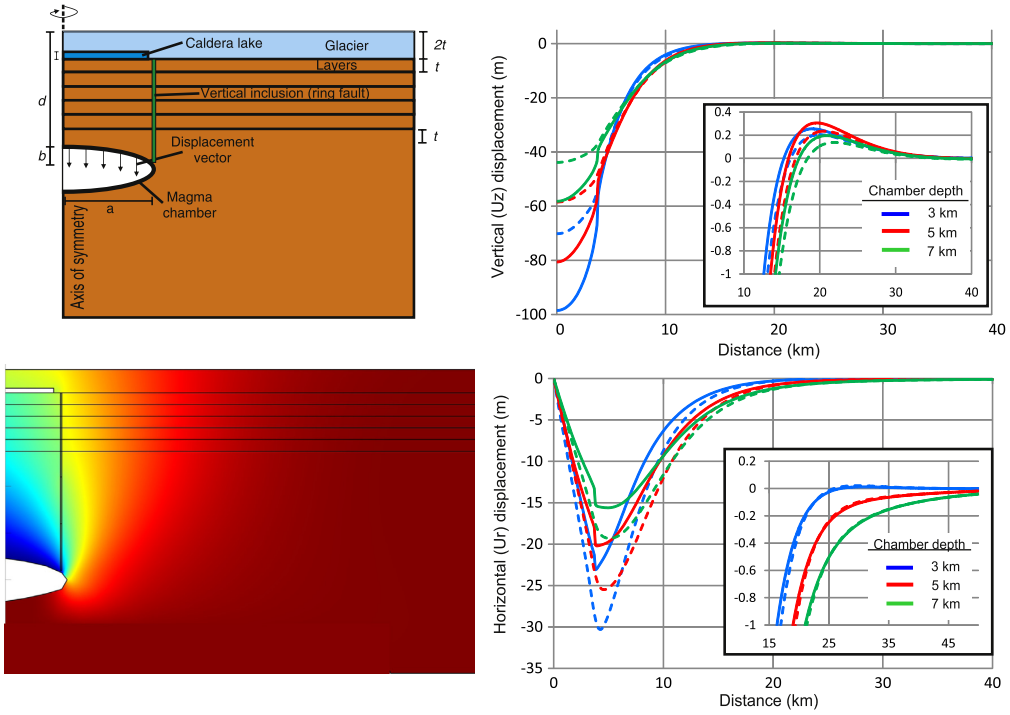

Fig. 10. Resultant displacements from a model which includes a soft (Young's modulus 1 GPa) fault zone, representing a ring-fault. In this model the crust is homogeneous and isotropic, i.e., not layered. Results are similar to those in models without the weak fault zone, but differ in that surface subsidence is concentrated within a narrower region. Additionally, the crustal segment experiences a positive vertical displacement (~30 cm), inflation between around 15 and 20 km from the chamber centre. Chamber radius (a) is 4 km and half-thickness (b) is 1 km, depth below the surface (d) is 5 km.

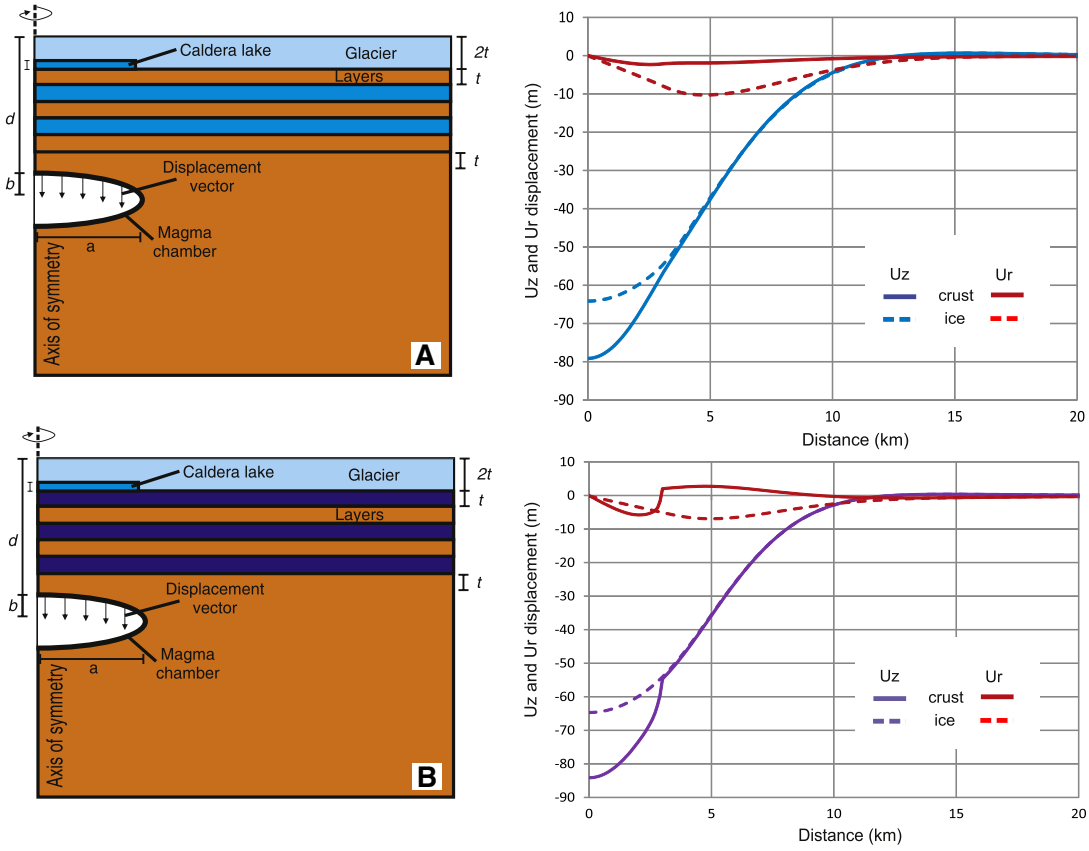

Fig. 11. Displacements generated through chamber-roof subsidence of 100 m in a layered crustal model. In the upper model (A), the layering is configured so that two soft layers (Young's modulus E = 1 GPa) lie in-between stiffer units which have the same Young's modulus as the crust. In the lower model (B) we add three soft layers in between crustal units, where the uppermost is in contact with the glacier. Coloured layers indicate soft hyaloclastite as material inputs shown in the model setups on the left. Graphs on the right indicate the vertical and horizontal displacements in the crustal (solid) and ice (dashed) surface for each layer configuration. Generally, there is a reduction in far-field displacements and the magnitude of local displacements is less in both model set-ups, compared to the previous homogeneous setups. Chamber radius (a) is 4 km and half-thickness (b) is 1 km, depth (d) is 5 km.

surface stresses and deformation/displacement relate to emplacement of dykes and other vertically fluid-driven fractures (Gudmundsson, 2003; Philipp et al., 2013).

6. Ring-fault subsidence

We also modelled the effects of a piston-like subsidence along a ring-fault on the surface displacement fields. In view of the results from Bardarbunga, where inferred vertical maximum displacement in the ice inside the collapse caldera is about 60 m (Hensch et al., 2015), we impose 50 m vertical displacement on the ring-fault (Fig. 12). The ring-fault, the fault zone, is modelled as a soft inclusion, with a Young's modulus of 0.1 GPa. We tried other stiffnesses for the fault zone, such as 0.01 GPa, but the overall results remained similar. The crust itself is non-layered in this model with the properties used in the earlier non-layered models (Table 1).

The results (Fig. 12) show that the displacement, both the vertical and the horizontal, becomes more concentrated at and within the caldera (the ring-fault) than in the previous roof-subsidence models without ring-fault. The maximum subsidence of the bedrock/crust is the same as that of the fault, namely 50 m, but the ice subsidence is greater, or 60 m. This is because the ice can bend or subside somewhat into the caldera lake (and/or soft sediments) at the contact between the ice and the crust, whereas the crust clearly cannot do so. For the same reason, the horizontal displacement (towards the centre) at the surface of the ice also exceeds that of the crust. Both reach a maximum at the location of the ring-fault, the vertical displacement of the ice (the fault throw) being up to about 17 m and that of the bedrock/crust up to 10 m.

These results illustrate various aspects of the effect of ring-fault subsidence in a caldera located beneath ice, including the following:

(1) The crustal displacements, the horizontal and, in particular, the vertical, reflect strongly the ring-fault geometry. This means that both displacements are maximum at the caldera fault. In fact, the vertical displacement reaches its maximum of 50 m at the fault and stays the same throughout the roof of the chamber.
(2) The caldera lake magnifies the surface displacement of the ice. The horizontal displacement in the ice is considerably larger than that in the crust. And, most importantly, the total vertical displacements in the ice exceed that imposed on the ring-fault by about 10 m. This is because of the caldera lake beneath the ice into which the ice can subside.
(3) Displacement of 50 m is so large that it would certainly cut through the ice as a fault. The inferred vertical displacement at the location of the ring-fault are about 17 m. No tensile or shear strength is given to ice in the model, so it does not fracture. But 50 m vertical displacement in an ice sheet of thickness, say, 800–1000 m would become very clearly through-faulted.

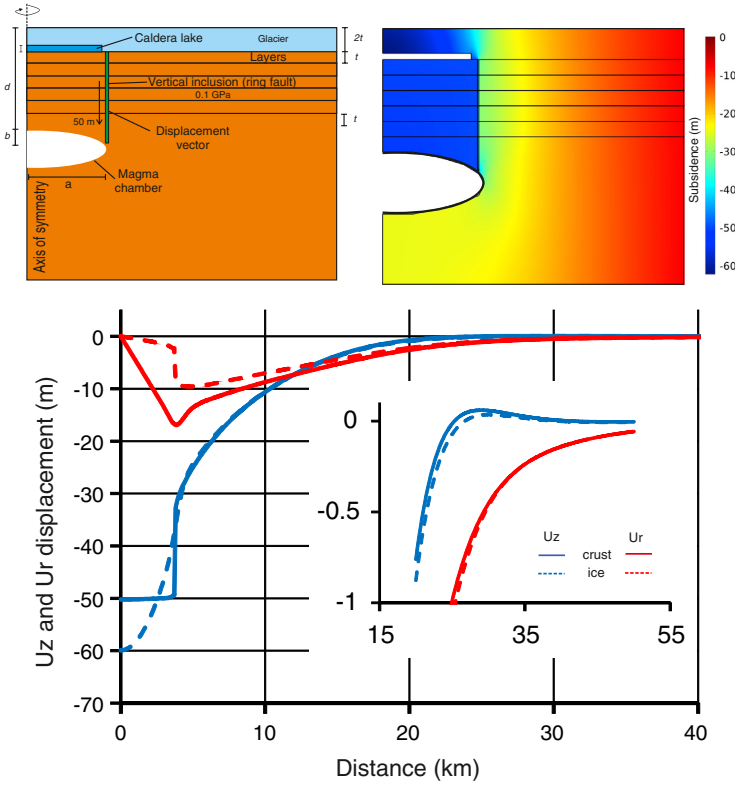

Fig. 12. Piston-like vertical subsidence of 50 m along the inner edge (z-axis) of a ring-fault, a soft elastic zone which extends from the crustal surface to 3 km depth. The soft fault zone has a Young's modulus of 0.1 GPa and the crustal segment is homogeneous and isotropic. Displacements are highly focussed within the caldera region, with maximum vertical and horizontal displacement greatest in the ice surface. The caldera lake acts to magnify displacements within the ice, presumably because the ice is able to subside into the lake surface. Chamber radius (a) is 4 km and half-thickness (b) is 1 km, depth below the surface (d) is 5 km.

7. Discussion: Implications for the 2014–15 Bardarbunga–Holuhraun episode

The underpressure or withdrawal-of-magmatic-support model is often favoured when explaining the formation of calderas, both in analogue-model setups (Acocella et al., 2000; Holohan et al., 2011) and for explaining geophysical observations (Peltier et al., 2008; Kusumoto and Gudmundsson, 2009). Most recently this model has been invoked to explain ice surface subsidence above the Bardarbunga Caldera (Sigmundsson et al., 2015). The assumption is then that a volume of magma was removed from a chamber by lateral magma propagation, eventually forcing an eruption some 45 km from the central volcano. Similar ideas have been offered to explain the occurrence of lavas outside the main central volcanoes and within the active rift zone of Iceland (Sigurdsson and Sparks, 1978), although more recent studies have shown that alternative explanations with predominating vertical magma propagation are equally plausible (Hartley and Thordarson, 2012). The competing hypothesis is that the Holuhraun lavas, and many other large and rather primitive basaltic fissure eruptions in Iceland, are fed by regional dykes which are injected from magma reservoirs at a much greater depths (15–25 km) than the shallow chambers (Gudmundsson et al., 2014).

The models presented in this paper have certain implications for volcano-tectonic processes in central volcanoes in general. Further implications apply primarily to calderas located in ice sheets such as many calderas in Iceland – Bardarbunga in particular. We consider first the implication for the magnitude of the surface displacements and the size of the area affected (the surface area showing significant displacement). Both aspects of the deformation are very important, particularly when trying to separate the deformation associated with a caldera and/or a shallow magma chamber from that associated with simultaneous dyke emplacement.

7.1. Surface displacements

Vertical surface displacements of 10–20 cm extend out to distances of 15–16 km from the centre of the caldera, and horizontal displacements of similar magnitude to 20–30 km (Fig. 8). For the horizontal displacement, 10 cm displacements occur out to 40–50 km from the centre, depending on the depth of the chamber. These refer to the non-layered models and the exact distances for the displacement mentioned depend on the depth of the chamber: the surface displacements induced by the deepest chamber, at 7 km, extend for the greatest distances from the centre. If the surface displacement would relate partly to a deep-seated reservoir, as we propose here, say a reservoir at the depth of 15–20 km, then significant surface displacements would extend still further from the centre. Using the same model configuration and properties but roof-subsidence varying from 20 m to 100 m, the results are similar – significant displacements extend to 15–20 km from the centre (Fig. 13A) and are only slightly less when a vertical ring-fault is introduced (Fig. 13B).

The layered models produce less displacements, both in magnitude and lateral extension from the centre (Fig. 11). However, these models are with somewhat extreme layering since the soft layers have stiffness or Young's modulus of only 1 GPa, which is low for hyaloclastites and sedimentary rocks. Nevertheless, there are still large surface

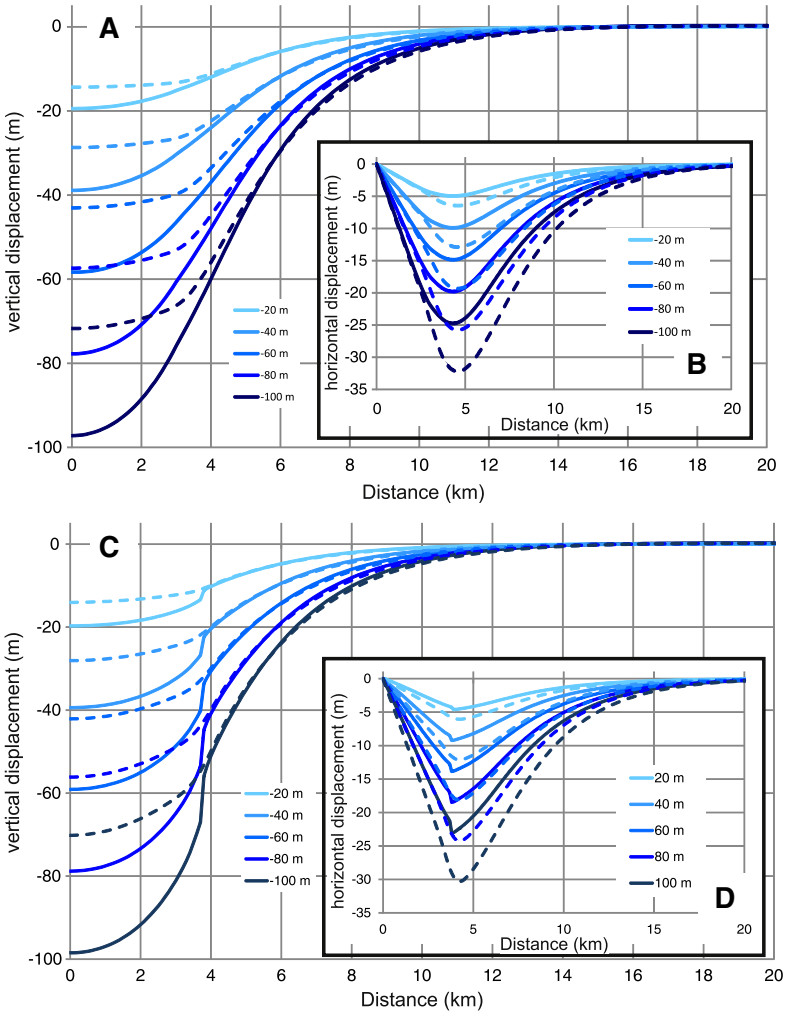

Fig. 13. Total vertical (A and C) and horizontal (B and D) displacements in crustal-surface (solid lines) and ice-surface (dashed lines) resulting from vertical chamber roof subsidence of between 20 and 100 m. Upper displacement curves (A and B) are from a homogeneous crustal model, whereas the lower curves (C and D) are from models which include a soft vertical zone, a ring-fault (C and D). The results are similar for both types of models, with slight variations in subsidence around the fault area. All models indicate significant far-field surface displacements, irrespective of the amount of roof subsidence. However, roof subsidence has a major control on the local surface displacements directly above the magma chamber. In all model runs shown here chamber radius (a) is 4 km and half-thickness (b) is 1 km, with a chamber depth of 3 km.

displacements of 50 cm at distances of about 12 km (for the vertical displacement) and 12–17 km (for the horizontal displacement) in the bedrock/crust, and somewhat larger distances in the ice (Table 2). Larger displacements are obtained from the 50-m-fault displacement model (Fig. 12).

Overall the displacement results indicate that, for the models considered, large displacements, of the order of tens of centimetres or hundreds of millimetres, should be detected out to distances of 10–20 km, for the vertical displacement, and 20–30 km or more for the horizontal displacements. Even for a small roof-subsidence of 20 m, the horizontal displacement at 10–12 km distance from the centre is still of the order of tens of centimetres (Fig. 13). Results of this kind show clearly the effect of nearby subsidence of a magma-chamber roof, or a collapse caldera displacement, and should make it possible to distinguish between displacements induced by such a subsidence and those induced by a dyke formed in the same volcano-tectonic episode.

The displacement field associated with the subsidence of the ice in the Bardarbunga episode in 2014–15 is educational in this respect. For the period up to 6 September 2014 the GPS-estimated maximum displacement or subsidence in the ice in the Bardarbunga Caldera was about 16 m (Sigmundsson et al., 2015), and the entire cumulative displacement during the episode 2014–15 is estimated at over 60 m (Hensch et al., 2015). Dyke emplacement was essentially completed by 31 August when the main eruption began (Gudmundsson et al., 2014; Sigmundsson et al., 2015), and no significant horizontal dyke-induced displacements were detected after 4 September 2014 (Ofeigsson et al., 2015). The horizontal displacements induced by the dyke can thus largely be separated from those induced by the subsidence measured in the Bardarbunga Caldera.

Our model results suggest that vertical displacement of about 16–20 m, corresponding to period up to about 6 September, should generate horizontal displacements of the order of tens of centimetres towards the Bardarbunga Caldera within 10–12 km from the centre of the caldera. Similarly, horizontal displacements of many tens of centimetres are expected out to distances of up to tens of kilometres, depending on the model used – in particular, the assumed depth of

the shallow chamber and mechanical properties of the host rock and the ring-fault. The measured displacements at the GPS stations in the crust outside the ice, some of which are at 13–17 km from the centre of the caldera, are significantly less than expected from the models (Ofeigsson et al., 2015; Sigmundsson et al., 2015). The difference may be partly related to the modelling procedure but most likely indicates that only part of the subsidence in the ice within the Bardarbunga Caldera is actually directly related the magma-chamber roof subsidence, or ring-fault displacement.

The last point is also of importance when interpreting the subsidence measured in the ice within the caldera. There are several remarkable features of the ice subsidence, as shown in maps by Sigmundsson et al. (2015), including the following:

(1) The maximum subsidence is about 3 km from the northern caldera rim and about 5 km from the southern and south-eastern rims.
(2) The subsidence at the rims, at the ring fault itself, is much smaller than the maximum subsidence – in fact about zero in the early stage of the subsidence.
(3) Fracture development at the surface of the ice is comparatively small, with no major caldera-related fault cutting through the ice.

These observations and measurements, when compared with the ring-fault subsidence model (Fig. 13), suggest the following interpretations. First, the displacement along the ring-fault is small in comparison with the overall subsidence in the ice. In particular, displacements of the order of 20–60 m along the ring fault would without doubt have propagated faults through the ice (say, vertical displacements of 10–20 m; Figs. 11 and 12) – and these faults are not observed. From standard fracture mechanics (Gudmundsson, 2011) and the mechanical properties of a typical ice (Schulson and Duval, 2009; Table 2), a close-to vertical normal fault (Hensch et al., 2015) with displacement of up to tens of metres in ice of thickness of several hundred metres – in fact, the ice thickness is only 200–300 m above part of the caldera rims – would become a through crack, that is, reach the bottom and surface of the ice sheet. This conclusion is the same even if there is a caldera lake beneath the ice (Fig. 13). Since normal faults with these throws are not observed, the cumulative vertical ring-fault displacements cannot be of the of the order of tens of metres, and is most likely of the order of metres or less.

Second, for a porous-media chamber, as most chambers presumably are (Gudmundsson, 2012), the maximum subsidence, if caused by magma flow out of an underlying magma chamber, would normally be, initially at least, close to the 'outlet', that is, the intersection of the dyke or sheet transporting the magma with the boundary of the chamber and the active ring-fault. Sigmundsson et al. (2015) propose that the subsidence of the ice is directly related to chamber roof-subsidence associated with magma flowing laterally along a dyke that dissects a chamber along its southeast margin. It is not clear from the subsidence data, however, why the maximum subsidence is then not at the outlet and the active ring-fault but rather close to the northern margin of the chamber/caldera.

In fact, the inferred segmentation of the dyke, with distances between nearby tips of segments up to kilometres (Sigmundsson et al., 2015), is a strong argument against lateral flow of magma from a chamber beneath Bardarbunga and to the volcanic fissures in Holuhraun and an argument for vertical flow of magma from a deep-seated reservoir (Gudmundsson et al., 2014). The arguments against the lateral flow between dyke segments are many, including the following. (1) There is no seismicity between the nearby ends of some of the 8 segments, particularly between segments 1 and 2 and 5 and 6 (Sigmundsson et al., 2015, Extended Data Fig. 2), suggesting that no magma migrated laterally between them. The zones connecting many of the segments, being highly oblique to the overall strike of the dyke, are zones of high shear stress making it highly unlikely that a magma-driven fractures could propagate along the zones without triggering earthquakes. Earthquakes are, in fact, used as criteria for identifying magma paths. It follows that absence of earthquakes, that is, seismically quiet zones, would normally mean absence of magma paths. (2) In the unlikely event of aseismic magma-path formation at shallow depths from segment 1 to 2, and from segment 5 to 6, then the same magma would have to flow from the shallow depths vertically down to at least 10 km depth in segments 2 and 6. Downward flow of magma on this scale is not supported by any observations and does not agree with well-established physical principles of fluid dynamics and dyke propagation (Gudmundsson, 2011). Thus, the segments of the regional Bardarbunga–Holuhraun dyke were presumably formed primarily through vertical flow of magma from the proposed deep-seated magma reservoir (Gudmundsson et al., 2014).

7.2. Mechanisms for the ice and ring-fault subsidences

If excess magma pressure decrease in a shallow chamber is not the main cause of the subsidence in the ice in Bardarbunga, what alternative mechanisms exist? One obvious mechanism, well known from caldera studies, is slight doming or inflation of the volcanic field hosting a shallow magma chamber. Doming was in fact detected at GPS stations in a large area surrounding the Bardarbunga Caldera a few months before the unrest (Ofeigsson et al., 2015). Such a doming, as small as of the order of centimetres, is known to be one of the principal mechanisms for generating caldera collapses (Gudmundsson, 2007), particularly along normal ring-faults (Gudmundsson, 1998). Focal mechanisms suggest that the slip on the ring-fault of Bardarbunga in the 2014–15 episode was primarily through normal faulting (Bjarnason, 2014; Hensch et al., 2015; Riel et al., 2015). Most of the ring-fault seismicity occurred at shallow depths (<3 km) (Hjörleifsdóttir et al., 2015), in agreement with the ring-fault seismicity being related to stress concentration above the margins of a proposed shallow magma chamber, which is the model suggested here (cf. Gudmundsson, 2007).

The doming or inflation of the volcanic field or system containing the Bardarbunga Caldera is most likely related to the associated deep-seated reservoir receiving new input of melt or magma. As doming begins, stress concentration at the ring-fault of the Bardarbunga Caldera results in subsidence – by how much we do not really know. The subsidence and associated faulting and possible ring-dyke formation (Gudmundsson et al., 2014) reduces the effective thickness of the crustal segment or plate above the shallow magma chamber (Figs. 5 and 9). The reduction in the effective plate thickness d_e encourages further doming of the volcanic field hosting the Bardarbunga caldera even if the magmatic excess pressure at the deep-seated reservoir remains constant or decreases slightly for a while (Gudmundsson, 1998).

7.3. Relation between dyke emplacement and subsidence in the caldera

This last point brings us to the 45-km-long regional dyke and associated eruption, and how they relate to the subsidence in the Bardarbunga Caldera. The first thing to notice is that the strike of the dyke close to the caldera/chamber is in perfect agreement with the local trajectories of the maximum horizontal principal stress around a circular or slightly elliptical cavity under tension (Savin, 1961; Gudmundsson, 2011). Further from the chamber/caldera the regional stress field took over, and the dyke followed the field that has existed in this part of Iceland for at least 8–10 Ma (Gudmundsson et al., 2014). The main dyke was injected when the excess pressure in the deep-seated reservoir reached the conditions (Gudmundsson, 2011):

$$p_l + p_e = \sigma + T_0 \tag{4}$$

where p_l is the lithostatic stress or overburden pressure at the reservoir rupture site (in the reservoir roof), $p_e = p_t - p_l$ is the difference between the total fluid pressure p_t in the reservoir and the lithostatic stress at the time of reservoir rupture, σ_3 is the minimum compressive or maximum tensile principal stress, and T_0 the local in situ tensile strength at the rupture site. When the dyke became injected into the roof of the reservoir and began to propagate up into the crustal layers above, its overpressure p_o changed as:

$$p_0 = p_e + (\rho_r - \rho_m)gh + \sigma_d \quad (5)$$

where p_e is the magmatic excess pressure in the reservoir at the time of rupture (and equal to the in-situ tensile strength of the roof at the rupture site, T_0), ρ_r is the host-rock density, ρ_m is the magma density, g is acceleration due to gravity, h is the dip dimension or height of the dyke above the rupture site, and σ_d is the differential stress at a particular depth in the crust (the depth of interest). At the magma-chamber rupture site itself, the stress difference is included in the excess pressure term, so that there $\sigma_d = 0$. Also, at the rupture site, before the dyke has propagated and reached any significant height, we have $h = 0$, so that the third term in Eq. (5), the buoyancy term, becomes zero. It follows that the only pressure available to rupture the reservoir roof and drive the magma out at and close to the roof contact with the magma is the excess magmatic pressure p_e. We also know that $p_e = T_0$, that is, the excess pressure at the time of roof rupture is equal to the in-situ tensile strength, with in-situ (field) values ranging from 0.5 to 9 MPa (Amadei and Stephansson, 1997), the most common values being 2–4 MPa (Gudmundsson, 2011).

It follows that during the rupture and initial propagation of the resulting dyke, the only driving pressure is p_e, of the order of several mega-pascal. As the dip dimension (height) of the dyke increases, however, positive buoyancy adds to the driving pressure, so long as the average magma density is less than the average density of the rock layers through which the dyke propagates. The magma is olivine tholeiite (Haddadi et al., 2015) so that its density may be taken as about 2700 kg m^{-3} (Murase and McBirney, 1973). The erupted magma originated at depths somewhere between 10 and 20 km (Bali et al., 2014; Haddadi et al., 2015), that is, from a deep-seated magma reservoir as have been proposed under most volcanic systems in Iceland, and the Bardarbunga System in particular (Gudmundsson et al., 2014). Given the crustal density in Iceland, then from Eq. (5) the magmatic overpressure p_0 or driving pressure of the dyke, at different crustal depths (and thus with different σ_d values) could easily have reached 10–15 MPa (cf. Becerril et al., 2013; Gudmundsson et al., 2014).

In the model presented here, the injection of the main dyke from the deep-seated reservoir, as well as the subsidence in the Bardarbunga Caldera, were both primarily the consequence of the same process: namely inflow of magma into the deep-seated reservoir. This inflow may have started many years before the 2014 episode, particularly from 2006 and onwards as indicated by seismicity (Vogfjörd et al., 2015), and was certainly noticeable as widespread doming or uplift on GPS instruments for months before the regional dyke injection began in August 2014 (Ofeigsson et al., 2015). There may have been magma flow into the shallow chamber associated with the caldera, and several smaller dykes may have been emplaced during the early stages of the episode – some from the deep-seated reservoirs, others (small radial dykes) from the shallow chamber. The only dyke to develop into a major dyke, however, was the 45-km-long regional dyke emplaced over a period of 2 weeks in August 2014 (Gudmundsson et al., 2014; Sigmundsson et al., 2015).

The regional dyke presumably came from depths of at least 15–20 km, perhaps deeper. This is suggested partly by the chemistry of the erupted lavas (Bali et al., 2014; Haddadi et al., 2015), partly by the widespread doming detected in the months before the episode, discussed above, and partly by the earthquake distribution in the area. From 2012 there were many earthquakes north and northeast of the Bardarbunga Caldera (Vogfjörd et al., 2015), where one of the earthquake swarms (and possible dyke injection) occurred during the first days of the August 2014 episode. Even more importantly, deep earthquakes occurred in a vertical zone southeast of the Bardarbunga Caldera from about this time and extended until August 2014 (Vogfjörd et al., 2015) at roughly the location of the first segment of the regional dyke, as formed in the first days of the August 2014 episode.

The regional dyke had enormous stress effects on the Bardarbunga Caldera and, by implication, the associated shallow magma chamber (Gudmundsson et al., 2014). The stress field induced by the dyke around the caldera contributed to three important aspects of the 2014 episode; (1) normal faulting along the caldera ring-fault, (2) elongation of the caldera in a roughly north-south direction, and (3) ductile deformation and flow of the ice, primarily inside the caldera.

Normal faulting is the dominating mechanism on the Bardarbunga ring-fault during the present episode (Bjarnason, 2014; Hensch et al., 2015; Riel et al., 2015). This is in agreement with the two main mechanisms of caldera slip proposed here, namely: (1) a combination of stresses concentrating at the ring-fault as a consequence of slight doming due to excess pressure increase in the deep-seated reservoir (Gudmundsson, 2007) and (2) dyke-induced stress concentration, particularly at the northern and southern sectors of the ring-fault (Gudmundsson et al., 2014). Both encourage normal faulting on the ring-fault itself, while the dyke-induced stresses also encourage strike-slip and reverse-faulting on differently oriented faults away from the ring-fault (Gudmundsson et al., 2014).

The elongation of the ring-fault in the roughly north-south direction is due to the compressive and shear stresses that concentrate in the "breakout areas" around the caldera (Gudmundsson et al., 2014). Elongation of collapse calderas due to "breakouts" is well known from other areas (Bosworth et al., 2003). The elongation would encourage flow of magma to the ring-fault in these sectors, possible ring-dyke formation – which may partly explain the common non-double couple earthquakes (Riel et al., 2015) – and contribute to the subsidence of the caldera roof. The main reason why the earthquake activity along the Bardarbunga Caldera has been so concentrated in the north and south parts of the caldera is presumably related to the dyke-induced stresses in these sectors (Gudmundsson et al., 2014).

While no attempts were made to measure or monitor ice flow in the ice-sheet cover of the Bardarbunga Caldera and its vicinity during the 2014–15 episode, such flow is likely to have occurred. During the emplacement of the regional dyke east and northeast of the caldera, the magmatic overpressure in the dyke (Eq. 5) may easily have reached 10–15 MPa. The dyke induced major displacements and thus stresses, within the caldera, and the high mountains of the caldera rim must have transmitted those compressive stresses (σ_H) from the dyke into the ice (Fig. 14). Depending somewhat on the strain rate, ice flows at

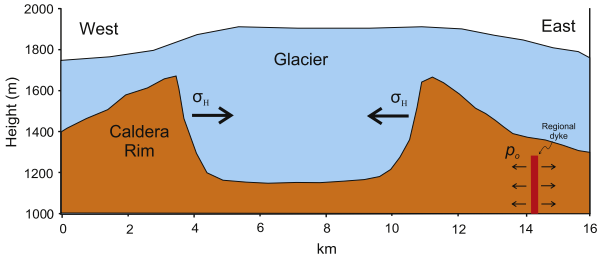

Fig. 14. A simplified E–W profile of the sub-glacial caldera at Bardarbunga volcanic system. Overpressure (p_o) from a regional dyke emplaced to the east of the caldera rim imposes large horizontal compressive stresses (σ_H) on the high caldera walls. The compression acts to squeeze ice within the caldera, making the ice behave as ductile up to the surface, and leading to increased ice flow out of the caldera. The resulting ice flow is likely to have contributed largely to the measured ice subsidence at Bardarbunga. The regional dyke is not to scale in this diagram and the sub-glacial caldera topography is a representation of the likely topographic setting of Bardarbunga, modified from Björnsson (1988).

pressures or stresses of less than 1 MPa, so that stresses of up to 10 MPa – somewhat diminishing with distance from the dyke – would certainly have caused flow in the ice within the caldera. The main flow would have been within the caldera because that is where the mountains are high – the caldera rim – and can thus most easily transmit the dyke-induced stresses to shallow levels in the ice sheet (Fig. 14). Since ice flows from higher to lower pressure, the dyke-induced stresses would have encouraged ice flow out of the caldera.

How much the ice flow may have contributed to the measured 60 m subsidence in the ice is unknown. The comparatively minor fracturing at the surface of the ice during its subsidence would suggest that the ice was flowing right up to the surface. Flow in and down-bending of the ice may have contributed significantly to the measured subsidence. In this model, the flow or creep or strain rate was highest just after the emplacement of the regional dyke, and then became gradually lower, as is typical for a creeping response to sudden load or displacement (here the dyke emplacement). Down-bending would be encouraged by a caldera lake and/or soft sediments (subject to earthquake shaking) existing beneath the glacier (Fig. 5).

As the excess pressure p_e in the deep-seated reservoir declined, the doming-related ring-fault displacement also gradually decreased and, as p_e approached zero, the subsidence stopped altogether. It is clear that long before the eruption came to an end on 27 February 2015 the earthquake activity associated with the Bardarbunga Caldera had greatly diminished. Also, the subsidence measured in the Bardarbunga Caldera ceased several weeks before the end of the eruption. These and other observations suggest that the pressure decrease in the deep-seated reservoir was partly responsible for the ring-fault slips and associated earthquakes.

8. Conclusions

We present general numerical models on the effects of “shallow” magma chamber contraction at various depths, namely the result of chamber roof subsidence at depths of 3 km, 5 km, and 7 km. In all the models, the magma chambers are associated with a collapse caldera which is located beneath a thick glacier or ice sheet. The models are general, and apply to many volcanoes in Iceland and elsewhere, but the results are here applied to the 2014–15 volcano-tectonic episode in Bardarbunga–Holuhraun in Iceland.

Several models were tested for the shrinkage of the magma chamber through vertical downward displacement of its roof. Some of the models use a simple elastic crust (elastic half space) hosting the chamber, with an ice sheet on the top. Others use layered (anisotropic) crust above the shallow magma chamber, that is, layers with different stiffnesses (Young's moduli). And still other models have a caldera lake between the ice sheet and the rock or crustal surface. The simplest loading used is 100 m vertical downward displacement of the chamber roof. Other models include different vertical displacement of the roof (in steps from 20 m to 100 m), as well as displacement of 50 m along a vertical caldera fault (the ring-fault). Some of the main results are as follows:

(1) For chamber-roof displacements in the range of 20–100 m, the models suggest large vertical and particularly horizontal displacements in the ice and in the bedrock/crust surface under the ice out to distances of 10–40 km from the caldera centre, depending on the depth of the chamber and the exact type of modelling used. The vertical displacements in all models reach maximum at the surface of the bedrock/crust and the surface of the ice right above the centre of the subsiding magma-chamber roof. The horizontal displacements at the surface, however, reach their maximum values (maximum displacement towards the chamber or caldera centre) at a distance of 4–5 km from the centre.
(2) For a non-layered (isotropic) crustal model with a 100 m roof subsidence, the vertical displacement exceeds 50 cm to a distance of 14 km from the centre and the horizontal displacement exceeds 50 cm to a distance of 19 km from the centre. A chamber located at 3 km depth produces horizontal displacement of 20 cm to a distance of 21 km from the centre, and for a chamber at 7 km depth horizontal displacement of 20 cm is produced to a distance of 33 km from the centre. Similar results are obtained if a vertical non-slipping ring-fault is added to the model, but the displacements show an abrupt change (a break) at the location of the fault.
(3) The general effect of crustal layering (using mechanically layered or anisotropic models) is to reduce the displacements measured at the surface in comparison with those generated in the non-layered (isotropic) models. The reasons are partly that the stresses become "dissipated" at contacts between still and soft layers.

In a model where the subsidence is related to vertical downward piston-like displacement by 50 m of the ring-fault, the results show that the vertical displacement in the crust/chamber roof exactly reflects that of the ring-fault and reaches a maximum of 50 m. By contrast, the vertical displacement in the ice follows a curve that reaches its maximum of 60 m in the centre of the caldera. This "extra" vertical displacement in the ice is partly because it can bend or subside somewhat into the caldera lake below. Displacement of 50 m along the ring-fault is so large that the fault would most definitely cut through the ice, forming a through fault with displacements of up to tens of metres (which is not observed in Bardarbunga, however).

The modelling results have several implications for the interpretation of the 2014–15 Bardarbunga–Holuhraun episode.

(1) First, the measured horizontal displacements in the surface rocks outside the ice appear to be significantly less than expected from modelling 60 m vertical displacement. At stations west of the Bardarbunga Caldera, horizontal displacements towards the caldera of the order of tens of centimetres would be expected but are not observed. This indicates that the vertical displacement in the bedrock/crust, and thus the chamber roof-subsidence, is significantly less than the maximum of about 60 m measured in the ice.
(2) Second, a 50 or 60 m piston-like displacement along the ring-fault is ruled out. The ring-fault would, for such a large displacement, definitely cut through the ice to form a large and easily visible fault, but this has not happened. By contrast, there has been comparatively little fracturing in the ice within the Bardarbunga Caldera during the subsidence, which suggests that the ice behaved as ductile, was flowing, right up to its surface. The results seem to limit the actual ring-fault (piston-like) subsidence to, at most, a few metres.
(3) Which brings us to the third implication, namely that the 45-km-long regional dyke generated compressive stresses in the ice within the caldera which resulted in ice flow out of the caldera, thereby contributing to the measured subsidence in the ice. How large factor the ice flow (and possible down-bending into lake/sediments) may have been is unknown since no measurements of the ice flow were made. What is known, however, is that ice flows easily at low pressures, of the order of 1 MPa, and our calculations suggest magmatic overpressure in the regional dyke of the order of 10–15 MPa.

We interpret the geochemical, seismic, and geodetic data so that the regional dyke was injected from a large reservoir at 15–20 km depth, perhaps deeper. Earthquake data suggest that the reservoir received new magma over many years before the beginning (in August 2014) of the Bardarbunga–Holuhraun episode, particularly from the year 2006 and onwards. The magma injection resulted in widespread doming (uplift), as detected by GPS instruments in the months prior to August 2014 when the dyke emplacement began (Ofeigsson et al., 2015).

In our interpretation, the August 2014 reservoir rupture and regional dyke injection as well as the ring-fault displacement (caldera subsidence) are all primarily the consequence of the associated reservoir magmatic pressure increase and doming. The conditions for reservoir rupture, dyke injection, as well as the overpressure change with vertical propagation of the dyke, are presented in Eqs. (4) and (5). The effects of ring-fault formation or reactivation as a result of reservoir-pressure increase, slight doming, and stress concentration around the chamber/caldera are discussed in the paper with reference to earlier numerical models (Gudmundsson, 1998, 2007), all of which suggest doming as a main mechanism of ring-fault displacement. This mechanism is also in agreement with the dominating normal-fault focal mechanisms of the ring-fault earthquakes (Bjarnason, 2014; Hensch et al., 2015; Riel et al., 2015).

We interpret the seismic and geodetic data so that, in addition to the 45-km-long regional dyke, there may have been several other dyke injections, including a northwest-striking dyke emplaced some 15 km north of the caldera and several smaller radial dykes/inclined sheets injected from the shallow chamber beneath the caldera. The shallow chamber may have received magma from the reservoir during the episode before the radial dyke injection; alternatively, stress concentration around the shallow chamber, through the external loading (doming), can have triggered the radial dyke injection (Gudmundsson et al., 2014).

The regional dyke induced stress concentration at the caldera/shallow chamber, in addition to that generated by the doming. The dyke-induced stress concentration contributed to three processes during the 2014–15 episode. First, normal-fault slip along the ring-fault. Focal mechanisms indicate dominating normal-fault slip along the ring-fault (Bjarnason, 2014; Hensch et al., 2015; Riel et al., 2015). Much of the faulting occurred at the northern and southern sectors of the ring-fault, exactly in the areas where numerical and analytical models suggest that dyke-induced stress encourages normal faulting (Gudmundsson et al., 2014). Second, caldera elongation and "breakout" mechanisms at the northern and southern sectors of the caldera/chamber were induced by the dyke. These may have encouraged ring-dyke emplacement. Third, ductile deformation and flow in the ice inside the caldera. The caldera rim is composed of tall mountains that transmitted the compressive stress induced by the dyke to the ice, resulting in ice flow out of the caldera. The rate of flow of ice was greatest immediately following the dyke emplacement, and then gradually declined, as is typical of creeping material response to a sudden load (here the dyke emplacement). How much the ice flow contributed to the measured 60-m-subsidence in the ice is as yet unknown.

As the excess pressure in the reservoir p_e decreased below a certain level, the stress concentration around the ring-fault became too small for further significant to large slips and associated earthquakes to occur. This follows because the main slips were through normal faulting, so that the slips were controlled by the available driving stress at any time. Thus both the ice flow and the ring-fault subsidence gradually decreased with time. Significant subsidence in the caldera had apparently stopped in early February, several weeks before the eruption in Holuhraun came to an end on 27 February 2015. That the eruption continued for several more weeks indicates that it ceased only when the excess pressure in the deep-seated reservoir had vanished completely, that is, its excess pressure p_e had become zero.

Acknowledgements

We thank the Editor, Joan Marti, and two anonymous reviewers for very helpful comments. AG thanks Ari Trausti Gudmundsson and Thorvaldur Thordarson for many discussions about the Bardarbunga–Holuhraun episode. The outstanding services provided by the Iceland Meteorological Office in general, and the SIL-network group in particular, during the episode are very much appreciated. All the data from the SIL-network referred to in the present paper, however, are from published work.

References

Acocella, V., 2007. Understanding caldera structure and development: an overview of analogue models compared to natural calderas. Earth Sci. Rev. 85, 125–160.
Acocella, V., Cifelli, F., Funiciello, R., 2000. Analogue models of collapse calderas and resurgent domes. J. Volcanol. Geotherm. Res. 1–4, 81–96.
Amadei, B., Stephansson, O., 1997. Rock Stress and its Measurement. Chapman and Hall, New York.
Anderson, E.M., 1936. The dynamics and formation of cone-sheets, ring dikes, and cauldron-subsidence. R. Soc. Edinb. Proc. 128–157.
Bali, E., Gudfinnsson, G.H., Gunnarsson, H., Halldorsson, S.A., Jakobsson, S., Riishuus, M.S., Sigmarsson, O., Sigurdsson, G., Sverrisdottir, G., Thordarson, T., 2014. Petrology of the new fissure eruption north of Dyngjujökull. Geoscience Society of Iceland, Autumn Meeting. Reykjavik, pp. 5–6.
Becerril, L., Galindo, I., Gudmundsson, A., Morales, J.M., 2013. Depth of origin of magma in eruptions. Sci. Rep. 3, 2762. http://dx.doi.org/10.1038/srep02762.
Bjarnason, I., 2014. Earthquake sequence 1973–1996 in Bardarbunga volcano: seismic activity leading up to eruptions in the NW-Vatnajokull area. Jökull 64, 61–82.
Björnsson, H., 1988. Hydrology of Ice Caps in Volcanic Regions. University of Iceland, Societas Scientarium Islandica.
Bosworth, W., Burke, K., Strecker, M., 2003. Effect of stress fields on magma chamber stability and the formation of collapse calderas. Tectonics 22. http://dx.doi.org/10.1029/2002TC001369.
Browning, J., Gudmundsson, A., 2015. Caldera faults capture and deflect inclined sheets: an alternative mechanism of ring dike formation. Bull. Volcanol. 77, 1–13. http://dx.doi.org/10.1007/s00445-014-0889-4.
Cole, J., 1990. Structural control and origin of volcanism in the Taupo volcanic zone, New Zealand. Bull. Volcanol. 52, 445–459. http://dx.doi.org/10.1007/BF00268925.
Cole, J., Milner, D., Spinks, K., 2005. Calderas and caldera structures: a review. Earth Sci. Rev. 69, 1–26. http://dx.doi.org/10.1016/j.earscirev.2004.06.004.
De Natale, G., Pingue, F., 1993. Ground deformations in collapsed caldera structures. J. Volcanol. Geotherm. Res. 57, 19–38.
Deb, D., 2006. Finite Element Method: Concepts and Applications in Geomechanics. Prentice-Hall, New York.
Druitt, T., Sparks, R.S.J., 1984. On the formation of caldera during ignimbrite eruptions. Nature 310, 679–681.
Folch, A., Martí, J., 2004. Geometrical and mechanical constraints on the formation of ring-fault calderas. Earth Planet. Sci. Lett. 221, 215–225.
Fritz, W.J., Howells, M.F., Reedman, A.J., Campbell, S.D.G., 1990. Volcaniclastic sedimentation in and around an Ordovician subaqueous caldera, Lower Rhyolitic Tuff Formation, North Wales. Geol. Soc. Am. Bull. 78, 1246–1256. http://dx.doi.org/10.1130/0016-7606.
Gammon, P.H., Kiefte, H., Clouter, M.J., Denner, W.W., 1983. Elastic constants of artificial and natural ice samples by Brillouin spectroscopy. J. Phys. Chem. 29, 433–460. http://dx.doi.org/10.1021/j100244a004.
Geshi, N., Shimano, T., Chiba, T., Nakada, S., 2002. Caldera collapse during the 2000 eruption of Miyakejima Volcano, Japan. Bull. Volcanol. 64, 55–68. http://dx.doi.org/10.1007/s00445-001-0184-z.
Geyer, A., Bindeman, I., 2011. Glacial influence on caldera-forming eruptions. J. Volcanol. Geotherm. Res. 202, 127–142.
Geyer, A., Gottsmann, J., 2010. The influence of mechanical stiffness on caldera deformation and implications for the 1971–1984 Rabaul uplift (Papua New Guinea). Tectonophysics 483, 399–412. http://dx.doi.org/10.1016/j.tecto.2009.10.029.
Geyer, A., Folch, A., Martí, J., 2006. Relationship between caldera collapse and magma chamber withdrawal: an experimental approach. J. Volcanol. Geotherm. Res. 157, 375–386.
Gray, J.P., Monaghan, J.J., 2004. Numerical modelling of stress fields and fracture around magma chambers. J. Volcanol. Geotherm. Res. 135, 259–283.
Gregg, P.M., De Silva, S.L., Grosfils, E.B., Parmigiani, J.P., 2012. Catastrophic caldera-forming eruptions: thermomechanics and implications for eruption triggering and maximum caldera dimensions on Earth. J. Volcanol. Geotherm. Res. 241–242, 1–12. http://dx.doi.org/10.1016/j.jvolgeores.2012.06.009.
Grosfils, E.B., McGovern, P.J., Gregg, P.M., Galgana, G.A., Hurwitz, D.M., Long, S.M., Chestler, S.R., 2015. Elastic models of magma reservoir mechanics: a key tool for investigating planetary volcanism. Geological Society of London, Special Publications http://dx.doi.org/10.1144/SP401.2.
Gudmundsson, A., 1998. Formation and development of normal-fault calderas and the initiation of large explosive eruptions. Bull. Volcanol. 60, 160–171. http://dx.doi.org/10.1007/s004450050224.
Gudmundsson, A., 2003. Surface stresses associated with arrested dykes in rift zones. Bull. Volcanol. 65, 606–619. http://dx.doi.org/10.1007/s00445-003-0289-7.
Gudmundsson, A., 2007. Conceptual and numerical models of ring-fault formation. J. Volcanol. Geotherm. Res. 164, 142–160.
Gudmundsson, A., 2011. Rock Fractures in Geological Processes. Cambridge University Press, Cambridge.
Gudmundsson, A., 2012. Magma chambers: formation, local stresses, excess pressures, and compartments. J. Volcanol. Geotherm. Res. 237–238, 19–41.
Gudmundsson, A., 2014. Elastic energy release in great earthquakes and eruptions. Front Earth Sci. 2, 10. http://dx.doi.org/10.3389/feart.2014.00010.
Gudmundsson, A., 2015. Collapse-driven large eruptions. J. Volcanol. Geotherm. Res. 304, 1–10. http://dx.doi.org/10.1016/j.jvolgeores.2015.07.033.
Gudmundsson, M.T., Sigmundsson, F., Björnsson, H., 1997. Ice–volcano interaction of the 1996 Gjálp subglacial eruption, Vatnajökull, Iceland,. Nature 389, 954–957.
Gudmundsson, M.T., Sigmundsson, F., Björnsson, H., Högnadóttir, T., 2004. The 1996 eruption at Gjálp, Vatnajökull ice cap, Iceland: efficiency of heat transfer, ice deformation, and subglacial water pressure. Bull. Volcanol. 66, 46–65. http://dx.doi.org/10.1007/s00445-003-0295-9.

Gudmundsson, M.T., Thordarson, T., Höskuldsson, A., Larsen, G., Björnsson, H., Prada, F.J., Oddsson, B., Magnusson, E., Högnadottir, T., Petersen, G.N., Hayward, C.L., Stevenson, J.A., Jonsdottir, I., 2012. Ash generation and distribution from the April–May 2010 eruption of Eyjafjallajökull, Iceland. Sci. Rep. 2. http://dx.doi.org/10.1038/srep00572.

Gudmundsson, A., Lecoeur, N., Mohajeri, N., Thordarson, T., 2014. Dike emplacement at Bardarbunga, Iceland induces unusual stress changes, caldera deformation, and earthquakes. Bull. Volcanol. 76, 1–7. http://dx.doi.org/10.1007/s00445-014-0869-8.

Haddadi, B., Sigmarsson, O., Devidal, J.L., 2015. Determining intensive parameters through clinopyroxene-liquid equilibrium in Grímsvötn 2011 and Bárðarbunga 2014 basalts. Geophys. Res. Abstr. 17 (EGU2015-5791-2).

Hartley, M.E., Thordarson, T., 2012. Formation of Oskjuvatn caldera at Askja, North Iceland: mechanism of caldera collapse and implications for the lateral flow hypothesis. J. Volcanol. Geotherm. Res. 227-228, 85–101.

Hensch, M., Cesca, S., Heimann, S., Rivalta, E., Hjörleifsdottir, V., Jonsdottir, K., Vogfjörd, K., Dahm, T., the SIL Earthquake Monitoring Team, 2015. Earthquake focal mechanisms associated with the dyke propagation and caldera collapse at the Bardarbunga volcano, Iceland. Geophys. Res. Abstr. 17 (EGU2015-5854-1).

Hickey, J., Gottsmann, J., 2014. Benchmarking and developing numerical finite element models of volcanic deformation. J. Volcanol. Geotherm. Res. 280, 126–130.

Hjörleifsdóttir, V., Jónsdóttir, K., Hensch, M., Guðmundsson, G., Roberts, M., Ófeigsson, B., M. T., Gudmundsson, M., 2015. Numerous large and long-duration seismic events during the Bárðarbunga volcanic eruption in 2014: what do they tell us about the caldera subsidence? Geophys. Res. Abstr. 17 (EGU2015-8143-1EGU).

Holohan, E.P., Troll, V.R., Walter, T.R., Münn, S., McDonnell, S., Shipton, Z.K., 2005. Elliptical calderas in active tectonic settings: an experimental approach. J. Volcanol. Geotherm. Res. 144, 119–136.

Holohan, E.P., Schöpfer, M.P.J., Walsh, J.J., 2011. Mechanical and geometric controls on the structural evolution of pit crater and caldera subsidence. J. Geophys. Res. 116. http://dx.doi.org/10.1029/2010JB008032.

Kennedy, B., Stix, J., Vallance, J.W., Lavallée, Y., Longpré, M.A., 2004. Controls on caldera structure: results from analogue sandbox modeling. Geol. Soc. Am. Bull. 116, 515. http://dx.doi.org/10.1130/B25228.1.

Kinvig, H.S., Geyer, A., Gottsmann, J., 2009. On the effect of crustal layering on ring-fault initiation and the formation of collapse calderas. J. Volcanol. Geotherm. Res. 186, 293–304.

Kusumoto, S., Gudmundsson, A., 2009. Magma-chamber volume changes associated with ring-fault initiation using a finite-sphere model: application to the Aria caldera, Japan. Tectonophysics 471, 58–66. http://dx.doi.org/10.1016/j.tecto.2008.09.001.

Lavallée, Y., Stix, J., Kennedy, B., Richer, M., Longpré, M.A., 2004. Caldera subsidence in areas of variable topographic relief: results from analogue modeling. J. Volcanol. Geotherm. Res. 129, 219–236.

MacDonald, G.A., 1965. Hawaiian calderas. Pac. Sci. 19, 320–334.

Manconi, A., Walter, T.R., Amelung, F., 2007. Effects of mechanical layering on volcano deformation. Geophys. J. Int. 170, 952–958. http://dx.doi.org/10.1111/j.1365-246X.2007.03449.x.

Marti, J., Geyer, A., Folch, A., 2009. A genetic classification of collapse calderas based on field studies and analogue and theoretical modelling. In: Thordarson, T., Self, S. (Eds.), Volcanology: The Legacy of GPL Walker. IAVCEI-Geological Society of London, London, pp. 249–266.

Masterlark, T., 2007. Magma intrusion and deformation predictions: sensitivities to the Mogi assumptions. J. Geophys. Res. 112, 6419. http://dx.doi.org/10.1029/2006JB004860.

Michon, L., Massin, F., Famin, V., Ferrazzini, V., Roult, G., 2011. Basaltic calderas: collapse dynamics, edifice deformation, and variations of magma withdrawal. J. Geophys. Res. 116. http://dx.doi.org/10.1029/2010JB007636.

Mogi, K., 1958. Relations between eruptions of various volcanoes and the deformations of the ground surfaces around them. Bull. Earthquake Res. Inst. 36, 99–134.

Murase, T., McBirney, A.R., 1973. Properties of some common igneous rocks and their melts at high temperatures. Geol. Soc. Am. Bull. 84, 3563–3592.

Ofeigsson, B.G., Hreinsdottir, S., Sigmundsson, F., Fridriksdottir, H., Parks, M., Dumont, S., Arnadottir, T., Geirsson, H., Hooper, A., Roberts, M., Bennett, R., Sturkell, E., Jonsson, S., Lafemina, P., Jonsson, T., Bergsson, B., Kjartansson, V., Steinthorsson, S., Einarsson, P., Drouin, V., 2015. Deformation derived GPS geodesy associated with Bardarbunga 2014 rifting event in Iceland. Geophys. Res. Abstr. 17 (EGU2015-7691-4).

Parameswaran, V., 1987. Orientation dependence of elastic constants for ice. Def. Sci. J. 37, 367–375. http://dx.doi.org/10.14429/dsj.37.5924.

Paterson, W.S.B., 1994. The Physics of Glaciers. 3rd ed. Pergamon/Elsevier, Kidlington (480 pp.).

Peltier, A., Famin, V., Bachèlery, P., Cayol, V., Fukushima, Y., Staudacher, T., 2008. Cyclic magma storages and transfers at Piton de La Fournaise volcano (La Réunion hotspot) inferred from deformation and geochemical data. Earth Planet. Sci. Lett. 270, 180–188.

Philipp, S.L., Afsar, F., Gudmundsson, A., 2013. Effects of mechanical layering on hydrofracture emplacement and fluid transport in reservoirs. Front Earth Sci. 1. http://dx.doi.org/10.3389/feart.2013.00004.

Phillipson, G., Sobradelo, R., Gottsmann, J., 2013. Global volcanic unrest in the 21st century: an analysis of the first decade. J. Volcanol. Geotherm. Res. 264, 183–196.

Riel, B., Milillo, P., Simons, P., Lundgren, P., Kanamori, H., Samsonov, S., 2015. The collapse of Bardarbunga caldera, Iceland. Geophys. J. Int. 202, 446–453. http://dx.doi.org/10.1093/gji/ggv157.

Roche, O., Druitt, T.H., Merle, O., 2000. Experimental study of caldera formation. J. Geophys. Res. 105, 395. http://dx.doi.org/10.1029/1999JB900298.

Savin, G.N., 1961. Stress Concentration Around Holes. Pergamon, New York.

Schulson, E.M., Duval, P., 2009. Creep and Fracture of Ice. Cambridge University Press, Cambridge.

Sigmundsson, F., Hooper, A., Parks, M., Spaans, K., Gudmundsson, G.B., Drouin, V., Samsonov, S., White, R.S., Hensch, M., Pedersen, R., Bennett, R.A., Greenfield, T., Green, R.G., Sturkell, E., Bean, C.J., Mo, M., Femina, P.C. La, Bjo, H., Pa, F., Braiden, A.K., Eibl, E.P.S., 2015. Segmented lateral dyke growth in a rifting event at Bardarbunga volcanic system, Iceland. Nature 517, 191–195.

Sigurdsson, H., Sparks, S.R., 1978. Lateral magma flow within rifted Icelandic crust. Nature 274, 126–130.

Stix, J., Kobayashi, T., 2008. Magma dynamics and collapse mechanisms during four historic caldera-forming events. J. Geophys. Res. 113. http://dx.doi.org/10.1029/2007JB005073.

Vogfjörd, K., Hensch, M., Hjörleifsdottir, V., Jonsdottir, K., 2015. High-precision mapping of seismicity in the last decades at Bardarbunga volcano, Iceland. Geophys. Res. Abstr. 17 (EGU2015-13430-2).

Williams, H., 1941. Calderas and their origin, University of California Publications. Bull. Dep. Geol. Sci. 25, 239–346.

Zienkiewicz, O.C., 1979. The Finite Element Method. McGraw-Hill, New York (787 pp.).

6.1 Further discussion

It is important to further consider the limitations of this modelling study. The most significant of which concerns the assumption of linear elasticity with respect to caldera-fault deformation. Faults are discontinuities that allow elastic movement of adjacent walls when experiencing a required stress. However, the fault movement can be considered as an essentially anelastic process. The finite element method modelling used here does not model an anelastic process as the bonds that join each mesh node cannot be broken. The deformation therefore likely represents a maximum, although it is clear that at Bardarbunga-Holuhraun there was no substantial development of a ring-fault as evidenced by the lack of ice surface fractures.

Our interpretation is that subsidence within the ice surface is at least partly related to loading from the emplaced regional dyke. This idea relies on the assumption that the dyke loading effectively alters the physical state of the ice from a brittle material to a partially ductile material and is thus able to flow. If the ice remained brittle throughout then instead of subsidence we would expect a stacking or inflation signal, which is not found anywhere on the ice surface.

Chapter 7: Discussion, critical evaluation and future directions

7.2 Forecasting worldwide magma chamber failure conditions

Most studies of volcano deformation concentrate on identifying the source of magma inflation or deflation, for example importance is often concentrated on estimating the depth and size of an underlying magma chamber (e.g. Segall, 2013; Sigmundsson, 2006). Deformation studies have also focussed attention to host rock characteristics and how deformation is affected by varying host rock rheologies and heterogeneities (Geyer and Gottsmann, 2010; Hickey et al., 2013; Masterlark, 2007). Very few studies attempt to constrain conditions for the chamber wall failure and then estimate dyke propagation paths, but these are important questions that need to be addressed when any volcano is experiencing unrest. In chapter 3 (Browning et al., in press) we have offered a new method for constraining magma chamber failure, and it is hoped that the model will be expanded upon at other volcanoes, and then tested during periods of unrest. To build on this study it would be useful to constrain magma chamber volumes and likely failure conditions at other well studied caldera volcanoes, particularly those that are believed to possess a double magma chamber feeder system, i.e many of the calderas in Iceland (Camitz et al., 1995; Gudmundsson, 1987; Sigmundsson, 2006), Miyakejima and other volcanoes in Japan (Geshi et al., 2002), the volcanoes of the Taupo volcanic zone (Wilson et al., 1994) to name just a few.

The major limitation of our study on magma chamber failure concerns the simplicity of the analytical solutions. Pre-existing faults and fractures can greatly influence magma propagation (Browning and Gudmundsson, 2015) and ground deformation (Browning and Gudmundsson, in press). Several well-known major fault systems exist at Santorini caldera, for example the Kameni Line and the Coloumbo line, as well as the caldera faults from the Minoan eruption and early events. These tectonic features are likely to affect ground deformation and seismicity during periods of

magmatic recharge at Santorini (Konstantinou et al., 2013; Papoutsis et al., 2013). Therefore, whilst beyond the scope of the current study, it will be important to incorporate fault dynamics and heterogeneities when applying the method to forecasting magma chamber failure. This will likely involve a numerical modelling approach as the number of parameters becomes too great to model analytically. Firstly however, detailed information on how faults and heterogeneities affect ground surface displacements is needed, supplementing previous work on this topic (e.g Manconi et al., 2007; Masterlark, 2007). Much of the discussion of this thesis describes the limitations of the models presented and suggests further studies which may improve such methods.

All assumptions of tension related host rock failure, i.e dyke injection, assume tensile strengths of between 0.5 and 6 MPa (Amadei and Stephenson, 1997). More recent laboratory studies, concerned primarily with the injection of fluid driven fractures, have estimated maximum values of tensile strength around 7-11 MPa (Benson et al., 2012). Numerical studies of geothermal systems in New Zealand estimate the tensile strength of the Rotakawa andesite to be in the range 10 to 24 MPa (Siratovich et al., 2015). It is clear from the literature that the range of host rock strengths is variable, and that further studies are needed to constrain the range at individual caldera volcanoes. Here we use relatively minimal values of tensile strength to estimate the range over which rocks will fail as a result of an excess (or driving) pressure, based on these assumptions.

The qualitative nature of our final forecast model (Browning et al., in press) means that the thresholds between the various phases of chamber failure likelihood are highly subjective, although based on data from rock mechanics experiments and borehole data so reasonably robust. Therefore any tests of the model should aim to constrain using statistical methods, the probability of failure occurrence over time during the unrest, and it is hoped that our method will help inform such a probabilistic study. In addition, future studies should look to assess how long it takes to create forecast models. The length of time in this case will be governed by the speed at which simple Mogi solutions for depth and pressure (volume) change can be solved during a magma chamber inflation event. In the age of broadband seismometers, strain meters and continuously recording and transmitting GPS

stations, this task should be completed within a reasonable timeframe. If the model relied on InSAR data then this could present problems for forecasting chamber rupture, because the technique commonly relies on the repositioning of suitable satellites, such that temporal resolution or timescale of deployment may not be sufficient to capture the beginning of a magmatic recharge event. Similar techniques may be hampered by meteorological conditions, or ground cover. For example much of the early inflation at Bardarbunga in 2014 was dominated by regional doming (Ofeigsson et al., 2015); the local subsidence signal from the caldera was not detected until much later on, partly because of the availability of GPS stations on the glacier. It should be noted that our study on the implications of the Bardarbunga-Holuhraun episode (Browning and Gudmundsson, in press) assume the presence of a caldera lake based on studies of other sub-glacial caldera volcanoes, but may not be the case at Bardarbunga. It is hoped that these theoretical models are useful for understanding and delimiting various aspects of caldera deformation associated with rapid subsidence.

Deformation studies focusing on the size and depth of magma chambers, whilst important and valid, should aim to give more consideration to providing forecasts of magma movement. Such forecasts should not initially be used as a mechanism to alert at risk communities until they have been sufficiently tested at the volcano in question. The data provide a first step in forecasting volcanic eruptions, which is one of the ultimate goals in volcanology. Then the task of predicting how large and for how long that eruption will last is an equally important problem.

7.3 Towards a characterisation of caldera fault damage zones

Whilst the structural and topographic boundaries of many active and ancient caldera systems are well mapped and constrained (Geyer and Martí, 2008); very few studies have measured the frequency of micro and macro fracture damage directly adjacent to caldera faults. This is partly because so few calderas faults around the world are well exposed. For example, the compilation of calderas produced by Geyer and Marti (2008) contains information on caldera size predominantly based on

topographical boundaries, in which case the area of a caldera fault is already ambiguous, as is highlighted by the large error and uncertainty of areas and volume estimates. In addition, those geological studies that directly observe caldera faults, or fracture zones (e.g. Acocella, 2006; Branney, 1995; Browning and Gudmundsson, 2015; Lipman, 1984), are hampered often by significantly weathered and altered rocks. This is of course a consequence of the complex geothermal and hydrothermal systems that operate near caldera faults (Kokelaar 2007). Still, almost all of the aforementioned studies have focused predominantly on macro-fractures surrounding caldera faults. It would be useful and worthwhile to conduct a similar detailed study, probably in Iceland, Western USA, New Zealand or Japan of micro-fractures within and around caldera faults.

Many permeability studies of major fault systems have been conducted (e.g Caine et al., 1996; Evans et al., 1997; Faulkner et al., 2003). Detailed geological studies have shown the development of fault damage zones based on the frequency of micro and macro fractures as a function of distance from major faults (Mitchell and Faulkner, 2012). Such studies have been used to infer a mechanism of principal stress rotation within low angle normal faults (Faulkner et al., 2006). The quantification of damage zones at caldera faults are difficult for the reasons given above and perhaps impossible because the original ring-fault has long been eroded or experienced mass wasting (Hartley and Thordarson, 2012; Wilson et al., 1994).

Several assumptions have been made regarding the mechanical state of the rocks within and surrounding the caldera ring-fault at Hafnarfjall, Western Iceland (Chapter 4). Future work could try to quantify the state of damage within the fault core and surrounding host rock using the methods of (Mitchell and Faulkner, 2012, 2008). Whilst such a study would not provide precise information about the stiffness of rocks at the time of magma emplacement, it would give clues as to the how caldera faults propagate and influence host rock properties. An interesting study would be to compare caldera fault damage with data from well-studied fault systems (Gudmundsson and Brenner, 2003; Mitchell and Faulkner, 2012). At present there is no direct quantification of caldera fault damage zones, the only studies that hypothesize the occurrence of such mechanical situations rely on interpretation of numerical or dynamic wave velocity models (e.g Browning and Gudmundsson,

2015; Giannopoulos et al., 2015). Many if not most caldera faults remain active for many hundreds or thousands of years following their formation, as shown by repeated seismic unrest associated with the Bardarbunga caldera faults (Fichtner and Tkalčić, 2010; Gudmundsson et al., 2014; Konstantinou et al., 2003; Sigmundsson et al., 2014), and Santorini caldera faults (Druitt and Francaviglia, 1992; Konstantinou et al., 2013) making fault zone evolution is likely an important consideration. Several fault core and damage zones may develop by repeated slip and re-activation, as is known from studies of major tectonic related fault systems worldwide (Faulkner et al., 2010), Figure 7.1. Estimates of damage accumulation in caldera fault zones may be useful for understanding permeability development during periods of volcanic unrest. Fault zone permeability models can be constrained by ice melting at subglacial calderas (Reynolds and Gudmundsson, 2014), or degassing (Padrón et al., 2008; Shinohara, 2008) due to increased fluid flow and geothermal activity (Axelsson et al., 2006).

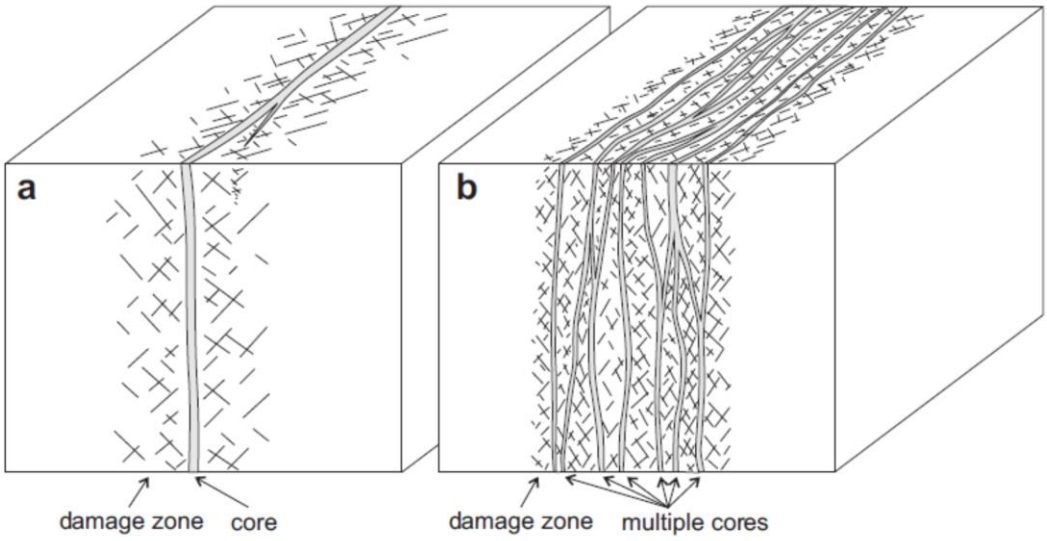

Figure 7.1: Models of relationship between damage and core zones, a) shows a single core and associated damage zone, b) shows multiple cores and associated damage zones modified after (Faulkner et al., 2010).

An appropriate question at this point may then be, 'to what effect does ring-fault damage control ground deformation during fault-slip or inflation or deflation episodes?'. In Browning and Gudmundsson (in press) we have shown that

significant surface subsidence occurs many tens of kilometres away from a gravity driven roof collapse. However, a zone of weak rock, i.e. a ring-fault damage zone, reduces the total amount of ground surface subsidence (Masterlark, 2007). It has also been noted that the development of fracture networks can act to mask a related subsidence inversion signal (e.g Holohan et al., 2015). For example, original inversions of the summit collapse at Piton de la Fournaise in 2007 using standard techniques (Mogi, 1958) presented three potentially distinct sources of deformation. However, discrete element method models show that the deformation can be easily explained by the deflation and collapse of one 'sill like' source (Holohan et al., 2015). The difference between the 'standard' models and the 'newer' method is the inclusion of fracture networks generated in conjunction with collapse, therefore understanding fracture distribution, through field studies, statistical techniques and seismic tomography are vitally important for properly constraining ground deformation signals.

7.4 Assessing the influence of thermo-mechanical damage accumulation

It has been shown through the various chapters presented within this thesis that fractures and other heterogeneities within rock layers can have a direct impact on magma propagation and magma chamber failure. It is possible that part of that damage can be created by thermal stresses generated during magmatic and host rock cooling. Much more work is needed to understand crustal thermal stress and the resultant effect on damage accumulation within and around shallow magma systems. We have found that the dominant mechanism of thermal stress damage accumulation in the crust and in eruptive products is likely to result from contraction due to cooling rather than expansion through heating, e.g. extrusive lava domes and lava flows where the controlling thermal regime following emplacement is cooling. In this case cooling generates cracks which, through increased surface area, further increase cooling potential and may act as pathways for gas escape. The two mechanisms of cooling and gas escape combine to dramatically increase viscosity which is a primary control on the velocity of a lava flow and also influences the lava final flow length. In the shallow crust, both heating expansion and cooling

contraction stresses operate, probably by similar amounts. It is though contractive, and therefore overall tensile stress which is likely to generate the predominant damage, simply because crustal rocks are weaker in tension.

7.5 What is a 'realistic' magma chamber host rock rheology?

This brings us to an important question, namely, 'what are the conditions of rocks surrounding magma chambers?'. Many of the models discussed within this thesis have simulated either a linear elastic or a poro-elastic crust with various combinations of internally pressurised cavities and differential boundary or loading conditions. Many studies have shown that linear elasticity does not fully represent crustal rheology at great depths and surrounding 'hot' magma (e.g Gregg et al., 2012). In high temperature tests on basaltic rocks from Iceland we noted the development of melt induced fractures on the outer surface of samples (Browning et al., 2015). The textures observed indicate partial melt was able to generate sufficiently high internal overpressure to overcome the tensile strength of the brittle sample surface. Although the outcome was not expected and largely unwanted, as it hampered crack annealing, such tests may be developed to understand more about the high temperature host rock halo that surrounds magma chambers. Although some authors suggest otherwise (e.g Hooper et al., 2011), it is clear from field and laboratory evidence that dykes 'magma filled fractures' propagate using the same mechanism as almost every other fluid driven fracture, namely as mode I fractures. At several localities in Iceland, but perhaps the best exposed at Slafrudalur in the East, felsic dykes can be observed cutting through the sharp granophyre to basalt contact of the extinct pluton and host rock (Gudmundsson, 2012). These field observations together with experimental observations suggest that magma chamber envelopes can remain predominantly brittle, particularly in response to fluid overpressure driving forces.

7.6 Towards a method of quantifying crack annealing in volcanic rocks

Whilst the timescales of viscous relaxation are relatively well constrained (Dingwell and Webb, 1989; Giordano et al., 2008; Hess et al., 2008), almost no work has been done to apply that process to measure crack annealing in volcanic rocks. The most relevant work has utilised analogue materials such as glass beads in order to constrain viscous annealing 'or sintering' in volcanic ash and rheomorphic flows (Vasseur et al., 2013; Wadsworth et al., 2014). Such studies utilise perfect glasses to measure the time taken for the spheres to sinter, which is a function of the glass viscosity, controlled partly by temperature, and the effects of surface tension. Whilst the setup is suitable for deciphering processes in silicic, glass rich magma such as is abundant in explosive ash fragments, the method is a poor analogue for intrusions and lavas that contain abundance of crystals and groundmass, all of which seeks to impede melt relaxation and fracture annealing. Our original method for characterising crack annealing, based on the principle of P-wave velocity changes in rocks due to the presence (or absence) of cracks proved ineffective. This was a consequence of the need for a suitably long wave-guide to ensure that all moveable parts (springs etc.), and signal transducers were located outside of the furnace hot-zone. The consequence was substantially reduced P-wave transmission resulting from wave attenuation. It is suggested that much more future work can be done to understand fracture annealing in volcanic rocks, and ideally build on the conventional models of viscous relaxation which really only apply to glasses and silicates.

7.7 The 'gravity problem'

In COMSOL Multiphysics there is an option to apply a gravity load to the model domain. It has been speculated that omitting the loading force due to gravity provides inaccurate results in terms of pressures associated with magma chamber rupture and the location of rupture (see Grosfils 2007 for details). For example most published numerical studies of pressurized ellipsoidal magma reservoirs give modest estimates of rupture pressures (0.5-9 MPa) (e.g Jellinek & DePaolo 2003; Trasatti et al. 2008; Gudmundsson 2012). However, those studies which add additional gravity effects as a loading condition in the finite element model output failure related

pressures in excess of 100 MPa (Currenti and Williams, 2014; Grosfils, 2007; Grosfils et al., 2015). This issue can be clarified by considering initially the geostatic state of stress, or vertical stress (σ_v) which can be given as:

$$\sigma_v = \rho_r g z \qquad (7.1)$$

with a simple assumption that all the crustal layers have the same density, ρ_r. The vertical co-ordinate z is positive downwards, i.e toward increasing crustal depth, and g is the acceleration due to gravity. Vertical stress can also be termed 'lithostatic stress' (Gudmundsson, 2012). As has been discussed in Chapter 3, throughout the majority of a magma chambers lifespan it will reside in lithostatic equilibrium, that is, have a magma-pressure close to the pressure of the stresses in the host rock. It is only during periods of unrest when the host rock deforms as an immediate response to pressure changes (e.g Mogi 1958; Dzurisin, 2006; Segall, 2010). A magma chamber wall will rupture when the magma pressure inside the chamber exceeds the tensile strength of the host rock (T_o), and then a magma filled fracture will propagate perpendicular to the minimum principal compressive stress (σ_3). The normal state of stress in a rift zone, for example, is such that σ_3 is horizontal and therefore the propagation direction of dykes is vertical or parallel with the vertical stress σ_1. From eq. 1 we see that the vertical stress, σ_1, includes the effects of the acceleration due gravity (g). If we consider Newton's second law of motion, where force (F) is defined as mass (m) times acceleration (a):

$$F = m \times a \qquad (7.2)$$

Close to the Earth's surface the acceleration a in the Earth's gravity field can be interchanged with g (i.e 9.81 m s^{-2}), so that eq. 2 can be re-written as:

$$F = m \times g \qquad (7.3)$$

7.9 The unknowns of magma volume expansion and compressibility

Volume expansion and compressibility of magmas and host rock is reasonably poorly constrained with limited data available. Most work done to measure

compressibility in magmas and volcanic rocks was completed over three decades ago (Murase and Mcbirney, 1973), and provides generally little constraints on the error and uncertainty of values. It is well known that magma chamber rupture occurs as a result of volatile exsolution or magmatic recharge in shallow chamber system. What is much less well known or investigated is the contribution of melt volume expansion. Such a processes could occur as a result of hot mafic magma entering and melting a partially solidified felsic chamber, with the pressure increase in that chamber represented by 1) a new volume of mafic magma V_m, 2) gas exsolution and bubble growth in both magmas, which is directly related to compressibility of magma β_m and 3) expansion related to the phase change from a solid to a steady state liquid. Data for parameters 2 and 3 are much less abundant, and most data available for parameter 1 is acquired from geodetic studies that may underestimate the contribution of 2 and 3. This creates a problem interpreting the underlying causes of ground deformation during periods of unrest, as such, further work is needed.

7.10 The 'state-of-the-art'

The work that comprises this thesis has made several key contributions to understanding many aspects of volcano-tectonics on both a regional and local scale. The chapters are arranged such that the reader has been guided from a depth of approximately 10 to 20 km in the Earth's crust, where we find deep magma reservoirs. Parental magma from these reservoirs periodically recharges shallow magma chambers. A model has been proposed to estimate the timing of magma chamber roof rupture associated with resultant volume and pressure increases. When a shallow chamber does rupture a dyke is initiated, estimating the pathway of that magma is crucial for predicting the location of an eruption. We have found that caldera faults can significantly influence the propagation potential of favourably oriented sheets through a mechanism of principal stress rotation and elastic mismatch. Magma chambers, dykes and sheets are emplaced into cooler host rocks which then heat as a result. The thermal stresses resulting from heating and cooling throughout the emplacement cycle generate seismicity. Experimental results indicate that the predominant micro-crack development occurs during cooling in an overall tensile stress field. It has not been possible to relate acoustic emissions generated

within small laboratory scale samples held at atmospheric pressure to seismicity from magma chambers and intrusions at depth in the crust. Future work should consider these links and investigate the potential for combing these laboratory data with seismic data. Thick regional dykes can have significant regional stress effects, for example by changing the flow dynamics of nearby glaciers as has been demonstrated during the Bardarbunga-Holuhraun 2014-15 episode. Collapse of a magma chamber roof should also encourage significant far-field surface subsidence.

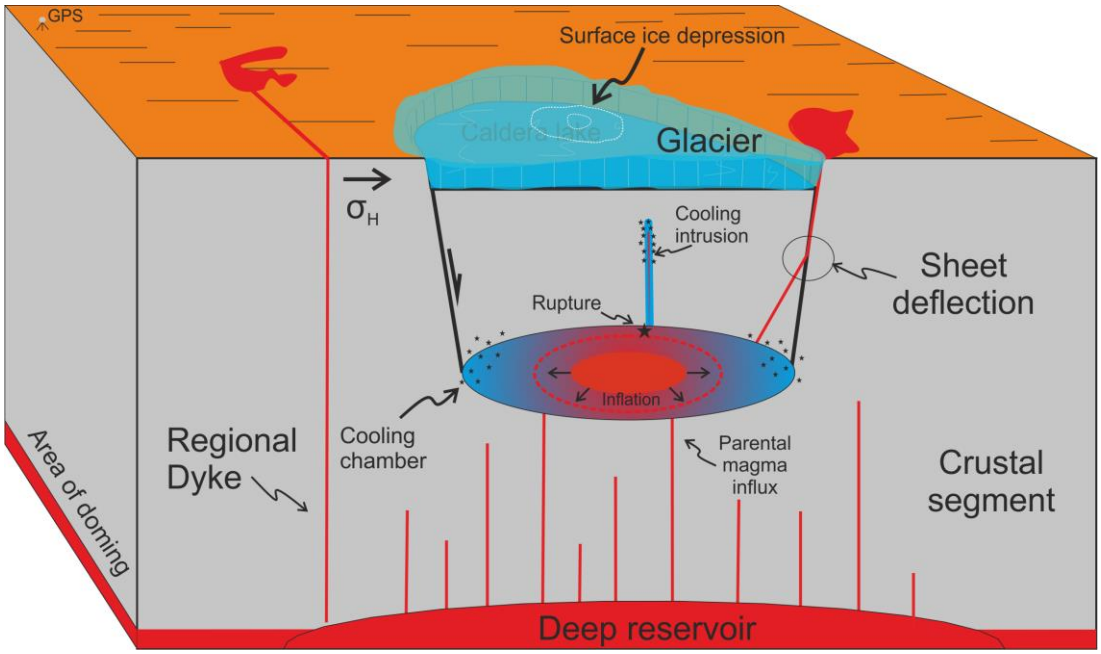

Figure 7.2: Schematic diagram illustrating the main contributions of this thesis. Parental magma recharge from a deep reservoir to a shallow chamber induces pressure changes, inflation and eventual rupture. When the chamber roof ruptures and initiates a sheet or dyke, the pathway is influenced by pre-existing discontinuities such as fault zones, encouraging, in the case of calderas deflection into ring-dykes. Shallow magma chambers and intrusions heat and cool the host rock leading to thermal stressing and seismicity. Emplacement of substantial regional dykes can have far reaching stress effects, for example influencing glacial flow dynamics. Magma chamber roof collapse induces regional scale subsidence. Not to scale.

Bibliography

Acocella, V., 2006. Regional and local tectonics at Erta Ale caldera, Afar (Ethiopia). *Journal of Structural Geology.* **28,** 1808-1820

Acocella, V., 2007. Understanding caldera structure and development: An overview of analogue models compared to natural calderas. *Earth-Science Reviews*. **85**, 125–160.

Amadei, B. & Stephenson, O., 1997. *Rock stress and its measurement*. Chapman and Hall, London. 516p

Anderson, E.M., 1937. Cone-sheets and Ring-dykes : the dynamical explanation. *Bulletin of Volcanology*. **1**, 35-40

Annen, C., 2011. Implications of incremental emplacement of magma bodies for magma differentiation, thermal aureole dimensions and plutonism-volcanism relationships. *Tectonophysics*, **500**, 3–10

Applegarth, L.J., Tuffen, H., James, M.J., Pinkerton, H., Cashman, K.V. 2013 Direct observations of degassing induced crystallisation in basalts, *Geology*, **41**, 243-246

Axelsson, G., Thorhallsson, S., Bjornsson, G., 2006. Stimulation of geothermal wells in basaltic rock in Iceland. *Enhanced geothermal innovation network for Europe Workshop*, Zurich Switzerland, **3,**

Barnett, Z. A. & Gudmundsson, A., 2014. Numerical modelling of dykes deflected into sills to form a magma chamber. *Journal of Volcanolology Geothermal Research*. **281**, 1–11.

Barton, M. & Huijsmans, J.P.P., 1986. Post-caldera dacites from the Santorini volcanic complex, Aegean Sea, Greece: an example of the eruption of lavas of

near-constant composition over a 2,200 year period. *Contributions to Mineralogy and Petrology*. **94**, 472–495.

Bathke, H., Nikkhoo, M., Holohan, E.P., Walter, T.R., 2015. Insights into the 3D architecture of an active caldera ring-fault at Tendürek volcano through modeling of geodetic data. *Earth and Planetary Science Letters*, **422**, 157–168.

Benson, P.M., Heap, M.J., Lavallée, Y., Flaws, A., Hess, K.-U., Selvadurai, a. P.S., Dingwell, D.B., Schillinger, B., 2012. Laboratory simulations of tensile fracture development in a volcanic conduit via cyclic magma pressurisation. *Earth and Planetary Science Letters*. **349-350**, 231–239.

Bond, A. & Sparks, R.S.J., 1976. The Minoan eruption of Santorini, Greece. *Journal of the Geological Society London*. **132**, 1–16.

Branney, M.J., 1995. Downsag and extension at calderas: new perspectives on collapse geometries from ice-melt, mining, and volcanic subsidence. *Bulletin of Volcanology* **57**, 303–318.

Browning, J., Meredith, P. G., Gudmundsson, A., Lavallée, Y., Drymoni, K. 2015. Are magma chamber boundaries brittle or ductile? Rheological insights from thermal stressing experiments. *European General Assembly*, Vienna.

Browning, J., Drymoni, K., Gudmundsson, A. in press. Forecasting magma chamber rupture at Santorini volcano, Greece. Scientific Reports.

Browning, J. & Gudmundsson, A., 2015. Caldera faults capture and deflect inclined sheets: an alternative mechanism of ring dike formation. Bulletin of Volcanology, 77

Browning, J. & Gudmundsson, A. in press. Surface displacements resulting from magma chamber failure and roof collapse, with application to the 2014 Bardarbunga-Holuhraun episode. Journal of volcanology and geothermal research.

Burchardt, S. & Gudmundsson, A., 2009. The infrastructure of the Geitafell Volcano, Southeast Iceland. Special Publication IAVCEI, 349–369.

Burchardt, S., Tanner, D.C., Krumbholz, M., 2010. Mode of emplacement of the Slaufrudalur Pluton, Southeast Iceland inferred from three-dimensional GPS mapping and model building. *Tectonophysics* **480**, 232–240.

Burchardt, S., Tanner, D.C., Troll, V.R., Krumbholz, M., Gustafsson, L.E., 2011. Three-dimensional geometry of concentric intrusive sheet swarms in the Geitafell and the Dyrfjall volcanoes, eastern Iceland. *Geochemistry, Geophys. Geosystems* **12**, 1–21.

Burchardt, S., Troll, V.R., Mathieu, L., Emeleus, H.C., Donaldson, C.H., 2013. Ardnamurchan 3D cone-sheet architecture explained by a single elongate magma chamber. *Scientific Reports*, **3**, 2891.

Caine, J.S., Evans, J.P., Forster, C.B., 1996. Fault zone architecture and permeability structure. *Geology* **24**, 1025–1028.

Camitz, J., Sigmundsson, F., Foulger, G., Jahn, C.H., Völksen, C., Einarsson, P., 1995. Plate boundary deformation and continuing deflation of the Askja volcano, North Iceland, determined with GPS, 1987-1993. *Bulletin of Volcanology*, **57**, 136–145.

Carlos, J., Day, S.J., Perez, F.J., 1999. Giant Quaternary landslides in the evolution of La Palma and El Hierro, Canary Islands. *Journal of Volcanology and Geothermal Research,* **94**, 169-190

Carracedo, J.C., 1999. Growth, structure, instability and collapse of Canarian volcanoes and comparisons with Hawaiian volcanoes. *Journal of Volcanology and Geothermal Research*. **94**, 1–19.

Cashman, K. V. & Giordano, G., 2014. Calderas and magma reservoirs. *Journal of Volcanology and Geothermal Research*. **288**, 28–45.

Coppo, N., Schnegg, P.-A., Heise, W., Falco, P., Costa, R., 2008. Multiple caldera collapses inferred from the shallow electrical resistivity signature of the Las Cañadas caldera, Tenerife, Canary Islands. *Journal of Volcanology and Geothermal Research*. **170**, 153–166.

Cox, S.J.D. & Meredith, P.G., 1993. Microcrack formation and material softening in rock measured by monitoring acoustic emissions. *International Journal of Rock Mechanics and Mining Sciences & Geomechanics Abstracts*, **30**, 11–24.

Currenti, G & Williams, C. A., 2014. Numerical modeling of deformation and stress fields around a magma chamber: Constraints on failure conditions and rheology. *Physics of the Earth and Planetary Interiors*, **226**, 14–27.

De Natale, G., Pingue, F., 1993. Ground deformations in collapsed caldera structures. *Journal of Volcanology and Geothermal Research*. **57**, 19–38.

De Zeeuw-van Dalfsen, E., Pedersen, R., Hooper, A., Sigmundsson, F., 2012. Subsidence of Askja caldera 2000-2009: Modelling of deformation processes at an extensional plate boundary, constrained by time series InSAR analysis. *Journal of Volcanology and Geothermal Research*. **213-214**, 72–82.

Dingwell, D.B. & Webb, S.L., 1989. Structural relaxation in silicate melts and non-Newtonian melt rheology in geologic processes. *Physics and Chemistry of Minerals*. **16**, 508–516.

Dominey-Howes, D. & Minos-Minopoulos, D., 2004. Perceptions of hazard and risk on Santorini. *Journal of Volcanology and Geothermal Research*. **137**, 285–310.

Druitt, T.H., 2014. New insights into the initiation and venting of the Bronze-Age eruption of Santorini (Greece), from component analysis. *Bulletin of Volcanology*. **76**, 1–21.

Druitt, T.H., Costa, F., Deloule, E., Dungan, M., Scaillet, B., 2012. Decadal to monthly timescales of magma transfer and reservoir growth at a caldera volcano. *Nature*, **482**, 77–80.

Druitt, T.H., Edwards, L., Mellors, R.., Pyle, D.., Sparks, R.S.J., Lanphere, M., Davies, M., Barriero, B., 1999. *Santorini Volcano*, Geological Society, London, Memoirs, 19

Druitt, T.H. & Francaviglia, V., 1992. Caldera formation on Santorini and the physiography of the islands in the late Bronze Age. *Bulletin of Volcanology*. **54**, 484–493.

Druitt, T.H. & Sparks, R.S.J., 1982. A proximal ignimbrite breccia facies on santorini , Greece. *Journal of Volcanology and Geothermal Research*. **13**, 147–171.

Faulkner, D.R., Jackson, C. A. L., Lunn, R.J., Schlische, R.W., Shipton, Z.K., Wibberley, C. A J., Withjack, M.O., 2010. A review of recent developments concerning the structure, mechanics and fluid flow properties of fault zones. Journal of Structural Geology. **32**, 1557–1575.

Faulkner, D.R., Lewis, A. C., Rutter, E.H., 2003. On the internal structure and mechanics of large strike-slip fault zones: Field observations of the Carboneras fault in southeastern Spain. *Tectonophysics* **367**, 235–251.

Faulkner, D.R., Mitchell, T.M., Healy, D., Heap, M.J., 2006. Slip on "weak" faults by the rotation of regional stress in the fracture damage zone. *Nature*, **444**, 922–925.

Fichtner, A. & Tkalčić, H., 2010. Insights into the kinematics of a volcanic caldera drop: Probabilistic finite-source inversion of the 1996 Bárdarbunga, Iceland, earthquake. *Earth and Planetary Science Letters*. **297**, 607–615.

Filson, J., Simkin, T., Leu, L., 1973. Seismicity of a caldera collapse: Galapagos Islands 1968. *Journal of Geophysical Research* **78**, 8591.

Fossen, H. 2010. *Structural Geology*. Cambridge University Press, p480

Friedrich, W.., 2009. *Santorini*. Aarhus University Press, p380

Fytikas, M., Innocenti, F., Manetti, P., Peccerillo, A., Mazzuoli, R., Villari, L., 1984. Tertiary to Quaternary evolution of volcanism in the Aegean region. *Geological Society London, Special Publications*. **17**, 687–699.

Garcia-Piera, J.O., Ledesma, A., Hu, M., 2000. Causes and mobility of large volcanic landslides : application to Tenerife , Canary Islands **103**, 121-134

Gautneb, H. & Gudmundsson, A., 1992. Effect of local and regional stress fields on sheet emplacement in West Iceland. *Journal of Volcanology Geothermal Research*, **51**, 339–356.

Gautneb, H., Gudmundsson, A., Oskarsson, N., 1989. Structure , petrochemistry and evolution of a sheet swarm in an Icelandic central volcano. *Geologic magazine* **126**, 659–673.

Geyer, A. & Martí, J., 2008. The new worldwide collapse caldera database (CCDB): A tool for studying and understanding caldera processes. *Journal of Volcanology Geothermal Research*. **175**, 334–354.

Geyer, A. & Gottsmann, J., 2010. The influence of mechanical stiffness on caldera deformation and implications for the 1971-1984 Rabaul uplift (Papua New Guinea). *Tectonophysics*, **483**, 399–412.

Geyer, A. & Marti, J., 2014. A short review of our current understanding of the development of ring faults during collapse caldera formation. *Frontiers in Earth Sciences*. **2**, 1–13.

Geshi, N., Kusumoto, S., Gudmundsson, A., 2010. Geometric difference between non-feeder and feeder dikes. *Geology* **38**, 195–198.

Geshi, N., Shimano, T., Chiba, T., Nakada, S., 2002. Caldera collapse during the 2000 eruption of Miyakejima Volcano, Japan. *Bulletin of Volcanology*. **64**, 55–68.

Giannopoulos, D., Sokos, E., Konstantinou, K.I., Tselentis, G. A., 2015. Shear wave splitting and VP/VS variations before and after the Efpalio earthquake

sequence, western Gulf of Corinth, Greece. *Geophysical Journal International* **200**, 1436–1448.

Giordano, D., Russell, J.K., Dingwell, D.B., 2008. Viscosity of magmatic liquids: A model. *Earth and Planetary Science Letters*, **271**, 123–134.

Gray, J.P. & Monaghan, J.J., 2004. Numerical modelling of stress fields and fracture around magma chambers. *Journal of Volcanology and Geothermal Research*, **135**, 259–283.

Gregg, P.M., De Silva, S.L., Grosfils, E.B., Parmigiani, J.P., 2012. Catastrophic caldera-forming eruptions: Thermomechanics and implications for eruption triggering and maximum caldera dimensions on Earth. Journal of Volcanology and Geothermal Research. **241-242**, 1–12.

Grosfils, E.B., 2007. Magma reservoir failure on the terrestrial planets: Assessing the importance of gravitational loading in simple elastic models. *Journal of Volcanology and Geothermal Research*, **166**, pp.47–75.

Grosfils, E.B., McGovern, P.J., Gregg, P.M., Galgana, G. A., Hurwitz, D.M., Long, S.M., Chestler, S.R., 2015. Elastic models of magma reservoir mechanics: a key tool for investigating planetary volcanism. *Geological Society London, Special Publications*, **401**, 239-267

Gudmundsson, A., 1983. Form and Dimensions of dykes in Eastern Iceland, *Tectonophysics*, **95**, 295–307.

Gudmundsson, A., 1986a. Possible effect of aspect ratios of magma chambers on eruption frequency. *Geology*, **14**, 991.

Gudmundsson, A., 1986b. Mechanical Aspects of Postglacial Volcanism and Tectonics of the Reykjanes Peninsula, Southwest Iceland. *Journal of Geophysical Research*, **91**, 12711–12721.

Gudmundsson, A., 1987a. Lateral magma flow, caldera collapse, and a mechanism of large eruptions in Iceland. *Journal of Volcanology and Geothermal Research*. **34**, 65–78.

Gudmundsson, A., 1987b. Formation and mechanics of magma reservoirs in Iceland. *Geophysical Journal International*, **91**, 27-41

Gudmundsson, A., 1990. Emplacement of dikes, sills and crustal magma chambers at divergent plate boundaries. *Tectonophysics*, **176**, 257–275.

Gudmundsson, A., 1998. Formation and development of normal-fault calderas and the initiation of large explosive eruptions. *Bulletin of Volcanology*, **60**, 160–170.

Gudmundsson, A. & Brenner, S.L., 2003. Loading of a seismic zone to failure deforms nearby volcanoes: A new earthquake precursor. *Terra Nova*. **15**, 187–193.

Gudmundsson, A. & Philipp, S.L., 2006. How local stress fields prevent volcanic eruptions. *Journal of Volcanology and Geothermal Research*. **158**, 257–268.

Gudmundsson, A. & Nilsen, K., 2006. Ring-faults in composite volcanoes: structures, models and stress fields associated with their formation. Geological Society of London, Special Publication, **269**, 83–108.

Gudmundsson, A., 2011. Deflection of dykes into sills at discontinuities and magma-chamber formation. *Tectonophysics* **500**, 50–64.

Gudmundsson, A., 2011b. *Rock Fractures in Geological Processes*. Cambridge University Press, Cambridge. 592p

Gudmundsson, A., 2012. Magma chambers: Formation, local stresses, excess pressures, and compartments. *Journal of Volcanology and Geothermal Research*. **237-238**, 19–41.

Gudmundsson, A., Lecoeur, N., Mohajeri, N., 2014. Dike emplacement at Bardarbunga , Iceland, induces unusual stress changes, caldera deformation, and earthquakes. *Bulletin of Volcanology*, **76** 1–7.

Gudmundsson, A., 2015. Collapse-driven large eruptions. *Journal of Volcanology and Geothermal Research*. 1–26.

Haddadi, B., Sigmarsson, O., Devidal, J. L. 2015. Determining intensive parameters through clinopyroxene-liquid equilibrium in Grímsvötn 2011 and Bárðarbunga 2014 basalts. *Geophysical Research Abstracts*, **17**, EGU2015-5791-2

Hartley, M.E. & Thordarson, T., 2012. Formation of Oskjuvatn caldera at Askja, North Iceland: Mechanism of caldera collapse and implications for the lateral flow hypothesis. *Journal of Volcanology and Geothermal Research*. **227-228**, 85–101.

Hartley, M.E. & Thordarson, T., 2013. The 1874-1876 volcano-tectonic episode at Askja, North Iceland: Lateral flow revisited. Geochemistry, Geophys. Geosystems **14**, 2286–2309.

Heiken, G., Mccoy, F., 1984. Caldera development during the minoan eruption, Thira, Cyclades, Greece. *Journal of Geophysical Research*. **89**, 8441–8462.

Hernández-Pacheco, A., 1996. Geología y estructura del Arco de Taganana (Tenerife, Canarias), *Rev Soc Geol Espaœa*, **9**, 169–181.

Hess, K.U., Cordonnier, B., Lavallée, Y., Dingwell, D.B., 2008. Viscous heating in rhyolite: An in situ experimental determination. *Earth and Planetary Science Letters*, **275**, 121–126.

Hickey, J., Gottsmann, J., Del Potro, R., 2013. The large-scale surface uplift in the Altiplano-Puna region of Bolivia: A parametric study of source characteristics and crustal rheology using finite element analysis. *Geochemistry, Geophys. Geosystems* **14**. 540-555

Hickey, J. & Gottsmann, J., 2014. Benchmarking and developing numerical Finite Element models of volcanic deformation. *Journal of Volcanology and Geothermal Research*, **280**, 126–130.

Hjartardóttir, Á.R., Einarsson, P., Sigurdsson, H., 2009. The fissure swarm of the Askja volcanic system along the divergent plate boundary of N Iceland. *Bulletin of Volcanology*. **71**, 961–975.

Holohan, E., Schöpfer, M., Walsh, J., 2015. Stress evolution during caldera collapse : a Distinct Element Method perspective. *Earth Planetary Science Letters*, **15**, 2208.

Hobbs, T, 2011. *Stress induced seismic anisotropy around magma chambers*. PhD thesis, University of Bristol, UK

Holohan, E., Schöpfer, M. & Walsh, J., 2015. Stress evolution during caldera collapse : a Distinct Element Method perspective. *Earth and Planetary Science Letters*, **15**, 2208.

Hooper, A., Ófeigsson, B., Sigmundsson, F., Lund, B., Einarsson, P., Geirsson, H., Sturkell, E., 2011. Increased capture of magma in the crust promoted by ice-cap retreat in Iceland. *Nature Geoscience*. **4**, 783–786.

Hu, M., Ledesma, A., Marti, J., 1999. Conditions favouring catastrophic landslides on Tenerife (Canary Islands), *Terra Nova*, **11**, 106-111

Hutnak, M., Hurwitz, S., Ingebritsen, S.E., Hsieh, P. a., 2009. Numerical models of caldera deformation: Effects of multiphase and multicomponent hydrothermal fluid flow. *Journal of Geophysical Research*, **114**, 1–11.

Jellinek, A. M. & DePaolo, D.J., 2003. A model for the origin of large silicic magma chambers: precursors of caldera-forming eruptions. *Bulletin of Volcanology*. **65**, 363–381.

Jónsson, S., 2009. Stress interaction between magma accumulation and trapdoor faulting on Sierra Negra volcano, Galápagos. *Tectonophysics*, **471**, 36–44.

Key, J., White, R.S., Soosalu, H., Jakobsdóttir, S.S., 2011. Multiple melt injection along a spreading segment at Askja, Iceland. *Geophysical Research Letters* **38**, 1–5.

Kokelaar, P., 2007. Friction melting, catastrophic dilation and breccia formation along caldera superfaults. *Journal of Geological Society of London*. **164**, 751–754.

Konstantinou, K.I., Kao, H., Lin, C.H., Liang, W.T., 2003. Analysis of broad-band regional waveforms of the 1996 September 29 earthquake at Bardarbunga volcano, central Iceland: Investigation of the magma injection hypothesis. *Geophysical Journal International*. **154**, 134–145.

Konstantinou, K.I., Evangelidis, C.P., Liang, W.T., Melis, N.S., Kalogeras, I., 2013. Seismicity, Vp/Vs and shear wave anisotropy variations during the 2011 unrest at Santorini caldera, southern Aegean. *Journal of Volcanology and Geothermal Research*. **267**, 57–67.

Lipman, P.W., 1984. The Roots of Ash Flow Calderas in Western North America ' Windows Into the Tops of Granitic Batholiths *Journal of Geophysical Research*, **89**, 8801–8841.

Lipman, P.W., 1997. Subsidence of ash-flow calderas: relation to caldera size and magma-chamber geometry. *Bulletin of Volcanology*. **59**, 198–218.

Lockner, D. A., Byerlee, J. D., Kuksenko, V., Ponomarev, A., & Sidorin, A. 1992. Observations of quasistatic fault growth from acoustic emissions. *International Geophysics*, **51**, 3-31.

Manconi, A., Walter, T.R., Amelung, F., 2007. Effects of mechanical layering on volcano deformation. *Geophysical Journal International*, **170**, 952–958.

Marinoni, L.B. & Gudmundsson, A., 2000. Dykes, faults and palaeostresses in the Teno and Anaga massifs of Tenerife (Canary Islands). *Journal of Volcanology and Geothermal Research*. **103**, 83–103.

Marsh, B. D. 1989. Magma chambers. Annual Review of Earth and Planetary Sciences, **17**, 439-474.

Marti, J. & Gudmundsson, A., 2000. Ä adas caldera (Tenerife , Canary Islands): The Las Can an overlapping collapse caldera generated by magma-chamber migration, *Journal of Volcanology and Geothermal Research,* **103**, 161–173.

Marti, J., Mitjavilaf, J., Aranaj, V., 1994. Stratigraphy , structure and geochronology of the Las Canadas caldera (Tenerife , Canary Islands), *Geological Magazine,* **131**, 715–727.

Masterlark, T., 2007. Magma intrusion and deformation predictions: Sensitivities to the Mogi assumptions. *Journal of Geophysical Research*, **112**, 1–17.

McGarvie, D.W., 1984. Torfajokull: a volcano dominated by magma mixing. *Geology*. **12**, 685-688

Menand, T., 2011. Physical controls and depth of emplacement of igneous bodies: A review. *Tectonophysics,* **500**, 11–19.

Michon, L., Villeneuve, N., Catry, T., Merle, O., 2009. How summit calderas collapse on basaltic volcanoes: New insights from the April 2007 caldera collapse of Piton de la Fournaise volcano. *Journal of Volcanology and Geothermal Research*. **184**, 138–151.

Miller, A.D., Julian, B.R., Foulger, G.R., 1998. Three-dimensional seismic structure and moment tensors of non-double-couple earthquakes at the Hengill-Grensdalur volcanic complex, Iceland. *Geophysical Journal International,* **133**, 309–325.

Mitchell, T.M., Faulkner, D.R., 2008. Experimental measurements of permeability evolution during triaxial compression of initially intact crystalline rocks and implications for fluid flow in fault zones. *Journal of Geophysical Research,* **113**, 1–16.

Mitchell, T.M. & Faulkner, D.R., 2012. Towards quantifying the matrix permeability of fault damage zones in low porosity rocks. *Earth and Planetary Science Letters*, **339-340**, 24–31.

Mogi, K., 1958. Relations between the eruptions of various volcanoes and the deformations of the ground surfaces around them. *Bulletin of the Earthquake Research Institute*, **36**, 99-134

Mori, J., McKee, C., 1987. Outward-dipping ring-fault structure at rabaul caldera as shown by earthquake locations. *Science* **235**, 193–195.

Mori, J., White, R.A., Harlow, D.H., Okubo, P., Power, J.A., Hoblitt, R.P., Bautista, B.C., 1996. Volcanic earthquakes following the 1991 climactic eruption of Mount Pinatubo: Strong seismicity during a waning eruption. Fire Mud eruptions lahars Mt. Pinatubo, Philipp. *USGS publications*, 339–350.

Murase, T. & McBirney, A.R., 1973. Properties of some common igneous rocks and their melts at high temperatures. Geological Society of America Bulletin, **84**, 3563-3592

Nelson, P.P. & Glasar, S.D., 1992. Acoustic Emissions Produced by Discrete Fracture in Rock. International *Journal of Rock Mechanics and Mining Sciences*, **29**, 237–251.

Nomikou, P., Parks, M.M., Papanikolaou, D., Pyle, D.M., Mather, T. a., Carey, S., Watts, a. B., Paulatto, M., Kalnins, M.L., Livanos, I., Bejelou, K., Simou, E., Perros, I., 2014. The emergence and growth of a submarine volcano: The Kameni islands, Santorini (Greece). *GeoResJ*, **1-2**, 8–18.

Ofeigsson, B.G., Hreinsdottir, S., Sigmundsson, F., Fridriksdottir, H., Parks, M., Dumont, S., Arnadottir, T., Geirsson, H., Hooper, A., Roberts, M., Bennett, R., Sturkell, E., Jonsson, S., Lafemina, P., Jonsson, T., Bergsson, B., Kjartansson, V., Steinthorsson, S., Einarsson, P., and Drouin, V., 2015. Deformation derived GPS geodesy associated with Bardarbunga 2014 rifting event in Iceland. *Geophysical Research Abstracts*, **17**, EGU2015-7691-4.

Padrón, E., Hernández, P.A., Toulkeridis, T., Pérez, N.M., Marrero, R., Melián, G., Virgili, G., Notsu, K., 2008. Diffuse CO2 emission rate from Pululahua and the lake-filled Cuicocha calderas, Ecuador. *Journal of Volcanology and Geothermal Research*. **176**, 163–169.

Papazachos, B.C. & Panagiotopoulos, D.G., 1993. Normal faults associated with volcanic activity arc. *Tectonophysics* **220**, 301–308.

Papoutsis, I., Papanikolaou, X., Floyd, M., Ji, K.H., Kontoes, C., Paradissis, D., Zacharis, V., 2013. Mapping inflation at Santorini volcano, Greece, using GPS and InSAR. *Geophysical Research Letters*, **40**, 267–272.

Parks, M.M., Biggs, J., England, P., Mather, T. a., Nomikou, P., Palamartchouk, K., Papanikolaou, X., Paradissis, D., Parsons, B., Pyle, D.M., Raptakis, C., Zacharis, V., 2012. Evolution of Santorini Volcano dominated by episodic and rapid fluxes of melt from depth. *Nature Geosciences*, **5**, 749–754.

Parks, M.M., Moore, J.D.P., Papanikolaou, X., Biggs, J., Mather, T.A., Pyle, D.M., Raptakis, C., Paradissis, D., Hooper, A., Parsons, B., Nomikou, P., 2015. From quiescence to unrest: 20 years of satellite geodetic measurements at Santorini volcano, Greece *Journal of Geophysical Research*, **120**, 1309-1328

Peltier, A., Staudacher, T., Bachèlery, P., Cayol, V., 2009. Formation of the April 2007 caldera collapse at Piton de La Fournaise volcano: Insights from GPS data. *Journal of Volcanology and Geothermal Research*. **184**, 152–163.

Pollard, M., 2010. Learning to recognise volcanic non-eruptions. *Geology*, **38**, 287–288.

Pryor, R.., 2011. *Multiphysics modelling using COMSOL?: A first principles approach*, Jones and Bartlett education.

Pyle, D.M., 1997. The global impact of the minoan eruption of Santorini, Greece. *Environmental Geology*, **30**, 59–61.

Reynolds, H.I. & Gudmundsson, M.T., 2014. Variations in geothermal heat flux at Grímsvötn, Iceland, **16**, *EGU General Assembly*. Vienna.

Roche, O., Druitt, T.H., 2001. Onset of caldera collapse during ignimbrite eruptions. *Earth and Planetary Science Letters*, **191**, 191–202.

Saunders, S.J., 2001. The shallow plumbing system of Rabaul caldera: A partially intruded ring fault? *Bulletin of Volcanology*, **63**, 406–420.

Saunders, S.J., 2004. The possible contribution of circumferential fault intrusion to caldera resurgence. *Bulletin of Volcanology*. **67**, 57–71.

Scandone, R. & Malone., S.D., 1985. Magma supply, magma discharge and readjustment of the feeding system of Mount St. Helens during 1980. *Journal of Volcanology and Geothermal Research*, **3**, 239–262.

Segall, P., 2013. Volcano deformation and eruption forecasting. *Geological Society London, Special Publications*, **380**, 85–106.

Shelley, D., 1993. *Igneous and Metamorphic Rocks Under the Microscope: Classification, Textures, Microstructures and Mineral Preferred Orientation*, Springer.

Shinohara, H., 2008. Excess degassing from volcanoes and its role on eruptive and intrusive activity. *Review of Geophysics*. **46**.

Sigmundsson, F., 2006. *Iceland geodynamics: Outlook*. In: Iceland Geodynamics: Crustal Deformation and Divergent Plate Tectonics. 175–176.

Sigmundsson, F., Hooper, A., Parks, M., Spaans, K., Gudmundsson, G.B., Drouin, V., Samsonov, S., White, R.S., Hensch, M., Pedersen, R., Bennett, R.A., Greenfield, T., Green, R.G., Sturkell, E., Bean, C.J., Mo, M., Femina, P.C. La, Bjo, H., Pa, F., Braiden, A.K., Eibl, E.P.S., 2014. Segmented lateral dyke growth in a rifting event at Barðarbunga volcanic system, Iceland. *Nature*.

Simmons, G. & Cooper, H.W., 1978. Three Igneous Rocks, **15**, 145–148.

Siratovich, P. A., von Aulock, F.W., Lavallee, Y., Cole, J.W., Kennedy, B.M., Villeneuve, M.C. 2015. Thermoelastic properties of the Rotokawa Andesite: A geothermal reservoir constraint. *Journal of Volcanology and Geothermal Research*, **301**, 1–13.

Stevenson, D.S. & Blake, S., 1998. Modelling the dynamics and thermodynamics of volcanic degassing. *Bulletin of Volcanology*, **60**, 307–317.

Sturkell, E., Einarsson, P., Sigmundsson, F., Geirsson, H., Ólafsson, H., Pedersen, R., de Zeeuw-van Dalfsen, E., Linde, A.T., Sacks, S.I., Stefánsson, R., 2006a. Volcano geodesy and magma dynamics in Iceland. *Journal of Volcanol. Geothermal Research* **150**, 14–34.

Sturkell, E. & Sigmundsson, F., 2000. Continuous deflation of the Askja caldera, Iceland, during the 1983–1998 noneruptive period. *Journal of Geophysical Research*, **105**, 256-271.

Sturkell, E., Sigmundsson, F., Slunga, R., 2006b. 1983-2003 decaying rate of deflation at Askja caldera: Pressure decrease in an extensive magma plumbing system at a spreading plate boundary. *Bulletin of Volcanology*, **68**, 727–735.

Thirlwall, M. F., Singer, B. S., & Marriner, G. F. 2000. 39 Ar–40 Ar ages and geochemistry of the basaltic shield stage of Tenerife, Canary Islands, Spain. *Journal of Volcanology and Geothermal Research*, **103**, 247-297.

Trasatti, E., Giunchi, C., Agostinetti, N.P., 2008. Numerical inversion of deformation caused by pressure sources: Application to Mount Etna (Italy). *Geophysical Journal International*, **172**, 873–884.

Turcotte, D. L., & Schubert, G. 2002. *Geodynamics*, Cambridge University Press, New York 456 pp.

Vasseur, J., Wadsworth, F.B., Lavallée, Y., Hess, K.U., Dingwell, D.B., 2013. Volcanic sintering: Timescales of viscous densification and strength recovery. *Geophysical Research Letters*, **40**, 5658–5664.

Vinciguerra, S. et al., 2005. Relating seismic velocities, thermal cracking and permeability in Mt. Etna and Iceland basalts. *International Journal of Rock Mechanics and Mining Sciences*, **42**, 900–910.

Wadsworth, F.B., Vasseur, J., Aulock, F.W. Von, Hess, K.U., Scheu, B., Lavallée, Y., Dingwell, D.B., 2014. Nonisothermal viscous sintering of volcanic ash. *Journal of Geophysical Research*, **119**, 8792-8804

Walker, G.P.L., 1960. Zeolite zones and dike distributions in relation to the structure of the basalts of eastern iceland. *Journal of Geology*, **68**, 515–528.

Walker GPL. 1975 Intrusive sheet swarms and the identity of Crustal Layer 3 in Iceland. *Journal of the Geological Society of London*, **131**, 143-161.

Wilson, C.J.N., Houghton, B.F., McWilliams, M.O., Lanphere, M. a, Weaver, S.D., Briggs, R.M., 1994. Volcanic and structural evolution of Taupo Volcanic Zone, New Zealand: a review. *Journal of Volcanology and Geothermal Research*, **68**, 1–28.

Yun, S., Segall, P., Zebker, H., 2006. Constraints on magma chamber geometry at Sierra Negra Volcano, Galapagos Islands, based on InSAR observations. Journal of Volcanology and Geothermal Research **150**, 232–243

Appendix A

Additional experimental measurements

A1

Differential scanning calorimetry conducted at University of Liverpool (a) and Lancaster (b&c) University was used to provide insights into melting and crystallisation regimes in all rock types tested. All DSC results require a degree of interpretation (shown as annotation on each figure) that is highly subjective. Therefore these results were used to compliment TMA data, rather than act as stand-alone evidence for meting and annealing. Clear endothermic peaks indicate partial melting in AP and IB around 1100°C, and a peak at approximately 750°C in NKD matches well with the expected Tg temperature.

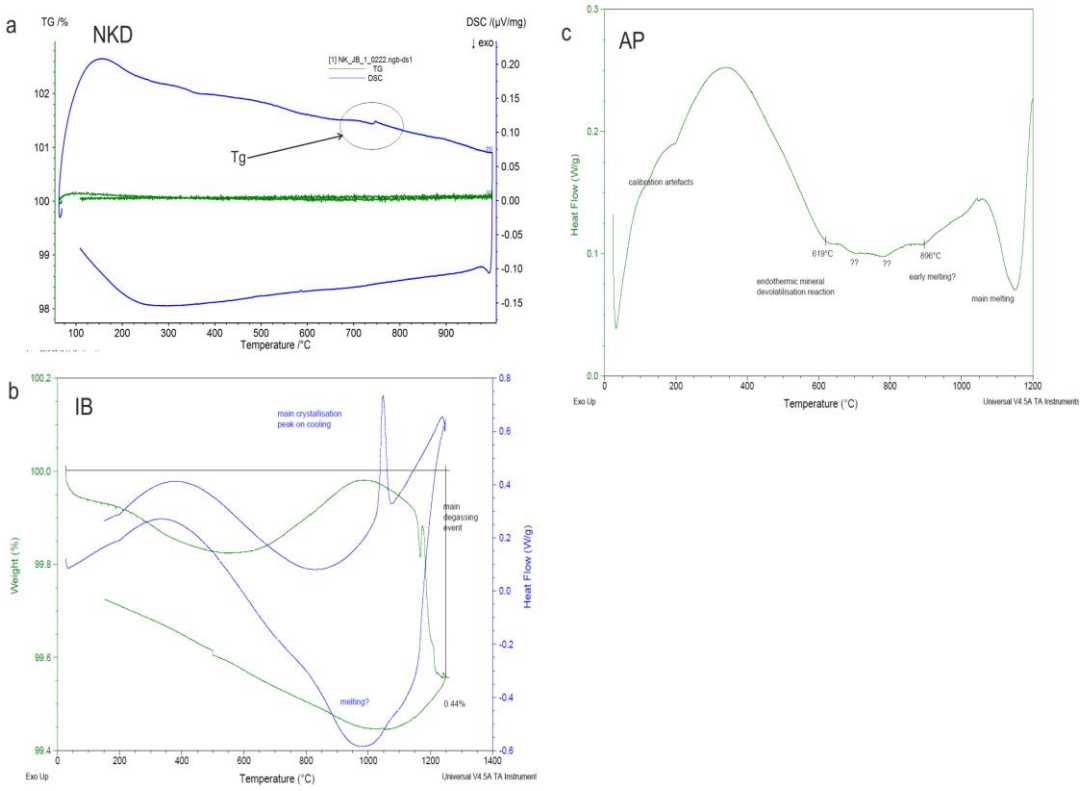

A2

Hot-stage microscopy results proved largely inconclusive for evidence of melting at high temperature. AP displayed no observational changes. Evidence of melt relaxation was observed in IB over a 10 minute period in the temperature range 1100°C to 1200°C. Here we see microscopic changes in the light passing through the edge of a pyroxene crystal, indicating in melt delamination around the crystal surface.

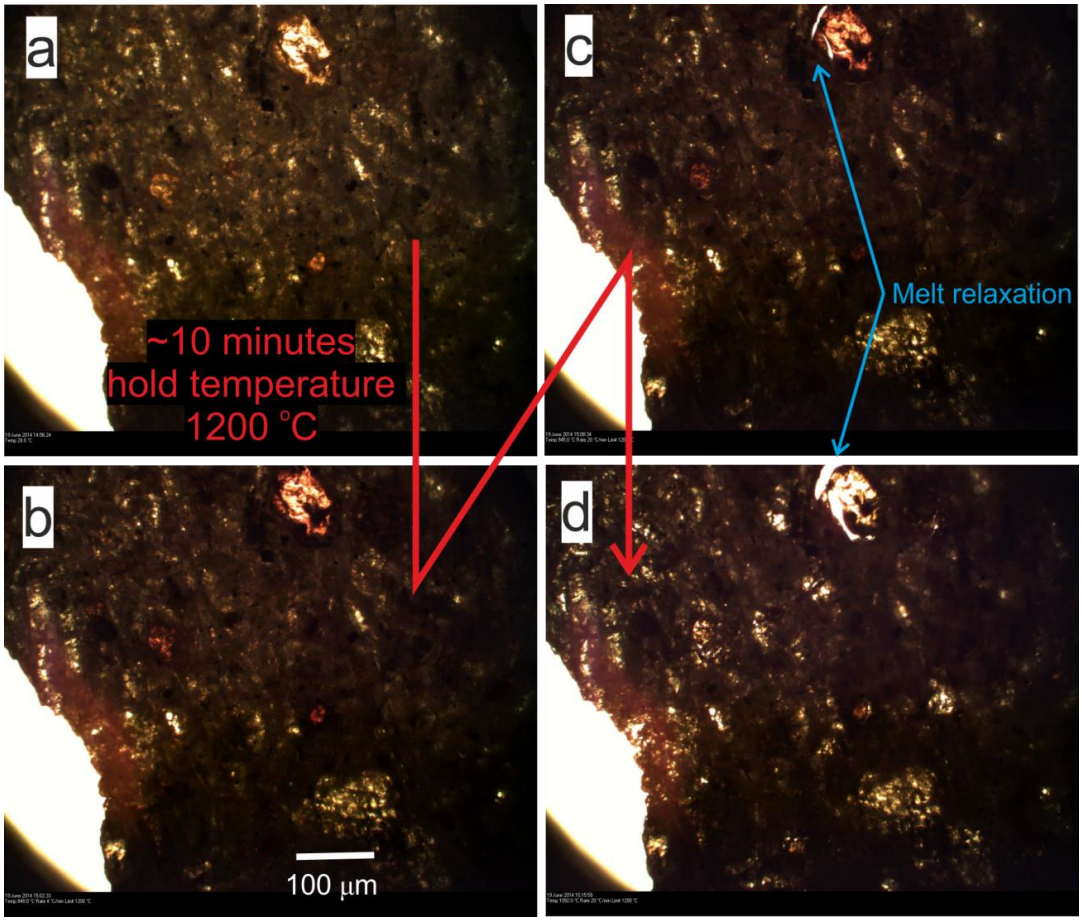

A3

Acoustic emission hit energy as a function of temperature for three rock types (Basalt, IB, Phonolite, AP, Dacite, NKD). Samples heated at a rate of 4˚C/min and cooled naturally (black dashed line). Onset of high energy bursts occur at the onset of cooling (blue lines) with most energy generated around 800˚C upon cooling. Similarly AE hit energy is shown on different scales for the same reason. Corresponding b values are calculated using Aki's maximum likelihood method for 200 hits at 100 hit intervals shown as orange lines.

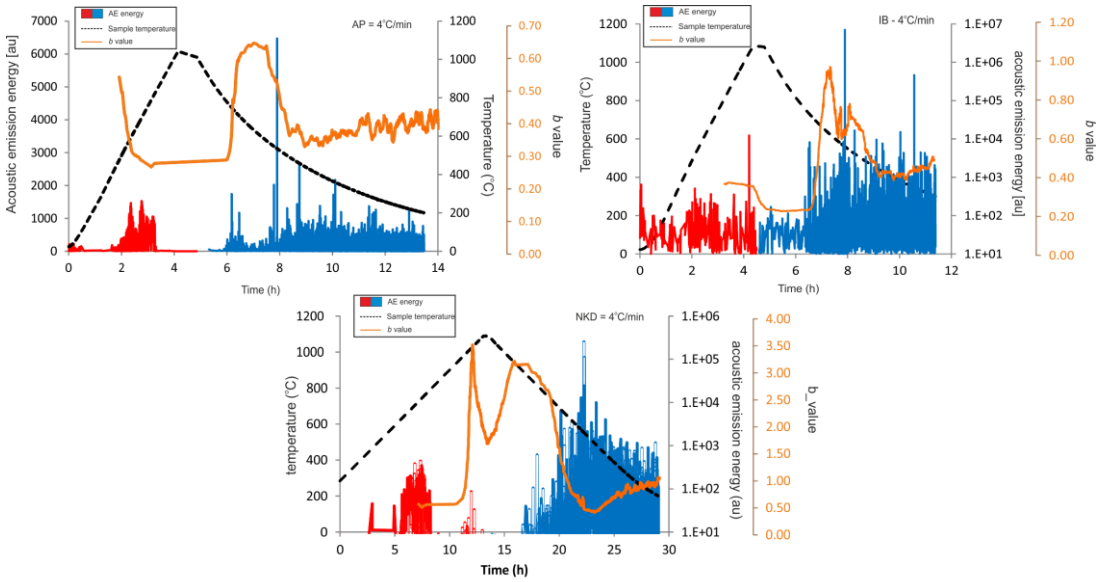

A4

SEM images and micro-crack analysis of a non-heat treated Anaga Phonolite. a) original SEM image x 250 zoom, c) x 500 zoom of the same area, b) crack map drawn in Adobe Illustrator and then imported into MATLAB, d) rose diagram showing the orientation and frequency of cracks.

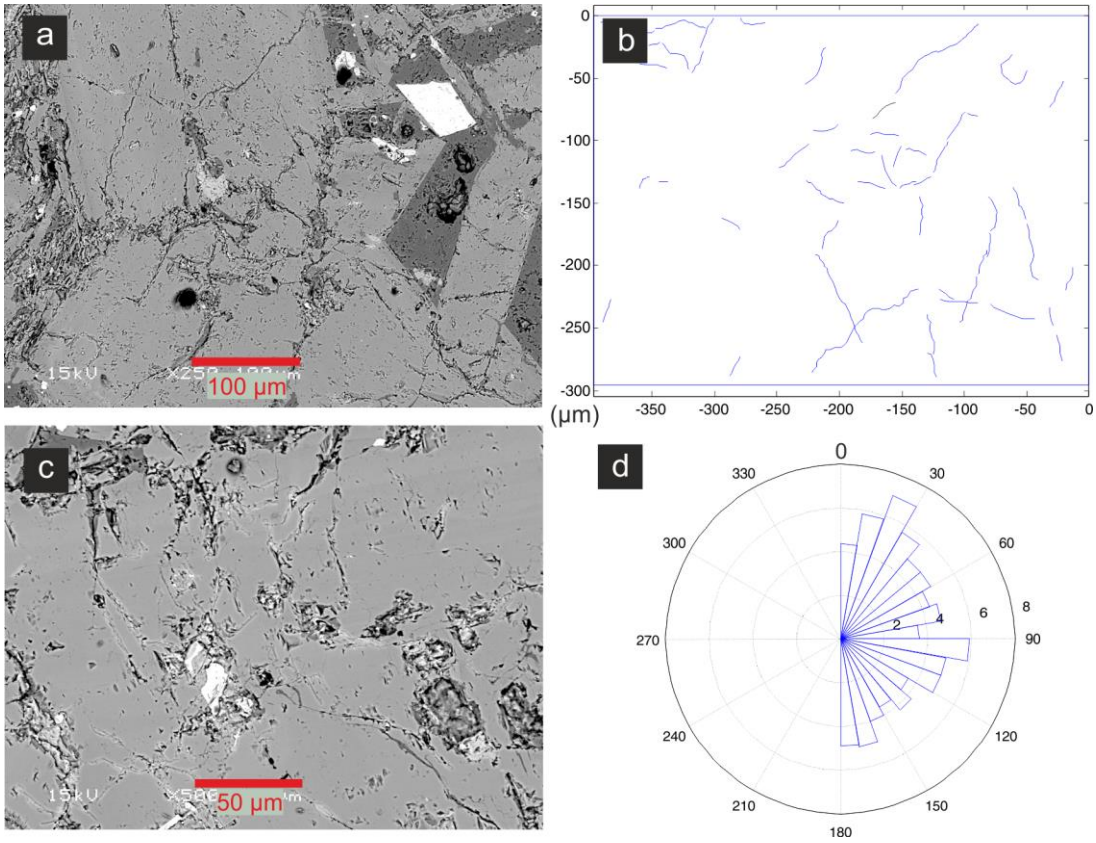

A5

SEM images and micro-crack analysis of a heat treated Anaga Phonolite. a) original SEM image x 250 zoom, c) x 500 zoom of a different area, b) crack map drawn in Adobe Illustrator and then imported into MATLAB, d) rose diagram showing the orientation and frequency of cracks.

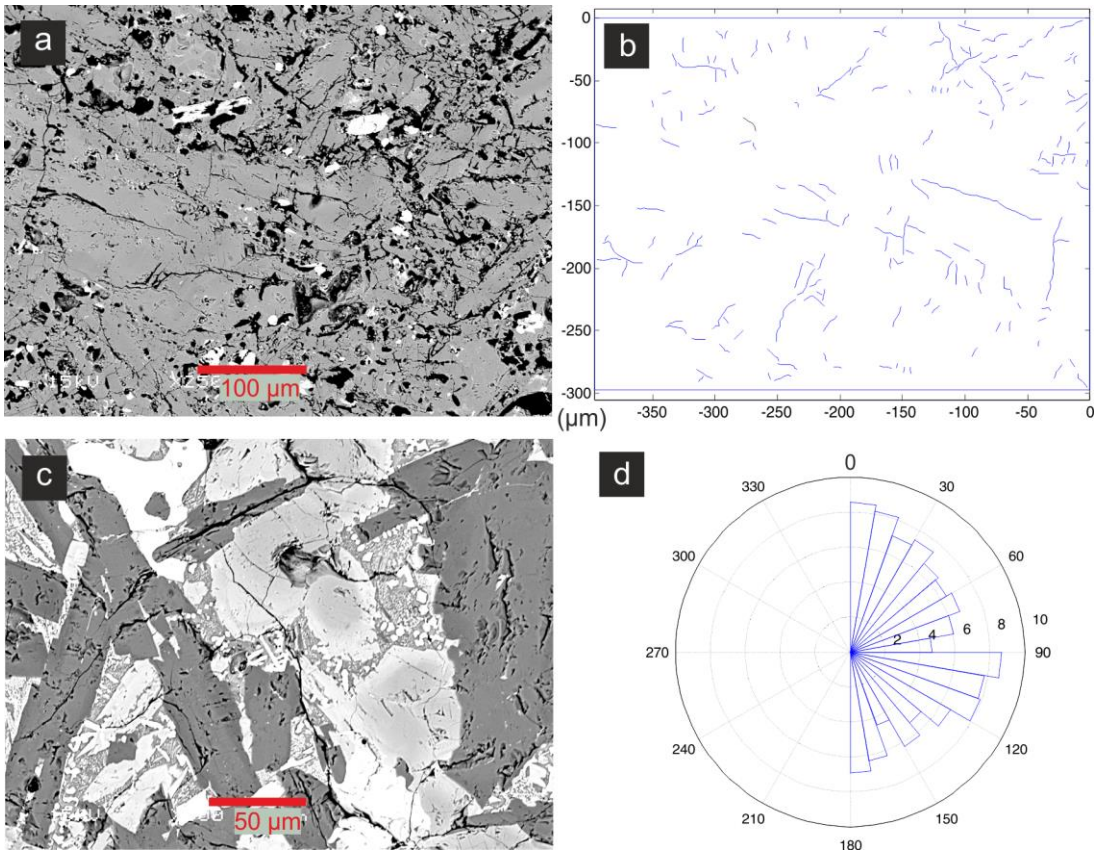

Appendix B

Supplementary data of Browning et al., (in press) (Chapter 3).

B1

The mean lava flow volume (common eruption) at Nea Kameni was calculated by averaging all known lava volumes. The original data was collected and published by Nomikou et al., (2014), partly using bathymetric datasets and satellite techniques.

Table 1. Kameni island lava volumes

Eruption (name or date)	**Duration (days)**	**Average volume (km3)**
Konus	-	0.00065
1950	23	0.000009
1939	682	0.01054
1925	949	0.082
NK	-	0.057
1866	1723	0.17
1707	1575	0.11
1570	-	0.068
Drakon	-	0.0164
NK East	-	0.044
726	-	0.02
46	-	0.139
	Total Average Volume	**0.06**

Appendix C

Supplementary data of Browning and Gudmundsson (2015) (Chapter 3)

C1

Numerical setup showing the continuation of an inclined sheet that has been captured within the fault and propagated vertically up the fault.